THE UNIVERSITY OF TOKYO

Doctoral Dissertation 博士論文

A Comparative study of novel materials for electrochemical reduction of CO_2 in aqueous solutions

(電解液中二酸化炭素の電気化学還元に適した新規材料の比較検討）

Research Supervisor Prof. Yoshiaki Nakano

Department of Advanced Interdisciplinary Studies,
Graduate School of Engineering,
University of Tokyo

学籍番号 37-167168

Fahd Sikandar Khan

Acknowledgements

I would like to thank Prof. Yoshiaki Nakano for giving me the opportunity to do this research in his lab at the Department of Advance Interdisciplinary Studies. I found Prof Nakano to be a kind supervisor who always had a very friendly attitude. My background knowledge in electrochemistry was limited but Prof. Nakano gave me the chance to conduct research and study in the very exciting field of electrochemical reduction of CO_2.

I would also like to thank my co-supervisor, Prof. Masakazu Sugiyama who showed great patience and provided great insight on my research. He was always considerate and eager to help and discuss, for which I will always be grateful.

Next, I wish to acknowledge the help and guidance of Prof Katsushi Fuji. Discussions with him and his thoughtful suggestions played a significant part in the progress of my research.

It is important for me to acknowledge former Nakano group members Mr. Heng Zhong and Mr. Hiroshi Hashiba from whom I learned a great deal. Their experience in this field and their willingness to help was very pivotal in my doctoral research and I remain indebted to their assistance.

Nakamura San and Koike San were two senior members of the PEC group when I had joined the lab and I am grateful for their help in setting up my experiments.

I am grateful to PEC group members Yuki Imazeki, Maruyama San, Dr. Sato who helped me in working with the lab equipment. My gratitude to all the other members of the Nakano-Suigyama Lab for their support. Despite the cultural differences and language restrictions, I was able to have a great experience.

I also want to show my appreciation to the Japanese Government for the financial support provided to me to carry out my research. The assistance of Yamanaka San and the RCAST office was also very important for my comfortable research life in Japan and I am sincerely grateful to them.

Lastly, I would like to thank my parents, family and friends. Their constant encouragement and support was the most important factor in the successful completion of my studies.

Abstract

Carbon dioxide (CO_2) is the main greenhouse gas emitted through human activities and is also present in the atmosphere as part of the Earth's carbon cycle. There is a natural carbon cycle which exists between the soil, plants and oceans but the increased human activities over the centuries have started to alter this carbon cycle. The addition of more CO_2 to the atmosphere and its impact on our planet necessitates finding novel and efficient materials which can convert CO_2 into valuable chemicals. This process dubbed as 'Artificial Photosynthesis' essentially replicates the use of sunlight towards the generation of value-added chemicals and thus helps to capture the energy in chemical bonds, a form of energy that can be readily stored and transported and can help to mitigate the challenges posed to climatic cycle by CO_2.

In the light of this objective, my first doctoral study was to reduce CO_2 under natural intermittent solar irradiation in order to observe its impact on the progression of CO_2 reduction with time. A novel Maximum Power Point Tracking circuit, working on Perturbation and Observation algorithm was employed to track and transfer the optimum V,I values on to the EC cells. The bulk metal electrodes of tin and gold were used to produce formic acid and carbon-monoxide, respectively. The maximum Solar-to-CO_2 reduction of about 4.3% efficiency was achieved. The affect of current density on the fardaic efficiency of CO_2 reduction reaction (CO_2RR) was studied along with the analysis of each individual sections in the solar-to-fuel scheme.

The next chapter changed the focus from bulk metal to metal nanoparticles. Copper (Cu) and Gold (Au) were chosen as the target materials for the nanoparticles. Au mainly produces CO as a result of CO_2RR and since CO acts as an intermediate specie for the generation of higher-order carbon products, copper was also chosen due to its higher propensity towards electron-intensive reactions. Arc Plasma Deposition (APD) technique was used to deposit the nano-sized particles on the surface of the substrate since the APD technique is characterized by highly ordered deposition of nanoparticles. The first phase of the study employed the conducting FTO glass as the substrate material. The nanoparticles were co-deposited in order to allow a composite reaction for the CO_2 reduction. The FTO-based electrodes were able to generate formic acid as a result of CO_2RR with a faradaic efficiency of up to 60%. FTO suffered surface deterioration during the experiments however the results did demonstrate improved activity towards CO_2RR and so the second half of this study focused on a more stable, metal-based substrate of In-Sn alloy. Exclusive deposition of Cu and Au was also carried in addition

to the co-deposition so that the individual roles of the Cu and Au nanoparticles could be determined. The results reflected that Cu nanoparticles were the most active towards increasing the faradaic efficiency as well as the production rates for formic acid during CO_2RR.

Since a great deal of research has been reported on metal catalysts, our subsequent focus shifted towards the use of new materials that are abundantly available in foreseeable future so as to ensure elemental sustainability for long-term commercial use of CO_2 reduction. Chalcogenide sulfide glass was chosen as the working electrode material for the reduction of CO_2. The experimental data from these samples showed that due to their amorphous structure, chalcogenide glasses were not active for photocatalytic reduction, possibly because of high recombination rate. The IV data from the bulk sulphides reflected that the current generation was directly proportional to the area of the ohmic contact between the copper wire and sample surface. Furthermore, the CO_2 reduction sites also seemed to be proportional to the distance from the ohmic contacts and meant that the surface further away from the ohmic contact, visually showed lesser formation of bubbles. The only product from CO_2RR was the gaseous CO, which formed at a maximum faradaic efficiency of about 15%. The next half of this study used the particle form of the same glass structures and was formed by crushing the bulk material into micron-sized particles. These particles were then stirred in nafion and ethanol solution. The resulting mixture was drop casted onto a Carbon Paper (CP) substrate and then left to dry. CP along with being hydrophobic, is very conductive and hence an ideal choice for a substrate. The experimental results showed that the product selectivity had changed and formic acid with up to 26% faradaic efficiency was observed for this particle-based chalcogenide electrode.

The sulfide chalcogenides were found to be active for CO_2RR but in order to increase the product selectivity, our research direction switched to chalchogenide oxide materials that were reported to be more stable than sulfides. Cuprous oxide was employed since it is a stable oxide form of Cu and has been shown to generate a product range different from metals. The gas phase analysis after the experimental results showed presence of ethylene (C_2H_4) along with hydrogen and CO while formic acid was observed during the liquid phase analysis. Methane was interestingly not observed and this demonstrated that the use of micron-sized catalyst particles on carbon paper had an impact on the adsorption of certain transitory species during CO_2 reduction which in turn affected the reduction mechanism of CO_2 and thus the selection of end-products.

Another chalchogenide oxide material tested was Co_3O_4 since Co has two different

oxidation states within its oxide structure and this could impact the charge transfer mechanism and hence CO_2 reduction. Acetic acid and formic acid were observed as a result of CO_2RR however the results remained inconsistent and it was our conclusion that the redox couple mechanism of the catalyst was responsible for reducing CO_2 which caused inconsistency in results.

In summary, this doctoral research explored the usability of bulk and nano-range metal catalysts along with new and novel chalcogenide-based electrode structures for electrochemical reduction of CO_2. The comparative analysis of these various studies show that the goal of a carbon-neutral society can be achieved by the electrochemical reduction of CO_2 using renewable energy-source of CPV in tandem with copper-based catalysts deposited on metal alloy substrate. Such a solar-to-fuel setup can pave the way for an environmentally-sustainable world.

Contents

CHAPTER 1

Introduction

1.1 Introduction to CO_2 emissions

Carbon dioxide (CO_2) is the primary greenhouse gas emitted through human activities. In 2014, CO_2 accounted for about 80% of all greenhouse gas emissions from human activities. This gas is also naturally present in the atmosphere as part of the Earth's carbon cycle, (the natural circulation of carbon among the atmosphere, oceans, soil, plants, and animals) however the increased human activities over the centuries have begun to alter the carbon cycle. This extremely dangerous disturbance is being caused both by adding more CO_2 to the atmosphere and by affecting the ability of natural sinks, like forests, to remove CO_2 from the atmosphere. While it is true that CO_2 emissions originates from a variety of natural sources, the human-related emissions are responsible for the increase that has occurred in the atmosphere since the industrial revolution.

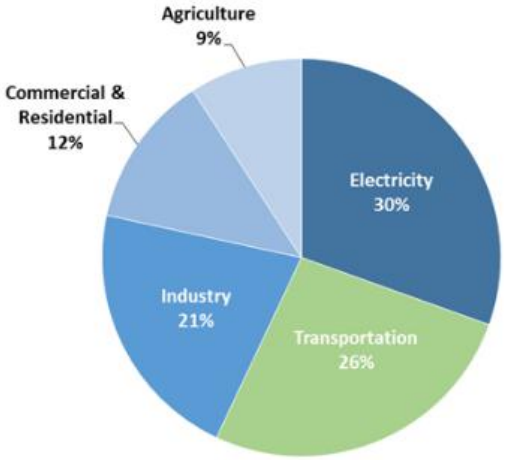

Fig. 1.1: CO_2 emissions sources sources by sector [1]

The principal human activity that emits CO_2 is the combustion of fossil fuels (coal, natural gas, and oil) for energy and transportation. This is in addition to the certain industrial processes and land-use changes which also emit CO_2. The main sources of CO_2 emissions are listed in the sub-sections [1]. Fig. 1.1 provides a visual summary of the sector-wise contribution of such emissions.

1.1.1 Electricity

It is a significant source of energy all over the world and is used to power all human activity; homes, industries, markets etc. The combustion of fossil fuels to generate electricity is the largest single source of CO_2 emissions. United States happen to be the single biggest source of CO_2 emissions and its power sector had accounted for about 37% of total U.S. CO_2 emissions and 30% of total U.S. greenhouse gas emissions over the last decade. The type of fossil fuel used to generate electricity also allows variation in emission of CO_2 amounts. For example a coal-fired power plant emits more than the amount of CO_2 generated from a plant operating on natural gas [1].

1.1.2 Transportation

The combustion of fossil fuels such as gasoline and diesel to transport people and goods is the second largest source of CO_2 emissions. The world average of emissions generated from transportation sector accounts for about 31% of total CO_2 emissions and 25% of total greenhouse gas emissions. This category includes transportation sources such as highway vehicles, air travel, marine transportation, and rail.

1.1.3 Industry

Many industrial processes emit CO_2 through fossil fuel combustion. Several processes also produce CO_2 emissions through chemical reactions that do not involve combustion, for example, the production and consumption of mineral products such as cement, the production of metals such as iron and steel, and the production of chemicals. Fossil fuel combustion from various industrial processes accounted for about 15% of total CO_2 emissions and 12% of total greenhouse gas emissions. It is pertinent to note that industrial processes also use electricity and therefore indirectly cause the emissions from the electricity production.

Carbon dioxide is constantly being exchanged among the atmosphere, ocean, and land surface as it is both produced and absorbed by many microorganisms, plants, and animals. However, emissions and removal of CO_2 by these natural processes tend to balance the cycle but ever since the Industrial Revolution, which began around 1750, human activities have contributed substantially to climate change by adding CO_2 and other heat-trapping gases to the atmosphere. [1]

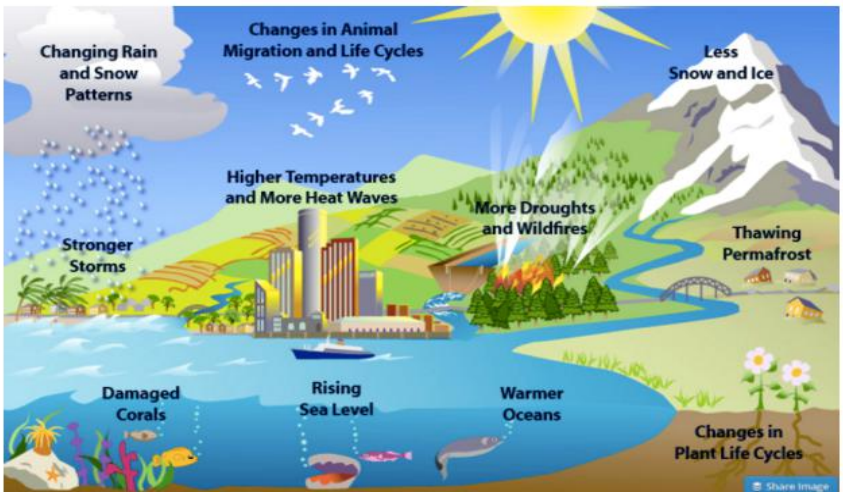

Fig. 1.2: Affects of CO_2 emission on eco-system [2]

1.2 Existential threat posed by CO_2 [2]

The current state of CO_2 emissions show the highest trajectory envisaged by climate scientists and this means that if nothing is done to reduce emissions significantly over the coming decades, over half of common plants and one-third of the animals could see a serious decline. These assessments have been made by estimating the current and future geographical ranges of nearly 50,000 widespread and common species to see how rising temperatures are likely to affect their territorial limits as defined by the sort of climate they are adapted to live in.

It has been concluded that plants, amphibians such as frogs and toads, and reptiles such as lizards are the groups that are likely to suffer the most from a changing climate because of their relative vulnerability to rising temperatures and inability to move rapidly from one territory to another. One of the first detailed assessments of how common species will be able to cope with climate change, showed that many of these animals and plants are very important since they perform fundamental 'ecosystem services' such as cleaning up water supplies and decomposing waste produce. Current research also predicts that climate change will greatly reduce the diversity of even very common species found in most parts of the world. This loss of global-scale biodiversity would significantly impoverish the biosphere and the ecosystem services it provides.

The effect of rising global temperatures alone cannot account for the changes since other symptoms of climate change such as extreme weather events, pests and diseases mean that current estimates are conservative. Animals in particular may decline more as the rising temperature predictions will be compounded by a loss of food from plants. There will also be a knock-on effect for humans because these species are important for things like water and air purification, flood control, nutrient cycling and eco-tourism [1].

It can thus be concluded that immediate and stringent mitigation – measures to reduce CO_2 emissions – can substantially avert the biodiversity disaster facing our planet and our very existence. A recent study published in the Nature Climate Change had concluded that the faster mitigation measures are enacted, the more time plants and animals will have, to adapt to any unavoidable rise in temperatures. A lot of academic work been done that provides crucial evidence of how swift action to reduce CO_2 and other greenhouse gases can prevent the biodiversity loss by reducing the amount of global warming to 2 degree centigrade rather than 4 degree centigrade.

The linkage between temperature and CO_2 concentration has been observed and studied extensively by multiple agencies. Following the trend of CO_2 concentration in the

atmosphere, the temperature keeps increasing over the years. The 10 hottest years have all occurred since 1997. Besides, rising sea levels and melting of glaciers are two obvious results of global warming while other less noticeable effects have also gradually increased. Examples are changes in precipitation patterns, especially near the equator, more volatile storms, ocean acidification, dwindling of crop yields, increasing morbidity from heat or diseases like malaria, biodiversity loss, and others. Recent extreme weather patterns are an example. The 2013-2014 winter was the 34th coldest in U.S., according to National Oceanic and Atmospheric Administration (NOAA) report, and probably the coldest in the past 20 years, yet the following year, 2014, was the hottest ever recorded [3]. The temperature is predicted to keep rising, and according to the Intergovernmental Panel on Climate Change (IPCC) the predicted average surface temperature rise by 2100 will likely reach 4 ºC if counter measures are not immediately taken [1].

1.3 Solutions to this menace [3]

There is no single solution to global warming, which is primarily a problem of heat-trapping due to carbon dioxide (CO_2). However the technologies and approaches outlined below can help to bring down the emissions of these gases.

1.3.1 Increasing energy efficiency

The energy used to power, heat, and cool our homes, businesses, and industries is the single largest contributor to global warming. Such technologies can be improved in a manner which would require less energy to get the same levels of production, service, and comfort. Such a method could have a vast potential to save both energy and money.

1.3.2 Going green in transportation

This sector's emissions have increased at a faster rate than any other energy-using sector over the past decade. Some solutions that can be used, include improving efficiency (km per gallon) in all modes of transport, switching to low-carbon fuels, and reducing vehicle miles traveled through better and bigger mass transportation systems.

1.3.3 Litting up with renewables

Solar, wind, geothermal and bio-energy are available around the planet and numerous studies have shown that renewable energy has the technical potential to meet the vast majority of our energy needs. Renewable technologies are increasingly becoming cost-effective, and can also help to create jobs while reducing pollution.

1.3.4 Phasing out fossil fuel electricity

Dramatically reducing our use of fossil fuels is important to tackle the climate change. There are many ways to begin this process. Key action steps include: not building any new coal-burning power plants, initiating a phased shutdown of coal plants starting with the oldest and dirtiest, and capturing and storing carbon emissions from power plants. The technology exists to store carbon emissions underground or through chemical capture. It has not been deployed on a large scale but recently active research and developmental projects have open great business opportunities in this field. Demonstration projects to test the viability and costs of this technology for power plant emissions are worth pursuing.

1.3.5 Managing forests and agriculture

Taken together, tropical deforestation and emissions from agriculture represent nearly 30 percent of the world's heat-trapping emissions [1]. Global warming can be fought by reducing emissions from deforestation and forest degradation and by making our food production practices more sustainable.

1.3.6 Exploring nuclear

Nuclear power results in fewer global warming emissions and an increased share of nuclear power in the energy mix could help reduce global warming. However the nuclear technology poses serious threats and the recent unfortunate accident at the Fukushima Diaichi plant in Japan illustrates the potential consequences to health and the environment if this approach goes awry.

1.3.7 Developing and deploying new low-carbon and zero-carbon technologies

Research into and development of the next generation of low-carbon technologies will be critical to CO_2 reductions in global emissions. Current research on battery technology, new materials for solar cells, harnessing energy from novel sources like bacteria and algae, and other innovative areas could provide important breakthroughs.

1.3.8 Ensuring sustainable development

The contributions of the developed to the least developed countries vary dramatically and so it is important that for those nations that tend to make the transition between the various development stages, they are also mindful of the risks of CO_2 emissions and should inculcate the low-carbon program within the growth stages. Since the capacities to confront climate change are different, a successful global compact on climate change must include financial assistance from richer countries to poorer countries to help make the transition to low-carbon development pathways and to help adapt to the impacts of climate change.

1.4 The most viable solution

In review of the present scenario as well as the financial investments required for changing the current infrastructure, the most viable option right now is to use captured CO_2 to synthesize sustainable hydrocarbon fuels [4].

Liquid fuels (e.g. petroleum, diesel and others) have a great advantage since they have intrinsic chemical energy content and they can be stored and transported with relative ease since no changes are required to the current infrastructure. It is possible to reduce CO_2 with electricity, to synthesize sustainable fuels. However it is important to use a renewable energy source for the power required to reduce CO_2 into fuels. Renewable energy would ensure that no net contribution to CO_2 emissions would take place. An idealized energy cycle is one where the CO_2 gas is transformed into carbon neutral liquid fuels or renewable electricity is used to produce hydrogen and the subsequent Fischer-Tropsch process would produce liquid fuels [5].

The energy requirements for the production of such renewable fuels depend on the methods that are used to capture CO_2 and to produce hydrogen. A recent survey of the available scientific reports has concluded that it is commercially possible to chemically transform CO_2 from a detrimental greenhouse gas causing global warming into a valuable, renewable and inexhaustible carbon source of the future, allowing environmentally neutral use of carbon fuels and derived hydrocarbon products [6].

Therefore, the aim throughout the world is currently to improve the capture and storage technologies which will allow large amount of CO_2 to be obtained, and then can be used as a feedstock for innovative conversion to synthetic fuels.

The shortage in the reserves of oil and natural gas as well as the strong dependence of developed countries on fossil fuels is also a main reason for considerable interest in the development of renewable energy resources. One of the primary and inexhaustible energy sources is sunlight reaching the earth's surface [7]. However, two of the main problems of sunlight, as a source of energy, are the circadian cycle between day and night together with the dependence on seasons and weather conditions and the low sunlight power that makes it necessary to accumulate the energy for long periods with large surfaces. Considering the problems associated with the direct use of sunlight, the two general strategies to use sunlight as a primary energy source are both based on the accumulation of solar energy. The first consists of converting photons from the sun into electrical energy that can be stored in batteries or supercapacitors as well as in any other form of conventional mechanical energy already existing for electricity storage [8]. Particularly for transportation, where high energy powers are required, there is a necessity to accumulate sunlight into an intermediate energy vector that can be, for instance, charge capacitors or batteries [9]. However, one of the main problems associated with this strategy is the limited resources of lithium and other metals that are currently employed in batteries, making sustainability problematic.

An alternative to store sunlight as electrical energy is to convert photons from the sun into chemical energy. The concept of solar fuels refers to the production of chemicals that can release chemical energy using sunlight as a primary energy resource. While water reduction only affords hydrogen, there are a series of products that can be formed from CO_2 reduction. The list includes oxygenated C1 and C2 compounds, such as oxalic acid, formic acid, formaldehyde, methanol and CO. In addition to these compounds, methane and C2–C4 saturated and unsaturated hydrocarbons can also be obtained.

1.5 Electrochemical Reduction of CO_2 (CO_2RR)

The process of CO_2 conversion can be achieved by a number of ways including chemical methods [10-12], by photocatalytic or electrocatalytic reduction [13-14] and by a few other means [15-16]. However, there are certain barriers which pose a problem for the practical application of CO_2 capture, conversion, and utilization. These impediments include (a) the high costs of CO_2 capture, separation, purification, and transportation to user sites; (b) the high energy requirements for CO_2 chemical/electrochemical conversion; (c) limitations in market size and investment incentives; (d) lack of industrial

commitment to enhance CO_2-based chemicals; and (e) insufficient socio-economic driving forces [17].

Despite theses challenges, CO_2 capture, conversion, and utilization is still recognized as a feasible and promising cutting-edge area of exploration in energy and environmental research. In recent years, CO_2 conversion using electrochemical catalysis approaches has attracted great attention because of several advantages:

(a) the process is controllable by electrode potentials and reaction temperature;

(b) the supporting electrolytes can be fully recycled so that the overall chemical consumption can be minimized to simply water or wastewater;

(c) the electricity used to drive the process can be obtained without generating any new CO_2—sources include solar, wind, hydroelectric, geothermal, tidal, and thermoelectric processes;

and (d) the electrochemical reaction systems are compact, modular, on-demand, and easy for scale-up applications.

However, challenges remain, such as the slow kinetics of CO_2 electroreduction, even when electrocatalysts and high electrode reduction potential are applied, the low energy efficiency of the process due to the parasitic or decomposition reaction of the solvent at high reduction potential and high energy consumption.

Researchers have recognized that the biggest challenge in CO_2 electroreduction is low performance of the electrocatalysts (i.e., low catalytic activity and insufficient stability). Electrochemical reduction of CO_2 can proceed through two-, four-, six-, and eight-electron reduction pathways in gaseous, aqueous, and non-aqueous phases at both low and high temperatures. The major reduction products are carbon monoxide (CO), formic acid (HCOOH) or formate (HCOO), oxalic acid ($H_2C_2O_4$) or oxalate (C_2O_4 in basic solution), formaldehyde (CH_2O), methanol (CH_3OH), methane (CH_4), ethylene (CH_2CH_2), ethanol (CH_3CH_2OH), as well as others.

The chemical reactivity of CO_2 is low however the equilibrium potentials of CO_2 reduction are not very negative as compared with that of the hydrogen evolution reaction (HER) in aqueous electrolyte solutions. Common CO_2 reduction half-reactions and their standard reduction potentials referenced to SHE at pH 0 are shown in figure 1.3.

Half-reaction	E^0 (V)
$CO_2 + H_2O + 2e^- \rightarrow CO + 2OH^-$	-0.11
$CO_2 + H_2O + 2e^- \rightarrow HCOO^- + OH^-$	-0.02
$CO_2 + 5H_2O + 6e^- \rightarrow CH_3OH + 6OH^-$	0.03
$CO_2 + 6H_2O + 8e^- \rightarrow CH_4 + 8OH^-$	0.16
$2CO_2 + 5\ H_2O + 8e^- \rightarrow CH_3COO^- + 7\ OH^-$	0.12
$2CO_2 + 9H_2O + 12e^- \rightarrow C_2H_5OH + 12OH^-$	0.08
$2CO_2 + 8H_2O + 12e^- \rightarrow C_2H_4 + 12OH^-$	0.07
$2CO_2 + 10H_2O + 14e^- \rightarrow C_2H_6 + 14OH^-$	0.14
$3CO_2 + 13H_2O + 18e^- \rightarrow C_3H_7OH + 18OH^-$	0.09

Fig. 1.3: CO_2 reduction half-reactions and their standard reduction potentials [15]

Nevertheless, CO_2 reduction does not take place easily, and the actual electrolysis potentials for CO_2 reduction are much more negative in most cases than the equilibrium ones. One of the major reason is considered to be the formation of intermediate species $CO_2^{\cdot-}$, formed by an electron transfer to a CO_2 molecule, possible at highly negative potential, such as –2.21 V vs. saturated calomel electrode (SCE) [14]. The standard potentials for CO_2 reduction and HER, estimated from thermodynamic data, increase linearly with pH. HER prevails over CO_2 reduction in acidic solutions, and most studies of CO_2 reduction in aqueous media have been conducted in neutral pH region. As both CO_2 reduction reactions (CO2RR) and hydrogen evolution reactions (HER) occur within the same potential region, the competition between the two reactions becomes one of the biggest challenges [18] in electrochemical CO_2RR research. A good catalyst would thus be highly selective toward CO_2RR and therefore be a poor catalyst for HER, but on most metal electrodes, this is not the case [18].

The electrochemical conversion of CO_2 has the potential to utilize large quantities of emissions that would otherwise be free to enter the atmosphere however this process needs to be implemented successfully and should be economically viable. From a cost analysis standpoint, the energy cost and the market rates for each product must be considered. While researchers cannot do much about the state of the chemical market, the goal is to find an efficient catalyst that would lower production costs and therefore allow for a profit to be made. Thus the quest remains to find an efficient catalyst which could be selective toward a single product and be highly active at low overpotentials.

The next chapter in this dissertation would discuss in detail the most important factors, issues and considerations that contribute in the research for electrochemical reduction of CO_2.

1.6 References

1. NRC (2010). Advancing the Science of Climate Change. National Research Council. The National Academies Press, Washington, DC, USA.
2. Connor S., Life on Earth under threat from CO_2. Independent newspaper. Op-Ed. 13th May 2013.
3. Solutions to Global warming. Climate Hot Map Annual report. 2011.
4. Olah G.A. *Angewandte Chemie Int. Ed.* 2005, **44**, 2636-2639
5. Jiang Z, Xiao T, Kuznetsov VL, Edwards PP. Turning carbon-dioxide into fuel. Philosophical Transaction of the Royal. Society A 2010; 368: 3343-3364
6. Olah GA, Goeppert A, Surya Prakash GK. *The Journal of Organic Chemistry,* 2002, 74, 487-498.
7. Gust D., Moore T., Moore A., *Acc. Chem. Res.* 2001, **34**, 40–48.
8. Heller, A. *Acc. Chem. Res.* 1981, **14**, 154–162.
9. Wrighton M.S., Miller, J.S., *American Chemical Society:Washington, DC, USA*, 1982, 99–132.
10. Centi G., Perathoner S., *Catal. Today*, 2009, **148**, 191–205
11. Omae I., *Coord. Chem. Rev*., 2012, **256**, 1384–1405.
12. Concepcion J., House R., Papanikolas J., Meyer T., *Proc. Natl. Acad. Sci. U. S. A*., 2012, **109**, 15560–15564.
13. Schneider J., Jia H., Muckerman J., Fujita E., *Chem. Soc. Rev*., 2012, **41**, 2036–2051.
14. Mori K., Yamashita H., Anpo M., *Rsc. Adv*., 2012, **2**, 3165–3172.
15. Aresta M., Carbon dioxide recovery and utilization, *Springer*, 2003.
16. Halmann M., Chemical Fixation of Carbon Dioxide-Methods for Recycling CO_2 into Useful Products, *CRC*, 1993.
17. Song C. S., *Catal. Today,* 2006, **115**, 2–32.
18. Schreier M., Curvat L.Giordano F.. Gratzel M. et. al., *Nat. Communs.*, 2015, **6**, 7236-7248

CHAPTER 2

Important Factors in the electrochemical study of CO_2 reduction

Multiple factors influence the electrochemical reduction of CO_2 and thus it is important to discuss those factors in detail before moving on to the experimental stage.

2.1 Choice of Electrode

The primary factor in the electrochemical reduction of CO_2 is the choice of the working electrode, which can efficiently transfer charges to the CO_2 molecules saturated in the electrolyte and determine the ease with which the redox reaction can take place. Historically, bulk metal electrodes have been the most extensively used and based on the products, these metal surfaces can be divided into three groups of materials (visually shown in figure 2.1):

1) materials that primarily produce CO as a result of CO_2 reduction

2) materials that primarily produce HCOOH as a result of CO_2 reduction

3) materials that produce carbon-oxygen compounds to hydrocarbons or alcohols as a result of CO_2 reduction

Studies dedicated to the reduction of CO_2 to CO have been extensively studied on metal catalysts [1] such as Au [2-3] and Ag [4-5]. More recently metal-nitrogen-carbon (M-NC) based catalysts have also been reported to be active for CO evolution [6-7] due to structural motifs. These metal-nitrogen-carbon based structures can increase the selectivity of the CO_2 reduction reaction (CO_2RR) over the competing hydrogen evolution reaction (HER) [8].
Formic acid production via the reduction of CO_2 is also a very popular topic and can easily take place on metal catalysts [1]. Specifically, Sn [9-10] and Pb [11] have been reported to be very active towards formic acid production.
The distinction between CO or formic acid products has also attracted theoretical considerations [12]. The intermediates COOH and OCHO (other notations may be HCOO* or HCO*O*) have been proposed for CO and formic acid products, respectively [13]. The asterik represents electron vacancy. The further reduction of the intermediates has been suggested to be constrained by the ability of the catalyst to bind CO, while not having adsorbed hydrogen (H_{ads}). Among the metals, only Cu is able to fulfill these unique attributes of being able to further reduce CO while having affinity towards H_{ads} to the minimum [7]. However, the product distribution from CO reduction depends on the Cu catalyst pre-treatment. While the Cu foil catalyst [1] produces mainly methane (CH_4)

and ethylene (C_2H_4), the main product of a catalyst composed of reduced copper oxides (Cu-OD) [14] is ethanol (C_2H_5OH) and only a small fraction of methane and ethylene. In addition, different plasma treatments of Cu show tuneability of the ethylene to methane ratio [15]. Besides the Cu catalysts, Fe-NC and Mn-NC based catalysts show traces of methane [7] however all catalysts suffer from HER. To better understand the difference between production of multiple carbon products, researchers have tried to study the experimental impact of structural facets [16] and have also analyzed theoretical considerations [17-18]. Many different proposals for the reaction schemes have been given on the basis of these studies [19-20]. Figure 2.1 shows the classification of various metals according to the products produced by them during CO_2 reduction.

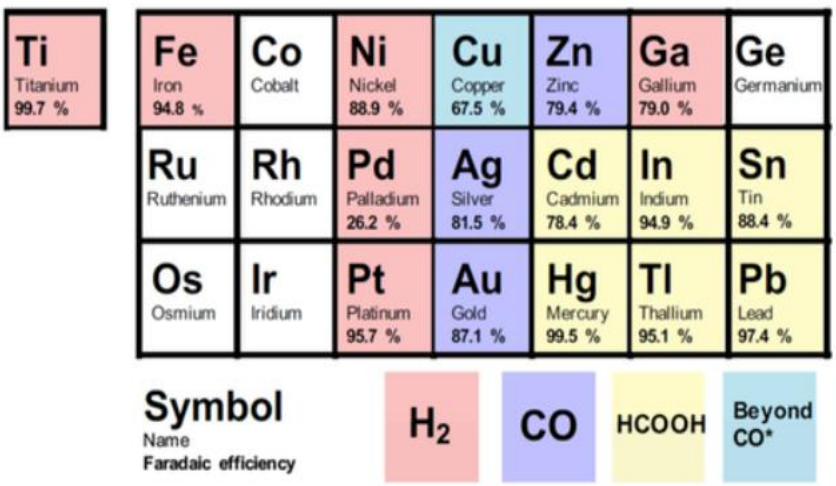

Fig. 2.1 Major product classification of metal catalysts for electroreduction of CO_2 [1]
Four groups are identified: H_2 (red), formic acid (yellow), CO (blue) and beyond CO (cyan), which will be applied throughout the work.

2.2 Electrode potential

The standard redox potentials for various CO_2 reduction reactions have already been shown in table 1.1. In real-time experimental conditions, the actual thermodynamic potentials are usually much more negative due to the overpotentials. The actual CO_2 electrochemical reduction on metal electrodes occurs at potentials more negative than 1

V [21-24]. During the initial phase, there were various studies dedicated on the impact of selectivity of products and reaction rates on the applied cathodic potential [1, 25-26]. These results have usually remained reproducible [27-29] because this data is obtained by performing relatively short potentiostatic experiments from 30 min to 1 hour which permits the catalytic prowess of the working electrodes to remain intact and is usually not sufficient time to allow changes on the surface start to become apparent. These changes include surface poisoning, variations in electrode crystal orientation etc.

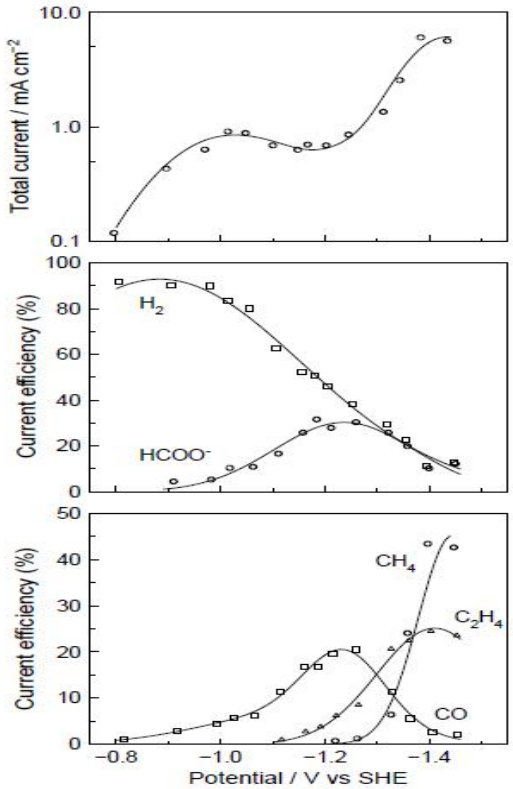

Fig. 2.2 Current Efficiency vs Applied potential for various products from CO_2RR [1]

Figure 2.2 provides a good example on the dependence of selectivity of products on the applied cathodic potential. The electrode is Cu metal and it can be seen that at less negative presents i.e. low overpotentials, the products obtained as a result of CO_2RR are HCOOH and CO since the requirement of electrons per molecule is limited to 2 only. Hydrogen Evolution Reaction (HER) remains active as well however as the cathodic potential becomes more negative, CH_4 and C_2H_4 starts to evolve in increased faradaic efficiencies and continue up to -1.5 V vs SHE. And as the selectivity towards electron-intensive products starts to increase, the HER as well as CO and HCOOH begin to decrease. However at more negative potentials (figure 2.3), the HER again begins to

rise which leads to overall decrease in CO_2RR products [26]. The increase in HER is attributed to the limitations in mass transport of dissolved CO_2 (0.033 M at 25 °C and 1 atm pressure in aqueous solutions [30]) to the electrode surface, that allows hydrogen evolution to be the exclusive product at extremely negative cathodic potentials.

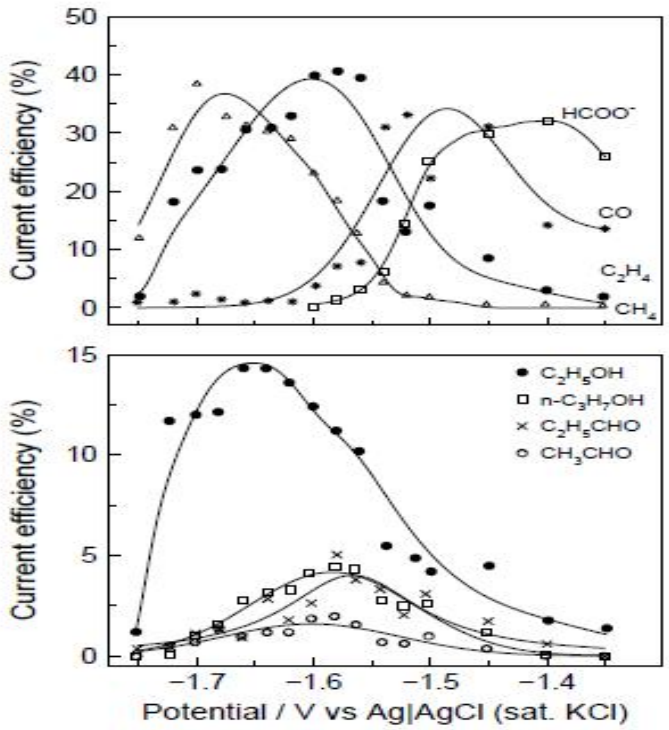

Fig. 2.3 Current Efficiency vs Applied potential for various products from CO_2RR [26]

A study by Kuhl *et al.* [31] had reported that C1 product such as CH_4 also increase at more negative potentials compared to the C2 products which was due to the favorable PCET (proton coupled electron reactions) that occur between the adsorbed intermediate species of CO_2 reduction. The C-C bond coupling required for production of multi-carbon products is decreased as a result of more hydrogen adsorbtion which limits such bond coupling and enhance HER evolution.

The dependence of the applied cathodic potentials on the selectivity of the produced products provides insight on the reduction mechanism as well. The formation of CO and HCOOH starts to occur at low overpotentials but decrease at more negative potentials in parallel with increase in electron-intensive reactions. This reflects that CO and HCOOH

may be the intermediate species in multi-carbon products. There have been reports which investigate the electrochemical reduction of CO [23, 32-33] and $HCOO^-$ [1, 34] and as a result, it was discovered that CO is indeed an initial reactant for hydrocarbon formation. However on the other hand $HCOO^-$ was found to not be readily reducable. It was on the basis of these results that it was hypothesized that CO is a necessary intermediate specie and that formate did not play a role in the formation of multi-carbon products. Experimental evidence has also shown that adsorbed CO exists during formation of multi-carbon products [35-37].

Another important factor pertains to the fact that the onset of C_2H_4 always occurs at a more positive potential than methane. This has been suggested because of the two carbon atoms in C_2H_4 and which require coupling of C-C bond between intermediates like CO_{ads}, COH_{ads} etc.. Methane does not require such a bond and thus the pathways between these products (methane and ethylene) should be separate. Therefore, it can be suggested that the local rate determining step (RDS) for C_2H_4 evolution must be taking place at smaller overpotentials. It has also been suggested that the local RDS for C_2H_4 is a pH-independent electron mediated dimerization step between two C-containing intermediates, likely CO_{ads}, while the local RDS step for CH_4 is the pH-dependent proton-electron transfer to either CHO_{ads} or COH_{ads} [38-39].

The studies on electrode potential dependence show that most common products of aqueous electrochemical CO_2 reduction on Cu metal are H_2, CO, HCOOH, CH_4 and C_2H_4. Other works have reported the production of ethanol with decent efficiencies, e.g. around 10% current efficiency [26, 31], and multi-carbon products C2 and C3 oxygenates (with efficiencies as low as 1% or less). It has also been reported these multi-carbon products have a similar potential dependency as C_2H_4 [31].

2.3 Choice of Electrolyte

Electrolyte parameters have been extensively reported and a large range of different electrolyte systems have been used [40-43]. They can be classified as either aqueous or non-aqueous solvents. The type of solvent used can have very significant influence on the reaction mechanism and product selectivity. Non-aqueous solvents have been mainly studied for the electrochemical reduction of CO_2 reduction because of the much higher CO_2 solubility achievable in non-aqueous media. In such a system, the mass transport limitations can be alleviated. Furthermore, the non-aqueous solvents can suppress the

parasitic hydrogen evolution because of the limited presence of water. The absence of H_2O can also allow CO_2 reduction to be studied at temperatures below 0 °C. In relation to the study of reaction mechanisms, non-aqueous solvents are arguably preferred due to the ability to accurately regulate the concentration of water [23,40]. Some good examples of non-aqueous solvents investigated for CO_2 reduction are propylene carbonate, acetonitrile, dimethylformamide (DMF), dimethylsulfoxide (DMSO) and methanol. In these nonaqueous media, with the exception of methanol [41-43] the usual CO_2 reduction products on various electrodes including Cu are carbon-monoxide, formic acid, oxalic acid etc [44]. Oxalic acid (or oxalate) is prevalent in non-aqueous electrolytes, which is due to the lack of dimerization promotion of $CO_2^{\bullet-}$ to $(COO)^{2-}$ over the formation of formate. Additionally CO is formed, not by reaction with water but through an oxygen-carbon coupling mechanism between $CO_2^{\bullet-}$ and CO_2, forming CO and CO^{2-}, respectively [45-46]. The product selectivity is highly sensitive to the presence of water, and its introduction into the non-aqueous electrolyte increase the production of formic acid over oxalic acid and CO [45], and also helped to partially reduce the oxalic acid to glycolic and glyoxylic acid [46]. In addition to the non-aqueous electrolytes, ionic liquids, e.g. EMIM-BF_4, are also gaining significant attention [47-48],. Such electrolytes help to reduce CO_2 reduction by lowering the energy of the $CO_2^{\bullet-}$ intermediate [49].

Using non-aqueous systems for CO_2 reduction is very costly since the non-aqueous solvents are definitely more expensive than water however, such electrolytes are not used up during the reaction and hence are recyclable [49]. Aqueous-based electrolytes are on a comparative scale, much cheaper and easier to prepare. So despite the relatively poor CO_2 solubility, aqueous electrolytes are extensively used in many studies. The most commonly used aqueous electrolyte is bicarbonate, specifically $KHCO_3$. It is interesting that the reason for this choice is never explicitly explained, other than the fact that it was regularly used by early researchers [23, 33, 50- 52] and is now followed by many others. Another important reason is the common use of caustic KOH as an absorbent for CO_2 in its capture and concentration [53-55]. KOH after the absorption process ultimately becomes $KHCO_3$ through the $CO_2/HCO_3^-/CO_3^{2-}$ equilibria. Therefore doing reduction of CO_2 directly on a CO_2 saturated $KHCO_3$ solution is logical for future CO_2 capture, concentration and reduction technologies. Since the HCO_3^- and CO_3^{2-} species definitely exist in CO_2 saturated aqueous solutions, another possible reason for using $KHCO_3$ is to simplify the electrolyte system by limiting any anionic effects to HCO_3^- and CO_3^{2-} species, since it is possible that additional anions such as halides [56-58], sulfides [59] and sulfates [60] can influence results by adsorption on the electrode surface. Other types

of electrolytes occasionally used are phosphate buffers, e.g. KH_2PO_4 + K_2HPO_4, halides, e.g. KCl, and sulphates, e.g. K_2SO_4. By comparison, these electrolytes have shown to give distinct product selectivities on Cu electrodes. At similar electrolyte concentrations (0.1 M) and reaction conditions (5 mA/cm^2 , 19 °C), Hori et al. [1, 61] showed that in KCl and K_2SO_4, C_2H_4 and alcohols are much more selective than CH_4 (C_2H_4/CH_4 ratio of 4.2 and 3.7, respectively), while H_2 production is significantly suppressed **(**table 2.1**).**

In $KHCO_3$ electrolyte, C_2H_4 and CH_4 are equally selective (ratio 1.02), but the selectivity to alcohols is significantly lower. In phosphate buffer (0.1 M K_2HPO_4), CH_4 is much more selective than C_2H_4 (ratio 0.11), however H_2 is found to be predominant (72.4%). The electrode potential required for the current is about 200 mV less negative in 0.1 M K_2HPO_4. Such effects in the phosphate buffer are further accentuated when a higher concentration (0.5 M K_2HPO_4) is used. Apart from the anion interactions with the Cu surface, e.g. anion adsorption, the differences in reaction selectivities presented in table 2.1 are largely attributed to the indirect influence of the electrolyte's buffer capacity, which is also dictated by the type of anion and its concentration.

Table 2.1 Faradaic Efficiency vs electrolyte solution for various products from CO_2RR on Cu [1]

Solution	Conc. M	pH	Potential V vs.SHE	Faradaic efficiency (%)							
				CH_4	C_2H_4	EtOH	PrOH	CO	$HCOO^-$	H_2	Total
$KHCO_3$	0.1	6.8	−1.41	29.4	30.1	6.9	3.0	2.0	9.7	10.9	92.0
KCl	0.1	5.9	−1.44	11.5	47.8	21.9	3.6	2.5	6.6	5.9	99.8
KCl	0.5		−1.39	14.5	38.2			3.0	17.9	12.5	
$KClO_4$	0.1	5.9	−1.40	10.2	48.1	15.5	4.2	2.4	8.9	6.7	96.0
K_2SO_4	0.1	5.8	−1.40	12.3	46.0	18.2	4.0	2.1	8.1	8.7	99.4
K_2HPO_4	0.1	6.5	−1.23	17.0	1.8	0.7	tr	1.3	5.3	72.4	98.5
K_2HPO_4	0.5	7.0	−1.17	6.6	1.0	0.6	0.0	1.0	4.2	83.3	96.7

Since the electrochemical reduction of CO_2 in aqueous solutions produces OH^- or consumes H^+ ions, the electrode and local pH at the electrode surface is almost always higher than the bulk solution pH due to concentration gradients of species during reaction evolution. Although dissolved CO_2 reacts with OH^- to form $HCO3^-$, this reaction is relatively slow (rate constant, k = 7.7 × 103 M^{-1} s^{-1} [62]), therefore the interfacial pH is usually considered to not be in equilibrium. In electrolytes with buffering abilities such as phosphate buffers and $KHCO_3$, the rise in electrode-electrolyte interface pH is

considered to be less extreme compared to those without, such as KCl and K_2SO_4. Between phosphate buffers and $KHCO_3$ at similar concentrations, phosphate buffers generally have a stronger buffer capacity compared to $KHCO_3$ at the neutral pH range. Most CO_2 reduction studies have been performed at this neutral pH since the pKa of $H_2PO_4^-$ (pKa 7.21) is closer to 7 than the pKa of HCO_3^- (pKa 10.33) [63]. Hence, it can be shown (by numerical modelling for example [64]) that the interfacial pH at the electrode surface is highest in non-buffering electrolytes (0.1 M KCl and 0.1 M K_2SO_4), followed by 0.1 M $KHCO_3$, and 0.1 M phosphate buffers at similar reaction conditions. Because the buffer capacity increases with concentration, the interfacial pH in the more concentrated 0.5 M phosphate buffer would be the lowest. As the reaction selectivity is strongly influenced by pH, lower pH increase the selectivity towards H_2 and CH_4 due to a higher availability of H^+ /H_{ads} [65-66] and the pH-dependence of the CH_4 formation pathway, the observed differences in reaction selectivity between the various electrolytes can largely be explained by the rise in electrode pH by the buffering capacities of the electrolyte, which is a function of the anion and its concentration.

Many researchers overlook the pH impact and since the reaction selectivity is very much influenced by pH, it can lead to wrong analysis whereby observed changes are incorrectly attributed to other factors. The impact of the local electrode pH during CO_2 reduction has been shown by various studies by Hori's group [1, 67]. More recently, there have been more efforts dedicated to understanding the affects of local pH [66, 68-70]. Most of the studies have chosen K^+ based salts as the electrolyte, but it has been reported that the choice of the cation greatly influence the product selectivity of CO_2 reduction on metal electrodes [71]. In table 2.2, the selectivity to C_2H_4 and alcohols generally increases while that to H_2 and CH_4 decrease, with cation size (the cation size increases from $Li^+ < Na^+ < K^+ < Cs^+$). The influence of the cation is also clearly shown by the increasing C_2H_4/CH_4 ratio and electrode potential (toward more positive potentials) with cation size at similar current densities.

In general, the observed effects of the cations are thought to be derived from the propensity of the cations for specific adsorption on the electrode surface, which is basically governed by their hydration powers. Therefore Li^+ being the smallest cation among the four is more easily hydrated compared to Cs^+, which is the largest [72]. Because small cations are easily hydrated, the surrounding water molecules prevent them from being specifically adsorbed on the electrode surface. Larger sized cations have a higher propensity to be adsorbed due to their lower hydration powers [73]. Such an

adsorption causes the potential at the outer Helmholtz plane (OHP) to become more positive, which decreases the concentration of H^+ at the OHP [73]. Since the adsorbed cations are positive in charge, they repel H^+ away from the cathode surface. Thus because of limiting the supply of H^+ /H_{ads} at the electrode surface, the selectivity to H_2 and CH_4 will decrease as expected. On the other hand, smaller cations which do not adsorb on the electrode surface do not impede the supply of H^+ /H_{ads}. In fact, the water molecules surrounding smaller cations may actually increase the supply of H^+ to the electrode surface. This could explain the high selectivity to H_2 in $LiHCO_3$ compared to the other bicarbonate electrolytes (table 2.2). The adsorption of cations is also thought to stabilize anions through ion-pairing on the electrode surface [74]. In the case of CO_2 reduction, adsorbed cations could stabilize the $CO_2^{\bullet-}$ anion intermediate, and help to improve CO_2 reduction rates and efficiencies [75]. This causes an increase in total current efficiency toward CO_2 reduction, which further decreases the overpotentials (at similar current densities of 5 mA/cm^2) with cation size from Li^+ to K^+. The enhancements in overall CO_2 reduction with increasing cation size however is not strong between K^+ and Cs^+ and in fact the presence of Cs^+ may had decreased the overall selectivity toward CO_2 reduction. This was also demonstrated by Kyriacou *et. al.* [71], that the greater adsorption propensity of Cs^+ limits the available reaction sites for CO_2 reduction and hence the overall CO_2 reduction activity.

Similar impact of cations have also been observed during CO_2 reduction on Hg [76], and more recently on Ag electrodes [75]. These observations can explain why K+ based salts, and in particular $KHCO_3$, are usually used as electrolytes for aqueous CO_2 reduction on Cu electrodes.

Table 2.2 Faradaic Efficiency vs bicarbonate electrolyte solution for various products from CO_2RR on Cu [37]

Electrolyte	Potential V vs. SHE	Faradaic efficiency (%)								C_1/C_2
		CH_4	C_2H_4	CO	EtOH	PrOH	$HCOO^-$	H_2	Total	
$LiHCO_3$	−1.45	32.2	5.2	tr	1.6	tr	4.7	60.5	104.2	6.19
$NaHCO_3$	−1.45	55.1	12.9	1.0	4.2	0.6	7.0	25.1	105.9	4.27
$KHCO_3$	−1.39	32.0	30.3	0.5	10.9	1.6	8.3	14.5	98.1	1.06
$CsHCO_3$	−1.38	16.3	30.5	2.4	7.2	4.4	15.8	24.4	101.0	0.53

2.4 Impact of pH and CO_2 concentration

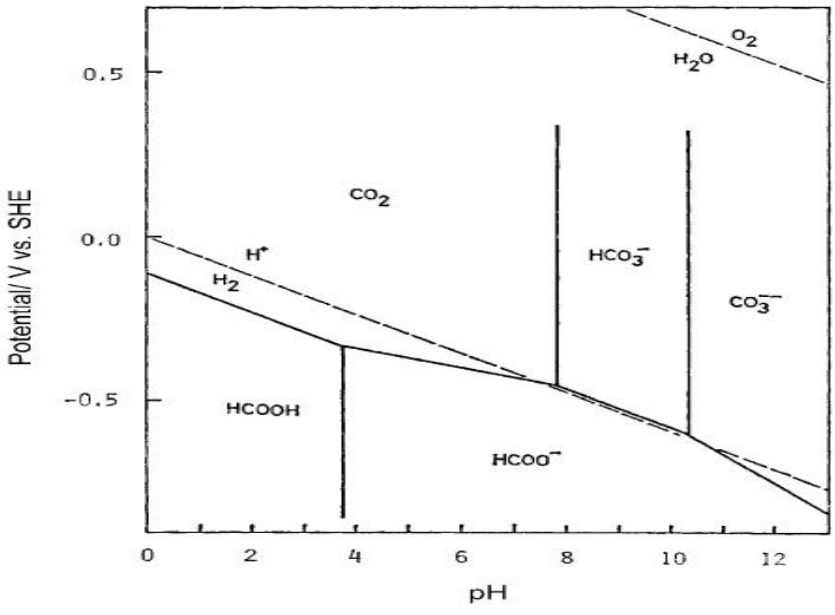

Fig. 2.4 pH-potential diagram of CO_2 [23]

As explained earlier, the pH is an important parameter in the electrochemical reduction of CO_2 since H^+/H_{ads} are required reactants for CO_2 reduction to hydrocarbons. There are various pathways for different products produced via electrochemical reduction of CO_2 and some of these pathways have been suggested to be strongly dependent on the pH, especially when the local RDS of a particular pathway involves H^+/H_{ads}. As shown earlier, the most common effect of the pH is seen in the change in reaction selectivity from H_2 and CH_4 to C_2H_4 and alcohols with increasing pH. While the enhancement of the HER at lower pH can be adequately explained by the increase in H^+/H_{ads} available at the electrode surface, the preference for CH_4 at lower pH and that for C_2H_4 and alcohols at higher pH is not easy to explain since the formation of each of these products require multiple steps of hydrogenation during the pathway. The relationship between the change in selectivity from CH_4 to C_2H_4 and its relationship with the local pH was extensively studied by Hori *et. al.* [1, 22, 61, 67]. It was reported that CH_4 formation rates are dependent on both the electrode potential and pH, while that for C_2H_4 and ethanol are dependent only on the electrode potential [77]. The onset potential of C_2H_4 formation was also an important point for investigation and it was found to be more positive than that of CH_4 [26-27, 78]. Additionally, it was also shown that the Tafel slope or transfer coefficient for the formation of CH_4 is usually different to that for C_2H_4. In order to explain the reason behind the observations, it was suggested that the formation of C_2H_4 follows a different generation pathway from CH_4, and that the C_2H_4 pathway is independent of pH. However on the other hand, the CH_4 pathway is pH dependent since it involves H^+ [78]. It was also suggested that the local RDS on the C_2H_4 pathway is the formation of a CO dimer from two CO molecules and it is pH independent because the electron transfer is uncoupled from H^+ ions. For CH_4, it was suggested that the local RDS on the CH_4 pathway is the breaking of the C−O bond in the formyl intermediate, CHO_{ads}, which deals with the proton-coupled electron transfer (PCET) and is thus effected by the pH. Another interesting observation in a study with high local pH was that the formation of both H_2 and CH_4 moves towards lower overpotentials [65]. It was also reported that these overpotential shifts in H_2 and CH_4 are similar in relation to the changes in pH, signifying some interdependent relationship. The decrease in overpotentials for H_2 formation at very high pH can generally be explained by a shift in the mechanism from proton discharge (which is pH dependent) to water discharge (which is pH independent), and this shift is suggested to occur around pH 11−12 [79]. Therefore, it is possible that the same shift in CH_4 generation exists at higher pH.

The reduction of CO_2 is dependent and limited by the diffusion of CO_2 to the electrode surface at high current densities. To overcome issues related to the mass transport, the concentration of CO_2 in aqueous electrolytes can be enhanced by reducing the temperature and by augmenting the pressure of CO_2. The solubility of CO_2 increases with lowering of temperatures and so many studies have focused on carrying out electrochemical reduction of CO_2 at lower temperatures (as low as −4 °C) [80-81]. The decrease in temperature has been reported to enhance the current efficiencies on various metal electrodes. Metals like Ni and Ti that generally produce H_2 in ambient conditions, start to produce CO, CH_4 and HCOOH at temperatures around 0−2 °C [51, 82]. These observed improvements in reduction of CO_2 reduction can thus be attributed to the higher concentrations at reduced temperatures. Hori *et. al*. [61] had reported that the efficiency for CH_4 improves with decreasing temperatures, while selectivity of other gases decrease. Selectivity towards formic acid is not dependent on temperature while methane and hydrogen selectivity remain similar [23, 82]. However it has been observed [80] that the partial current density toward reduction of CO_2 remains steady between −4 and 15 °C at a constant potential of −2.0 V vs Ag/AgCl. Current density toward hydrogen generation however decreases with lowering the temperatures. Similarly it was observed that the formation rate of methane is half but current efficiency twice higher at 0 °C compared to 22 °C. Therefore it can be suggested that the higher reduction of CO_2 is probably not due to increase in CO_2RR but because the hydrogen evolution is suppressed. This hydrogen suppression is due to an increase in surface coverage of CO_{ads}, which inhibits the HER by impeding reaction sites [83] due to the higher concentration of CO_2 at low temperatures. This suppression of hydrogen evolution is consistent with the shift of electrode potential from −1.33 V vs SHE at 40 °C to −1.39 V vs SHE at 0 °C at the same current density. This enhancement of overpotentials with temperature decrease may be due to the requirement of thermal activation for some of the CO_2 reduction reactions [81].

The concentration of CO_2 in aqueous electrolytes can also be increased by raising the CO_2 pressure in accordance to Henry's law [30]. Pressure autoclaves are generally used for increasing the pressure [49]. High pressure of CO_2 reduction has shown to produce highest current densities during reduction of CO_2 [84]. Gas diffusion electrodes (GDE) can also increase the current density and the reason for these observations can be attributed to the higher CO_2 concentration and thus higher mass transport rates of CO_2 to the electrode surface [66, 81, 84-85]. Thus, higher pressure leads to the increase in CO_2 reduction rates and efficiency. The selectivity can also be affected. It was observed that the reduction products evolve from hydrogen to hydrocarbons (CH_4, C_2H_4, C_2H_6 and

ethanol) and as the pressure is increased again, the formation of HCOOH and CO starts. The pressure in the study in [84] was varied between 1 to 60 atm at constant current density. The electrode potential remained almost constant (−1.60 V vs Ag/AgCl) since the current density was kept constant and therefore the changes were not a result of changing electrode potential. The change in product selectivity is also related to the suppression of the hydrogen evolution and enhancement of CO_2 reduction due to increased surface coverage of CO_{ads}. This increase in the coverage of CO_{ads} leads to decrease in H_{ads}. It has been reported [66] that the product selectivity changes with increasing CO_2 pressure when Cu nanoparticles are employed. Pressure was varied between 1 to 9 atm at −1.8 V vs Ag/AgCl and product change from CH_4 to C_2H_4,was observed along with gradual increase of CO. This change was also attributed to the CO_{ads} coverage, which promoted the production of C_2H_4 over CH_4 by increasing the rate of C−C coupling between CO_{ads}.

2.5 Electrode structure

The relationship between the electrode surface structure and the electrochemical activity is important in understanding the reaction mechanism of electrochemical reduction. The structural impact on reduction of CO_2 on Cu electrodes was first reported by Frese [86] who reported that the generation of CH_4 was highest on 111 surface. 110 and 100 also performed well for CO_2 reduction in 0.5 M $KHCO_3$ electrolyte and at various potentials. The relative binding energy of CO was suggested to be the reason for increased CH_4 generation on 111 surfaces since CO binding energy is weak on 111 compared to 110 and 100 and hence this promoted favourable thermodynamics and activation energy in the RDS. Hori's group further investigated the effects of crystal orientations on Cu [87-88] and concentrated on the 111, 100 and 110 planes.0.1 M $KHCO_3$ with 5 mA/cm^2 were the conditions in which testing was conducted and the results reflected that CH_4 remained dominated over C_2H_4 on 111 surfaces (consistent with Frese [86]). Furthermore, C_2H_4 was discovered to be favoured over CH_4 on 100 surfaces. It was also observed that as the selectivity of C_2H_4 improved, the C3 generation also increased. The electrode potential was kept between −1.3 to −1.4 V vs SHE however it has been observed that the electrode potential becomes more positive as C_2H_4 selectivity increases. Another important observation has been the lower potentials on 100 surfaces compared to 111 (for the

constant current density of 5 mA/cm^2). Additionally, it was also observed that formation of C2 products remained highest at the expense of CH_4 on 110 surfaces [88].
Further studies [65, 89] also built upon the work by Hori, especially on the selectivity for C_2H_4 on 100 surfaces. CO_2 and CO reduction was studied on the 100 and 111 surfaces on different pH and it was observed that C_2H_4 was being formed on 100 planar surface at relatively lower overpotential and that this pathway was independent of the electrolyte pH. On 111 surface the production of C_2H_4 was possible at more negative onset potentials and similar to CH_4 formation, was dependent on the electrolyte pH.

CO reduction instead of CO_2 reduction can help to observe observe changes on a wider range of pH values because of the absence of CO_2 /HCO_3^- /CO_3^{2-} equilibria in aqueous systems. The results from CO reduction studies are acceptable for CO_2 reduction since it is widely established that the CO is a major intermediate in the electrochemical reduction of CO_2. It has been reported that there are 2 distinct pathways for C_2H_4 production and out of those, first is pH dependent which is due to the presence of CHO_{ads}. This is considered true for 111 and 100 surfaces. The second pathway is considered pH independent and occurs only on 100 but at lower overpotentials, possibly because of the adsorbed CO dimer. Density functional theory (DFT) calculations have supported the suggested pathway at lower overpotentials on 100 surfaces. [90].
Thus, it can be said with reasonable certainty that the surface crystal orientation has impact on product selectivity and this can provide some explanation on research groups giving different results for the same electrode. It has also been suggested [64] that the current density and applied cathodic potentials can have an impact on the surface planes and orientations on the Cu surface. Since electrodeposition of metal electrodes for CO_2RR is the most popular technique, slightly different parameters can significantly impact the structural effects on electrodeposited electrode surfaces. Some pre-treatment procedures can also impact the electrode surfaces. Hori's group has previously suggested [91] that problems with surface pretreatment (electropolishing, ultra-sonication etc.) can have an impact on the structure and electrode surface orientation.

2.6 Deactivation of CO_2 reduction

An issue often reported is the decrease in CO_2 reduction and selectivity with time in favour of HER. Not just in Cu but Au [92] and Ag [93] have also reported similar results. The time-scale however remains different from as short as less than 1 hour [94] to a gradual decrease over multiple hours [66]. This different time-scales means that the mechanism of such deactivation vary with electrode structures. Although limited literature exists about this issue, one hypothesis is about the change in electrode structure. For example, the 100 and 011 Cu surfaces gradually change and become more active for HER [66]. Surface poisoning either by the increase in concentration of CO_2 reduced products and/or intermediates can also potentially be another reason. The trace impact of impurities in electrolyte or introduction of such impurities during electrodeposition etc. can also be another reason for such a behavior. Electrode surface poisoning is also possible by the deposition of organic impurities from the water or purged CO_2 gas. The oxide/hydroxide species that are formed at different pH on cathode surfaces can also account as a reason [95]. The reduction of metal species in the electrolyte on the surface can also pose another threat for CO_2 reduction activity and has been observed in CO_2RR studies which have reported characterization of electrolytes and electrodes by various methods such as XPS, AES, Raman spectroscopy and EDS. Hori had studied such impacts on CO_2 reduction on surface poisoning [96] and had reported that even small concentrations of Fe^{2+} and Zn^{2+} ions can drastically limit the reduction of CO_2 reduction and increase HER instead. The hypothesis about such metals being the source of poisoning was made on the basis of redox potential of the metals and anodic peaks observed in post-CO_2 reduction stripping cyclic voltammetry (CV). The impact of electrodeposited Fe and Zn was also observed by the deliberate addition of small quantities of sulphate salts of these materials into a pre-treated electrolyte solution through electrolysis. Due to the negative impact of impurities on the CO_2RR activity, it was suggested that electrolyte purification through electrolysis can help to reduce such effects. On the other hand, some studies have reported that pre-electrolysis was ineffective in their experiments [97]. Pre-electrolysis is performed by essentially scavenging the solution cathodically with a sacrificial electrodes such as a Pt cathode at $-25\ \mu A/cm^2$ for many hours under Ar atmosphere. The main reason for the deactivation of CO_2 reduction however still remains elusive and it is essential to understand that mechanism for electrode poisoning can vary between different electrode systems.

2.7 Mass transfer effects

Product selectivity during CO_2RR is directly dependent on the properties of electrocatalysts and on experimental conditions such as pressure, electrolyte molarity, temperature, stirrer usage etc. This is why it has been reported by many papers [40, 66, 70] that product selectivity and reaction mechanics cannot only be attributed to catalyst behavior and that a great deal of attention should be paid to the environmental conditions in the results. The stirring of electrolyte can have an impact on the selectivity of the products [23, 84] since it improves the mass transport of species to the surface of the electrode. This improvement is attributed to the decrease in the thickness of the diffusion layer. Therefore stirring of the electrolyte can shift the pH near the electrode surface. Concentration of CO_2 in the vicinity can also change which can cause the local pH to be more closer to bulk pH and hence increase the flux of CO_2 in the electrolyte towards the electrode [64].

It has been previously reported [23, 84] that the stirring the electrolyte can lead to higher production of CO when compared to a dormant electrolyte. CO is a key intermediate specie for CO_2 reduction [24, 33] and sabatier principle [35] dictates that it facilitates reduction to hydrocarbons. It has been shown previously [37] that CO can desorb easily when a stirrer is used in the electrolyte. Thus apart from the CO_2 concentration and surface pH, the adsorption and coverage of CO_{ads} is affected by the mass transport of CO. Due to the reduced coverage of CO_{ads}, production of electron-intensive products would decrease leading to enhanced CO evolution.

The impact of the agitation of electrolyte poses a hindrance in trying to compare results from different groups. It has been previously suggested [64] that stirring during CO_2RR studies should also be quantified so that the resulting influence on the mass transport of CO_2 can be standardized.

2.8 References

1. Hori Y., Murata A., Takahashi R., *J. Chem. Soc. Faraday Trans.*, 1989, **85**, 2309 – 2326.
2. Chen Y., Li C. W., Kanan M. W., *J. Am. Chem. Soc.* 2012, **134**, 19969 – 19972.
3. Mistry H., Reske R., Zeng Z., Greeley J., Strasser P., Cuenya B. R., *J. Am. Chem. Soc.,* 2014, **136**, 16473 – 16476.
4. Lu Q., Rosen J., Jiao F., *ChemCatChem,* 2015, **7**, 38 –47.
5. Ma M, Trzesniewski B.J., Xie J., Smith W., *Angew. Chem. Int. Ed.* 2016, **55**, 9748 – 9752
6. Varela A. S., Nastaran R. S., Steinberg J., Ju W., Oh H.-S., Strasser P., *Angew. Chem. Int. Ed*. 2015, **54**, 10758 – 10762
7. Tripkovic V., Vanin M, Karamad M., Bjçrketun M., Jacobsen K. W., Thygesen K.S., Rossmeisl J., J. *Phys. Chem. C* 2013, **117**, 9187– 9195.
8. Bagger A., Ju W., Varela A., Strasser P., Rossmeisl J., *Catal. Today* 2017, **288,** 74 –78.
9. Chen Y., Kanan M., J. Am. Chem. Soc. 2012, **134**, 1986 – 1989.
10. Baruch F., Pander J., White J., Bocarsly A., *ACS Catal.* 2015, **5,** 3148 – 3156.
11. Collins C, Wang S., Xin H., He K., Kang Y., Jiao F., *J. Am. Chem. Soc*. 2017, **139**, 1885–1893.
12. Lee C. H., Kanan M. W., *ACS Catal.* 2015, **5**, 465– 469
13. Kortlever R., Shen J., Schouten K. J. P., Calle-Vallejo F., Koper M., Catal. J. *Phys. Chem. Lett.* 2015, **6**, 4073 – 4082
14. Feaster J. T., Shi C., Cave E., Hatsukade T., Abram D., Kuhl K., Hahn C., Norskov J., Jaramillo T., *ACS Catal.* 2017, **7**, 4822 – 4827.
15. Li C. W., Ciston J., Kanan M., *Nature*, 2014, **508**, 504– 507
16. Mistry H., Varela A. S., Bonifacio C. S., Zegkinoglou I, Sinev I., Choi Y., Kisslinger
K., Stach E., Yang J., Strasser P., Cuenya B., *Nat. Commun.* 2016, **7**, 12123.
17. Schouten K. J. P., Qin Z., Gallent E., Koper M., *J. Am. Chem. Soc.* 2012, **134**, 9864 – 9867
18. Calle-Vallejo F., Koper M., *Angew. Chem. Int. Ed.* 2013, **52**, 7282 – 7285
19. Sandberg R. B., Montoya J. H., Chan K., Nørskov J., *Surf. Sci.* 2016, **654**, 56– 62.
20. Nie X., Esopi M., Janik M., Asthagiri A., *Angew. Chem. Int. Ed*. 2013, **52**, 2459 – 2462
21. Kas R., Kortlever R., Ylmaz H., Koper M., Mul, G. *ChemElectroChem* 2015, **2**, 354 – 358.
22. Wenzhen L., Electrocatalytic Reduction of CO2 to Small Organic Molecule Fuels on Metal Catalysts, A*dvances in CO2 Conversion and Utilization, American Chemical Society*, 2010, 55-76.
23. Hori Y., CO2-reduction, catalyzed by metal electrodes, *Handbook of Fuel Cells*, John Wiley & Sons, Ltd, 2010.
24. Kim J.J.*,* Summers D.P., Frese Jr. K.W, *Journal of Electroanalytical Chemistry*, 1988, **245**, 223-244.
25. Peterson A., Abild-Pedersen F., Studt F., Rossmeisla J., Nørskov J. K.,, *Energy & Environmental Science*, 2010, **3**, 1311-1315.
25. K.W. Frese Jr, Chapter 6 - Electrochemical Reduction of CO2 at Solid Electrodes, in: B.P. Sullivan (Ed.) *Electrochemical and Electrocatalytic Reactions of Carbon Dioxide,* Elsevier, Amsterdam, 1993, pp. 145-216.
26. H. Noda H., Shoichiro I., Yoshiyuki O., Kaname I.*, Chemistry Letters*, 1989, **18**, 289-292.
27. Chen C.*,* Handoko A., Wan J., Ma L., Rena D., Yeo B.S., *Catalysis Science & Technology*, 2015, **5**, 161-168.

28.Kim D., Lee S., Ocon J., Jeong B., Leeb J. K., Lee J., *Physical Chemistry Chemical Physics*, 2015, **17,** 824-830.
29. Ren D., *ACS Catalysis*, 2015, **5**, 2814-2821.
30. Butler J.N., *Carbon Dioxide Equilibria and Their Application*s, Taylor & Francis, 1991.
31. Kuhl K.P., Cave E., Abramc D., Jaramillo T., *Energy & Environmental Science*, 2012, **5**, 7050-7059.
32. Cook R., MacDuff R., Sammells A., *Journal of the Electrochemical Society*, 1988, **135**, 1320-1326.
33. DeWulf D., Jin T., Bard A., *Journal of the Electrochemical Society*, 1989, **136**, 1686-1691.
34. Cook R.L., MacDuff R., Sammells A., *Journal of the Electrochemical Society*, 1989, **136**, 1982-1984.
35. Wuttig, Liu C., Peng Q. Surendranath Y., *ACS Central Science,* 2016, **2**, 522-528.
36. Heyes J., *The Journal of Physical Chemistry C,* 2016, **120**, 17334-17341.
37. Hori Y., Murata A., Yoshinami Y., *Journal of the Chemical Society, Faraday Transactions,* 1991, **87**, 125-128.
38. Schouten K.J.P.,Kwon Y., van der Ham C. J. M., Qina Z., Koper M., *Chemical Science*, 2011, **2**, 1902-1909.
39. Gattrell M., Gupta N., *Journal of Electroanalytical Chemistry*, 2006, **594**, 1-19.
40. Kortlever R., Shen J., Schouten K., Calle-Vallejo F., Koper M., *The Journal of Physical Chemistry Letters,* 2015, **6**, 4073-4082. 162
41. Naitoh A., Ohta K., Mizuno T., Yoshida H., Sakai H., Noda H., *Electrochimica Acta*, 1993, **38**, 2177-2179.
42. Saeki T., Hashimoto K., Noguchi Y., Omata K., Fujishima A., *Journal of the Electrochemical Society*, 1994, **141**, L130-L132.
43. Saeki T., Hashimoto K., Fujishima A., Kimura N., Omata K., *The Journal of Physical Chemistry*, 1995, **99**, 8440-8446.
44. Hori Y., Electrochemical CO2 Reduction on Metal Electrodes, in: C.G. Vayenas, *et al.* (Eds.) *Modern Aspects of Electrochemistry*, Springer New York, 2008, pp. 89-189.
45. Shoichiro I., Takehiko T., Kaname I., *Bulletin of the Chemical Society of Japan*, 1987, **60**, 2517-2522.
46. U. Kaiser, E. Heitz, German title, 1973, **77**, 818-823.
47. Rosen B.A., Zhu W, Whipple D.T., Kenis P.J., Masel R.I.., *Science*, 2011, **334**, 643-644.
48. Snuffin L.L., Yu L., *Journal of the Electrochemical Society*, 2011, **158**, F155-F158.
49. Jones J.-P., Prakash G, Ola G.,, *Israel Journal of Chemistry*, 2014, **54,** 1451-1466.
50. Hori Y., Kikuchi K., Shin S., *Chemistry Letters*, 1985, **14**, 1695-1698.
51. Azuma M., Hashimoto K, Hiramoto M.,*Journal of Electroanalytical Chemistry and Interfacial Electrochemistry*, 1989, **260**, 441-445.
52. R.L. Cook, Macduff R., Sammells A., *Journal of the Electrochemical Society*, 1987, **134**, 1873-1874.
53. Stucki S. Schuler A., Constatinescu M., *International Journal of Hydrogen Energy*, 1995, **20**, 653-663.
54. A. Bandi, Spetchet M., Weimer T., Schaber K., *Energy Conversion and Management*, 1995, **36**, 899-902.
55. M. Gattrell, Gupta N., Co A., *Energy Conversion and Management*, 2007, 48, 1255-1265.
56. Varela A., Ju W., Reier T., Strasser P., ACS Catalysis, 2016, **6**, 2136-2144.
57. Ogura K., Salazar-Villalpando M., *JOM Journal of the Minerals Metals and Materials Society*, 2011, **63**, 35-38.
58. K. Ogura, *Journal of CO2 Utilization,* 2013, **1**, 43-49.

59. Hara K., Tusento A., Sakata T., *Journal of Electroanalytical Chemistry*, 1997, **434**, 239-243.
60. Dubé P., Brisard G., *Journal of Electroanalytical Chemistry*, 2005, **582**, 230-240.
61. Y. Hori, Murata A., Takahashi R., Suzuki S., *Journal of the Chemical Society, Chemical Communications*, 1988, **1**, 17-19.
62. Sullivan B.P., *Electrochemical and Electrocatalytic Reactions of Carbon Dioxide*, Elsevier, Amsterdam, 1993. 161
63. *CRC Handbook of Chemistry and Physics, 90th Edition* (Internet Version 2010), CRC Press/Taylor and Francis, Boca Raton, FL, 2010.
64. N. Gupta, Gattrel M., MacDougall B., *Journal of Applied Electrochemistry,* 2006, **36**,161-172.
65. K.J.P. Schouten, Gallent E., Koper M., *Journal of Electroanalytical Chemistry*, 2014, **716**, 53-57.
66. R. Kas, Kortlever R., Yilmaz H., Koper M., *ChemElectroChem*, 2015, **2**, 354-358.
67. Y. Hori, *Modern Aspects of Electrochemistry*, Springer New York, 2008, 89-189.
68. Katsounaros, I., Meier, J. C., Klemm, S. O., Topalov, A. A., Biedermann, P. U., Auinger, M., *Electrochemistry Communications*, 2011, **13**, 634-637.
69. M.R. Singh, Clark E, Bell A.*„ Physical Chemistry Chemical Physics*, 2015, **17**, 18924-18936.
70. A.S. Hall, Yoon Y., Wuttig A., Surendranath Y.*„Journal of the American Chemical Society*, 2015, **137**, 14834-14837.
71. G.Z. Kyriacou, A.K. Anagnostopoulos, *Journal of Applied Electrochemistry,* 1993, **23**, 483-486.
72. M.E. Essington, *Soil and Water Chemistry: An Integrative Approach*, CRC Press, 2004.
73. M. Akira, H. Yoshio, *Bulletin of the Chemical Society of Japan*, 1991., **64**, 123-127.
74. A.N. Frumkin, *Transactions of the Faraday Society*, 1959, **55**, 156-167.
75. M.R. Thorson, Siil K, Kenis P.*„Journal of the Electrochemical Society*, 2013, **160**, F69-F74.
76. W. Paik, Eyring H., *Electrochimica Acta*, 1969, **14**, 1217-1232.
77. Hori, Y., Takahashi, R., Yoshinami, Y., Murata, A., *J. Phys. Chem. B*, 1997, **101**, 7075– 7081
78. Hori, Y., Murata, A., Takahashi, R., Suzuki, S. *Journal of the American Chemical Society*, 1987, **109**, 5022-5023.
79. Bockris J., Pentland N., *Transactions of the Faraday Society*, 1952, **48**, 833-839.
80. S. Kaneco, Hiei N., Xing Y., Katsumoto H., Ohta K., *Journal of Solid State Electrochemistry,* 2003, **7**, 152-156.
81. A. Kudo, Nakagawa S., Tsuneto A., Sakata T., *Journal of the Electrochemical Society,* 1993, **140**, 1541-1545.
82. M. Azuma, Hashimoto K, Hiramoto M., *Journal of the Electrochemical Society*, 1990, **137**, 1772-1778.
83. Y. Hori*, Electrochimica Acta*, **1994**, 39, 2495-2500.
84. K. Hara K., Tsuento A, Kudo A., *Journal of the Electrochemical Society*, 1994, **141**, 2097-2103.
85. Hara K. Kudo A., Sakata T., *Journal of Electroanalytical Chemistry*, 1995, 391, 141-147.
86. Frese K. Jr, Chapter 6 in: B.P. Sullivan (Ed.) Electrochemical and Electrocatalytic Reactions of Carbon Dioxide, Elsevier, Amsterdam, 1993,145-216.
87. Ke F., Liu X., Wu J., Sharma P., *Catalysis Today* 2017**, 288**, 18-23
88. Y. Hori, Takahashi I, Hoshi N.*„Journal of Molecular Catalysis A: Chemical*, 2003, **199**, 39-47.
89. Schouten K.J.P., Qin Z., Koper M., *Journal of the American Chemical Society*, 2012, **134**, 9864-9867.

90. F. Calle-Vallejo, M.T.M. Koper, *Angewandte Chemie*, 2013, **125**, 7423-7426.
91. I. Takahashi, Koga O, Hori Y., *Journal of Electroanalytical Chemistry*, 2002, **533**, 135-143.
92. P. Kedzierzawski, J. Augustynski, *Journal of the Electrochemical Society*, 1994, **141**, L58-L60.
93. R. Kostecki, J. Augustynski, *Berichte der Bunsengesellschaft für physikalische Chemie*, 1994, **98**, 1510-1515.
94. S. Wasmus, Cattaneo E., *Electrochimica Acta*, 1990, **35**, 771-775.
95. Smith B., Irish D.Augunstysky J., *Journal of the Electrochemical Society*, 1997, **144**, 4288-4296.
96. Hori Y., Konish H., Futamura T.Murata A., Oguma K., *Electrochimica Acta*, 2005, **50**, 5354-5369.
97. Jermann B., Augustynski J., *Electrochimica Acta*, 1994, **39**, 1891-1896.

CHAPTER 3

Experimental

3.1 Electrochemical measurement

Electrochemical reduction of CO_2 was conducted in home-made H-type electrochemical cell, which was designed to be leak tight. The schematic of this cell is shown in figure 3.1 while the actual picture is shown in figure 3.2.

A standard Ag/AgCl (3.0mol/L NaCl) electrode (RE-1B, ALS Co., Ltd) was used as the reference electrodes. Platinum wire/plate was used as the counter electrode. The working and reference electrodes were put in the same compartment and separated from the counter electrode by a nafion film (DuPont: N117). By separating the working and counter electrodes, the recombination of generated products on these two electrodes can be effectively prohibited.

The electrode samples were sitrred in acetone, ethanol and then pure water solutions for 5 minutes before and after each experiment. The gas sample from the experiments was sampled manually through syringe with the gas chromatographer (GC) for online analysis. A Solartron 1280C electrochemical system was used to conduct the electrochemical experiments. A scan rate of 20 mV/s.was used for the I-V curve.

The electrochemical experiments were conducted by adding similar amount of electrolyte (30-40 mL) into both cathode and chambers of the electrochemical cell. Working, counter and reference electrodes were placed in the electrochemical cell. CO_2 gas was bubbled into the WE chamber for 25 min. Both I-V and potentiostatic methods were employed.

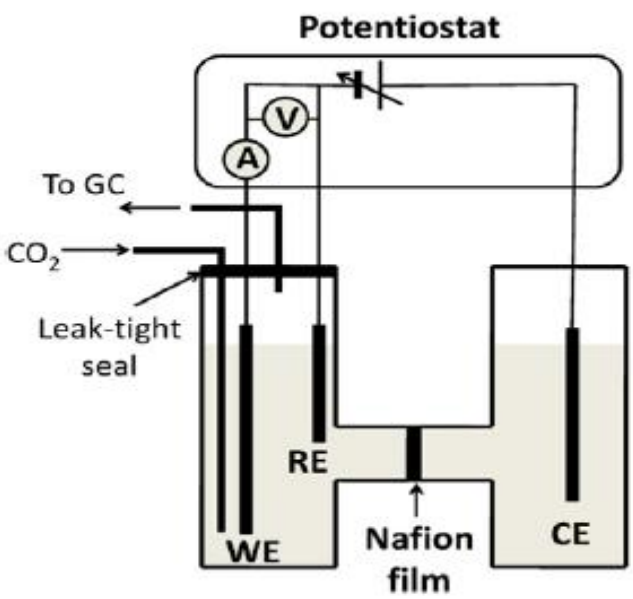

Fig. 3.1: Schematic of Electrochemical Cell

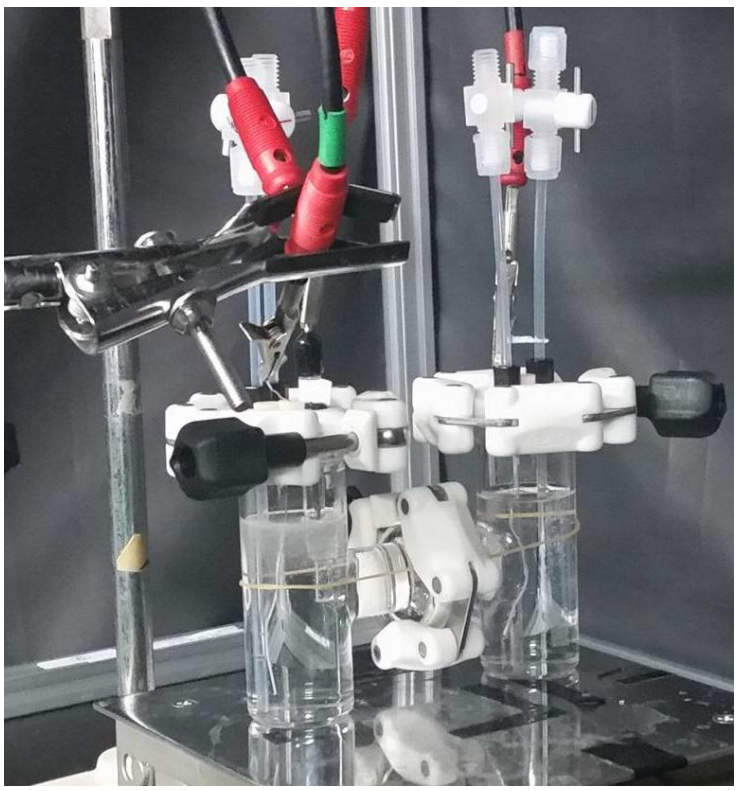

Fig. 3.2 Actual picture of the Electrochemical Cell

3.2 Gas Analysis

The HP Agilent Gas Chromatographer (GC) with a thermal conductivity detector (TCD), was used for the quantitative analysis of the sampled gaseous products. Inside the GC, the sampled gas passes through a series of columns where the different gases are separated. This separation takes place due to the adsorption strength differences among the different gases, which in turn causes differences in retention time. The changes in the thermal conductivities between the gas sample and carrier gas were used to quantify the amount of specific gas products. The schematic of the valves and columns working of the GC is shown in figure 3.3.

The HP Agilent 7890 A GC was used to analyse the gas products. The gas sample was manually sampled and injected by using a syringe. Our GC system flows the gas through five different columns and is able to analyze H_2, CO, CO_2, CH_4, C_2H_4, C_2H_6, O_2 and N_2

within one test. There are two sample loops in this system and each has a volume of 2 mL. The total volume of the sample route is about 10 mL, which means that at least 10 mL of sample needs to be injected to fill the sample route. According to the oven temperature program, a typical analysis process lasts 7 minutes.

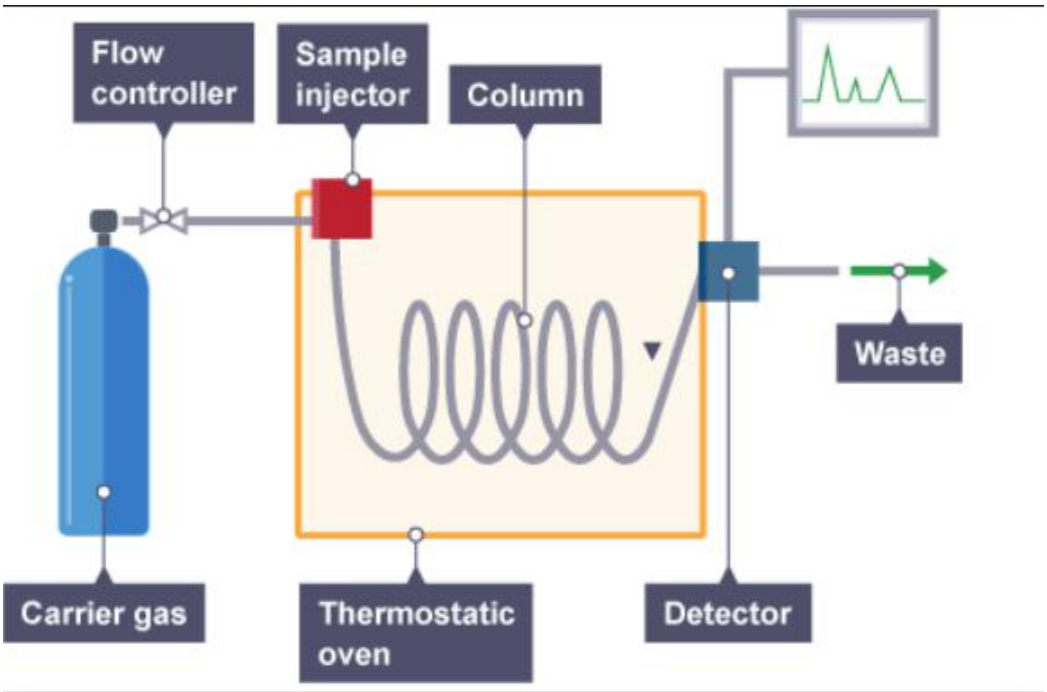

Fig. 3.3 Schematic design of GC operation [1]

3.3 Liquid Analysis

The liquid phase products were determined by Ion Chromatography (IC) and collected with a Thermo Scientific Dionex ICS-5000 system. Ion chromatography, a form of liquid chromatography, measures concentrations of ionic species by separating them based on their interaction with a resin. Ionic species separate differently depending on species type and size. Sample solutions pass through a pressurized chromatographic column where ions are absorbed by column constituents. An ion extraction liquid, known as eluent, runs through the column and the absorbed ions begin separating from the column. The retention time of different species determines the ionic concentrations in the sample.

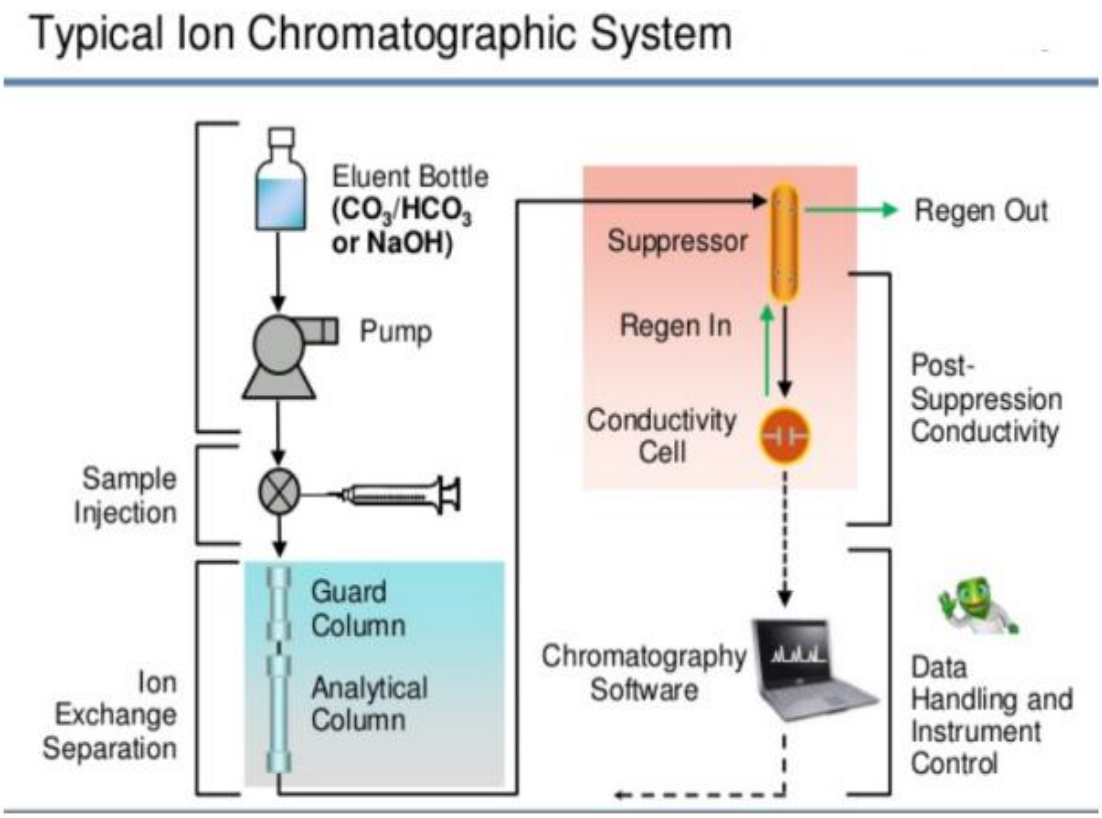

Fig. 3.4 Schematic design of IC operation [2]

3.4 Faradaic Efficiency

The faradaic efficiencies (FE) of different products were calculated by the following formula:

$$FE = \frac{n_{product} \times n_{electron} \times F}{Q} \times 100\%$$

where, n product means the molar amount of target product, nelectron represents electron transfer number per molecule (for CO, n = 2; CH_4, n = 8; C_2H_4, n = 12; H_2, n = 2), F is the faradaic constant (96485.3 C/mol), Q is the total electron transferred during the whole reaction. The number of Q can be obtained from the electrochemical software used for conducting the experiment. According to this equation, faradaic efficiency represents the efficiency of the product selectivity.

3.5 References:

1. Balram Pani, Textbook of Environmental Chemistry, IK International, ISBN : **9788189866365**
2. Detlef Johnson, Analysis of Desinfection products by Ion Chromatography, Thermo Ficher Scientific website

CHAPTER 4

Solar Fuel study using CPV and Au, Sn bulk metals

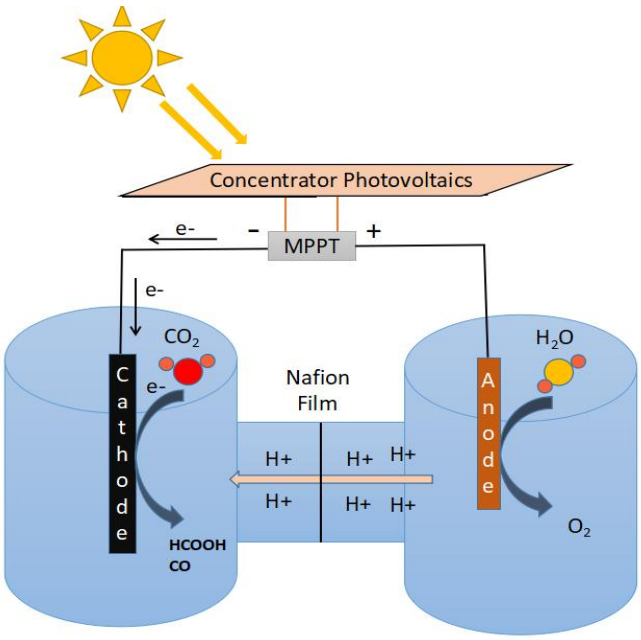

Figure 4.1 Graphical abstract of the Solar Fuel study

4.1 The need for Solar Fuel

The environmental concerns associated with CO_2 emissions necessitate research on solar fuel production since the concerns listed in the introductory chapter, merits activity on war footings. A very good method for conversion of CO_2 into reduced products should be large and scalable and this requires the use of utilizing natural sunlight so that a good benchmark can be set for testing the efficacy of the solar-to-fuel system. While a full-scale operational solar-to-fuel conversion plant may not yet be economically feasible, a smaller, demonstration-level system can be employed to test the practicality of the system and technology.

In order to put things into perspectives, it is important to quantify the ground realities to make a case for employing the renewable energy sources. Fossil fuels generate, on average, 0.837 kg of CO_2 per kilowatt-hour [1]. A carbon dioxide electrolyzer, producing formate at the cathode and oxygen at the anode at pH 7, requires at least 1.32 V (the thermoneutral voltage) to account for the enthalpic costs of the two reactions [2]. If this system were to operate with 1 V of total overpotentials and a current of 1.00 A at 80% efficiency, it would consume 2.32 W in an hour and convert 0.657 g of CO_2. The 2.32

Wh used, meanwhile, would have led to the emission of 1.94 g of CO_2, almost three times the amount reduced [2]. Even if this electrolyzer operated at the thermoneutral voltage at 100% efficiency (impossible for significant currents) the net conversion of CO_2 would still be -0.28 g CO_2 per hour [2]. Therefore, fossil-fuel-based energy sources for large-scale electrolyzers cannot produce significant amounts of CO_2 during power generation without negating any positive environmental effects of CO_2 conversion.
On the other hand, the use of renewable-energy-based fuel can allow for a new energy transport vector by allowing a medium for transfer of energy from geographical areas blessed with immense amount of solar intensity or wind blows, to areas which are energy consumers. Taking the example of solar, we can see in figure 4.2, that the highest solar irradiated regions such as parts of Africa, South America or Asia are actually geographically far away from Europe or northern North America, Japan etc. This means that a solar fuel study under natural sunlight, is important to provide a realistic method for transporting the renewable energy between energy-rich and energy-demanding regions of our planet.

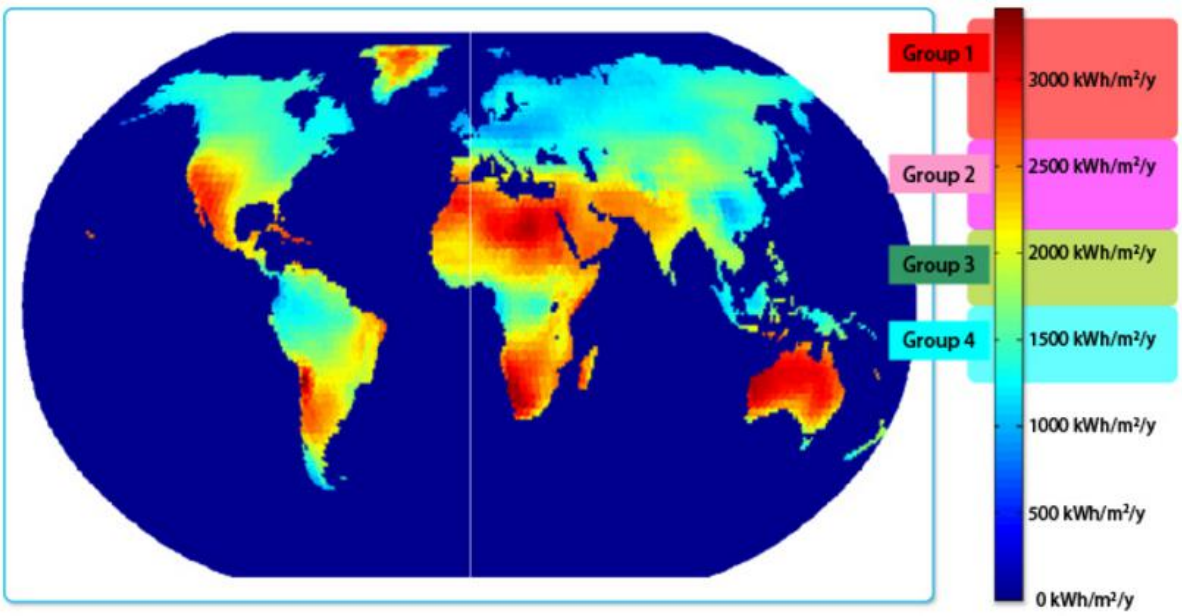

Fig. 4.2 Solar irradiation potential in different parts of the world [1]

Solar, wind, geothermal, tidal, and hydroelectric power are all viable and promising alternatives to coal and natural gas for driving CO_2 reduction at scale. However, the latter

four are all fairly limited geographically to particular areas in which they are economically viable. For instance, wind resources in the United States are limited to the great plains, mountainous regions, and offshore areas. Solar energy, especially as the price of installation decreases, can be exploited economically in wide swath of territory across the China, Africa, Australia and United States, as well as in many other countries where it can succeed as a major contributor to electricity generation [3].
The incident power of sunlight can be harnessed for CO_2 reduction in two main ways. The first and most studied method is through the direct use of a semiconducting material, both to absorb light and to perform the catalysis, either as a monolithic particle or as a photoelectrode in a circuit. While such systems have a variety of advantages that have proven to be encouraging, they are typically limited in application because the semiconductor must have a good absorption in the visible region of the solar spectrum, be able to reduce CO_2 and that too in better efficiency against the competing hydrogen generation, and be stable in aqueous solution. Photocorrosion of semiconductors is a significant concern and greatly reduces the longevity of typical photoelectrochemical (PEC) systems [4-5]. In addition, many research-level PEC cells utilize single-crystal semiconductors, which are not readily scalable (especially in a cost effective fashion) to large systems. Semiconductors fabricated using polycrystalline materials typically show reduced behavior towards photoelectrochemistry compared to their single-crystal counterparts.

Another technique that has gained more attention and is a more recent occurance is the coupling of a photovoltaic (PV) cell to what is called a ‘dark ‘electrolyzer, which is termed as a PV-biased electrosynthetic cell [6]. The separation of light collection and catalysis into two separate components allows optimization independently for each section and subsequently, the scaling of each becomes easier to manage [7]. A set of semiconductors whose bandgaps match the majority of incident sunlight can be combined in series with a PV array to produce the voltage necessary to carry out the the electrochemical mechanisms. Electrodes that have low overpotentials for CO_2 reduction and oxygen evolution, as well as high selectivity for particular products can thus be chosen without the restrictions imposed by the utilization of semiconductor photoelectrodes. An important consideration however, is to match the impedance of the electrolyzer to that of the PV device, so that the system operates near the ‘knee’ of the current-voltage curve, which is the maximum power point of the photovoltaic [8]. Without a good match between the two components, significant coupling losses occur and greatly reduce the efficiency of the overall system. Several such PV-powered systems

have already been demonstrated for hydrogen production and for CO_2 reduction [9-11]. In comparison with water splitting, electrochemical reduction of CO_2 (CO_2RR) presents considerably greater challenges, including product selectivity, electrolyte constraints and large voltage requirements. The combination of these effects makes sunlight-driven CO_2 reduction difficult to achieve but can be very useful if high efficiencies are realized [12].

Plants and vegetation generally operate at a 1% solar fuel efficiency i.e. the process of CO_2 capture and conversion. However in 2014, Bocarsly *et. al.* [13] was able to report the first demonstration of an artificial system exceeding the natural photosynthesis. The almost 2% solar fuel efficiency system was accomplished by separating light absorption and CO_2 reduction through the use of a commercial solar panel illuminated with natural AM1.5 sunlight to power a custom closed-loop electrochemical flow cell stack. Faradaic yields for formate of up to 67% were demonstrated in this system, yielding a solar energy to fuel thermionic conversion efficiency above 1.8%. In the subsequent year, a solar-to-fuel conversion efficiency of 4.6% was demonstrated for CO_2 photoreduction to formate utilizing water as an electron donor, under simulated solar light irradiation to a monolithic tablet-shaped device. This CO_2 photoreduction system worked by utilizing the effect of the carbon substrate on selective CO_2 reduction in the presence of oxygen while on the counter electrode, IrOx catalysts were used for the selective H_2O oxidation [14]. Recently, more studies have been conducted to make substantial progress toward decreasing the overpotential of copper-based electrodes. They have been conducted by employing catalysts derived from copper oxides. In one of these investigations [15], the surface of CuO nanowire electrodes were modified by addition of SnO_2 using atomic layer deposition (ALD). This led to a very efficient catalyst that selectively reduced the CO_2 to CO by electrochemical reaction. The use of modified SnO_2 on CuO nanowire electrodes in a bifunctional configuration allowing both CO_2 reduction and oxygen evolution reaction (OER), demonstrated a complete CO_2 electrolysis system that was resistant to poisoning and used a single earth-abundant catalyst for the electrochemical splitting of CO_2 into CO and oxygen. Using a triple-junction GaInP/GaInAs/Ge solar cell to drive the reaction and a bipolar membrane as the separator, the reduction of CO_2 was achieved under simulated light, with the solar-to-CO conversion efficiency reaching as high as 13.4%.

For a large-scale electrolysis system. there are many important considerations that have to be incorporated into the design. Low overpotentials and high currents are essential to the energy- and time-efficient generation of products. The former can be adjusted through

the use of excellent electrocatalysts for both the anode and the cathode. The latter can be increased linearly with larger electrode areas however, further gains can be obtained by enhancing mass transport of reactants to the electrodes. The ‘chlor-alkali’ process [16], is a highly developed industrial electrochemical method for generating carbon intensive products and can provide important insights for CO_2 electrolysis. Most chlor-alkali systems employ membrane-separated flow cells.

Based on these design features, CO_2-to-formate or CO electrolyzers have been developed by several other groups, employing a variety of cathodes, including lead [17-18] tin [19] indium [8] and some mixtures of those metals prepared in different ways [20-21]. Other conditions were also varied, including the membrane separator, anode material, catholyte, anolyte, and flow rates for the electrolytes. It has been shown that a membrane with high ionic conductivity but low permeation of products has to be chosen. Typically, sulfonated perfluoropolymer nafion, a cation exchange membrane (CEM), has been employed in such systems, though anion exchange membranes (AEMs) have occasionally also been used. AEMs. However AEMS usually have lower ionic conductivities than nafion [22]. In addition, they suffer from the fact that formate, a negatively charged species, can cross from catholyte to anolyte and be reoxidized to CO_2. Further considerations for an industrial-sized system include the long-term stability of the electrode materials as well as the acidification of formate and separation of the resulting CO and formic acid from electrochemical cells, however, these process engineering concerns will not be discussed.

4.2 Experimental Study

This solar-to-fuel study was conducted with a multiple of up to 4 electrochemical cells, which were combined in parallel to match the voltage output of the photovoltaic array. Tin and gold were chosen as the cathode materials in preference to silver, lead and indium for several reason. Tin has been demonstrated to yield stable CO_2 electrolysis for long times [23] while lead is too soft and malleable to form high surface area structures and has difficulty adhering to cathode materials when plated onto them. It also has lower activity than either tin or indium at high current densities [13]. On the other hand, the surface of indium changes over the course of an electrolysis, causing faradaic efficiency (FE) to decrease and requiring a reverse bias to rejuvenate the electrode, leading to a decrease in cell performance [24]. Therefore it was decided to use tin and gold for this study since they posed lesser challenges.

The efficiency of our system, in regards to both the electrochemical processes and the overall conversion of solar energy to chemical energy will be discussed in the next section. The electrolytes for the electrochemical cells were prepared using Millipore deionized water. Potassium bicarbonate and sulfuric acid, both at 0.5 molar concentration, were used as the catholyte and anolyte, respectively. Approximately 120 mL of each solution was used in every electrochemical cell (EC). Carbon dioxide was bubbled into the catholyte. During the experiments conducted with tin electrode, the product gases were free to escape to ensure that there was no pressure buildup in the electrochemical systems. For the experiments with gold electrode, leak-tight compartments were ensured in order to accurately measure the gas phase products. Between experiments, the EC was rinsed with and kept full of deionized water in order to prevent the drying and shrinking of the membranes.

After each experiment with gold electrode, 10 µl gas was sampled and analyzed using a Gas Chromatograph while the catholyte was drained from the EC after fixed time intervals. The catholyte volume was determined from its mass and density. Formate concentrations were determined by H nuclear magnetic resonance (NMR) spectroscopy. NMR spectra were obtained with a Bruker Avance III 500 MHz cryoprobe spectrometer with a water excitation-sculpting solvent-suppression pulse sequence. Each NMR sample consisted of 60 µl of D_2O for instrument lock, 530 µl of the measurable solution, and 10 µl of 10 mM 1,4-dioxane used as an internal standard, against which the formate concentration was calibrated.

Home-made concentrator photovoltaic (CPV) monomodule was used, which had a 25 cm^2 light-receiving area, and a 1 cm^2 InGaP-GaAs-Ge three-junction cell. This was placed in the focal position of the sunlight and which was operated at 25% efficiency. The output of the CPV modules was connected to a maximum power point tracking (MPPT) circuit which tracked the maximum power point. The output of the MPPT was given to the electrochemical cells. The MPPT circuit measured its input and output current and voltages.

As mentioned, home-made H-type leak-tight electrochemical cells were used for CO_2 reduction, with 100 cm^3 volume and 60 ml of electrolyte in each compartment. The end-products were collected for further analysis. The working and reference electrodes were put in the same compartment and separated from the counter electrode by a Nafion film (DuPont: N117). Ag/AgCl reference electrode was employed while platinum metal was used as the counter electrode. 0.5 M $KHCO_3$ with a pH of 7.9 was used in the

cathode while 0.5 M H_2SO_4 with pH of 2.2 was used as anode electrolyte. The pH changes were not observed during the experiment.

Since CO_2 reduction is a redox reaction, during the reduction of CO_2, O_2 is evolved at the counter electrode and so the separation between the working and counter electrodes helps to ensure that the recombination of the products produced on these two electrodes can be effectively prohibited. The gas product were then sampled manually.

The overall schematic of the design is shown in figure 4.3, in which CPVs were connected to a dual compartment EC. A Maximum Power Point Tracking (MPPT) circuit was connected in between to assist in the proper matching of input solar power and input EC power.

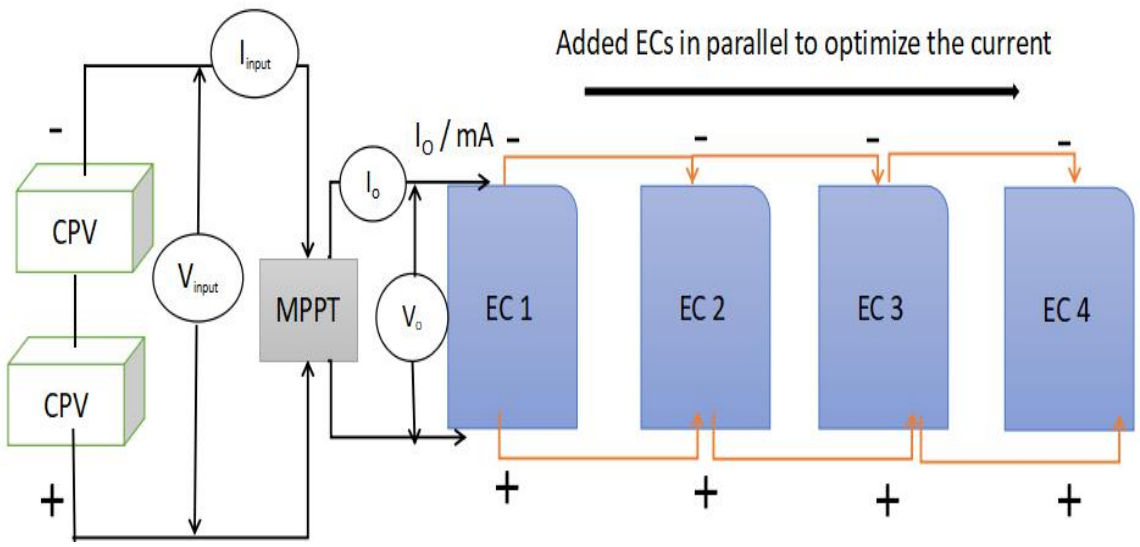

Fig. 4.3 Schematic of the Solar-to-CO_2 reduction system

MPPT was used so that an optimum solar CPV power could be matched with EC input. Since the amount of electric power being produced by the CPV module can have the potential to fluctuate continuously with various weather conditions [25], it was important to use an MPPT to adjust the matching accordingly. As there is always a special point on the IV curve for CPVs at which the power is maximum, this maximum power point was located by the MPPT using search algorithm known as the Perturbation and Observation (P&O) [26-27]. A descriptive graph is shown in figure 4.4.

The working model of the algorithm is as follows. When the output voltage of the CPV module is perturbed and $\mathrm{d}P/\mathrm{d}V > 0$, then it is reasonable to assume that the current operating point is on the left side of the MPP. The P&O algorithm would gradually increase the reference voltage of CPV module so that the operating point can be shifted towards the MPP. Similarly, when the output voltage of the CPV module is changed and $\mathrm{d}P/\mathrm{d}V < 0$, then the operating point has to be on the right side of the MPP. The P&O algorithm would reduce the reference voltage of the CPV module by shifting the operating point towards the Maximum Power Point. This process is subsequently repeated until the maximum power point is reached.

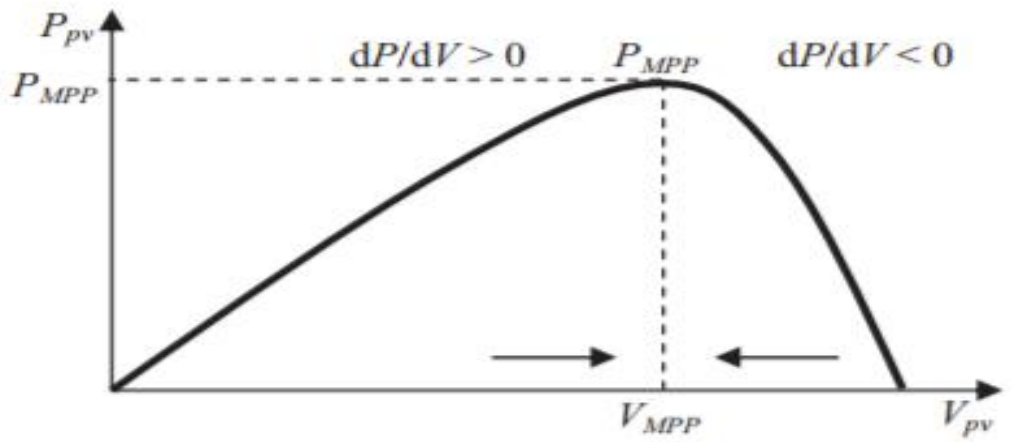

Fig. 4.4 Description of the conventional P&O algorithm [26]

For the choice of electrolyte, it has been demonstrated [13] that experiments employing K_2SO_4 as the supporting electrolyte on both sides of the cell do not produce a stable system, since the species begin to precipitate onto the cathode and this in turn begins to hinder mass transport once the formate concentration increases beyond a certain threshold. Substitution of 0.5 M $KHCO_3$ for the sulfate salt in the catholyte compartment eliminates this precipitation. Previous work has indicated that this electrolyte sustains high current and good faradaic yield [28]. Additionally, the bicarbonate catholyte helps to cushion pH to a neutral value which deters the hydrogen production and favors CO_2 reduced end-products. 0.5 M H_2SO_4 was used in the anode chamber because it helped in providing stable conductivity of the anolyte compartment and also ensured the provision of a constant proton flux across the membrane into the cathode compartment. The hydration of CO_2 is kinetically slow and dissolved CO_2 in the electrolyte does result in the production of bicarbonate. It is important to ensure that constant and necessary

amount of protons have been transported across the nafion film to satisfy the need of proton content in the cathode. The steady-state of proton concentration in the cathode chamber is an important factor in facilitating the reduction of CO_2. Furthermore the stream of protons from the anodic chamber can help to react with the HCO_3 to produce CO_2 and hence provide greater availability and replacement of CO_2 for the reduction experiment.

This research attempted to gain an insight about the impact of the natural conditions (intermittent sunlight and gusts of wind) on the stability of CO_2 reduction. The affect of such factors is crucial to understand the practical viability of solar fuel experiments. The experiments were conducted in Princeton University, NJ, USA under the natural sunlight. The conditions fared well with the purpose of the research, because of the frequent intermittence of light intensity due to the constant hovering of clouds around the sun.

4.3 Results and discussion

A total of 8 experiments were conducted initially under the intermittent sunlight in Princeton and a detailed table, providing the faradaic efficiency, the number of electrochemical cells used, electrode area, current density is given below in table 4.1 and table 4.2. The detailed P, I and V graphs for experiments 2 till 8 follow after these tables. The P, I, V data for experiment 1 was incomplete due to an error in MPPT and so is not shown here. The sampling time shows the time intervals (from the start of the experiment) at which the product analysis was conducted.

Table 4.1 Experiments with Gold electrode in natural sunlight

	Average Faradaic Efficiency (%)	Average Current (mA)	Average Current Density (mA/cm^2)	EC cells used	Electrode Area (cm^2)	First Sampling Time (min)	Second Sampling Time (min)	Third Sampling Time (min)
1	0	200	100	1	2	90		
2	0.09	80	20	1	4	40	60	
3	0.10	230	63	2	4	60		
4	0.43	136	35	2	4	40	60	
5	21.7	68	2.83	4	16	8	20	40
6	6.5	125	5.5	4	16	5	20	

Table 4.2 Experiments with Tin electrode in natural sunlight

	Average Faradaic Efficiency (%)	Average Current (mA)	Average Current Density (mA/cm^2)	EC cells used	Electrode Area (cm^2)	First Sampling Time (min)	Second Sampling Time (min)	Third Sampling Time (min)
7	7.95	108	9	3	12	10	30	
8	28.6	35	1.75	4	20	8	20	40

EXPERIMENT 2

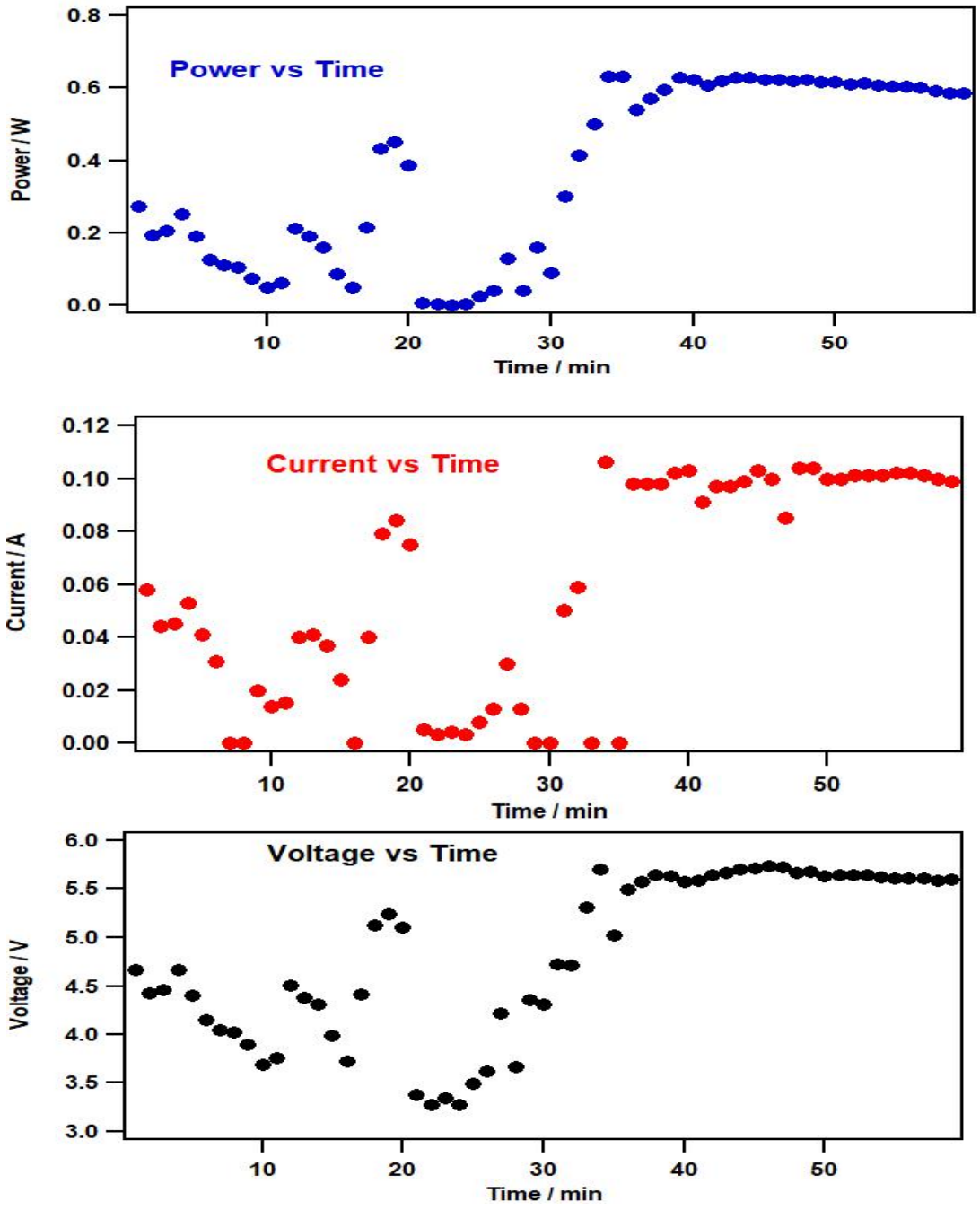

Fig 4.5 Power (top), current (middle) and voltage (bottom) for the duration of the second experiment using gold electrode.

EXPERIMENT 3

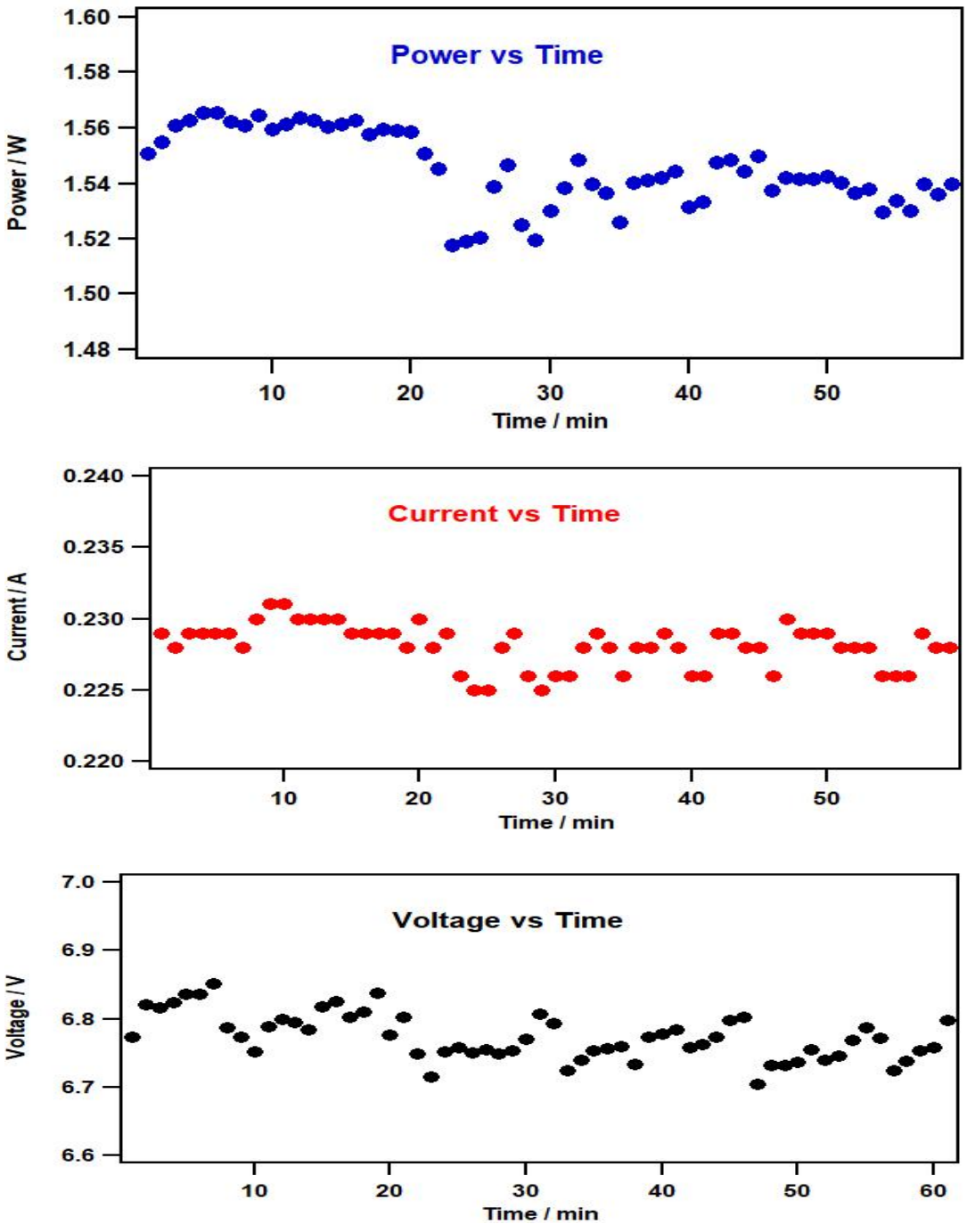

Fig 4.6 Power (top), current (middle) and voltage (bottom) for the duration of the third experiment which employed gold electrode.

EXPERIMENT 4

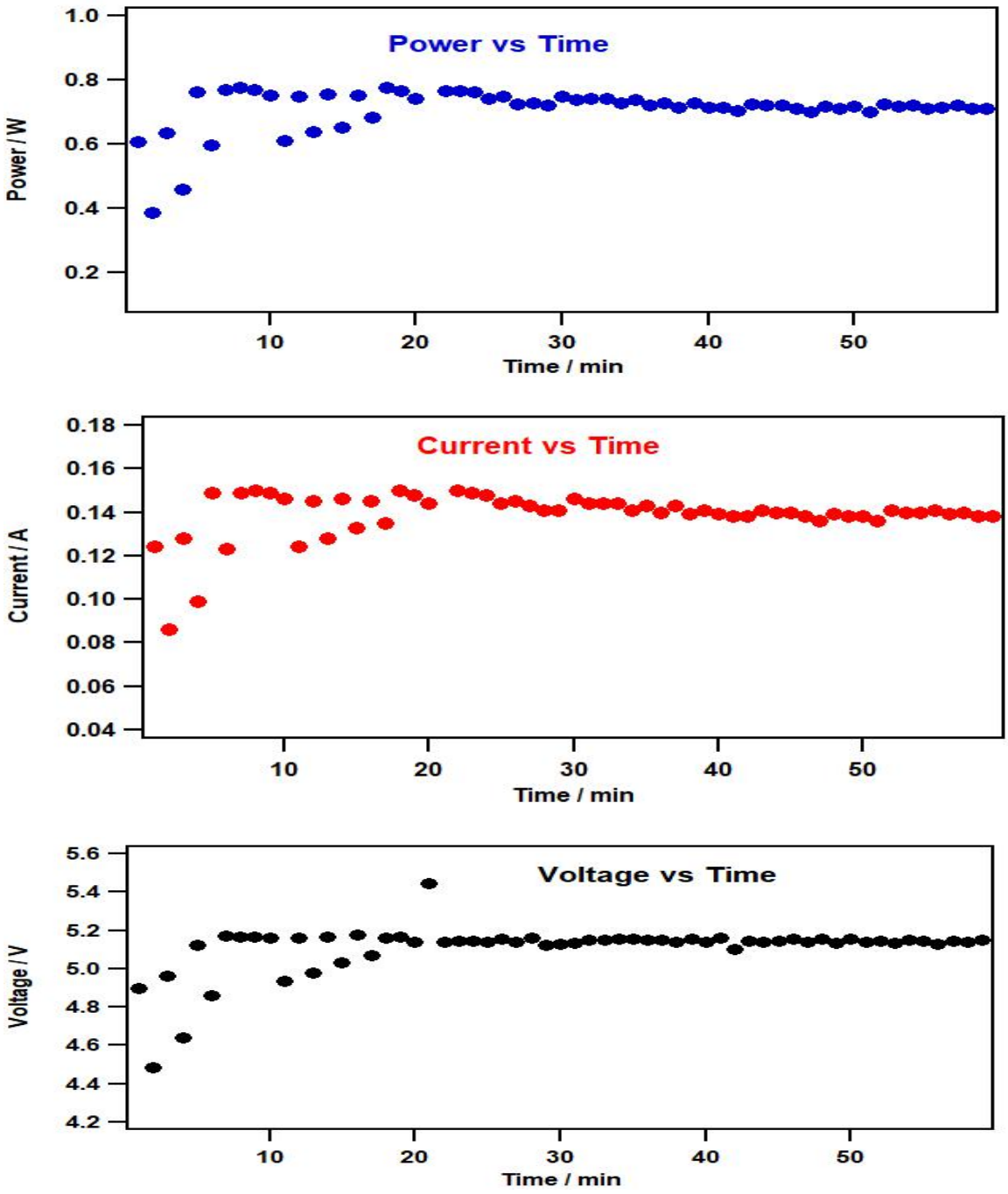

Fig 4.7 Power (top), current (middle) and voltage (bottom) for the duration of the fourth experiment using gold electrode

EXPERIMENT 5

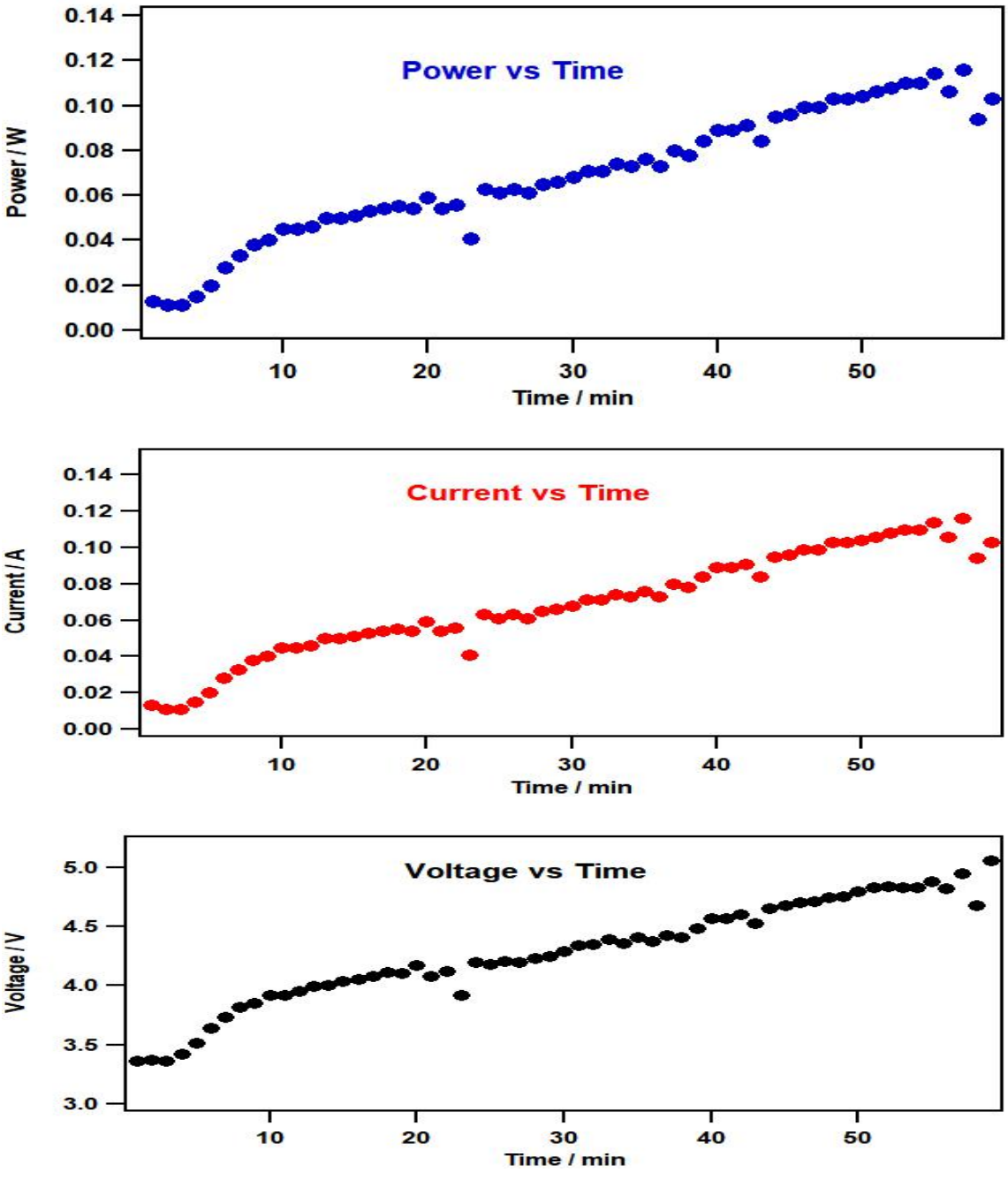

Fig 4.8 Power (top), current (middle) and voltage (bottom) for the duration of the fifth experiment using gold electrode.

EXPERIMENT 6

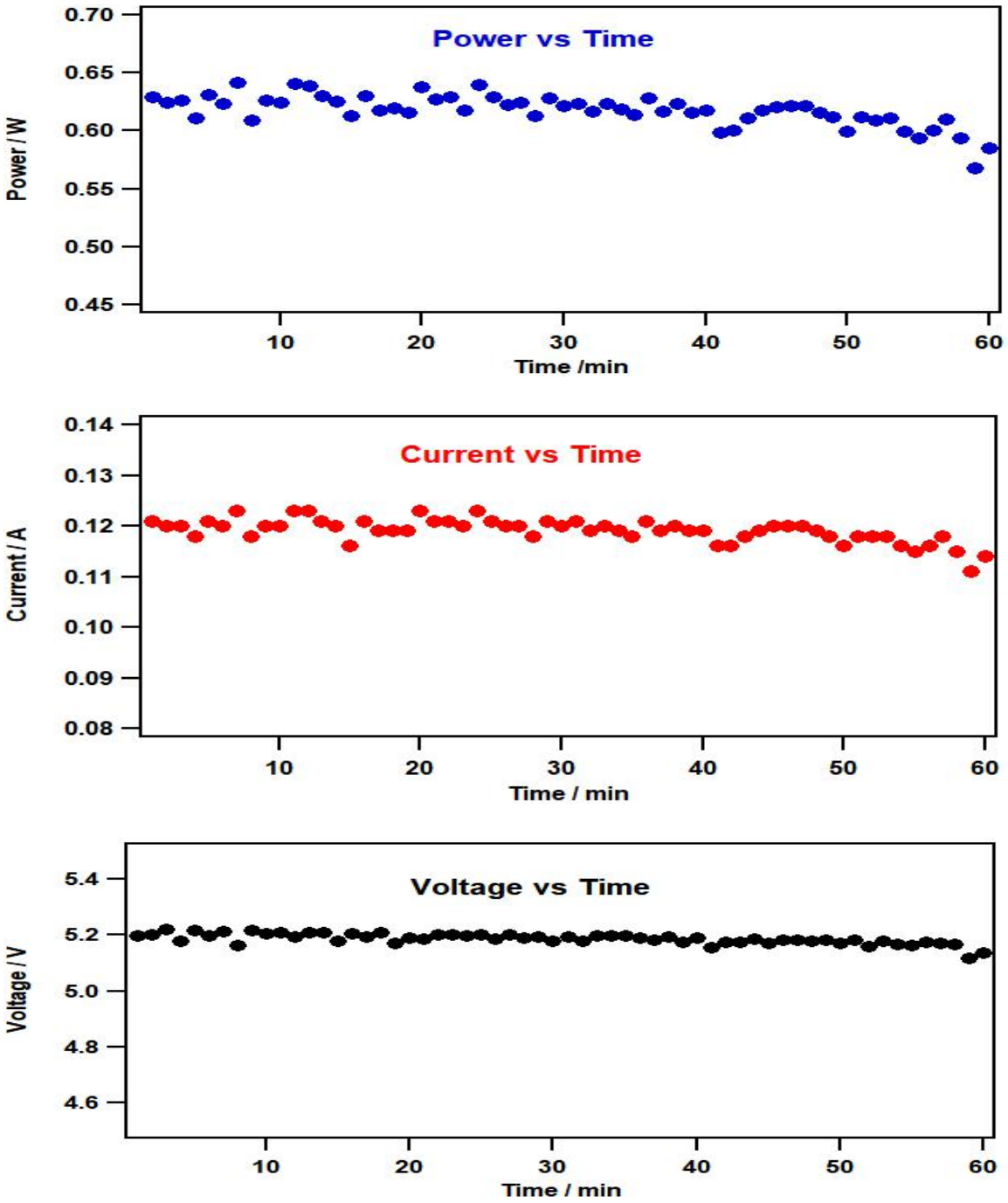

Fig 4.9 Power (top), current (middle) and voltage (bottom) for the duration of the sixth experiment using gold electrode.

EXPERIMENT 7

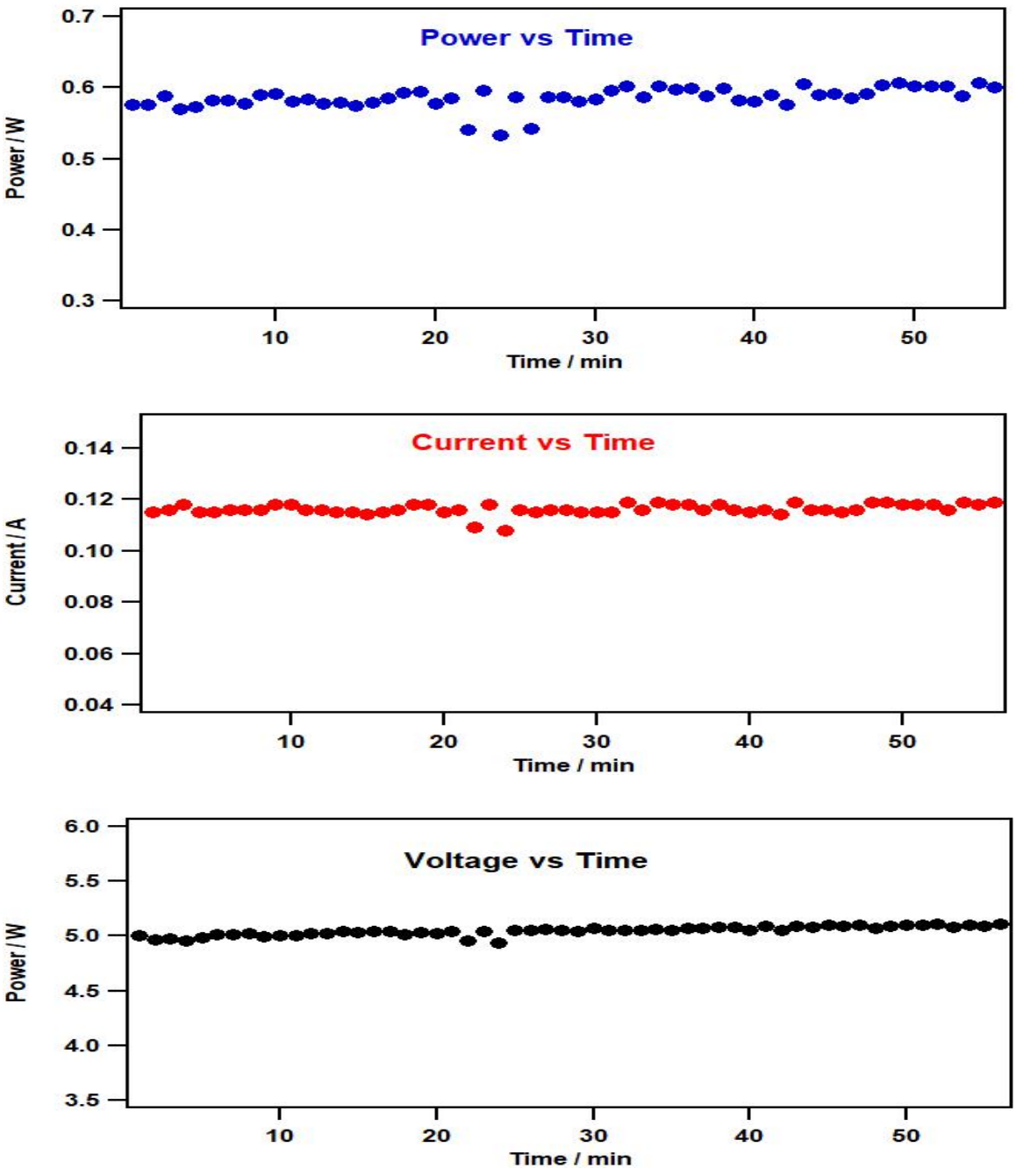

Fig 4.10 Power (top), current (middle) and voltage (bottom) for the duration of the seventh experiment using tin electrode.

EXPERIMENT 8

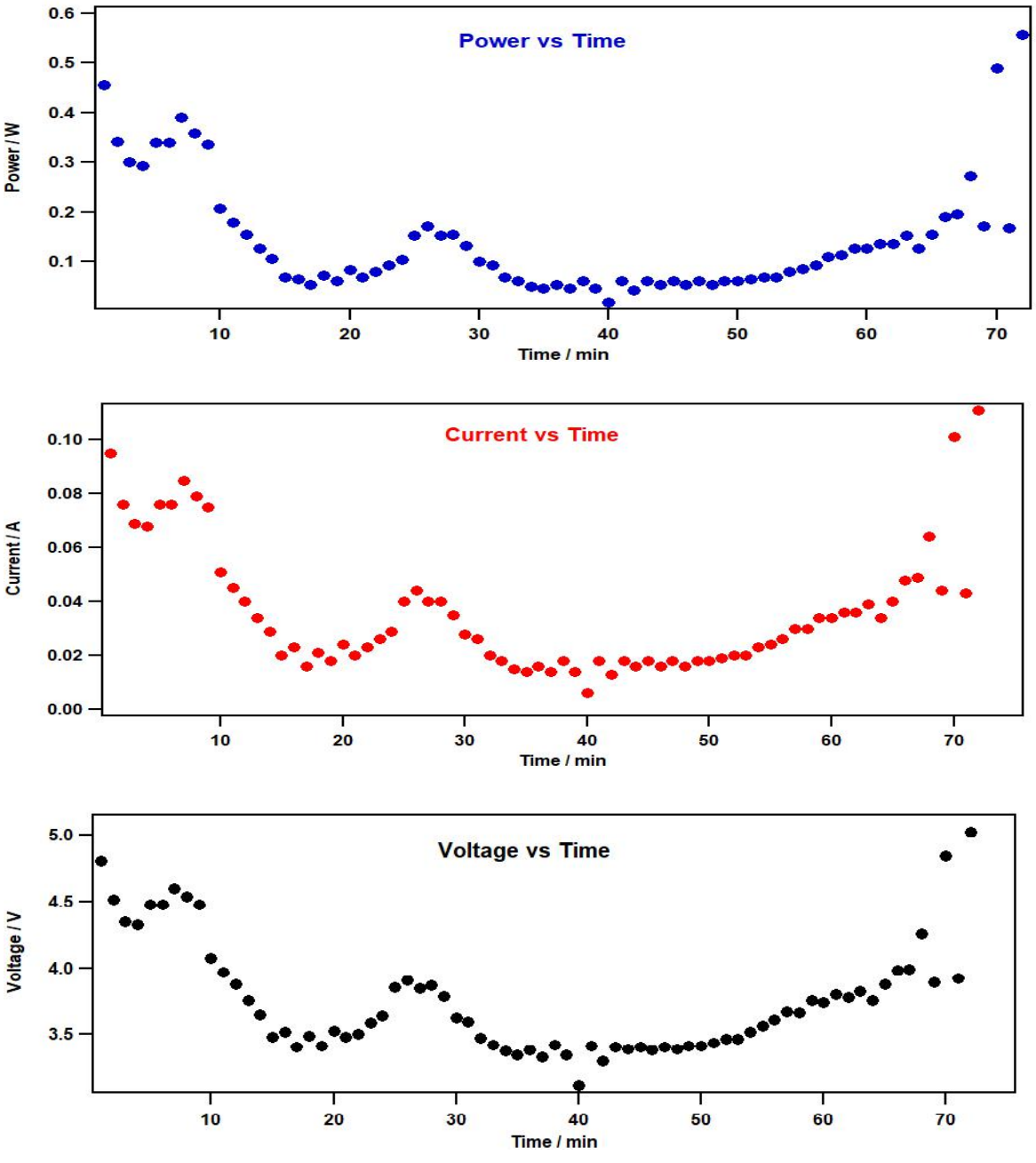

Fig 4.11 Power (top), current (middle) and voltage (bottom) for the duration of the eighth experiment using tin electrode.

The best performing experiments were analyzed. Experiment 5 (Exp 5) and Experiment 6 (Exp 6) with gold electrode and experiment 7 (Exp 7) and experiment 8 (Exp 8) with tin electrode were chosen as the benchmark experiments .

Hydrogen was the dominant product in all of these experiments while the solar modules operated at 24.9 to 25% efficiency. Figure 4.12 shows the comparative input current and voltage to the electrochemical cells (EC). The linear relationship between current and voltage for each experiment respectively, is indicative of the proper functioning of the CPV cells. The amount of current was directly proportional to the sunlight intensity and its unstable values (Exp 5 and 8) reflected the frequent appearance of clouds, hindering the power generation. The CPV efficiency at different solar intensities was experimentally calculated in controlled lab conditions.

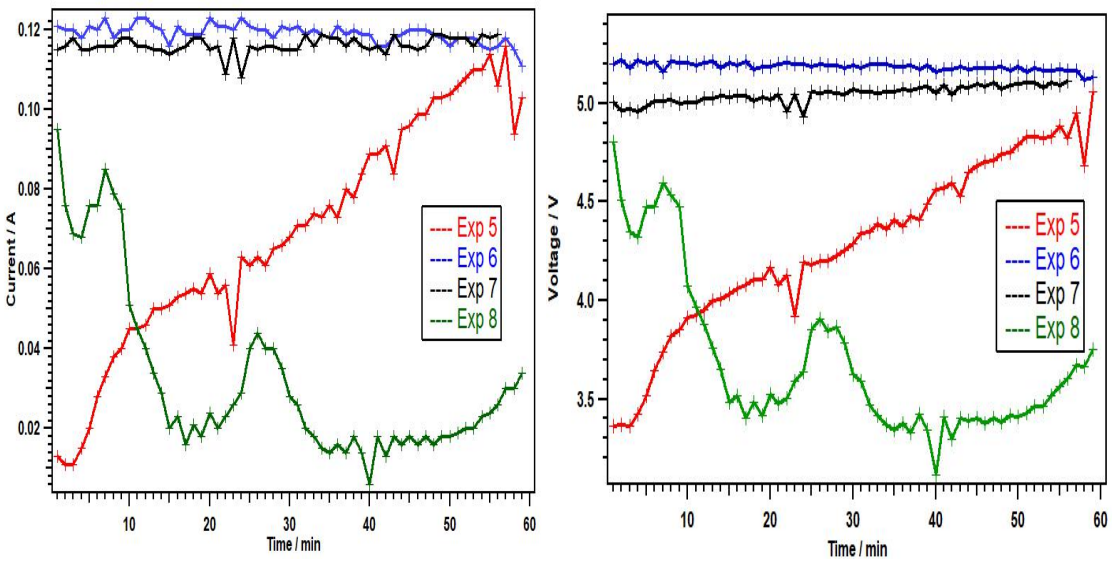

Fig. 4.12 Current output (left) and voltage output (right) of MPPT circuit for each of the four chosen experiments (Exp 5-8)

Due to the varying solar irradiation and cloudy weather conditions, it was an important factor to intermittently verify the amount of end-product produced and the faradaic efficiency achieved towards CO_2 reduction, in relation to the charge transfer and current density. It was for this reason that an assessment was made to understand the relationship between the changing weather conditions and the electrochemical process. Figure 4.13 provides the comparative power inputs to the EC setup while the figure 4.14 summarizes the impact of current density on the faradaic efficiency (FE).

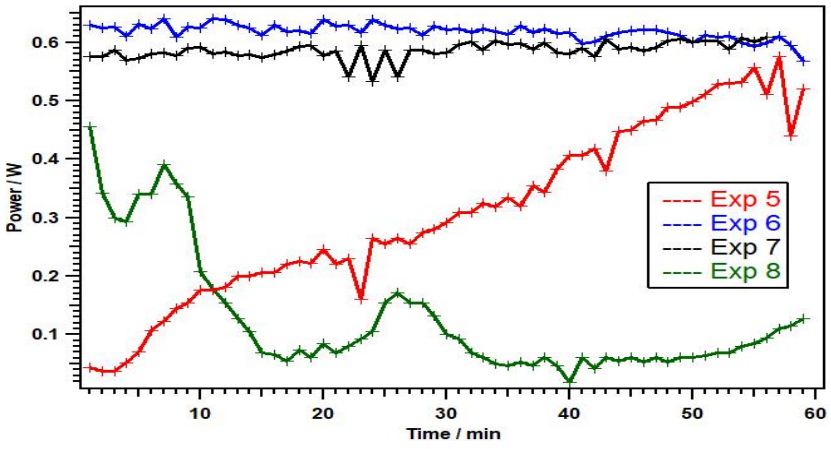

Fig. 4.13 Comparative power input to EC for Exp 5-8

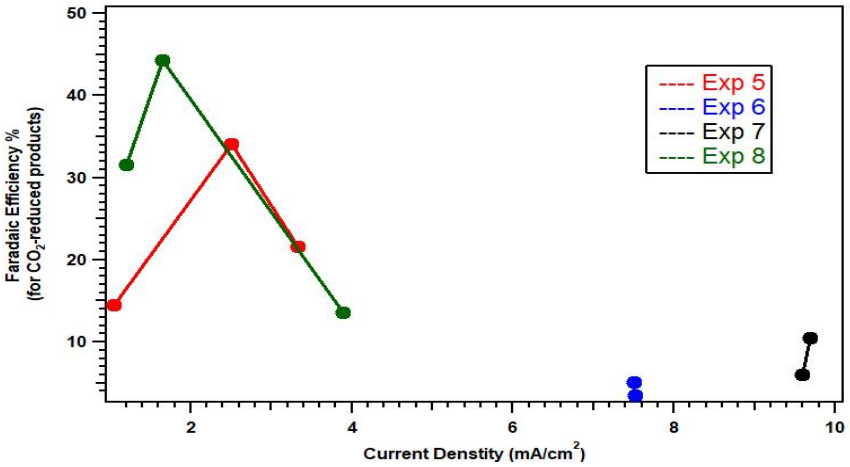

Fig. 4.14 Current density vs FE for exp 5-8

Exp 6 and 7 were conducted in almost stable sunlight conditions while Exp 5 and 8 had intermittent sunlight irradiation and the impact of these aberrations from the normal conditions provided an opportunity to observe its impact on charge transfer and electrolyte polarization, in terms of the resulting faradaic efficiency. The electrochemical responses in Exp 5 and 8 varied with time due to the changing sunlight intensities. The change of current density meant that there was a particular range of values, at which the optimum carbondioxide reduction was achieved. At the first point of observation in experiment 5, the current density generated was about 1 mA/cm^2 and the corresponding end-product analysis showed the faradaic efficiency (FE) for CO evolution to be about 14%. The CO_2 reduction however was significantly accelerated as the current density reached 2.7 mA/cm^2. This observation represents a shift from the conventionally assumed 'optimum current-density' range. Many researchers have theorized 5-15

mA/cm^2 of current density for optimum conversion of carbondioxide gas using single compartment electrochemical cell [13]. Bocarsly *et. al.* [13] had demonstrated a relatively high FE of 67% at an extremely large current density of 81 mA/cm^2. The 4 home-made glass H-cells which were used in these experiments, had total electrolyte of 220 ml, and demonstrated the best performance at a current density range of 1.7 to 2.5 mA/cm^2, influenced by common factors such as proton concentration, distance between the opposite electrodes, diameter of the interfacing region between the 2 compartments etc. Table 4.3 and 4.4 breakdown the faradaic efficiency in terms of the products and charges passed at fixed sampling time.

Table 4.3 Faradaic efficiency achieved against different sampling times and the total charge transfer for gold electrode.

Experiment 5

Faradaic Eff. towards CO	CO / micromoles	Total Columb Transferred at t (C)	Sampling Time / t (min)
14.46	7.64	10.2	0-8
33.31	79.88	46.32	0-20
21.6	142	126.52	0-40

Experiment 6

Faradaic Eff. towards Formic Acid %	Formic Acid / micromoles	Total Columb Transferred at t (C)	Sampling Time / t (min)
10.5	38	69.6	0-10
5.95	64	207.72	0-30

Table 4.4 Faradaic Efficiency achieved against different sampling times and the total charge transfer for tin electrode.

Experiment 7

Faradaic Eff. towards CO	CO / micromoles	Total Columb Transferred at t (C)	Sampling Time / t (min)
5.04	9.4	36	0-5
3.48	25.92	144	0-20

Experiment 8

Faradaic Eff. towards Formic Acid	Formic Acid / micromoles	Total Columb Transferred at t (C)	Sampling Time (min)
13.6	26.4	37.44	0-8
44.26	140.4	61.2	0-20
31.6	148	90.36	0-40

It had been observed in protein structures that the arrangement (density) of the charges influenced the transfer of electrons [29]. The concept behind this electron transfer was based on the Marcus theory of electron transfer. Assuming the same basis of electron transfer during CO_2 reduction, it can be stated that since the process of electron transfer is faster than the movement of any adsorbed species, the nuclear position of those species remain the same, before and after the electron exchange. However, after the electron exchange, the distribution of the species (density of charges) changes which impact the multiple transfer of electrons to the minority specie of CO_2, in favor of the dominant specie of proton (which do not require multi-electron transfers). Thus the structural design of the electrochemical cell and the electrode position within cathode and anode could had affected the transfer of electrons during intermittent sunlight since it affects the distribution of charges around electrode area.

The calculated thermodynamic potential drop for CO and HCOOH, based on the Nernstian anodic and cathodic half cell potential at vs SHE are -1.34 V -1.48 V, respectively. However, the electrochemical cell in reality (as discussed in chapter 2) operate at voltages much higher than those values. There are many different causes for this overpotential such as the Nafion proton exchange membrane and the cathodic overpotential. The pH gradient between the EC compartments in this study also resulted in an opposing voltage of about 480 mV (but as has been discussed before, helps in more longevity and efficacy [20]).

The faradaic efficiency of the cells for CO and formate production was determined from the measured molar concentration of the end-products, electrons required for the reaction, the total number of coulombs passed (Q) and Faraday's constant (F). Table 4.5 provides a breakdown for the efficiencies of each individual section of solar-to-fuel study.

Table 4.5 The average efficiency for each of the different processes in each experiment

Exp. No.	Max. FE. Towards CO_2-reduction	PhotoVoltaic efficiency	Operational Efficiency of MPPT	Electrolysis efficiency	Final Eff. %
5	0.331	0.249	0.960	0.35	2.8
6	0.050	0.250	0.994	0.26	0.32
7	0.105	0.249	0.990	0.30	0.77
8	0.443	0.249	0.961	0.40	4.3

The sunlight intensity data was observed from the Princeton Plasma Physics weather station from May 2017, so as to assess the photovoltaic efficiency. The conversion efficiency of the MPPT circuit was determined by the difference between input and output power. The electrolysis efficiency [13] is the ratio between the thermodynamic potential of the reaction and operational voltage of each EC cell.

The total efficiency of the Solar-to-CO_2 reduction system was calculated by simply multiplying the responses of each of the processes; efficiency of the PV cell, faradaic efficiency, the electrolysis efficiency of the EC cell and the conversion efficiency of the MPPT circuit. This separation of the solar current, maximum point tracking and chemical conversion subsystems in this study allows the freedom to focus on individual sections

for more optimum efficiency, as compared to PEC systems. The use of metal electrodes as compared to the semiconductors in the PEC system, also help to achieve much stable electrode surfaces and greater degree of control. This becomes more important when multi-electron and multi-proton reduction of CO_2 is to be targeted since a separate electrochemical reduction subsystem allows better scalability in terms of electrode area and multi-cell design.

The best IV matching between the CPV and EC setup (for experiment 8) is shown in figure 4.15. The solar sun IV has been measured in lab conditions for 0.5 sun to closely emulate the average sunlight intensity during the eighth experiment (which provided the best results). The IV input to EC reflect that the current output from MPPT circuit (EC input) did reach to the maximum power point during the intermittent irradiation.

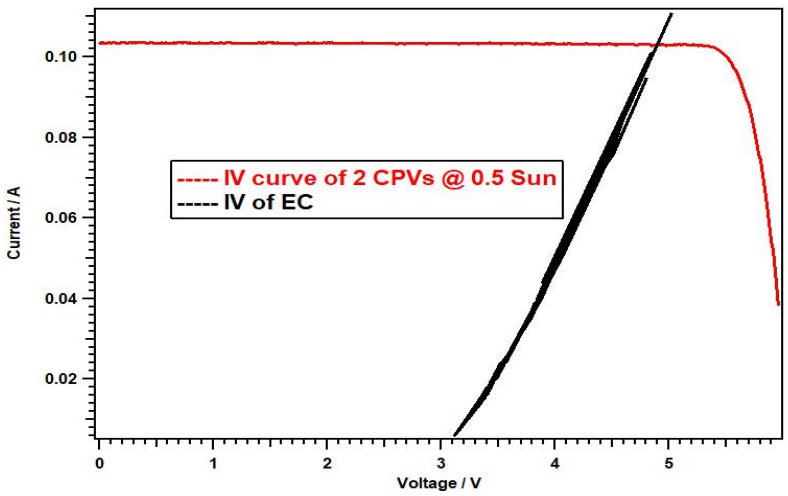

Fig. 4.15 IV matching between PV and EC for tin-based second experiment

In contrast to PEC systems, the separation of the solar current, maximum point tracking and chemical conversion subsystems in this study allows the freedom to focus on individual sections for more optimum efficiency. The CPV efficiency and MPPT conversion were relatively stable and was not affected by the intermittance of sunlight. The operational voltage of the EC determined the current density of the sample and hence in order to confirm the reproducability, we decided to focus on replicating the current densities under lab conditions for the best performing faradaic yield (Exp 8). A current density of 2.5 mA/cm^2 and 44.3% faradaic efficiency had been observed in

experiments under natural sunlight. The faradaic yield shown in figure 4.16 show the average faradaic conversion at 37.1% operating at current density of 2.66 mA/cm^2. It decreased to about 31.1% at around 2.1 mA/cm^2 and 22.2% at 1.4 mA/cm^2. For a current density of 3.8 mA/cm^2, the FE was observed to be 34.3%. Since the scope of this research was focused towards the current density in the range obtained from the solar fuel experiments, in terms of the faradaic efficiency obtained from replicating a stable current density of 2.66 mA/cm^2 in laboratory conditions, our solar-to-fuel efficiency could be adjusted to around 3.6%.

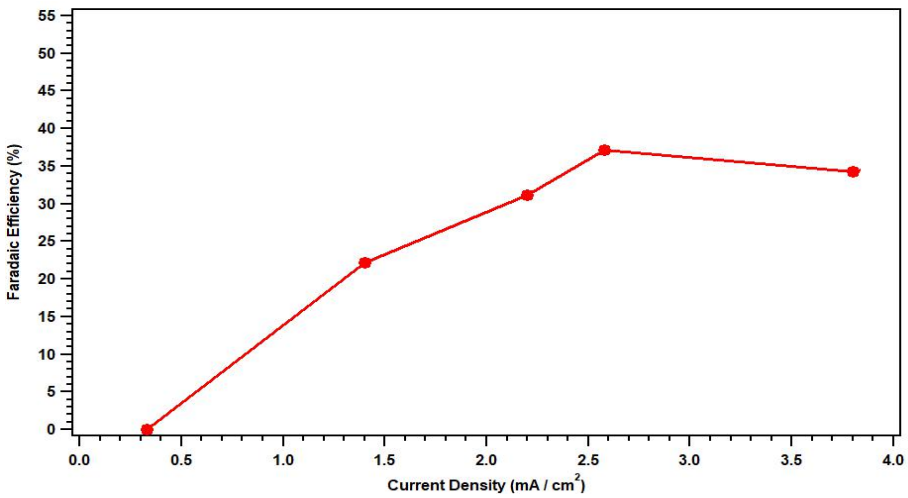

Figure 4.16 FE vs current density for Sn electrode

4.4 Summary:

1. A practical CO_2 reduction system was realized using Au and Sn electrodes for producing CO and formic acid, respectively.
2. The impact of varying solar irradiation under natural conditions was studied, in order to understand the impact of changing current densities and end-product formation.
3. The results show the impact of tracking the MPPT for the multijunction solar cell in cloudy conditions and the influence of intermittent light on current generation and faradaic efficiency at different points of time.
4. A maximum faradaic efficiency of about 44% was achieved, which resulted in a solar-to-fuel efficiency of about 4.3%. The comparative analysis for this study to other reported solar-to-fuel efficiencies has been shown in figure 4.17. The 44% FE figured

lower to the maximum of 67% FE observed in the previous study of CO_2-based solar fuel efficiency under natural sunlight. However the overall solar fuel efficiency was almost twice higher. The lower FE was due to the impact of current density on the competing evolution of hydrogen, while the overall higher efficiency was made possible due to higher PV efficiency of 24.9% and a highly precise tracking of the maximum power point.

5. Higher FE of almost 90% observed under simulated condition for previous solar fuel papers, can help to achieve a higher conversion rate of photons to chemical compounds.

6. Further improvement in the CPV module efficiency, use of electrodes with smaller overpotential and better matching of IV characteristics are the future research and development directions for solar-powered CO_2 reduction.

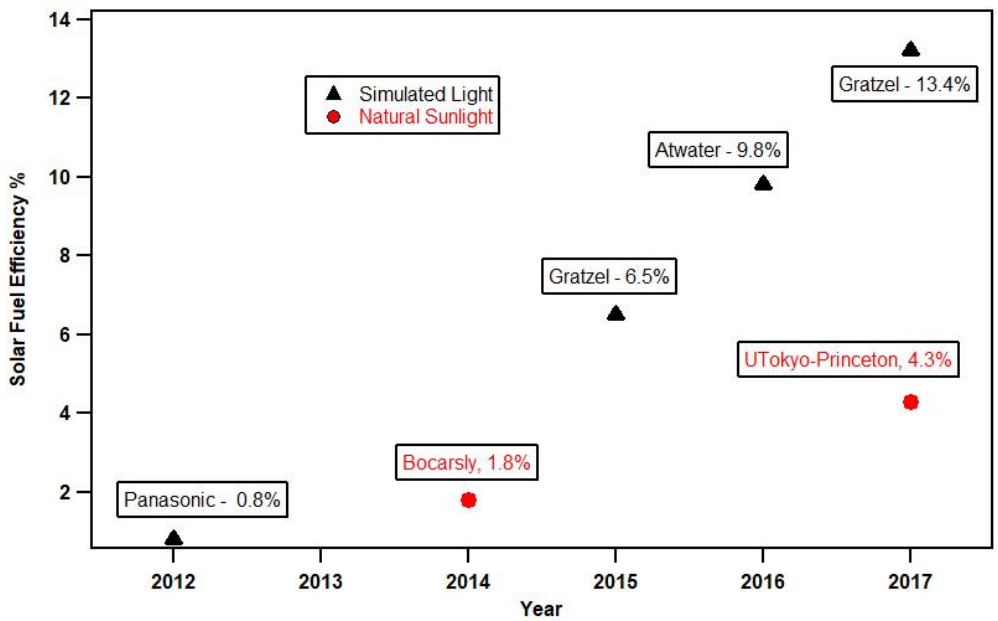

Fig. 4.17 The present status of the Solar Fuel study can be summed in this figure where the name of Principal Investigator along with the FE, is mentioned against the year it was conducted.

4.5 References

1. Voluntary Reporting of Greenhouse Gases Program, Table of Fuel and Energy Source: Codes and Emission Coefficients; Energy Information Administration, Office of Integrated Analysis and Forecasting, 2011.
2. Kumar, B., Llorente, M., Froehlich, J., Dang, T., Sathrum, A., Kubiak, C. P., *Phys. Chem*. 2012, **63**, 541–569.
3. Kauffman, D. R., Thakkar, J., Siva, R., Matranga, C., Ohodnicki P. R., Zeng, C., Jin, R., *ACS Appl. Mater. Interfaces*, 2015, **7**, 15626–15632.
4. Bard, A. J., Wrighton M. S., *J. Electrochem. Soc*., 1977, **124**, 1706–1710.
5. Gerischer H., *J. Electroanal. Chem*, 1977, **82**, 133–143.
6. Nielander A. C., Shaner M. R., Papadantonakis K. M., Francis S. A., Lewis N. S. A, *Energy Environ. Sci.,* 2014, **8**, 16– 25.
7. Oloman, C., Li, H., *ChemSusChem* 2008, **1**, 385–391.
8. Winkler M. T., Cox, C. R., Nocera, D. G., Buonassisi T., *Proc. Natl. Acad. Sci*. 2013, **110**, E1076–E1082.
9. White, J. L., Baruch, M. F., Pander III, J. E.; Hu, Y., Fortmeyer, I. C., Park, J. E., Zhang, T., Liao, K., Gu, J., Yan, Y., *Chem. Rev.,* 2015, **115**, 12888-935.
10. Jia, J., Sietz L. Jaramillo T., *Nat. Commun.* 2015*,* **7**, 13237-245
11. Luo, J., Im J., Gratzel M., *Science*, 2014, **345**, 1593–1596.
12. Ogura, K.; Yoshida, I., *J. Mol. Catal*. 1986, **34**, 309–311.
13. White, J. L.,Herb, J. T., Kaczur, J. J., Majsztrik, P. W., Bocarsly, A. B., *J. CO_2 Util.* 2014, **7** ,1
14. T. Arai, S. Sato, T.Morikawa, *Energy Environ. Sci*., 2015, **8**, 1998-2004
15. Schreier M., Gao P., Gratzel M., *Energy Environ. Sci*., 2015, **8**, 855-861
16. O'Brien, T. F., Bommaraju, T. V., Hine, F. *Handbook of Chlor-Alkali Technology*; Springer Science & Business Media, 2005
17. Innocent, B., Liaigre, D., Pasquier, D., Ropital, F., Léger J.-M., Kokoh, K. B., *J. Appl. Electrochem.,* 2008, **39**, 227–232.
18. Machunda, R. L., Lee, J., Lee, J., *Surf. Interface Anal.*, 2010, **42**, 564–567.
19. Oloman, C., Li, H., *ChemSusChem*, 2008, **1**, 385–391.
20. Subramanian, K., Asokan, K., Jeevarathinam, D., Chandrasekaran M., *J. Appl. Electrochem*., 2007, **37**, 255–260.
21. Li, H. Oloman, C., *J. Appl. Electrochem*., 2005, 35, 955–965.
22. Narayanan, S. R., Haines, B., Soler, J., Valdez, T. I., *J. Electrochem. Soc.*, 2011, **158**, A167–A173.
23. Alvarez-Guerra, M. Del Castillo, A. Irabien, A., *Chem. Eng. Res. Des*., 2014, **92**, 692–701.
24. Li, H., Oloman, C., *J. Appl. Electrochem*., 2005, **35**, 955–965.
25. Faranda R., Leva S., *WSEAS Trans. Power Syst.*, 2008, **3**, 446-455, 2008.
26. Sridhar R., Jeevananthan S., Selvan N., Chowdary S., *IEEE Int. Conf. Commun. Control and Comput. Technol.*, 2010, 191-195
27. Razali N. M., Rahim N.A., *IEEE First Conf. Clean Energy and Technol.*, 2011, 34-39.
28. Wu J., Risalvato F., Ke F., Pellechia P., Zhou X., *J. Electrochem. Soc.,* 2012, **159**, F353–F359.
29. Krishtalik L., *Biochemica et Biophysica Acta*, 2011, **1807**, 1444-1456

CHAPTER 5

Arc Plasma deposited Cu, Au metal nanoparticles

The solar fuel study employed bulk metals as electrodes which have been a staple for research in electrochemical reduction of CO_2. Therefore our subsequent interest shifted towards using nanaoparticles of the metals which increases the surface area to volume ratio which reportedly increases catalytic activity and improves product selectivity. The detailed relative advantages and previously reported work on the use of nanoparticles will be explained in sections 5.3 and 5.4. This work attempted to build upon and understand the impact of using nano-scale particles and the corresponding changes in terms of efficiency and product selectivity. A bimettalic deposition of the nanoparticles using Arc Plasma Deposition (APD) technique was utilized in order to investigate the usability of APD technique and co-deposition of copper and gold nanoparticles in CO_2 reduction reactions.

5.1 Use of Nanoparticles

As the definition suggests, nano-scale materials are structures that lie on the nanometer scale (100 nm) range. Recently, such structures have gained a lot of attention because of the distinct changes in the physical and chemical properties of new materials, which happen due to the transition from micro-scale materials to nano-scale materials [1]. It has been widely reported that the decrease in size and going to the nano-scale can greatly increase the surface area of the material and can aid in establishing new properties. There are several classifications of nanoparticles such as single or composite (also known as core-shell), and it is dependent on the composition of the material [1]. Usually single nanoparticles is made up of a single material while on the other hand, the composite comprises of at least two or more materials. This nano-scale co-deposition of multiple materials can be more interesting than single metallic nanoparticles because the synergistic or lattice strain effects between the two metals can give rise to new properties. Interest in bimettalic deposition has been reported due to the potential of new properties in the fields of biomedicine, optics and electrocatalysis. They are highly functional materials with improved properties [2]. Furthermore, the tunable composition of these core-shell nanoparticle structures can give rise to greatly enhanced functional materials. Such materials usually have certain surface modification which contribute to the stability, dispersion,functionality and catalytic properties of such materials [2]. Moreover, bimettalic nanoparticles can be modified to make eco-friendly materials since when a noble metal and non-noble metal are ‘wowen’ into the system, the catalytic operation is

increased at a lower consumption of precious metal compared with pure noble materials of the same size [3-4].

The fabrication method of bimettalic nanoparticles can be classified into "top down" and "bottom up" synthesis method [5]. The "top down" approach involves conventional physical operation such as cutting, polishing, and chipping particles into an ideal shape using external force. Techniques employing electron/ion beam, scanning probe, or laser beam processing, or similar mechanical techniques can be classified as ‘top down’. On the other hand, the "bottom up" approach uses the natural properties of molecules to assemble themselves by advantageous formation. Techniques employed in the “bottom up” are thermal synthesis, chemical vapor deposition and laser-tapping. The methods used, whether it is “top down” or “bottom up”, also help in establishing distinguished properties. Usually, a greater degree of control on the sizes of the nanoparticles is established when using the“bottom up”method. This technique can also help in fabricating smaller sized nanoparticles as compared with the “top down” method. On the flip side, the “bottom up” technique is effective in terms of cost control since it has more accuracy and more control procession which require less energy consumption than the ‘top down” method [1]. It is also feasible to use a combination of two methods.

The propensity of nanotechnology and advances had started to mature from the late 1990s. It was about that time that nanostructures emerged as a new type of material with unique advantages, such as large surface areas and high tunability in morphology as well as compositions. In terms of CO_2 reduction, most of the initial reports had focused on different types of gold- and silver-based nanostructures that had demonstrated as effective CO_2 electroreduction catalysts [6].

There is a general conclusion now that the surface engineering, morphology control, and composition manipulation to form alloy or core−shell nano-structures can greatly tune the catalytic properties of nano-structures, area and catalytic active sites [7-10]. One major example is the use of flat surfaces of the bulk gold and silver electrodes that show limited activity in CO_2 reduction, but when their surface is modified to form nano-structures on the surface of the electrodes, the electrodes become an effective approach for CO_2 reduction. [8]

5.2 Arc Plasma Deposition - mechanism and advantages

In the arc plasma deposition (APD) process, the target material for deposition is evaporated by vacuum arcs action. The source material is the cathode in the arc circuit. The main sections of the equipment can be divided into a cathode and an arc power supply, a vacuum chamber, source for initiating the arc on the cathode surface, an anode and biased substrate power supply. The arcs usually are initiated and sustained by voltages range typically between 15-150 V, and depends on the material being used as a cathode. Usually the currents remain between 30 to 400 A [11].

The act of initiating the arcs occurs through the application of a pulse with high voltage on to an electrode. This electrode is located next to the cathode (gas discharge ignition). A secondary and less used method is of mechanical ignition. The evaporation occurs as a result of the cathodic arc spots which move randomly on the surface of the cathode at speeds typically of the order of 102 ms [11-12]. The motion of the arc's spot can be controlled with appropriate confinement boundaries and magnetic fields [13-14]. These arc spots are then maintained by the material plasma generated by the arc itself. The cathodic material can be an insulator or a metal or semiconductor. The descriptive schematic for APD and the APD plasma picture is shown below in figure 5.1 and figure 5.2, respectively.

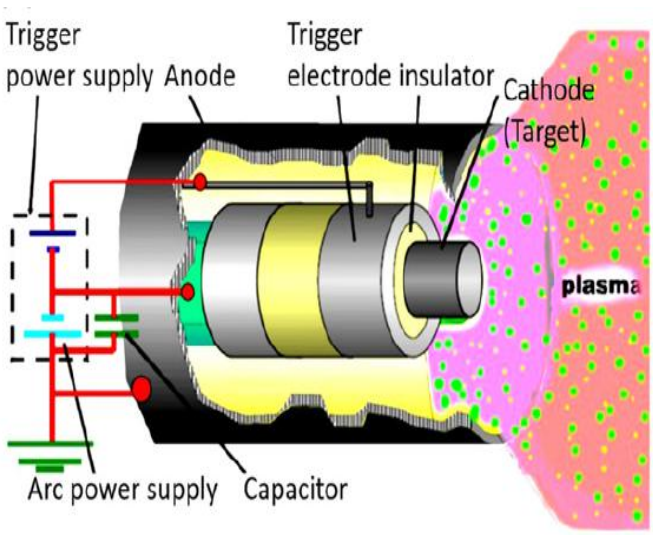

Fig 5.1 Schematic of the Arc Plasma Deposition [11]

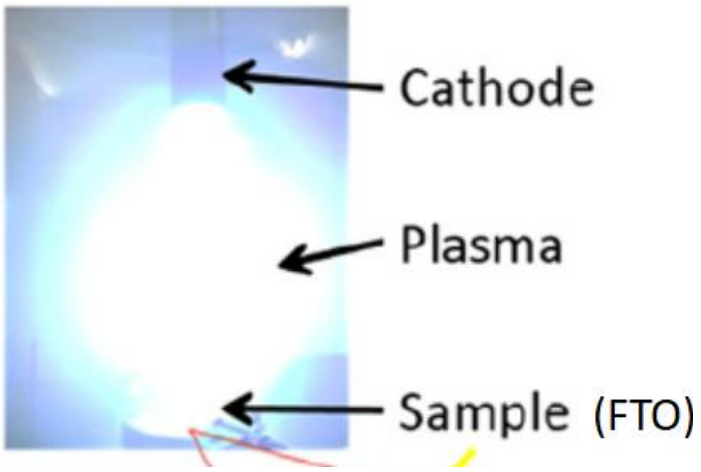

Fig. 5.2 The APD plasma from Cu being deposited on FTO substrate.
Source: Advance RIKO report

The APD process is a unique process and is markedly different from other physical vapor deposition (PVD) processes. Some of the characteristic features of the Cathodic APD process are as follows:

(i) The core of the APD process is the arc spot which generates material plasma.
(ii) A high percentage (30% - 100%) of the material evaporated from the cathode surface is ionized [15].
(iii) The ions exist in multiple charge states in the plasma, e.g. Ti, Ti^{+}, Ti^{2+} and Ti^{3+} etc. [11, 16].
(iv) The kinetic energies of the ions are typically in the range 10 - 100 eV [17].

As a result of such features, the depositions are of superior quality compared with those from other physical vapor deposition processes. Some of these advantages are as follows [18]:

(a) The quality of films remain good over a wide range of deposition conditions and remains true for various metal and compounds films.
(b) High deposition rates for metals, alloys and compounds with excellent coating uniformity.
(c) Low substrate temperatures
(d) Retention of alloy composition from source to deposits.

(e) Ease in deposition of compound films.

The cathodic arc originates the plasma discharge from the cathode surface. The arc spot is typically a few micrometres in size and carries current densities as high as 10 A/ um^{-2} [18]. The very high current density causes flash evaporation of the source material and the resulting evaporation consists of electrons, ions, neutral vapor atoms and microdroplets. The electrons are accelerated toward the cloud of positive ions. The emissions from the cathode spots are relatively constant over a wide range of arc current as the cathode spots split into a number of spots. The average current carrier per spot depends on the nature of the cathode material. It is likely that almost 100% of the material may be ionized within the cathode spot region [10]. These ions are ejected in a direction almost perpendicular to both electrodes

It has been suggested that the microdroplets discharge from the cathode surface at angles up to about 30° above the cathode plane [19]. This emission is due to the very high temperatures and forces that are present within emission craters. The microdroplet emission is greater for metals with low boiling points. The microdroplet emission is also observed to be lower with increased cathode spot velocity and surface contamination. The presence of a reactive gas in the chamber markedly affects the micro-droplet emission.

5.3 CO_2 reduction with Cu nanoparticles

Now that the benefits of nanoscale fabrication and the basic principle and advantages of arc plasma deposition have been established, it is important to discuss the background and literature review of the nanoparticles that were chosen to be arc plasma deposited on the substrates.

The first choice of the nanoparticle was obvious. Copper (Cu) has been the staple for the electrochemical reduction of CO_2 and is the only established metal that is able to generate electron-intensive reactions and higher-order carbon products. Therefore, using the Cu based nanoparticle catalysts allows the number of active low coordination sites per mass Cu, to increase. As will be discussed many a times in this thesis, the ratio of edges, corners and planes is important for CO_2RR and the use of APD can allow to enhance such lower coordination sites. In 2014, Reske *et al*. synthesized spherical Cu nanoparticles with sizes ranging from 2-15 nm using polymer micelles [20]. Methane and

ethylene production were decreased relative to the Cu foil on all the nanoparticle sizes. On the flip side, the selectivity towards CO and H_2 was relatively increased. These altered selectivities were enhanced most for the smallest nanoparticle sizes. It was suggested by the authors that the changes in selectivity were attributed to the low coordinated sites not being favorable for subsequent hydrogenation steps after CO. The figurative summary of the results can be seen in figure 5.3. In another study (by Manthiram *et al.*) it was reported that hydrogenation rates for CO had increased for Cu nanoparticles dispersion of about 23 nm and a 67% faradaic efficiency (FE) was registered for methane production [21]. The nanoparticles in the study by Manthiram *et al.* were synthesized by colloidal methods and dispersed on glassy carbon. There were other similar studies that suggested the difference in performance of Cu nanoparticles was because of the difference in dispersion of Cu. Another report [22] studied the effect of the size of Cu nanocatalysts by using 24-63 nm of Cu nanocubes synthesized using colloidal methods. Nanocubes displayed greater current density than similarly sized spheres. The 44 nm nanocubes displayed the highest faradaic efficiency towards the CO_2 reduction reaction and had the highest selectivity towards products such as CH_4 and C_2H_4 which required electron-intensive reactions. It was speculated by the researchers that this was a result of the ratio between edge, plane and corner sites being more favorable on cubes than on spheres. They had suggested that the edge sites are more favorable for CO adsorption and stabilization while planar sites are also required for increasing the formation of hydrocarbons.

For decreasing the HER on Cu nanoparticles, it has been suggested to place the them on a substrate or support, doped with nitrogen. A study by Song *et al.* had deposited 39 nm Cu nanoparticles on N-doped graphene spikes [23]. At -1.2V vs RHE in 0.1 M $KHCO_3$, the Cu nanoparticles gave a 63% Faradaic efficiency towards CH_3CH_2OH. DFT suggests that the N-doped graphene possesses an increased affinity for binding oxygenated carbon compounds. It was proposed that the substrate support coordinates with the Cu surface in adsorbing intermediates, particularly oxygenated C2 species, making the production of CH_3CH_2OH more feasible. Thus, the nature of the substrate material also plays a key role in the performance during CO_2RR. It was our speculation that the characteristics of APD technique could allow deposition of low coordinated Cu nanoparticles.

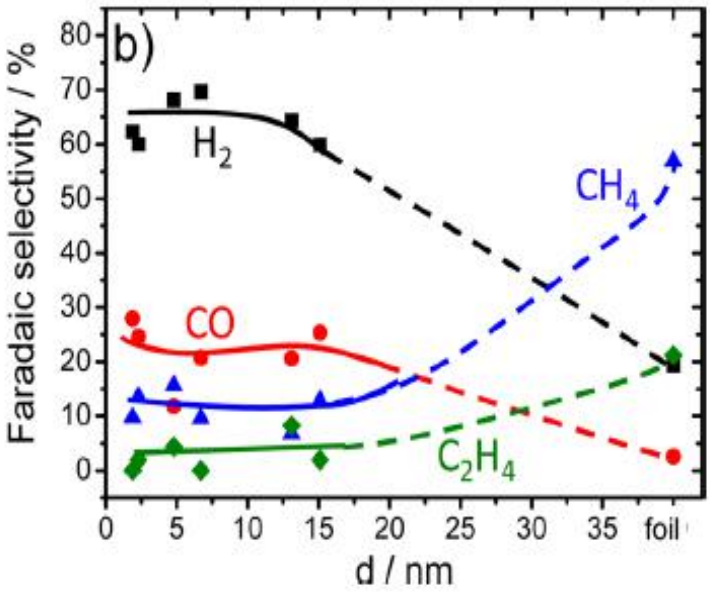

Fig. 5.3 FE for different products on different sizes of Cu NPs [20]

5.4 CO_2 Reduction on Au nanoparticles

Despite being a noble metal, Gold (Au) is an effective electrocatalyst for the reduction of CO_2 to CO. The use of Au was initially reported by Hori *et. al.* in 1987 as a CO_2 electroreduction catalyst [24]. The study had employed Au electrode in 0.5 M $KHCO_3$ electrolyte. CO, H_2 and $CHOO^-$ were observed as products, with faradaic efficiencies of 92%, 9% and 1% respectively at -0.98V vs NHE. Since it is difficult to hydrogenate CO_2 to any other product than CO on Au metals, it was our hypothesis that co-deposition of Cu nanoparticles along with Au could help to generate a composite reduction mechanism. Au nanoparticles have recently become an interesting area of study. In 2012, Kauffman *et al.* synthesized Au_{25} nanoparticles for use as CO_2 reduction catalysts [25]. Au_{25} nanoparticles consist of a Au_{13} core surrounded by a shell consisting of 12 Au atoms and 18 phenylethanethiol molecules held together by the S groups of the thiols. When employed in CO_2RR as catalyst in 0.1 M $KHCO_3$, the onset potential was shifted positively by 200-300 mV compared to bulk Au and generated carbon-monoxide at faradaic efficiencies of approximately 100%. These improvements are attributed to the inherent negative charge of the Au_{25} nanoparticle and the unique structure. The size and

structural effects of Au nanoparticles on CO_2 reduction have been noted by other groups as well. The size of the nanoparticles play a critical role and their impact have been observed by Mistry *et al*. [26] and Zhu *et al*. [27] who had reported that CO yields increased on nanoparticles possessing more low coordination sites such as edges and corners. Having synthesized and tested 4, 6, 8 and 10 nm spherical Au nanoparticles, Zhu *et al*. reported that the maximum CO selectivity occurs at 8 nm due to an optimal ratio of edge and corner active sites. It was also concluded that NPs with sizes below 2.7 nm will begin to display finite size effects. The results can be seen in figure 5.4. [27]. The ratio of edge and corner sites was also studied in detail by Zhu *et al*. in another study employing Au nanowires [28]. By increasing the amount of reactive edge sites, nanowires were able to reduce CO_2 to CO at up to 95% faradaic efficiency and at greater current densities than the previous 8 nm nanoparticle Au. Figure 5.5 provides the calculations for the ratio between different sites.

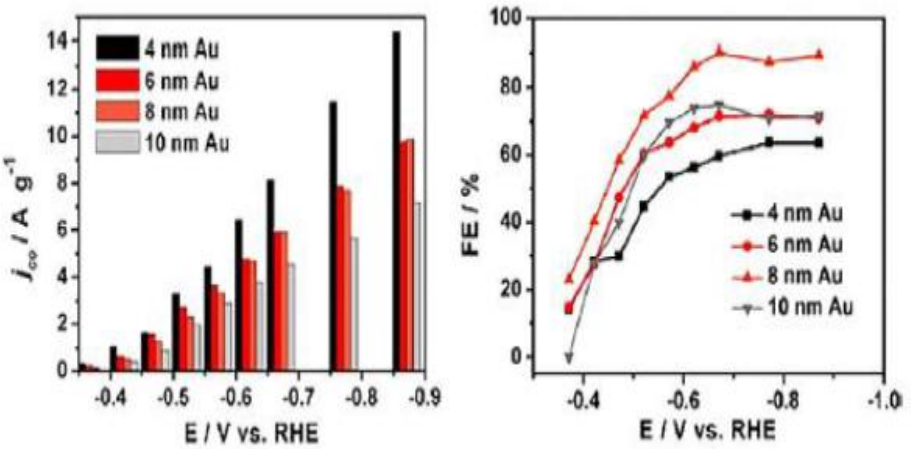

Fig 5.4 CO partial current density (top left) and faradaic efficiency (top right) on Au nanoparticles. [27]

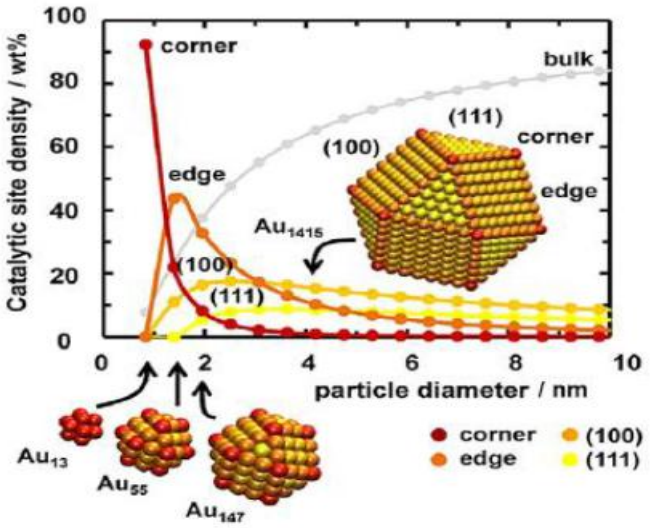

Fig. 5.5 Calculations assuming perfect cuboctahedra show the ratio between different active sites [27]

Other structural effects were noted by Chen *et al.* [29] who had synthesized nanostructured Au for CO_2 reduction. By oxidizing Au foil in H_2SO_4 using square wave voltammetry, oxidized electrodes with roughed surfaces were prepared as catalysts. Once under reductive potential, the oxide was quickly reduced, leaving a nanostructured Au layer. The nanostructured Au was able to produce CO at 100% faradaic efficiency while the overpotentials were 200 mV more positive than Au foils. Similarly, concave rhombic dodecahedral Au catalysts synthesized by Lee *et al.* [30] showed improvements as a result of nanoparticle structure. Under a reducing potential in 0.5 M $KHCO_3$ electrolyte, concave rhombic dodecahedral catalysts reached up to 93% Faradaic efficiency to CO, and shifted the onset potential for CO_2 reduction by 230 mV anodically compared to polycrystalline Au foil. The improvements were attributed to the high index facets available on the concave rhombic dodecahedron surface.

5.5. Co-deposition of copper and gold nanoparticles on FTO substrate

In this study, Cu and Au nanoparticles were deposited on the conductive glass material that of fluorine doped tin oxide (FTO). It was our contention that APD technique would be able to deposit highly dispersed and uniform nanoparticles of metallic states, which would exhibit high catalytic activities because of their lower coordinate sites. As earlier

discussed in section 5.2, APD is also useful because the process allows simultaneous deposition of Cu and Au nanoparticles, which may get implanted on to the substrate. The unique catalytic properties associated with implantation of bimetals [31] was based on the idea that the structure and reactivity and selectivity of certain metal nanoparticles can be promoted by the other metal elements.

Fluorine doped tin oxide (FTO) was chosen as the substrate material because of its conductivity as well as its disordered glass structure which can potentially allow unique reaction centers. The deposition of copper and gold nanoparticles, in principle can yield a composite reaction mechanism in which the CO_2 reductions can take place on multiple sites. The reduction of CO_2 using Au electrode can primarily only generate CO and since CO is known to be an intermediate specie for carbon intensive products, it can act as a feedstock for Cu nanoparticles [32-33]. We had theorized that CO generated during CO_2RR at Au can be utilized by the neighboring Cu nanoparticles, helping to reduce the number of steps for generating carbon intensive products at Cu hence raising faradaic efficiency during CO_2RR. Another reason for using FTO was based on the reports that using oxide based supports for the nanoparticles can alter properties of nanoparticles and aid in the CO_2 reduction reaction via synergistic effects. As already discussed before in section 5.2, the structure of the substrate support can play a key role in CO_2RR.

The descriptive design reflecting the theorized electrode structure is shown in figure 5.6 and 5.7 (top and side view, respectively) along with the mechanism in figure 5.8.

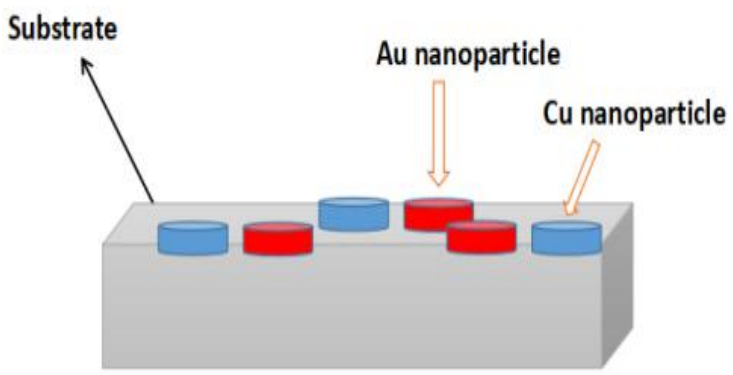

Fig 5.6 Side view of the theorized APD electrode structure

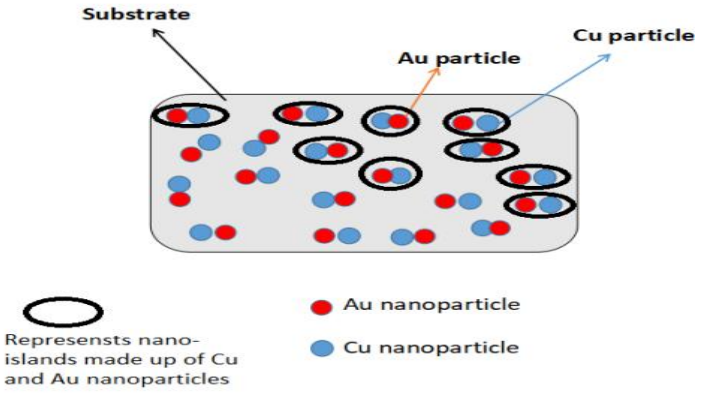

Fig. 5.7 Top view of the theorized APD electrode structure

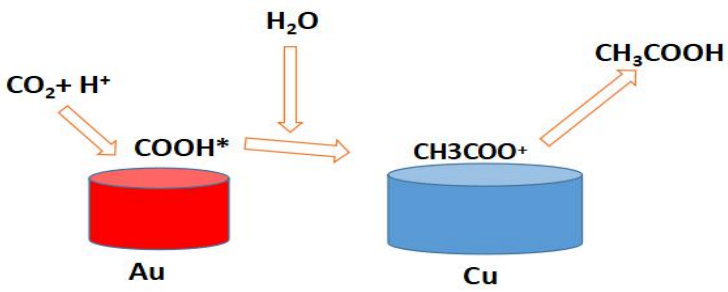

Fig 5.8 A possible composite CO_2RR for carbon intensive products on the catalytic surface of the electrode.

Fluorine-doped tin oxide (FTO) was prepared through mixed quantities of SnO_2 and SnF_2. These FTO substrates were commercially procured from Sigma Aldrich vendor after which the samples were sent to Advance Riko Inc for deposition of nanoparticles (NP). Cu and Au NPs were deposited on FTO by arc discharge of metallic Cu and metallic Au cathodes, respectively. All the depositions were carried out under vacuum (at 10^{-3} Pa) at room temperature. The number of arc discharge pulses (N) was 150 shots, the capacitance of the condenser (C) was 1080 mF, and the voltage for arc discharge (V) was 134 V for Cu and 142 V for Au. In this study, it was observed after the XPS analysis that the difference in arc discharge resulted in deposition of relatively smaller Au NPs and

bigger Cu NPs. Home-made H-type leak-tight electrochemical cells were used for CO_2 reduction, with 100 cm^3 volume and 70 ml of electrolyte.

Ag/AgCl reference electrode was employed while platinum was used as the counter electrode. 0.5 M $KHCO_3$ with a pH of 8.60 was used in the cathode and anode electrolyte, which dropped to 7.20 pH in the cathode half-cell after the CO_2 purging. The pH changes were not observed during the experiment.

In order to gauge the activity of the electrodes for CO_2RR, a comparative IV response was measured by using the same electrode in CO_2-saturated and Ar-saturated electrolyte, which is shown in figure 5.9. Enhanced current density was observed in CO_2-saturated electrolyte, which reflected CO_2RR activity.

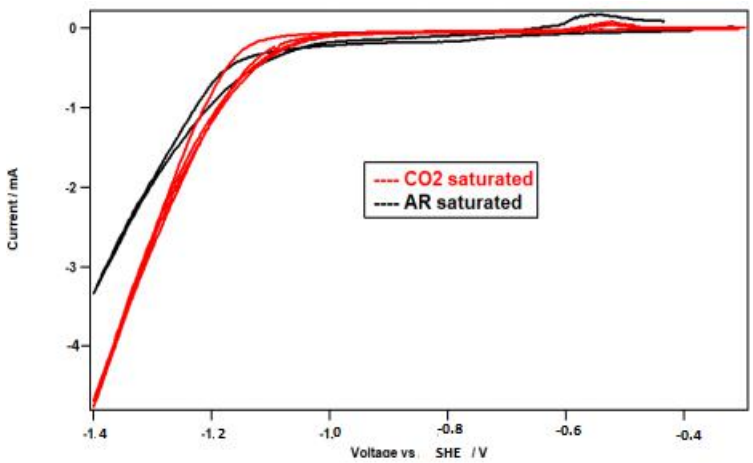

Fig. 5.9 IV response of APD samples in CO_2 and Ar saturated electrolyte

The result of the CO_2RR experiments are produced in figure 5.10 in which hydrogen remained the dominant product along with formic acid and CO. The formic acid FE was around 21% at the onset of CO_2RR at 1150 mV vs SHE and peaked at around 60% at 1300 mV after which it slid down again to almost zero at 1800 mV vs SHE. The minor product from CO_2RR was CO production which remained below 10% however in experiments employing only the control FTO substrate as the electrode, CO remained the only product from CO_2RR while hydrogen production continued as a parasitic product. The difference between CO and HCOOH is suggested to originate from the difference of intermediate specie, that of COOH and OCHO, respectively [34]. Chemically the

intermediate species contain the same elements however local pH alterations and overpotentials have been speculated to determine the outcome of the product. [35]

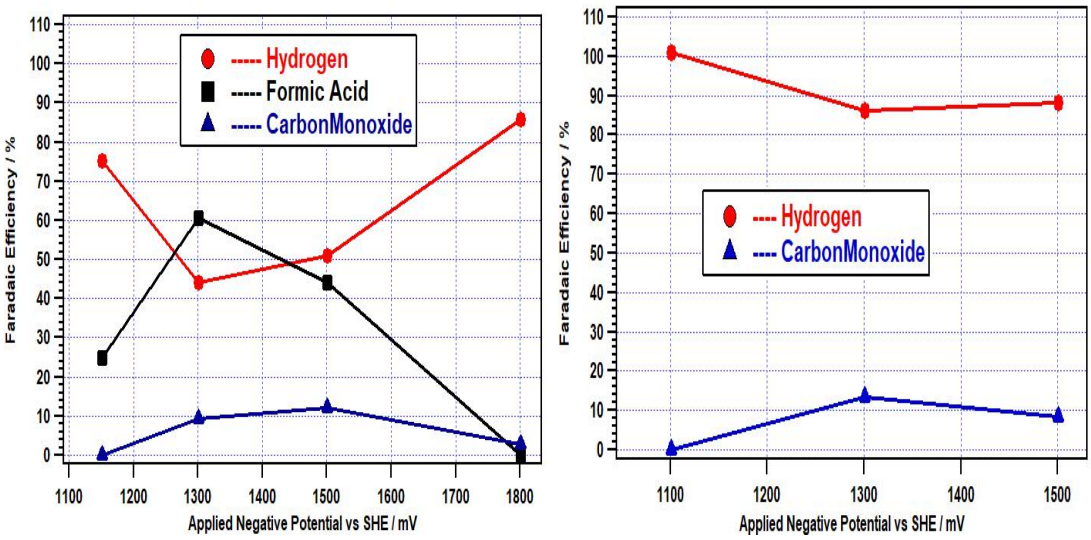

Fig. 5.10 Faradaic efficiency against negative cathodic potential for pristine APD electrode (left) and control samples (Pristine FTO)(right)

During the initial experiments, it was observed that a reddish-brown layer used to appear after the application of cathodic potential, which was indicative of surface deterioration and which increased with more negative cathodic potentials. However, after about 6 experiments, it was observed that no further substrate deterioration took place and substrate surface stability was achieved. The Scanning Electron Microscope (SEM) images in fig 5.11 shows the difference in surface between pristine and stabilized electrodes. The FTO glass film on pristine electrode had initially undergone deterioration after repeated experiments. The degeneration of surface partially disintegrates the thin film on the glass structure and the reddish-brown color suggests that it is SnO_2, which is subsequently cleaned off after the experiment.

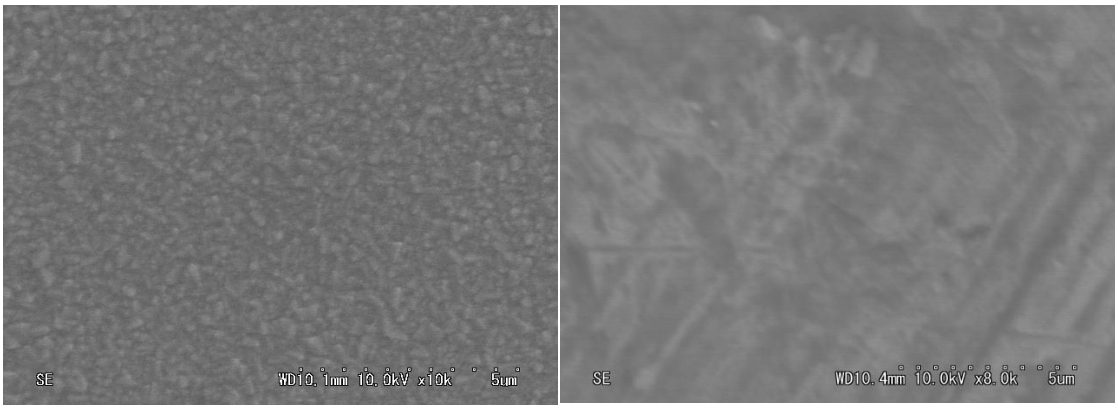

Fig. 5.11 SEM images for pristine APD electrode (left) and stabilized APD electrode (right)

It was important to gauge the impact of this surface disintegration on the deposited metal NPs as well as the surface of the FTO substrate. XPS analysis was conducted on pristine and stabilized electrode surfaces to analyze the comparative differences. Figure 5.12 shows the comparative peak intensities for Au where the clearly identifiable Au presence in pristine electrode had been reduced to no detectable Au peak in stabilized electrode. This represented that its atomic concentration was less than the detection limit. In figure 5.13, Cu was more clearly observed which reflected that the size of implanted Cu NPs was larger than Au and so implantation was more anchored into the surface.

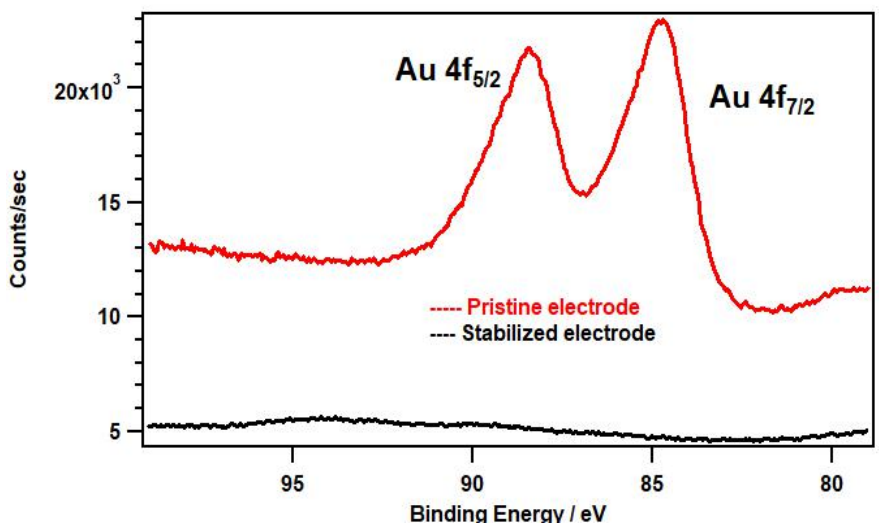

Fig. 5.12 XPS analysis comparison for Au element in pristine and stabilized electrode

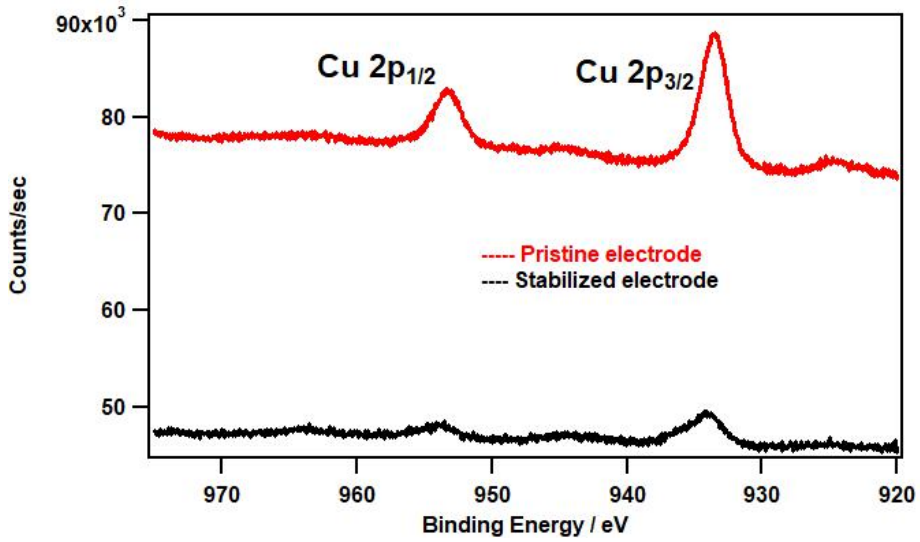

Fig. 5.13 XPS analysis comparison for Cu element in pristine and stabilized electrode

Table 5.1 shows the comparative analysis of the relative atomic concentrations of the surface elements. The atomic concentration of implanted Cu remained stable however the Au concentration decreased to below the detection limit. The erosion of SnO_2 meant that the presence of Sn would decrease and this can be seen in the relative increase of fluorine to tin in the stabilized electrode. Since the FTO substrate is a combination of polycrystalline SnO_2 and SnF_2, in which SnO_2 is usually the dominant entity [36], we speculate that the absence of detectable fluorine in the pristine electrode reflects that SnF_2 was not present within the nanometer range depth resolution of XPS and the top few nanometers of FTO is primarily composed of SnO_2.

Table 5.1 Comparative XPS analysis for pristine and stabilized electrodes

	Carbon	**Oxygen**	**Copper**	**Gold**	**Tin**	**Fluorine**	**Silicon**
Atomic Conc. for Pristine electrode / %	74.60	19.9	2.20	1.40	1.90	Below detection limit	Below detection limit
Atomic Conc. for stabilized electrode / %	61.1	28.4	2.0	Below Detection Limit	2.7	4.2	1.6

Carbon contamination on the surface (from the APD fabrication process) also decreased after the deterioration of the surface. Since the reaction centers for CO_2RR are suggested to be on the metal NPs and the surface continued to be conductive, the relative changes of Sn, O, F should not present a major drawback for CO_2 reduction. Post-stabilization, silicon was also observed after XPS analysis with an atomic concentration of about 1.6 %, which had originated from slight exposure of the underlying SiO_2 substrate beneath FTO, after degradation. This also explains the relative increase of oxygen, seen in the stabilized phase. The non-conductive silicon oxide substrate does not play any role in CO_2RR and the very small concentration of Si on the surface shows that the exposed substrate area was very small and cannot cause any meaningful decrease in the conductive electrode area to the electrolyte.

The impact of this electro-deterioration on the faradaic yields for the stabilized electrode can be seen in figure 5.14 for both the stabilized APD electrode as well as control FTO electrode.

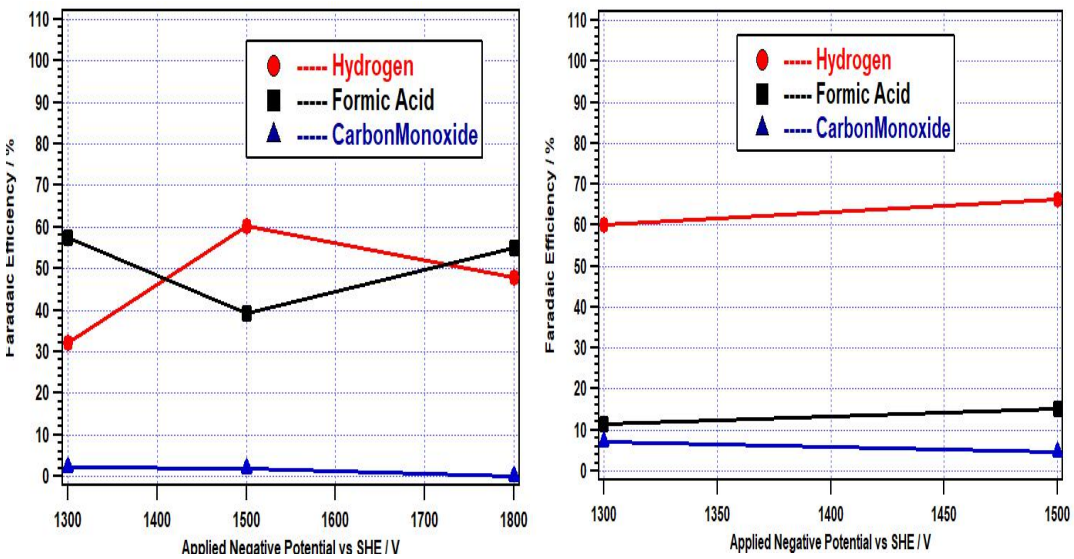

Fig. 5.14 Faradaic efficiency against negative cathodic potential for stabilized APD electrode (left) and control electrode (stabilized FTO)(right)

The product selectivity and faradaic difference of the stabilized electrode to the control electrode remained constant. In the stabilized phase, there was no visible physical difference in between the APD and control samples, since the atomic concentration and size of the implanted NPs was small. Formic acid was observed in control FTO substrate as well however the FE remained lower than that of APD electrode. The origin of formic

acid in the control sample is suggested to be from the SnO_2 in the disintegrated surface, which as reported in previous studies [37] does produce formic acid in CO_2RR experiments. FTO substrates are considered chemically inert and mechanically hard in ambient conditions however the flow of electrons in the liquid electrolyte partially disintegrates the surface structure upon which the exposure of sub-surface SnO_2 also takes place, increasing the surface area exposure to the electrolyte and hence facilitating formic acid production.

In the next phase of the study, the FTO substrate was replaced with a metal alloy so that the substrate surface remains intact and does not affect and change the response during the CO_2RR. In and Sn, individually, are well known electrocatalysts for CO_2 reduction to formic acid however limited work has been carried out on their alloy structure. Sn has been reported to promote tin oxide production in alloy structures which helps in enhancing current density and conductivity in mixed metal systems compared to pure phases of constituent metals [38-39]. Indium metal has also been reported [40] to have enhanced activity in the presence of oxide at the interface and thus it was our contention that the introduction of Sn within In would allow chemical coupling [41] and improve faradaic efficiency and production rate for formate production.

5.6. CO_2 reduction on Alloys

In metals, the selectivity of the product in CO_2 reduction is usually determined by the strength of the bond between the metal and the carbon species, CO_2 or adsorbed CO [42-43]. Metals that do not form a strong M-C bond with CO_2 favor formate because the poor binding strength does not mediate the dissociation of the C-O bond at the catalyst surface. When metals first reduce CO_2 into CO at the surface, the bonding strength with CO determines product selectivity. Metals that weakly bind to CO produce carbon-monoxide selectively because carbon-monoxide can be discharged from the surface before any more reduction steps. Metals that bind to CO too strongly produce few CO_2 reduction products because the CO bound metal sites become inaccessible for further CO_2 catalysis and thus HER takes over. The intermediate binding energy between carbon-monoxide and the surface of copper metal is the reason why the formation of reduced products increases. Although many different metals and morphologies have been tested for CO_2 electrocatalysis over the last several decades, relatively limited attention

has been made on the study of alloys. The use of a combination of metals as an alloy is a promising method to tailor the geometric and electric environments of active sites. The parameter space for discovering new alloys for CO_2 electrocatalysis is particularly large because of the myriad products that can be formed during CO_2 reduction [44]. Figure 5.15 gives an overview of the propensity for various products formed from CO_2 reduction. The black represents metals only while orange represent the alloy structures.

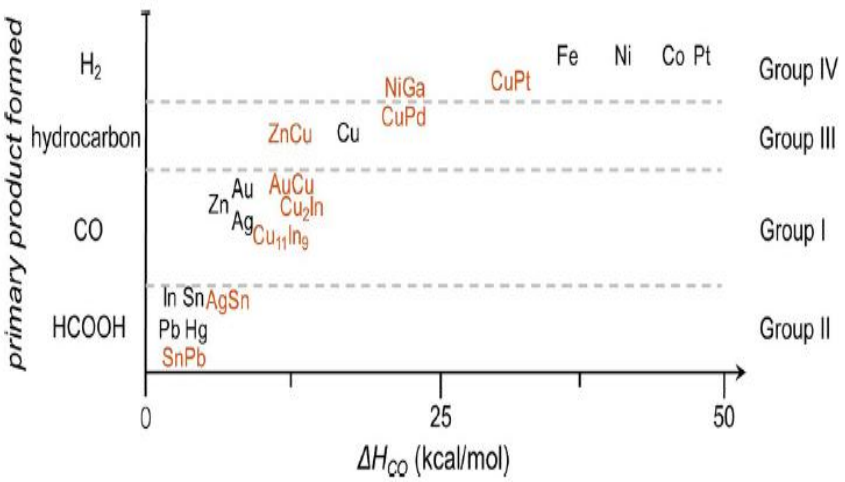

Fig. 5.15 Relationship between the primary product formed and delta-H_{CO} for Metal (black) and alloy (orange) CO_2 electrocatalysts [44]

Use of alloys can also help to address many of the challenges that persist in metals . One such problem is high selectivity toward CO while another is the production of HCOOH being confined to expensive noble metal catalysts that are typically associated with low current densities. Additionally, metals are plagued with poor selectivity and tunability for the formation of CxHy products. As discussed, overcoming these limitations requires consideration of both the electronic and geometric structures of catalytic surfaces. Alloys made up of mixed metals offer the opportunity to modulate the catalyst surface structure and chemical environment to affect the relative binding of different reaction intermediates.

It is our contention that alloys can provide a handle to tune catalyst selectivity and activity that has not been extensively explored in the study of CO_2 electrocatalysis. The

first study on the topic is a 1991 report by Watanabe *et. al*.,[45], who surveyed a series of bimetallic alloys of Cu with various metals (Pb, Zn, Cd, and Ag) through electroplating techniques. It was demonstrated that catalyst behavior seems to deviate from the scaling relation such that the a linear superposition of activities for the constituent metals was not observed. The ability for alloys to deviate from the scaling relation can be attributed to: 1) the electronic effect, which alters the binding of intermediates by changing the surface composition, and 2) the geometric effect, which alters the local atomic arrangement at the active sites [44]. The various types and orientations of the alloys or mixed-metal systems are shown in fig. 5.16.

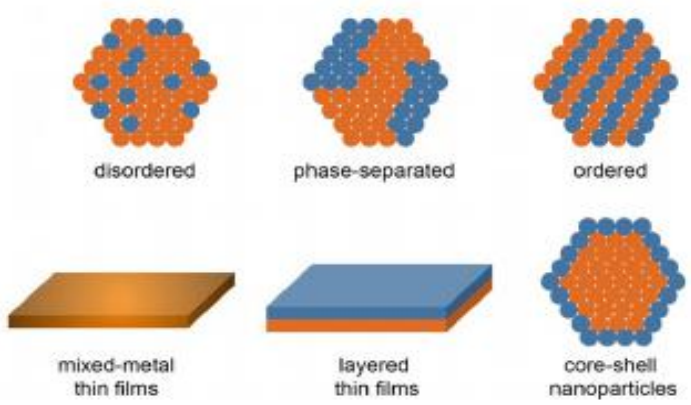

Fig 5.16 Schematic illustration of various metal mixing patterns (top) and geometric structures of alloy electrocatalysts (bottom) [44]

Thus, it can be stated with reasonable certainty that the alloy structures have the potential to achieve high product tunability and selectivity in the field of CO_2 electroreduction catalysis. Results from alloy compositions tested for various CO_2 reduction products (in comparison to their pure metal counterparts) have highlighted the potential of using mixed-metal systems to create unique properties and motivate further exploration into mixed-metal compositions that increase product selectivity.

Examples include study by Li *et. al.* [46], who had developed different methodologies to fabricate alloy catalysts and had reported copper–indium alloys as appealing alternative to Au for CO production. The study had used oxide-derived Cu (OD-Cu) electrodes, where Cu foil was annealed in air prior to electrochemical reduction. Takanabe *et. al.* had also produced copper–indium alloy samples with relatively large surface areas [47]. The Cu-In electrodes in [47] were prepared by electrochemical reduction of OD-Cu in a two-electrode system by using a solution containing 0.05 m $InSO_4$ and 0.4 m citric acid. The electrochemically reduced OD-Cu surface was enriched with indium to a thickness

of about 3 nm to form a $Cu_{11}In_9$ bimetallic alloy. At potential of 0.7 V vs. RHE, this cathode had reduced CO_2 to CO with a faradaic efficiency of about 95 %. DFT calculations suggested that In was preferentially located at the edge sites and that the electronic structure of the Cu sites had remained intact. However, the adsorption properties of neighboring Cu sites apparently are perturbed by the presence of In, which hinder HER but accelerate desorption of CO from Cu to enhance CO evolution. Another study for the Cu-In alloy reported fabrication of electrode by directly reducing the starting material, $CuInO_2$ [48]. $NaInO_2$ was mixed with CuCl in a 1:1 molar ratio and heated at 673 K for 12 h under N_2. The powders were then coated on a carbon cloth and reduced electrochemically in 0.1 M $KHCO_3$ saturated with CO_2 to form different phases containing: $Cu_{11}In_9$, Cu_7In_3 and Cu. Such electrodes, constituting of heterostructure, showed fardaic efficiency of 70% and 20%, for CO and H_2 respectively.
Another attention drawing metal-mix system has been of Cu with Sn which has also been reported to cause higher CO formation. Takanabe *et. al*. had employed a similar method described earlier for preparing Cu-In alloys to electrodeposit Sn into OD-Cu [49]. The concentration of Sn in the alloy was controlled by the total charge passed during the electrodeposition process. The study reported that a catalyst with Sn electrodeposited at 0.3 C/cm^2 could result in faradaic efficiency towards formic acid of more than 90 %. The current density was 1.0 mA/cm^2 while the potential was -0.6 V vs. RHE. On the other hand, the monometallic Cu and Sn surfaces had not selectively reduced CO_2 to CO, and in fact the Cu-Sn bimetallic alloys generated a surface that inhibited adsorbed H*, resulting in a higher fardaic efficiency towards CO.

Now a discussion on some previous studies reporting the use of Cu-Au combination based alloy will be made since it was this combination of catalysts that was used for our APD study. The Cu-Au combination has previously been studied as a means of integrating the strong CO_2 reduction activity observed for Au with the unique intermediate binding strength of Cu. Both metals are also characterized by FCC packing structures and therefore easily form solid solutions regardless of stoichiometry. Furthermore, CO desorption is more kinetically favorable at an Au surface than at an Cu surface, whereas the presence of adsorbed CO on Cu promotes the desorption of CO on Au. Another study had reportedly found that Cu-Au alloys suppress HER and enhance CO evolution. Stoichiometric amounts of each metal (i.e., $Au_{50}Cu_{50}$) performed best for CO production [46]. Yang *et. al.* [50] had carried out a detailed survey of Au-Cu bimetallic nanoparticles (NPs) in which they fabricated monolayers of the NPs on glassy carbon substrates. The reduction selectivity for CO_2 was ascertained as a function of

composition. By increasing the amount of Au relative to Cu, the partial current density towards CO evolution was enhanced until the ratio of Au to Cu reached 3:1. The selectivity of hydrocarbon formation by Cu was compromised by the presence of Au. An XPS analysis of the surface valence band spectra for these co-deposited NP monolayers showed that the d band and the centre-of-gravity position was gradually reduced in energy as the metal content shifted from pure Cu to pure Au. The shift demonstrated the tendency that binding with adsorbates is weakened by the occupancy of anti-bonding states. The intermediate stabilization and through it the chemical product profiles, can be varied by changing the composition of Cu-Au bimetallic structures. An interesting observation in this paper was that even though the band structures of pure Au metal and $CuAu_3$ are almost identical, but their product selectivities still varied significantly, indicating that selectivity is linked to the geometric arrangements of metal atoms and that electronic structure should not be considered exclusively.

5.7 CO_2 reduction on In-Sn alloy substrate with arc plasma deposited Cu, Au and co-deposited Cu-Au

Since an extensive discussion has been made on the significance of alloys, it would be pertinent to begin with the rationale behind using this particular alloy structure i.e. of In and Sn. As can be seen in figure 5.15, both metals produce formic acid however their mixed metal system has not been extensively studied. It is certainly possible (as suggested before) that the mixing of systems could enhance the fardaic yields of formic acid as a product of CO_2 reduction. The generation of formic acid has the advantage of a higher relative profitability index compared to all other major products obtained from CO_2 reduction. The profitability index is a term defined by the ratio of economic value to the required number of electrical energy per mole of products [51]. It is extensively used in agricultural, chemical and textile industries which in turn contributes to its high market value and wide use [52-53]. The formic acid market has maintained linear growth over the past few years, and the global production of formic acid is expected to reach 760 000 ton in 2019 [54].

This is the also reason that value analyses conducted by certain industrial bodies have also determined that the reduction of CO_2 to formic acid is most likely to be profitable compared to its competitors that produce methanol, CO, and long-chain hydrocarbons [55]. Additionally formic acid is gaining emergence an excellent source of fuel for a fuel cell [56]. Formic acid is a useful energy-storage medium, storing 4.35 wt % hydrogen. Thermodynamically, formate and hydrogen are oxidized at similar potentials indicating that formate itself is a viable energy source [57]. The 2 electron chemical reduction also bypasses the extensive energy input required to overcome kinetic barriers of activating multi-electron transfer.

As discussed before, metals which do not form a strong M-C bond with CO_2, favor formate production but are usually prone to issues such as lower current densities that cause lower formation rates. The standard potential for the reduction of CO_2 to formic acid ($CO_2 + 2H^+ + 2e^- \rightarrow HCOOH$) is - 0.62 V versus the standard hydrogen electrode (SHE). But usually an overpotential of up to 1 V is required to drive the reaction at reasonable rates. Since some studies mentioned in section 5.3 and 5.4 report bringing down the overpotentials due to nanoparticle deposition, we prepared samples deposited with nanoparticles (NP) of Cu, Au and co-deposited Cu-Au, on In-Sn electrode so that a comparative analysis could be reported.

In this regard, we carried the same hypothesis as represented in figures 5.6 and 5.7, that the deposition of copper and gold nanoparticles, in principle, would yield a composite reaction mechanism in which the CO_2 reductions would take place on multiple sites. The reduction of CO_2 using Au [39] can primarily only generate CO and, since CO is known to be an intermediate specie [40] for carbon-intensive products, it could act as a feedstock for electrocatalysis of CO_2 at Cu NPs.

As discussed in section 5.5, our study of using bimettalic deposition on FTO substrate had shown improved faradaic yields of formic acid. Using a more stable metal alloy based substrate in this part of our study was our attempt to compare the results of using different electrode structures. Furthermore, this study could clarify the exact role of each constituent metal NP since it cannot be certain that whether the composite mechanism was indeed taking place because of co-deposition.

The In-Sn alloy sheet was procured from the Sigma Aldrich vendor after which the samples were sent to Advance Riko Inc for deposition of nanoparticles (NP). The In:Sn ratio was determined to be 10:1, after XPS analysis. The Cu and Au nanoparticles were deposited on In-Sn substrate by arc discharge of metallic Cu and metallic Au cathodes, respectively. All the depositions were carried out under vacuum (at 10^{-3} Pa) at room temperature. The number of arc discharge pulses (N) was 150 shots, the capacitance of the condenser (C) was 1080 mF, and the voltage for arc discharge (V) was 134 V for Cu and 142 V for Au, with the size of nanoparticles determined by the company to be 30 nm and 2 nm, respectively. The deposition conditions remained the same for Cu and Au during co-deposition and individual deposition.

Ag/AgCl reference electrode was employed while platinum was used as the counter electrode. 0.1 M $KHCO_3$ with a pH of 8.60 was used in the cathode and anode electrolyte. The electrolyte was purged with CO_2 gas for 25 min prior to experiment. The value of pH dropped to 6.90 in the cathode half-cell after the CO_2 purging. Electrochemical experiments were performed using Solartron 1280C potentiostat while a stir bar was used within the electrochemical cell. Electrodes were prepared by affixing a copper wire to the substrate. The X-ray photoelectron spectroscopy (XPS) was conducted by Mg X-ray source in ULVAC-PHI 1600C to analyze the atomic concentration and impact of the electrochemical experiments on the working electrode structure.

5.7.1 In-Sn control sample

The control sample of In-Sn was tested first and reflected decent faradaic efficiency towards CO_2 reduction as can be seen in figure 5.17. During the CO_2RR experiments, the control electrode produced formic acid and CO.The faradaic efficiency towards formic acid from the starting cathodic potential of -1.5V vs SHE was fairly decent at about 45 %. The current density at about 5.2 mA/cm^2 resulted in a production rate of formic acid of around 50 µmol-cm^{-2} hr^{-1}. With the cathodic potential becoming more negative, the FE increased to 48 % and at -1.8 V vs SHE to 57.1 %, which was the highest FE registered for formic acid on this electrode.

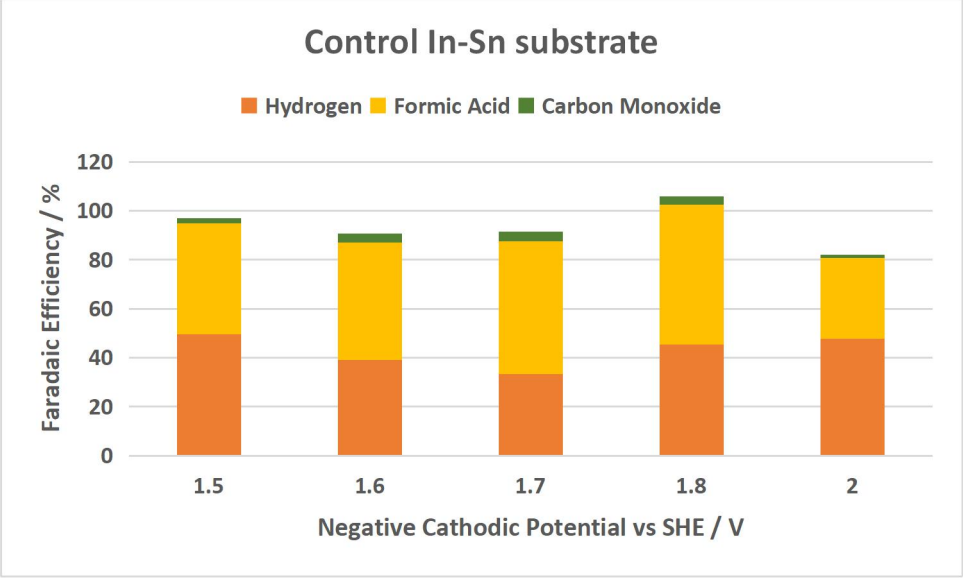

Fig. 5.17 Faradaic efficiency against negative cathodic potential for In-Sn control sample

In terms of the stability of the samples, figure 5.18 can clearly show that the metal alloy had not witnessed any deterioration (in contrast to the observation with FTO). The current density had remained constant despite repeated use at the same potential. After CO_2RR, the control samples showed production of formic acid and CO as a result of the CO_2 reduction.The faradaic efficiency towards formic acid nominally increased with increasing negative potential but the CO formation remained small. With shift towards the negative potential from -1.5 V to -1.7 V vs SHE, the current density increased and so did the formation rates for formic acid however between -1.8 V and -2 V, the formation of formic acid took a down turn showing that hydrogen evolution had increased. The figures showing the formation rates for formic acid and hydrogen will be shown in in section 5.7.5.

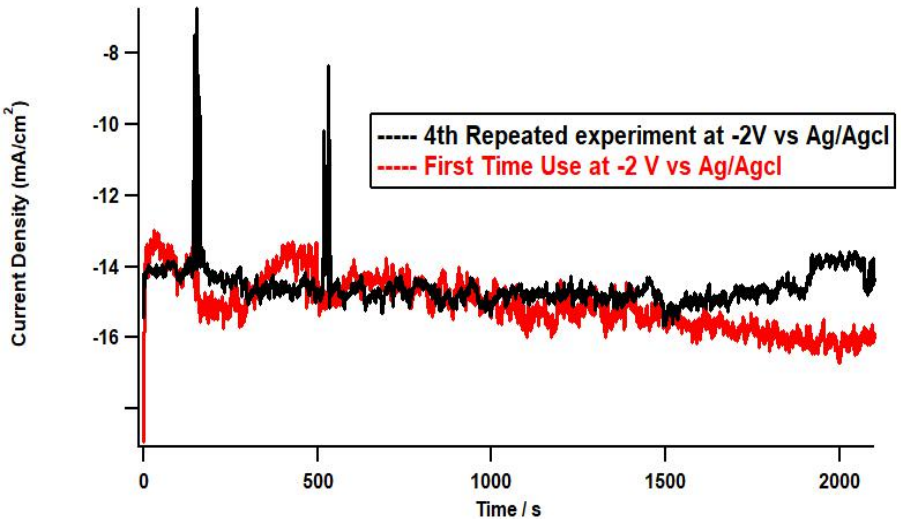

Fig 5.18 No relative current deterioration of the In-Sn sample showed that it was reasonably stable, unlike the FTO substrate.

The XPS analysis in table 5.2 was conducted for the samples to see if there was any major difference between used and unused control samples. The 'used' sample is defined as an electrode on which multiple experiments have taken place and a total of at least 100 C have passed. Potassium was observed and the source of which was the 0.1 M electrolyte that had been reduced at the electrode during the reduction experiments. XPS analysis had showed that the reduced K could easily be removed by the chemical cleansing of the samples after the experiments.

Table 5.2 Comparative XPS analysis for used and unused In-Sn control electrodes

	Carbon	Oxygen	Indium	Tin
Atomic Conc. for unsused electrode / %	37.45	34.69	25.38	2.48
Atomic Conc. for used electrode / %	47.22	33.46	17.60	1.73

5.7.2 In-Sn sample deposited with Cu only

The sample deposited only with Cu NPs enhanced the faradaic efficiency towards formic acid from the starting cathodic potential of -1.5V vs SHE, but only marginally (compared to the control electrode). The current density at about 7 mA/cm^2 was relatively higher as compared to the control electrode and hence the production rate of formic acid was increased from 50 μmol-cm^{-2} hr^{-1} to about 59.2 μmol-cm^{-2} hr^{-1}. This trend was further enhanced as the FE increased to 61.7 % and than peaking at 71.3% at -1.7 V vs SHE and can be seen in figure 5.19. The formation rate also naturally increased, reaching about 240 μmol-cm^{-2} hr^{-1} -1.7 V vs SHE. After this point, the faradaic efficiency (FE) for formic acid began to decrease while the HER started to proceed faster.

The formation rate for formic acid continued to increase since more negative potential meant that the current density was increasing as well. At a current density of almost 40 mA/cm^2, the formation rate for formic acid increased to a high of 382 μmol-cm^{-2} hr^{-1} however the FE for the same product had decreased to a low of 53.3%. This showed that Cu plays a crucial role in increasing the yield of formic acid and does not change the selectivity of the products since the products as a result of CO_2RR continued to remain CO and HCOOH.

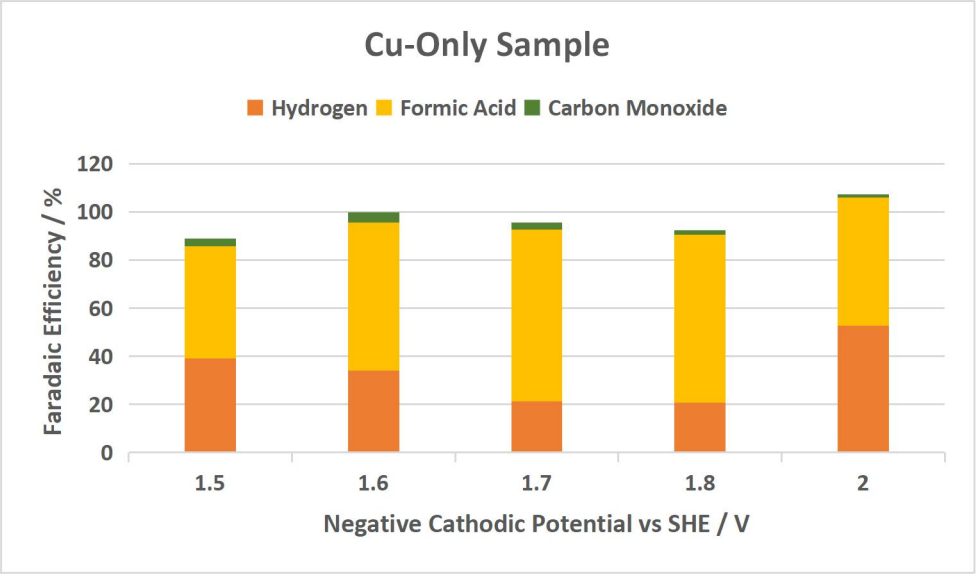

Fig 5.19 Faradaic efficiency against negative cathodic potential for Cu-only APD electrode

The In-Sn alloy as already shown in section 5.7.1. is stable which had confirmed that compared to FTO, In-Sn alloy was a more appropriate alternative substrate. The stability of the Cu nanoparticles was the next important aspect. The XPS analysis of the elemental surface signal is shown in table 5.3 while the comparative XPS peak for Cu (between used and unused electrode) is shown in figure 5.20.

Table 5.3 Comparative XPS analysis for used and unused Cu-based In-Sn electrodes

	Carbon	Oxygen	Copper	Indium	Tin	Potassium
Atomic Conc. for unsused electrode / %	52.54	27.83	13.96	5.00	0.67	N/A
Atomic Conc. for used electrode / %	41.57	32.00	1.19	22.58	1.93	0.74

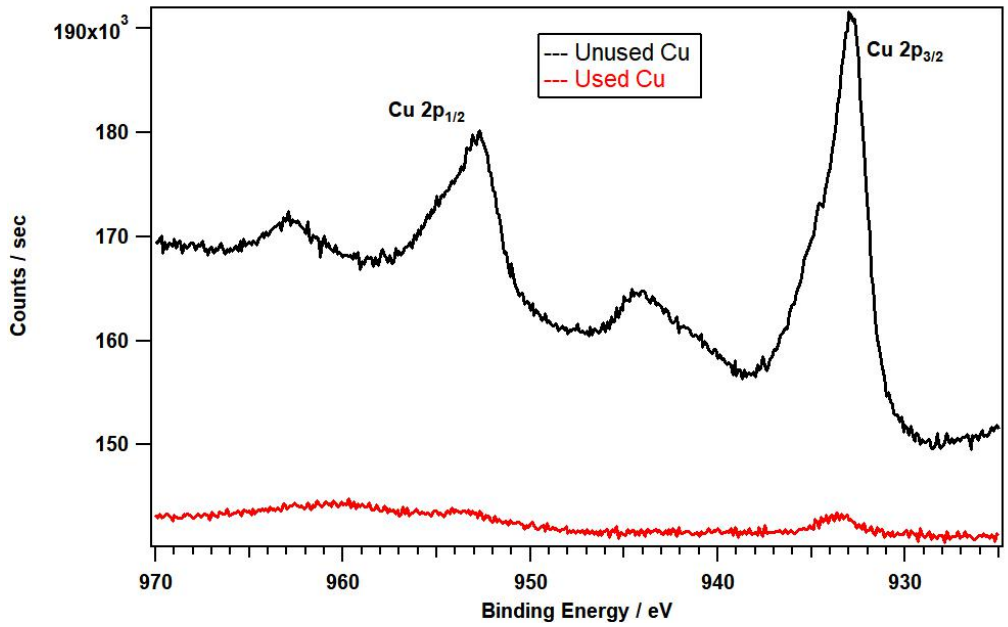

Fig 5.20 XPS analysis comparison for Cu element in used and unused electrode

Assuming typical values for the electron attenuation length of the photoelectrons, the XPS analysis depth (from which 95% of the measured signal originates) ranged between 5 and 10 nm for a flat surface. Since the actual emission angle is ill-defined for rough surfaces (ranging from 0°to 90°) the sampling depth may range from approximately 0 to 10 nm. The loss of Cu content means that that Cu aggregation sites have been lost.
It was important to check the impact of this loss since the experiments had been conducted in a linear fashion starting from the less negative cathodic potential to the more negative potentials. Figure 5.21 shows the impact of this copper loss on the faradaic efficiency of the formic acid.

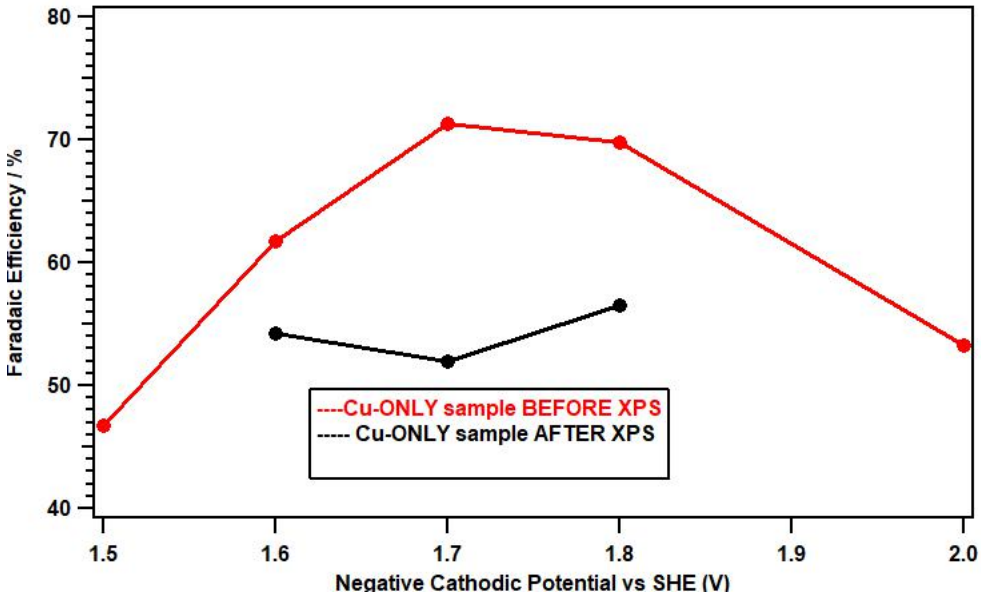

Fig. 5.21 FE comparison for Cu element in used and unused electrode

The results in figure 5.21 showed that the faradaic efficiency had indeed been affected by the loss of the copper nanoparticles. The faradaic efficiency on the same potentials had decreased after the coulomb passage of 160 C. In order to check the stability of a new sample at potentials up to -1.7 V vs SHE, applied cathodic potential range was confined to -1.5 to -1.7 V vs SHE. The total coulomb passage had been standardized at 160 C. The results showed some interesting behavior. The FE continued to remain high at 69.2 % even after a passage of 160 coulombs, which showed that the electrode was not affected by the surface intensity of the Cu nanoparticles but perhaps by the current density of the samples. It had been seen previously with the FTO substrate that the impact of increased current density had a negative impact and so therefore, it can be deduced that decrease in current density does indeed impact the structures of the electrodes however the exact mechanism of such an effect is not yet clear. More discussion in the relative difference will be made in section 5.7.5

5.7.3 In-Sn co-deposited with Cu-Au

The sample co-deposited with Cu and Au, showed a nominally better response than the control sample at -1.7V vs SHE (as can be seen in fig 5.22). The faradaic efficiency (FE) towards formic acid remained low at -1.5 V because of the parasitic activity of the Au NPs. We contend that since the size of Au NPs was only around 2 nm and since the onset potential of Au is lower than that of Cu, at less negative potentials it was the Au that played a dominant role and reduced the protons into hydrogen instead of enhancing CO_2RR. As the cathodic potential became more negative, the CO_2RR activity on the Cu NPs started to become more dominant. This is perhaps the reason why the formic acid generation started to enhance and the FE towards formic acid increased to about 61%, which was higher than the FE for formic acid on In-Sn electrode at similar cathodic potential. The products from CO_2RR, for the co-deposited samples continued to remain formic acid and CO. The faradaic efficiency towards formic acid from the starting cathodic potential of -1.5V vs SHE was only 14% while the current density remained higher than the Cu-deposited sample at less negative potentials. The current density for the co-deposited sample at - 1.5 V vs SHE was about 9 mA/cm^2 with a nominal production rate of formic acid of around 22 $\mu mol\text{-}cm^{-2}\ hr^{-1}$. As the cathodic potential became more negative, the production rate increased and reached 178 $\mu mol\text{-}cm^{-2}\ hr^{-1}$ at -1.7 V vs SHE showing that the formic acid generation has been enhanced due to the activity of Cu NPs.

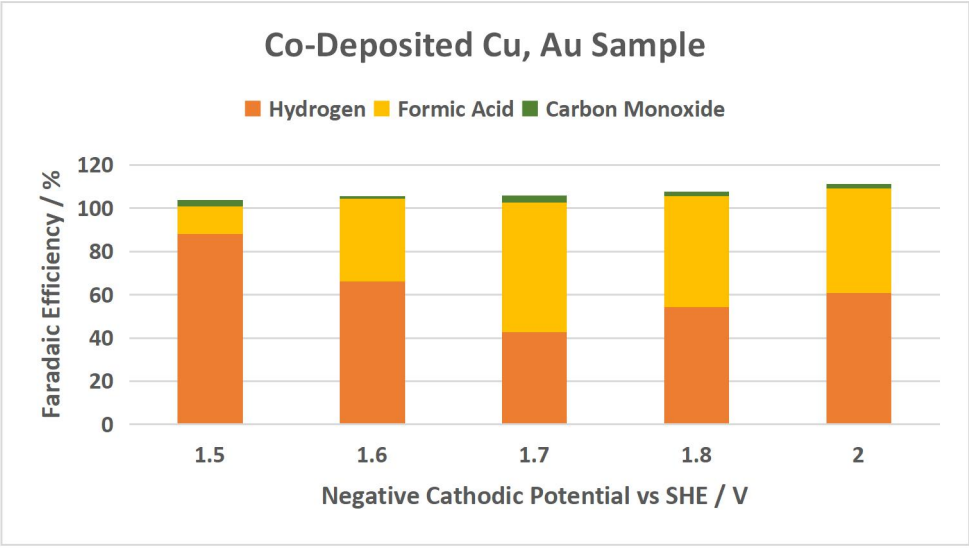

Fig 5.22 Faradaic efficiency against negative cathodic potential for co-deposited APD electrode

The surface content on the copper (figure 5.23) had decreased after repetitive application of cathodic potentials and the response was similar to what was seen in the previous section (samples deposited exclusively with Cu). The decrease in content is attributed to the increase in current density, which has an adverse impact on the deposited NPs. These results however do show that the part of the Cu NPs remain intact on the surface. Since the size of the particles was determined to be 30 nm by the company, it is suggested that only partial erosion of the NPs took place and the implanted portion of the NPs continued to exist on the surface. Since the XPS resolution is confined to no more than 10 nm, the partial erosion of NPs allow higher volume of substrate surface to be measured during the measurement, and hence cause the relative intensity of Cu NPs to decrease in relation to the In and Sn content. The comparative table for elemental surface intensity is shown in table 5.4.

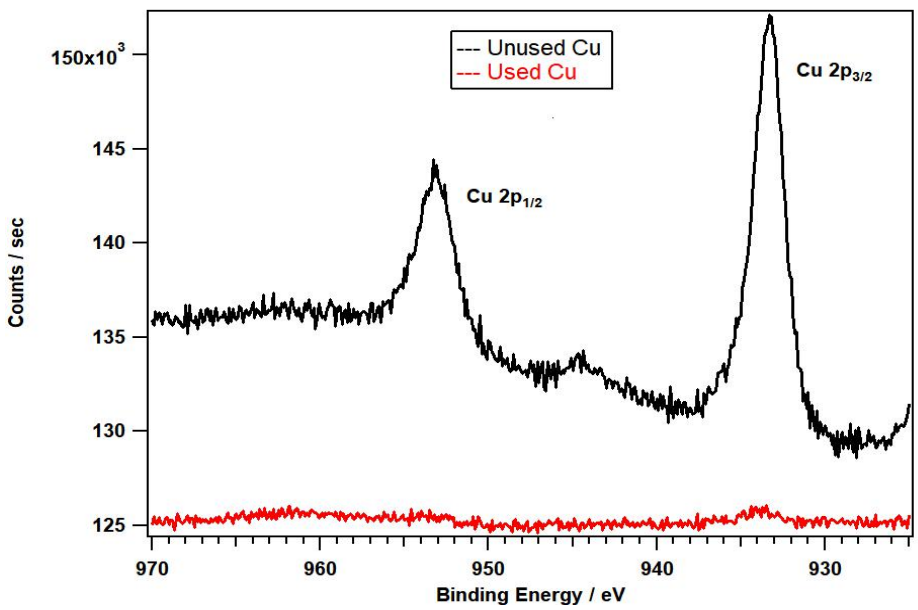

Fig 5.23 XPS analysis comparison for Cu element in used and unused electrode

The surface intensity of the Au NPs suffered from a similar decrease however since the size of the Au NP was determined to be 2 nm, the erosion was more stark in comparison to copper since the Au NPs were smaller in size and hence the implanted portion was also smaller. The role of Au NPs would be discussed further in the section 5.7.5. The relative surface intensities for Au in the pristine and used co-deposited sample is shown in figure 5.24 while the comparative elemental intensities can be seen in table 5.4.

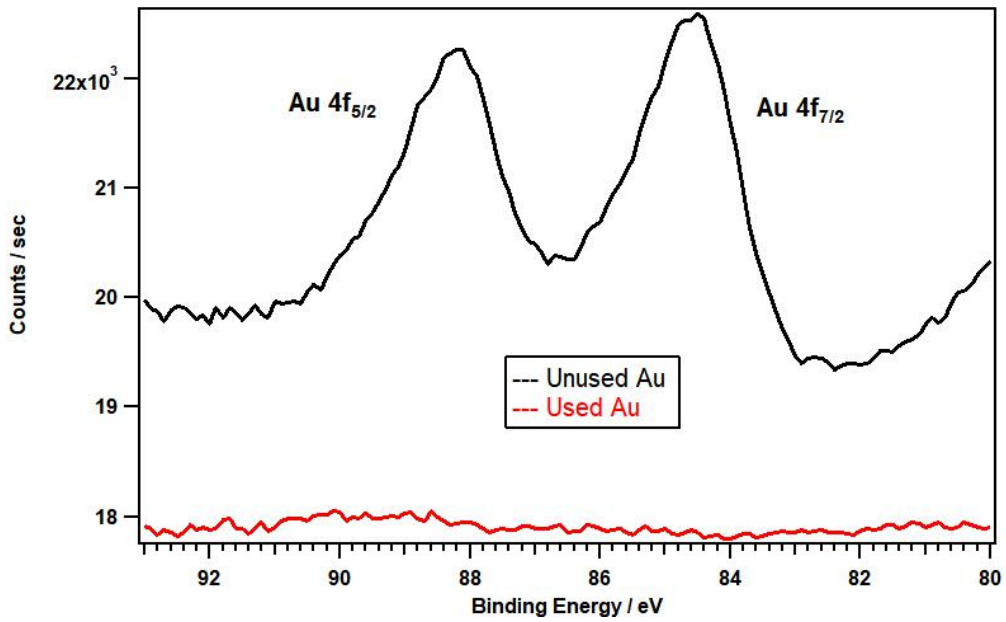

Fig. 5.24 XPS analysis comparison for Au element in used and unused electrode

Table 5.4 Comparative XPS analysis for used and unused co-deposited electrodes

	Carbon	Oxygen	Copper	Gold	Indium	Tin	Potassium
Atomic Conc. for unsused electrode / %	52.07	26.73	0.59	0.12	17.09	3.40	N/A
Atomic Conc. for used electrode / %	62.03	27.30	0.19	0.08	6.16	0.54	3.71

5.7.4 In-Sn deposited with Au only

Au-deposited In-Sn performed the poorest among all the comparable electrodes. The CO production did not experience any substantial increase in FE. The FE towards formic acid on the Au-deposited electrode was low at the onset but gradually increased with more negative cathodic potential, peaking at about 52.4 % at -1.7 V vs SHE and than falling back to 30.4% at -2 V vs SHE. Compared to the In-Sn control electrode, the FE towards formic acid on Au-only sample remained low for the entire potential range. Hydrogen evolution remained the dominant reaction and thus explains the relative decrease in CO_2RR.

The current density was the highest for Au-deposited samples and this is characteristic of electrodes active towards HER. The current density at the onset of the potential was 8.5 mA/cm^2, highest among the comparative electrode structures and increased with more negative cathodic potential. The current density reached 48 mA/cm^2 at a potential of -2 V vs SHE and majority of the passing charges were consumed by the H_2 production. The FE graph for the experiments is shown in figure 5.25.

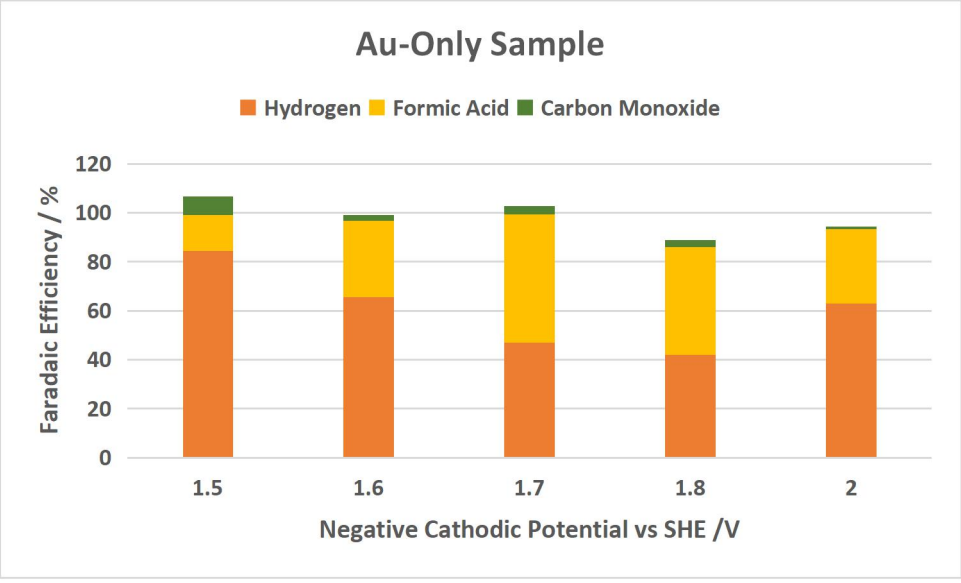

Fig. 5.25 Faradaic efficiency against negative cathodic potential for Cu-only APD electrode

The relative intensities of Au in the pristine and used electrodes is shown in figure 5.26. The figure reflects the erosion of NPs after application of cathodic potential. The Au deposition decreased in line with the results in previous section. As discussed in section 5.4, the size of the NP was around 2 nm which meant that it was not possible to be well implanted onto the surface and the erosion was easier. The relative surface intensity of Au peak after the application of negative cathodic potentials between -1.5 V to - 2 V vs SHE was measured to be only 1.69% in comparison to the surface intensity on the pristine electrode. The relative elemental intensities is shown in table 5.5.

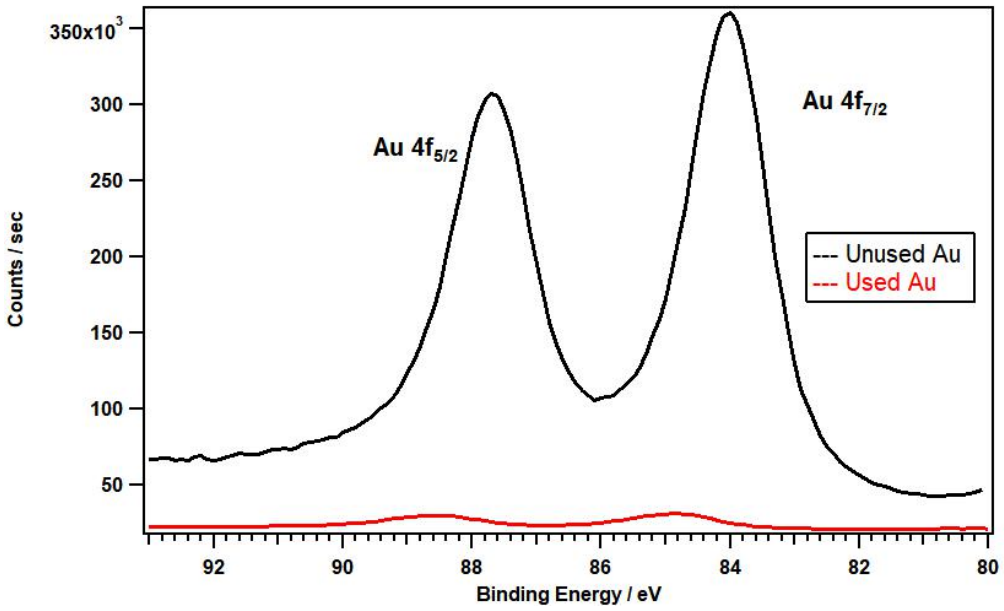

Fig 5.26 XPS analysis comparison for Au element in used and unused electrode

Table 5.5 Comparative XPS analysis for used and unused Au-deposited In-Sn electrodes

	Carbon	Oxygen	Gold	Indium	Tin	Potassium
Atomic Conc. for unsused electrode / %	43.43	9.97	41.40	4.82	0.38	N/A
Atomic Conc. for used electrode / %	45.33	29.06	1.69	18.38	1.51	4.03

5.7.5 Comparative analysis

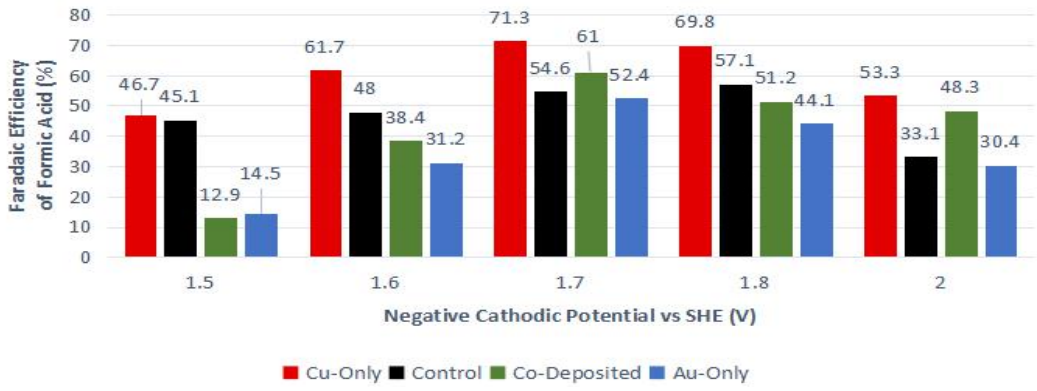

Fig 5.27 Comparative faradaic efficiency towards formic acid for different electrode structures

The comparative analysis of the faradaic efficiency (FE) towards formic acid can be seen in figure 5.27. The standard redox potential for formic acid is -0.62 V vs SHE at a pH of 6.90 but an overpotential of 880 mV (at -1.5 V vs SHE) was required to obtain a production rate of almost 50 μmol-cm^{-2} hr^{-1} with FE of about 45% on the control In-Sn electrode. At -1.4 V vs SHE or an overpotenital of about 780 mV, the faradaic conversion dropped to about 30% with a very nominal production rate of 15.9 μmol-cm^{-2} hr^{-1}. Therefore the potential range had been chosen in order to ensure better comparative difference in results from the various electrode structures.

The CO_2RR products remained unchanged during experiments between all the comparative electrodes since only formic acid and CO were observed along with the HER evolution. Compared to the control electrode, the electrode co-deposited with Cu and Au registered an improvement in FE as well as formation rates during CO_2RR with the maximum reduction of CO_2 occurring at -1.7 V vs SHE. The FE for formic acid was around 61% while CO continued to be produced as a minor product. In addition to the FE enhancement, the current density also registered an increase which indicated that NP deposition was playing a role in the increase of CO_2RR activity. The CO production remained similar to control electrode and this lack of CO improvement reflected that Au presence was not contributing in the reduction of CO_2 to CO and thus explains why there was no apparent composite reaction mechanism or production of higher order carbon products. In order to better understand the individual role of Au and Cu NPs in CO_2RR on In-Sn electrode, Au-deposited In-Sn electrode (Au-only) and Cu-deposited In-Sn

electrode (Cu-only) had been tested for CO_2RR. The results showed that the products remained unchanged with formic acid being the dominant product from CO_2 reduction while CO remained the minor product.

Compared to the In-Sn control electrode, the FE towards formic acid on Au-only sample remained low for the entire potential range. Hydrogen continued to be the dominant product which confirmed that Au-deposited electrode had a higher propensity for HER over CO_2RR. The best results, as seen in figure 5.27, were observed with the In-Sn electrode deposited only with Cu NPs. The best performing FE towards formic acid of 71.3% was observed on -1.7 V vs SHE which meant a significant enhancement from the 54.6% observed at the same potential in the In-Sn control electrode while hydrogen production had been suppressed.

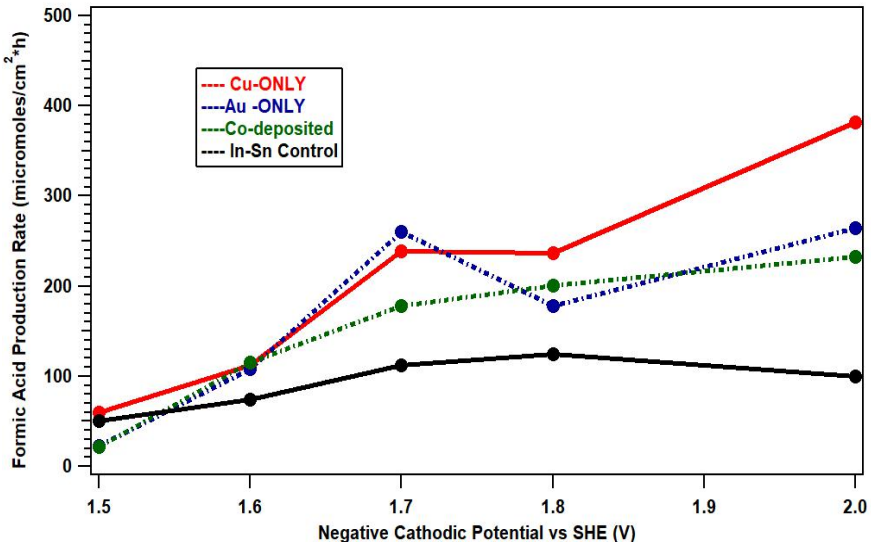

Fig. 5.28 Comparative formation rates for formic acid on different electrodes structures vs potential

The formation rates is an important consideration during CO_2RR and the formation rates of formic acid can be seen in figure 5.28. The formation rate of formic acid on the control electrode remained lowest among all the electrode structures reflecting that NP deposition had a significant impact on the CO_2RR activity. The co-deposited saple figured lower than the electrodes with single-metal NP deposition. This showed that a competing reaction was taking place between the Cu and Au NPs at the various applied cathodic potentials. The production trend of formic acid on Cu-deposited electrode (Cu-only), was the best and about 240 μmol-cm^{-2} hr^{-1} at -1.7 V vs SHE while the formic

acid production rate on Au-deposited electrode (Au-only), at the same potential, was 261 μmol-cm^{-2} hr^{-1}. The relative trend for formic acid on Cu-only continued to improve with increasing the applied negative potentials, reflecting that Cu NPs was contributing towards CO_2 reduction while on the control electrode, the trend for CO_2RR started to decrease at more negative potentials. This obviously showed that Cu implantation is very important for enhancing the activity of the substrate. The In-Sn alloy with Cu-only NPs deposition demonstrated formic acid formation rate of 382 μmol-cm^{-2} hr^{-1} at -2 V vs SHE while for the Au-only sample, the formic acid formation rate at the same potential slowed down to 265 μmol-cm^{-2} hr^{-1} because of the increase in HER.

The relative trend of product selectivity between the different electrodes is best represented in figure 5.29 which shows the partial current density towards formic acid, hydrogen and CO for all the different electrodes at -1.7V vs SHE.

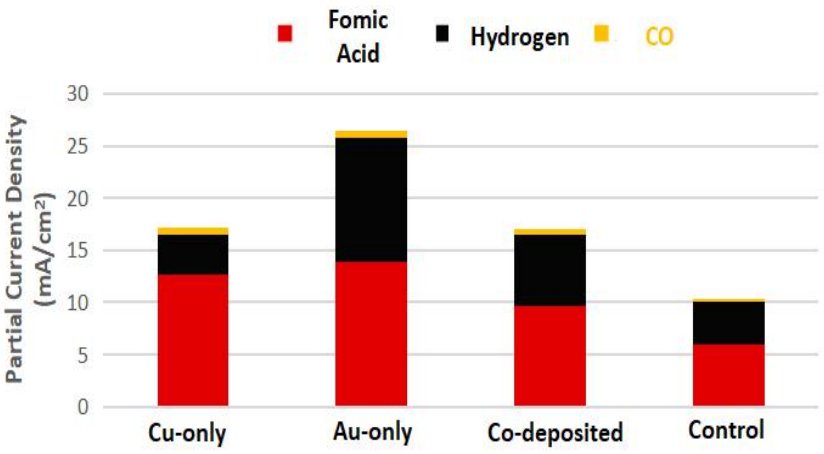

Fig. 5.29 Comparative partial current density of CO_2RR products for different electrodes at -1.7 V vs SHE

It can be seen that the current density for In-Sn control electrode was the lowest among the comparative electrodes. The co-deposition of Cu and Au on In-Sn (Co-deposited) increased the current density significantly as the partial current density towards formic acid (J_{HCOOH}) increased from 5.9 mA/cm^2 to 9.7 mA/cm^2 while partial current density towards HER (J_H) also registered an increase from 4.1 mA/cm^2 to 6.8 mA/cm^2. This meant that both type of reactions, CO_2RR and HER were enhanced with the hybrid deposition. Compared to the control electrode, for the Au-only electrode, the J_{HCOOH}

increased to 13.9 mA/cm^2 and J_H to 11.8 mA/cm^2 while the J_{HCOOH} on Cu-only electrodes increased to 12.7 mA/cm^2 but the J_H decreased to 3.8 mA/cm^2. This clearly reflects that Cu presence was enhancing CO_2RR and suppressing HER and explains the significantly improved results for FE as well as formation rates on Cu-only electrode. Thus the improvement in CO_2RR by Co-deposited electrode can be attributed to the presence of Cu NPs. The exclusive presence of Cu nanoparticles enhanced CO_2RR and suppressed HER at the same time, leading to the significant improvement in both FE and the formation rates for formic acid. Thus, we can deduce that the coexistence of Cu and Au nanoparticles on the Co-deposited electrode lead to a competing reaction between CO_2RR on Cu and HER on Au. This resulted in a mixed performance for Co-deposited electrode since increased Au activity at less negative potentials caused a preferential shift towards hydrogen generation while enhanced Cu activity at more negative potentials helped to improve the CO_2RR in comparison to the control electrode at those potentials.

The increase of total current density observed in Au-deposited samples was a result of HER on Au NPs. It has been previously reported that Au NPs of less than 5 nm size tend to favor hydrogen evolution over CO evolution during CO_2RR and the response is characterized by higher current density [58]. The tendency for increased HER on Au NPs has been suggested via water reduction pathway where water reduces to H^+ and OH^- ions and than subsequently H^+ is reduced to hydrogen gas [59].
The potential dependency in the results is characteristic of CO_2RR [60-62] since favorable reaction energetics and sufficient surface coverage of intermediate species is dependent on the applied potential relative to the standard redox potentials.

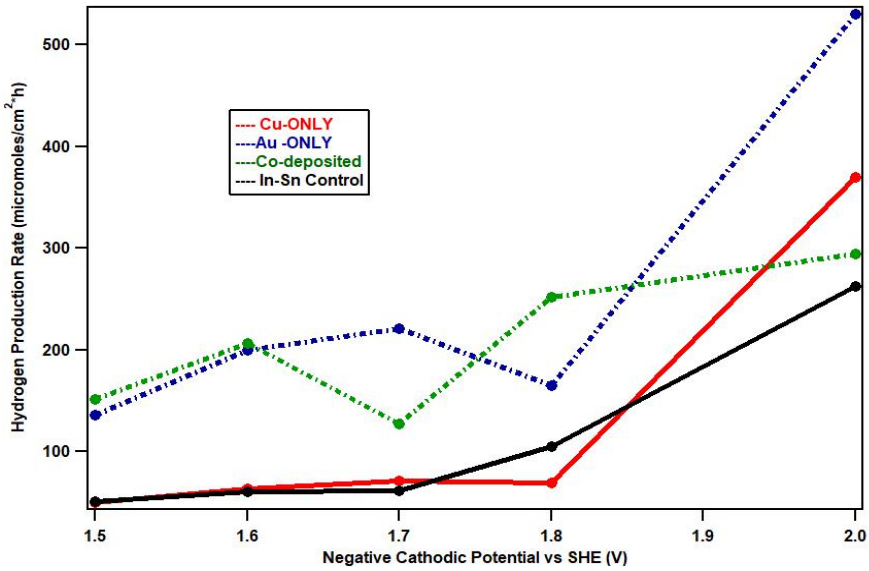

Fig. 5.30 Comparative formation rates for hydrogen on different electrodes structures vs potential

The hydrogen generation trend can be seen from fig 5.30 where it is apparent that the HER on Cu-only electrode was similar to In-Sn control electrode. The presence of Cu NPs clearly limited the hydrogen production from the onset potential for CO_2RR. This suppressed trend is consistent with the increase of formic acid generation and there was a reverse relationship between H_2 and formic acid generation. The hydrogen production increased substantially at more negative cathodic potentials where the coverage of the H+ ions on the cathode starts to saturate the active sites and hence decrease the reduction of carbondioxide. Au NPs as discussed before, was increasing the HER and this is clearly reflected in the comparative trend in fig 5.30. The hydrogen generation rate on co-deposited electrode initially was in the same range to the Au-only sample which is attributed to the Au presence on the co-deposited electrode. However it is our contention that the Cu presence on the co-deposited electrode played the main role in the relatively smaller increase of hydrogen production between -1.8 V to -2 V vs SHE. Fig 5.28 can help to understand this suppressed increase in hydrogen generation because the Cu presence had been shown to increase the formic acid production even at more negative cathodic potential of -2 V vs SHE. This showed that implanted Cu NPs helps to retain the activity towards CO_2RR despite the competing HER evolution especially at more negative cathodic potentials.

It is important to clarify the mechanism by which Cu presence is able to enhance the CO_2RR activity. Some insights into the mechanism of formic acid production on copper have been shown in theoretical calculations by Nørskov *et al.,* [63-64] where it is suggested that a formate pathway (F-intermediated pathway, eqn (1-3)) [65] on copper surfaces, allows selective formation of formic acid only. The asterisk below represents an active site or a specie bound to the surface site.

$CO_2 + H^+(aq) + e^- + * \rightarrow HCOO*$ (F intermediate) (1)

$HCOO* + H^+(aq) + e^- \rightarrow \quad HCOOH*$ (2)

$HCOOH* \quad \rightarrow HCOOH + *$ (3)

A recent DFT study [66] helps to explain the increase in faradaic efficiency of formic acid due to the deposition of Cu. The study reports that that the solid–liquid interface has significant impact on the catalysis process. It suggests that Cu can influence the reaction pathway in a way that decreases the energy barriers for formic acid production. The factors that impact the formic acid production on Cu were determined to be the oxidation states of H and OH ions and the availability of the water molecules around available surface sites.

This report provides support to the mechanism suggested by Nørskov et al. [63-64] that formic acid production may had followed the F-intermediate pathway. The possible decrease in barrier energies by Cu presence is suggested to be the cause for the increase in formic acid FE while the product type from CO_2RR had remained unchanged.

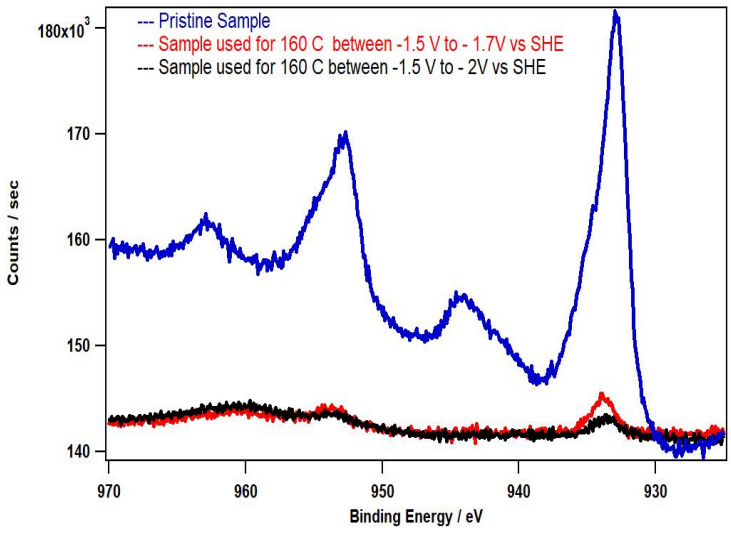

Fig. 5.31 XPS peaks for Cu-only samples; pristine (blue), operated for 160 C between -1.5 to -1.7 V vs SHE (red), for 160 C between -1.5 V to -2V vs SHE (black)

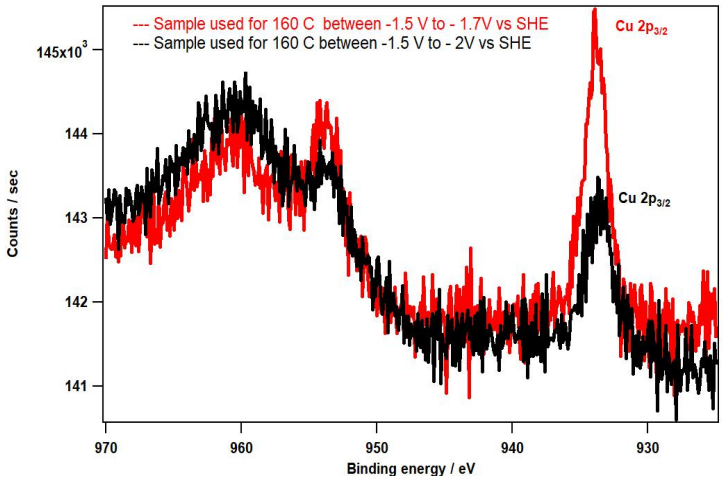

Fig 5.32 Magnified version of figure 4 to compare XPS spectrum for used Cu-only samples; samples operated for 160 C between -1.5 to -1.7 V vs SHE (red), for 160 C between -1.5 V to -2V vs SHE (black)

The XPS analysis for In-Sn electrodes deposited with Cu-only (figure 5.31), showed a decrease in the intensity of Cu NPs after the electrochemical experiments. The XPS analysis depth (from which 95% of the measured signal originates) ranges between 5 and 10 nm for a flat surface. Since the actual emission angle is ill-defined for rough surfaces (ranging from 0°to 90°) the sampling depth may range from approximately 0 to 10 nm. Figure 5.31 shows the Cu 2p spectra for the pristine sample (blue), the sample experimented at a potential range between -1.5 to -2.0 V vs SHE with total coulomb passage of 160 C (black), and the sample experimented at a potential range between -1.5 to -1.7 V vs SHE with a total coulomb passage of 160 C (red). The charges were calculated from the total current generated from the sample at fixed potentials. The decrease in intensity is likely associated with the decrease in sites that accommodate Cu aggregation. Figure 5.32 shows the comparative difference between the two used samples which reflects that the application of more negative potential and hence higher current density did have an impact on the stability of the Cu aggregation sites. During the course of each individual experiment, the fluctuation of current was negligible which reflected that the electrode structure remained stable indicating that impact on NP stability occurred immediately after the conclusion of experiment, during the open circuit position, which has been observed previously in an in-situ study on Cu catalysts [67].

The decrease in surface Cu content, however, does not necessarily reduce the faradaic efficiency. For sample tested between potential range of -1.5 to -1.7 V vs SHE for 160 C,

continued to exhibit formic acid FE of 69.2% at -1.7 V vs SHE. On the other hand, the Cu-deposited sample tested initially between a range of -1.5 to -2 V vs SHE for 160 C, when re-tested at the potential of -1.7 V vs SHE, showed formic acid FE of less than 60 %, compared to 71.3% registered previously at -1.7 V vs SHE, which meant that the current density (40 mA/cm^2) at -2 V vs SHE not only decreased the Cu content but also affected the local electrode structure. It has been reported by Gupta *et. al.* [65] that Cu based nano-catalysts continue to show high FE towards formic acid despite a decrease in surface Cu nanoparticles. The paper had suggested that surface area decrease of Cu NPs is not the primary factor in activity for formic acid production during CO_2RR and that other factors play a crucial role in reduction of CO_2. This is also confirmed in other studies [68-70] that the product selectivity, faradaic efficiency and current density during CO_2RR is determined by many other factors including morphology, phase, structural defects, local and surface pH, electrolyte molarity, chemical coupling between constituent metals etc.

It is our contention that APD technique allows the NPs to be anchored into the surface which plays a critical role in the orientation of those NPs. Partial submersion of Cu NPs into the surface is suggested to allow an increase in the number of low coordination sites and low index facets (edges, defects, and corners) of Cu surface. The increase of such sites has been reported to impact and aid the CO_2RR by either allowing more electron-intensive products [71-72] or as suggested earlier, decrease barrier kinetics for 2-electron products thereby increasing faradaic yields. The XPS results suggests that portions of NPs remained intact on the surface, assisting in CO_2RR. A comparative analysis of the In-Sn-based study with some of the latest reported studies on formic acid production is presented in table 5.6.

Table 5.6 Comparison of this study with some of the recent papers reporting production of formic acid.

Electrode	Faradaic Efficiency / %	Potential / V	Current Density (mA/cm^2)	Ref.
Cu-deposited In-Sn	71.3	-1.28 vs RHE	17.1	This work
Sulfur-doped Indium	85	-0.98 vs RHE	58	[73]
$Ag_{76}Sn_{24}$	80	-0.8V vs RHE	19.7	[74]
Heat treated Sn dendrite	55.6	-1.06 vs RHE	11.1	[75]
SnO_2 nanowires	80	-0.8 vs RHE	6.0	[76]
Increased Surface Area Bi	92	-1.5 vs SCE	3.75	[77]
Cu-Sn electrode	91.7	-1.4V vs SCE	1.0	[78]

5.6 Summary

1. Arc Plasma Deposition technique was employed to implant Cu and Au NPs on FTO and In-Sn substrates, respectively.
2. FTO was used as the substrate material in the first part of the study.and the electrochemical CO_2RR experiments showed formic acid generation with FE as high as 60% while CO was observed as a secondary product.
3. XPS spectroscopy confirmed the atomic concentration and presence of the NPs deposition.
4. Pristine FTO was used as control electrodes and produced only CO as a result of CO_2RR.
5. Surface degradation of FTO substrate was a parasitic result from the application of negative cathodic potential in bicarbonate electrolyte however the surface reached an equilibrium state after which no visible disintegration was observed.

6. The control FTO electrode started to produce formic acid in the electrode-stabilization phase however the FE towards formic acid in stabilized APD electrodes continued in relatively much higher yields.
7. In the second phase of study, different electrode structures employing In-Sn alloy as substrate were used. Exclusive deposition of Cu and Au along with co-deposited Cu-Au were compared for CO_2RR.
8. The results reflect that arc plasma deposited Cu NPs were by far the most effective to enhance the faradaic efficiency and formation rate for formic acid.
9. The highest faradaic efficiency of 71.3% towards formic acid with formation rate of 240 μmol-cm^{-2} hr^{-1} with Cu-deposited In-Sn, at a potential of -1.7 V vs SHE, is reported.
10. The products obtained as a result of CO_2RR remained unchanged between the various electrode structures and formic acid was the dominant product followed by CO and parasitic hydrogen.
11. The deposition of Cu NPs by the use of APD technique can be an innovative way to enhance faradaic efficiency and production rates from the electrochemical reduction of CO_2.

Author's note: Work in this chapter have been published in the Advances in Nanoscience and Nanotechnology

5.7 References

1. Chaudhuri, R. and Paria, S., *Chem Rev* 2012 **112**, 2373-2433
2. Peng, Y, Yang C., *Appl Surf Sci* 2012 **263**, 38-44
3. Wang, L. Gao, W, Liu Z., *Acs Catal* 2017 **8**, 35-42
4. Wang, L. Zeng Z., Ma C.,. *Nano Lett* 2017 **17**, 3391-3395
5. Zhao, J., Zhang, D. & Zhao, J. *J Solid State Chem* 2011 **184**, 2339-2344
   Da Silva A. G. M., Rodrigues, T. S., Haigh, S. J. & Camargo, P. H. C. *Chem Commun (Camb)* 2017 **53**, 7135-7148,
6. Clark, E. L., Hahn, C., Jaramillo, T. F. & Bell, A. T. *J Am Chem Soc* 2017, **139**, 15848-15857
8. Jones, J.-P., Prakash, G. K. S. & Olah, G. A. *Isr J Chem* 2014, **54**, 1451-1466,
9. Lim, H. K. & Kim, H. *Molecules,* 2017, **22**, 536-542.
10. Singh, A. K. & Xu, Q. *Chemcatchem,* 2013, **5**, 652-676
11. Davis W. D. and Miller H. C., J. *AppI. Phys.,* 1969 **40***,* 2212-2217.
12. Daalder J. E., J. *Phys. D.,* 1983 **16,** 17-24.
13. Mularie W. M. , *U.S. Patent 4,430,184,* February 1984.
14. I. I. Aksenov and A. A. Andreev, *Soy. Tech. Phys. Lett.,* 1978, **3**, 525.
15. Harris L. P. in J. M. Lafferty (ed.), *Arc Cathode Phenomena,* Wiley-Interscience, New York, 1980, 127 -128.
16. Lunev V. M.,Padalka V. G., Khoroshikh V. M. , *Soy. Phys. Tech. Phys., 1978,* **22***,* 858-862.
17. J. E. Daalder, *Physico* 1981, **104**, 91-.94
18. Randhawa H., Johnson P.C., *Surface and Coatings Technology, 1978,* **31***,* 303 - 318
19. Daalde J. E, Cathode erosion of metal vapor arcs in vacuum, *Ph.D. Thesis,* Technische Hugelschol, Eindhoven, Holland, 1978.
20. Reske, R., Mistry, H., Behafarid, F., *J. Am. Chem. Soc*., 2014, **136**, 6978-685.
21. Manthiram K., Beberwyck B., Alivisatos A., *J. Am. Chem. Soc*., 2014, **136**, 13319-13325.
22. Loiudice A., Lobaccaro P., Kamali E., Thao T., Huang B., Ager J., Buonsanti R., *Angewandte Chemie International Edition*, 2016, **55**, 5789-5792
23. Song Y, Peng R., Hensley D., Bonnesen P., Liang L., Wu Z., Meyer, H., Chi M, Ma C., Sumpter B., *ChemistrySelect*, 2016, 1, 6055-6061
24. Hori, Y., Murata, A., Kikuchi, K., Suzuki, S. *J. Chem. Soc., Chem Commun.* 1987, **10**, 728-729.
25. Kauffman, D. R., Alfonso, D., Matranga, C., Qian, H. F., Jin, R., *J. Am. Chem. Soc.* 2012, 134, 10237.
26. Mistry H., Reske R., Zeng Z., Zhao Z., Greeley J., Strasser P., Cuenya B., *J. Am. Chem. Soc.*, 2014, **136**, 16473-16476
27. Zhu W., Michalsky R, Metin Ö. , Lv H., Guo S., Wright C., Sun X., Peterson A., Sun S., *J. Am. Chem. Soc*., 2013, **35**, 16833-16836.
28. Zhu W., Zhang Y, Zhang Z, Lv H., Li Q., Michalsky R., Peterson A, Sun S., *J. Am. Chem. Soc*., 2014, **136**, 16132-16135.
29. Y. Chen, C. W. Li, and M. W. Kanan, *J. Am. Chem. Soc.,*2012*,* **134**, 19969-19972
30. Lee H., Yang K., Yoon S., Ahn H,, Lee Y., Chang H., Jeong D., Lee Y., Kim M., Nam K., *ACS nano,* 2015*,* **9**, 8384-8393
31. Homura H., Tomita O., Higashi M.,Abe R., *Sustainable Energy Fuels*, 2017, **1**, 699-709
32. Zhu W., Michalsky r., Metin O., Lv H, Guo S., Wright C., Sun X, Peterson A., Sun S, *J. Am. Chem. Soc.* 2013, **135**, 16833−16836
33. Schouten K., Kwon Y, van der Ham C., Qin Z., Koper M., *Chem. Sci.*, 2011, **2**, 1902-1906
34. Raciti D., Mao M., Park J.,,Wang C., *J. Electrochem. Soc*. 2018, **165**, F799-F804

35. Feaster J., Shi C., Cave E., Hatsukade T., Abram D., Kuhl K., Hahn C., Nørskov Jaramillo J., *ACS Catal*., 2017, **7**, 4822–4827
36. Banyamin Z., Kelly P., West G., Boardman J., *Coatings*, 2014, **4**, 732-746
37. Mu S., Wu J., Shi Q., Zhang F., *ACS Appl. Energy Mater*. 2018, **1**, 1680-1687
38. Choi, S.Y., Jeong, S.K., Kim, H. J., *ACS Sustainable Chem. Eng.*, 2016, **4**, 1311-1317.
39. Bai, X., Chen, W., Zhao,C., Li, S., *Angew. Chem. Int. Ed.*, 2017, **56**, 12219-12225
40. Detweiler, Z., White, J., Bernasek, S., Bocarsly A., *Langmuir*, 2014, **30**, 7593-7601.
41. Zhang, Z., Ahmad, F., Zhao, W., Yan, *Nano Lett*., 2019, **19**, 4029-4034
42. K. P. Kuhl, T. Hatsukade, E. R. Cave, D. N. Abram, J. Kibsgaard, T. F. Jaramillo, *J. Am. Chem. Soc.* 2014, **136**, 14107–14113.
43. Hori Y., *Mod. Aspects Electrochem*. 2008, **42**, 89–189.
44. He, J., Johnson, N.J., Huang, A., Berlinguette, C., *ChemSusChem*, 2018, **11**, 48-58
45. M. Watanabe, M. Shibata, A. Kato, M. Azuma, *J. Electrochem. Soc.,* 1991, **138**, 3382–3389.
46. Li C. W., Kanan M. W., *J. Am. Chem. Soc*. 2012, **134**, 7231–7234.
47. Rasul S., Anjum D., Jedidi A., Minenkov Y., Cavallo L., Takanabe K., *Angew. Chem. Int. Ed.* 2015, **54**, 2146–2150; *Angew. Chem*. 2015, **127**, 2174–2178.
48. Jedidi A., Rasul S., Masih D., Cavallo L., Takanabe K., *J. Mater. Chem. A* 2015, **3**, 19085–19092.
49. Sarfraz S., Garcia-Esparza A., Jedidi A., Cavallo L., Takanabe K., *ACS Catal.* 2016, **6**, 2842–2851.
50. Kim D., Xie C, Becknell N., Yu Y., Karamad M., Chan K., Crumlin E, Nørskov J., Yang P,, *J. Am. Chem. Soc*. 2017, **139**, 8329–8336.
51. Singha, R., Clarka, E.L., Bella, A.T., *PNAS*, 2015, **112**, 6111-6117.
52. Prez-Fortes, M., Schçneberger, J. C., Boulamanti, A., *Int. J. Hydrogen Energy*, 2016, **41**, 16444.
53. Schouten, K. J. P., Calle-Vallejo, F., Koper, M. T. M., *Angew. Chem. Int. Ed*., 2014, **53**, 10858.
54. Huang, Y., Deng, Y., Handoko, A. D., *ChemSusChem*, 2018, **11**, 320.
55. Agarwal, A. S., Zhai, Y., Hill, D., Sridhar, N., *ChemSusChem*, 2011, **4**, 1301.
56. Rice, C., Ha, S., Masel, R. I., Waszczuk, P., *J. Power Sources,* 2002, **111**, 83.
57. Reda, T., Plugge, C. M., Abram, N. J., Hirst, *J., Proc. Natl. Acad. Sci. India Sect. A*, 2008, **105**, 10654.
58. Zhu, W., Michalsky, R., Metin, O., *J. Am. Chem. Soc.,* 2013, **135**, 16833.
59. Qian, K., Brendan, S., Johnston-Peck, A., *J. Am. Chem. Soc.*, 2014, **13628**, 9842
60. Bagger, A., Ju, W., Varela, A., Strasser, P., *ChemPhysChem*, 2017, **18**, 3266.
61. Wua, J., Risalvatoa, F., Kea, F., *J. Electrochem. Soc.*, 2012, **159**, 353.
62. Kuhl, K., Cave, E., Abramc, D., Jaramillo, T., Energy Environ. Sci., 2012, **5**, 7050.
63. Peterson, A.,Abild-Pedersen,F., Studt, F., Energy Environ. Sci., 2010, **3**, 1311.
64. Durand, W., Peterson, A., Studt, F., *Surf. Sci*., 2011, **605**, 1354.
65. Gupta, K., Bersani, M., Darr, J., *J. Mater. Chem. A*, 2016, **4**, 13786.
66. Liu, S., Zhao, M., Zhu, Y., *Applied Catalysis A, General*, 2017, **547**, 214.
67. Mandal, L. Yang, K., Motapothulav, M., *ACS Appl. Mater. Interfaces,* Vol. **10**, 8574.
68. Chang, X., Wang T., Gong J., *Energy Environ. Sci.,* 2016, Vol. **9**, 2177.
69. Karaiskakis, A., Biddinger E., *Energy Technol.*, 2017, Vol.**5**, 901.
70. Kas, R., Kortlever R., Milbrat, A., *Phys. Chem. Chem. Phys.,* 2014, Vol. **16**, 12194.
71. Baturina, O., Lu, Q., Padilla, M., *ACS Catal.*, 2014, Vol. **4**, 3682.
72. Reske, R., Mistry, H., Behafarid, F., *J. Am. Chem. Soc.*, 2014, Vol. **136**, 6978.
73. Ma, W., Xie, S., Zhang, X., 2019, *Nature Communications* Vol. **10**, 892.
74. Luc, W., Collins, C., Wang, S., *J. Am. Chem. Soc.*, 2017, Vol. **139**, 1885.
75. Won, D., Choi, C., Chung, J., *ChemSusChem,* 2015, Vol. **8**, 3092.

76. Kumar, B., Atla, V., Brian, *J., Angew. Chem. Int. Ed*., 2017, Vol. **129**, 3645.
77. Zhang, H., Ma, Y., Quan, F., Electrochem. Commun., 2014, Vol. **46**, 63.
78. Zhao, C., Wang, J., *Chem. Eng. J*., 2016, Vol. **293,** 161.

CHAPTER 6

Sulfide-based chalcogenide material - Germanium-Sulfide-Indium

Although metal-based electrodes, as shown in previous chapters, can offer decent faradaic efficiency and selectivity, it is also important to focus on the use of new materials that are abundantly available in foreseeable future. This approach could help to ensure elemental sustainability for long-term commercial use of CO_2 reduction. Figure 6.1 shows that chalcogenide materials are one such class of materials that are most abundant in nature. This long-term sustainability of the materials as well as the cost of the electrode fabrication are extremely important factors for the practical realization of systems that can reduce CO_2 to useful end-products for long-term use. This research report will employ the use of glasses as electrode materials. Such glass materials are easier to fabricate on an industrial scale and therefore, apart from the long-term availability of materials can also allow cheaper prices.

Transition metals chalcogenides have started to attract attention due to their electrochemical properties and therefore we decided to use the amorphous glass phase of such sulphide-based materials since they have never previously been used. This approach led a shift of our focus from the metals to the use of germanium-indium-sulfide amorphous glass structures for the electrochemical reduction of CO_2

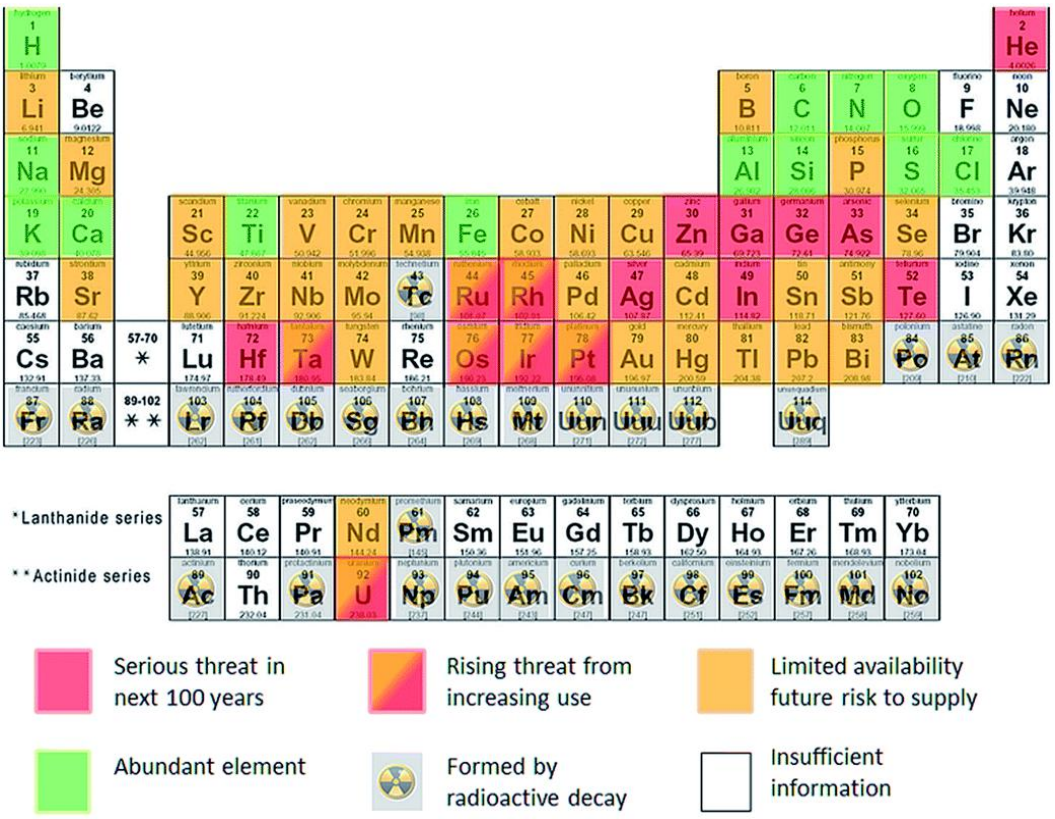

Fig. 6.1 Future outlook for the elemental sustainability and availability of the elements [1]

6.1 Chalcogenides background

Chalcogenide glasses are based on the chalcogen elements O, S, Se, and Te and are formed by the addition of other elements such as Ge, As, Sb, Ga, etc. They are low-phonon-energy materials and are generally transparent from the visible up to the infrared region. These glasses can also be doped with rare earth elements, such as Er, Nd, Pr, etc., and hence numerous applications of active optical devices have been proposed. The chalcogenide glasses can transmit in the IR and thereby have been extensively used for applications in the civil, medical, and military areas. Certain passive applications have also utilized chalcogenide fibers as a light conduit from one location to another point without changing the optical properties (other than those due to scattering, absorption, and reflection) [2]. A diagrametic representation of chalcogenide applications is shown in figure 6.2. Chalcogenide glasses are also optically nonlinear and thus have been used for all-optical switching (AOS) [3]. The sensitivity towards electromagnetic radiation reflected in chalcogenide glass structures have resulted in a variety of photo-induced effects as a result of illumination. Various models [4] have been put forward to explain these effects, which can be used to understand their role in the photoelectrochemical reduction of CO_2.

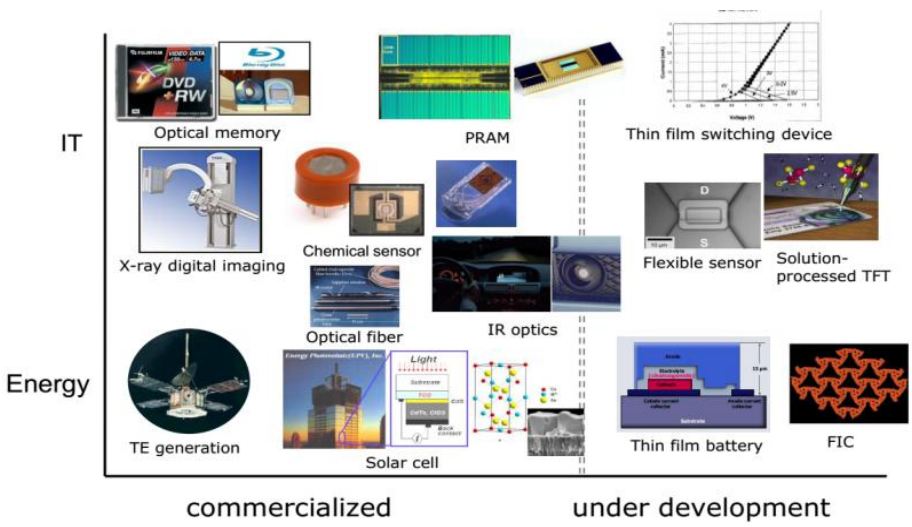

Fig. 6.2 Applications of chalcogenides [4]

6.2 Structure, fabrication and band-gap

Chalcogenide solids can be characterized by strong interactions between the constituent particles and exist in an ordered (crystalline) state or in a disordered (noncrystalline) state. The ordered state of a chalcogenide is limited to only a few structural forms while a disordered material is neither unique nor clearly defined. The chalcogenide glass structures are considered amorphous materials but there is also a short-range order (SRO) that may exist in such structures [5]. In an SRO, the first and second nearest-neighbor coordination shells are well-defined and atoms from the third coordination sphere start to become uncorrelated with those in the first one. Therefore the limit of short- and medium-range order is confined to the first 3–4 inter-atomic distances [6]. The result of short range is the appearance of fluctuations in angles and distances between the bonds. In terms of CO_2 reduction, it was our contention that these limited ordered structures could translate into small areas where electron transfer could be localized and hence act as centers to transfer electrons and possibly aid in the production of carbon intensive end-products. Chalcogenide gasses with such ideal noncrystalline network are prepared by different thermal treatments which lead to such kinds of noncrystalline arrangements of atoms. Melt quenching method is the most common method, shown in figure 6.3. To fabricate such glass composition, the respective weighed quantities of germanium, indium and sulfur were vacuumed in quartz ampoules and heated to the temperature of the melting point of sulfur. The synthesis is carried out under a gradual temperature increase in a rocking furnace. The temperatures of the furnace range between 900 K up to 1600 K. The ampoules are then held for upto 8 hours and then cooled in air.

Typical cooling rates of glass melts.

Cooling rate q ($K\ s^{-1}$)	Method
10^{-5}	Annealing of large telescope mirrors
approx. 2×10^{-4}	Annealing of optical glasses
10^{-3}–10^{-2}	Annealing of ordinary glasses
1–2	Air exposure of chalcogenide melts of 10–20 g in quartz ampoules (wall thickness 2 mm)
8 – 10	In water at 273 K
35	1 g (ampoule wall thickness 0.5 mm) in water
approx. 180	0.015 g in thin-wall ampoule in water
approx. 10^3	Spray-cooling of melts
10^5–10^6	Melt-spinning methods
10^6–10^7	Piston-and-anvil technique
10^6–10^{10}	Splat-cooling methods

Fig. 6.3 Melt quenching method and common cooling rate to fabricate glass structures of different properties and applications [4]

Other methods of fabrication have been the solution method or also known as low temperature wet method, physical vapor deposition by thermal or electron beam. Sputtering or Pulse Laser Deposition has also been reported to produce thin films of such materials. As mentioned before, the structure of such glasses are not described by means of a continuous random network and so materials like As_2S_3, GeS_2 , and $GeSe_2$ can be locally layer-like, while pure S and Se are chain like. However, there is considerable flexibility of the structure as a result of the weak van der Waal's bonding between layers or chains [7], so that changes in the structure can be relatively easily accommodated. Chalcogenide glasses can be characterized as being variously covalent, metallic, and ionic. The magnitude of the band gap is 1–3 eV depending on the composition and the band gap increases in the series Te → Se → S. Electrical conduction in many chalcogenide glasses is governed by holes. Accordingly, these glasses can be regarded as amorphous semiconductors. However, in a glass containing large amounts of Te, the band gap decreases (1 eV), and the metallic character increases. Moreover, in glasses such as Ag–As(Ge)–S, the coordination number of S is demonstrated to be 3–4 [21], and ionic conduction of Ag^+ (metal material) governs the electrical conductivity. So these glasses can be considered as ionic glasses or ion-conducting amorphous semiconductors.

For this study, samples of chalcogenide glasses with the general formula $(1\text{-}x)GeS_{1.5}\text{-}(x)In$ were prepared. Indium concentration was x= 0.01, 0.1, 0.4, 0.5, 0.6, 0.12. As mentioned before, the melt quenching method was used to fabricate such glass composition. The respective weighed quantities of germanium, indium and sulfur were vacuumed in quartz ampoules and heated to the temperature of the melting point of sulfur. The synthesis was carried out under a gradual temperature increase in a rocking furnace up to 1100 K; the ampoules were then held for 8 h and then cooled in air.

Electrodes were prepared by affixing a copper wire to an indium contact on the bulk surface. The exposed portion of the copper wire was also covered with indium using a solder. Indium contact acts as a schotkey contact between the metal and semiconductor for a smooth flow of electrons across the barrier. Bulk amorphous Ge-S-In samles were analyzed for its chemical composition using EDX spectroscopy. Oxygen content was observed within the sample, which may had been introduced during the furnace process, a common disadvantage of melt quenching fabrication process.

6.3 Electrochemistry of chalchogens

Because of their multiple oxidation states, the chalcogens, particularly sulfur, can engage in numerous redox couples participating in acid–base, oxidation–reduction, precipitation, and complexation equilibria [8].

In the anion electrochemical series, sulfur, being the less noble element compared to its heavier congeners, occupies an intermediate position between iodine and selenium [(+)F, Cl, Br, I, S, Se, Te(–)]. Selenium, regarded as a metalloid, is a relatively noble element. Tellurium is rather an amphoteric element: it can enter into solution in the form of both cations and anions [9-10]. The redox band for some of the common chalcogendies is shown in figure 6.4.

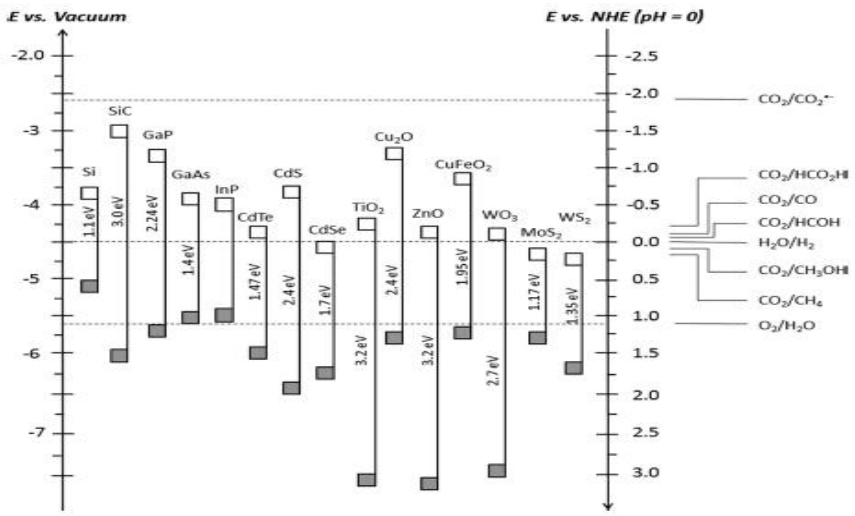

Fig. 6.4 The redox band for some of the common semiconducting chalcogenides [11]

6.4 Chalcogenides for CO_2 reduction

In CO_2 reduction studies, CdS and ZnS have been the most extensively studied chalcogenides because of their earth abundance [12-15]. As mentioned previously, the plethora of photo-induced properties means that such chalcogenides have predominantly been employed as photocatalytic systems for CO_2 reduction. CdS has a bandgap of 2.4 eV, which potentially results in better visible light absorption compared to many other oxide based photocatalysts. The comparative range of bandgaps for different chalcogenide materials has already been shown in figure 6.4.

The conduction and valence band positions need to be thermodynamically favorable for such CO_2 reduction related photocatalytic application. Another important aspect is the separation and transfer of photogenerated electron–hole pairs within the material and it needs to be efficient as well as resistant to the photocorrosion effect.

CdS has been reported as inefficient and so its use has become limited. However in comparison, ZnS is mostly inert in corrosive environment and has the optimum band structures as well however its wide bandgap energy (3.6 eV) results in poor visible light absorption.

In addition to single transition metal oxides and common chalcogenides, the photocatalytic properties of complex metal oxides and chalcogenides (e.g., binary and ternary metal compounds), nitrides, carbides and phosphides have been extensively reported [16-18]. CdTe, with a band gap of 1.5 eV, has also been widely studied for photo-induced CO_2 reduction due to the availability of its p-type form. Bockris *et al.* had reported that CO_2 can be reduced to CO on a p-CdTe photocathode in a 0.1 M tetrabutylammonium tetrafluoroborate (TBAF)/MeCN solution [19]. A Faradaic efficiency of 60% in the potential range of −0.9 to −2.4 V vs Ag/AgCl was reported. Another chalcogenide ZnTe, which was formed onto a Zn/ZnO nanowire substrate, has demonstrated stable photocatalytic activity toward the reduction of CO2 to CO [20]. ZnTe possesses a 2.26 eV bandgap and a conduction band position located at 1.63 V vs RHE at pH 7.5, which is more negative than the standard reduction potentials of the common CO_2 reduction reactions. The as-prepared ZnO/ZnTe core−shell nanowires exhibited p-type conductivity and great photoresponse. At −0.7 V vs RHE at pH 7.5 in 0.5 M $KHCO_3$ solution, the system reduced CO_2 to CO with a 22.9% faradaic efficiency [21]. Chalcogenides in the form of two-dimensional (2D) planar structures have also been suggested to be promising for photocatalytic applications and the large surface area of 2D planar nanostructures naturally provide more available active sites for catalytic

redox reactions with surface absorbed species [22-24]. Recently, MoS_2 has also gained popularity as efficient catalysts for hydrogen evolution, oxygen reduction, and hydrodesulfurization [25-26].

6.5 Germanium-Sulfide-Indium

Transition metal chalcogenides have received significant attention in their photoelectrochemical application. Most of the chalcogenides investigated with respect to CO_2 reduction have been metal sulfides. At present, there is a consensus that the catalytic activity in sulfides originate mainly from the unsaturated S atoms along its edges. Increasing the number of exposed active sites on the edges and improving the electrical conduction are effective ways to enhance the electrocatalytic efficiency [26]. Therefore, we decided to use sufide-based material for the study. Furthermore, the use of post-transition metal chalcogenide glass structures has never been reported. The glass structure allows for structural defects to exist on the surface that can potentially act as reaction centers for CO_2-reduction. Furthermore, the low mobility of chalcogenide glass structures can also assist to accumulate electrons along such defect sites, possibly catalyzing multiple-electron reduction processes. Another interesting feature is the semiconducting nature of of the chalcogenide glasses which can potentially mean that the electrons within such a matrix can only flow in the conduction band or valence band. It can be theorized that the flow of electrons at fixed band levels can have an impact on the selectivity of the CO_2 reduction. Indium metal has already been extensively used for electrochemical conversion of CO_2 into formic acid while the sulfide atoms have shown to increase the catalytic activity, In an attempt to combine such qualities, germanium-sulfide-indium was chosen as the heterogenous electrode material for the electrochemical reduction of CO_2. Indium metal has been the staple for electrochemical conversion of CO_2 into formic acid [27-28] while the sulfide atoms can be utilized to increase the catalytic activity as has been observed in previous studies [29-30].

6.5.1 Current generated under light and dark conditions

The Ge-In-S samples exhibited no noticeable photo-induced current, The photo-response of the samples was measured by excitation spectroscopy to observe the excitation response in room temperature however the samples did not exhibit any reaction to the

blue laser light (corresponding to its band gap potential), possibly due to the amorpohous nature of the structure. In non-crystalline structures [31-32], the recombination rate has been observed to be high which causes the photo-response of such samples to suffer. The affect of light irradiation at 100 mW/cm^2 (1.5 Solar AM) was studied for different concentrations of indium content but no impact was registered, in agreement with the observation of excitation spectroscopy. The sample with 2 % indium concentration did show some difference but we decided to follow the path of electrochemical reduction. Electrolyte used for the measurements was 0.5 M $KHCO_3$. Table 6.1 shows the concentration of indium in the sample along with the current measured. The results and characterization of each of the samples follow after the table.

Table 6.1 Comparative current density for samples under light and dark conditions

Indium Concentration (%)	**Currenr density under light irradiation (mA/cm^2)**	**Current density under dark conditions (mA/cm^2)**
2	4.43	2.1
4	1.14	3.1
5	0.94	0.92
6	0.05	0.07
12	0.98	0.97

6.5.2 (0.98)$GeS_{1.5}$ - (0.02)In

The IV characteristics of the sample is given below in figure 6.5. The relative response showed a nominal difference between the inert argon saturated electrolyte and CO_2 saturated electrolyte.

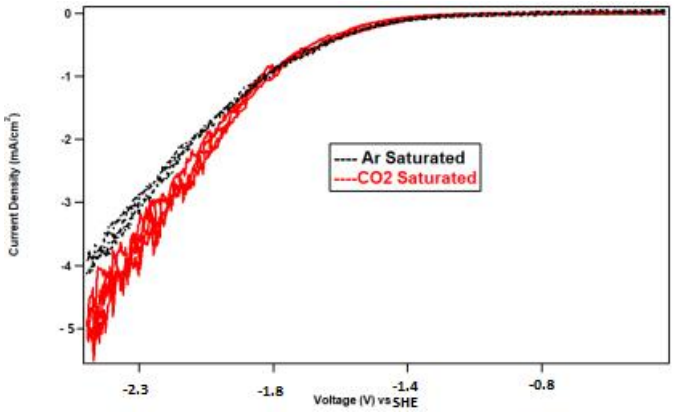

Fig 6.5 The IV response in CO_2 and inert electrolyte

Table 6.2 shows the faradaic efficiency during the CO_2 reduction experiments. The products from such experiments at different potentials continued to be hydrogen and CO and where hydrogen remained dominant. In experiments conducted at Nakanishi Lab, Osaka University, methane was detected in these experiments however it was never reproduced. The current density remained low for the duration of experiments and the highest FE for CO was observed at a potential of -1.45 V but since the current density was low, the product formation remained low. All the electrochemical experiment were conducted for a duration of 60 minutes and an average value for FE was recorded.

Table 6.2 FE for the sample at different potentials along with current density

		Faradaic efficiency (%)	
Potential (V) (vs Ag/AgCl)	**Current Density (mA/cm^2)**	**CO**	**H_2**
- 1.45	0.27	30.42	48.79
- 1.70	0.44	-	109
- 2.0	3.0	5.3	87.94
- 2.2	5.1	5.96	86.40
Cyclic (-1 to -2.5)		54.77	43.70

EDX measurement:

The characterization of the amorphous Ge-S-In chalcogenide glass was carried out for all the samples using EDX spectroscopy [33-36], which has an analysis depth of upto 2 μm. The elemental table for the sample with indium concentration of 2% is shown in table 6.3 while the EDX images is shown in figure 6.6. Oxygen poisoning was seen, which is a common occurrence during furnace fabrication processes. Sulfur deficiencies were also observed in all the samples and is considered to be characteristically particular to most of the amorphous chalcogenide glasses [37].

Table 6.3 Elemental analysis of the bulk samples by EDX

Element	Weight %	Atomic %	Error %
Oxygen	1.35	4.13	0.37
Sulfur	35.58	54.38	0.18
Germanium	58.69	39.62	0.24
Indium	4.38	1.87	0.74
	100.00	100.00	

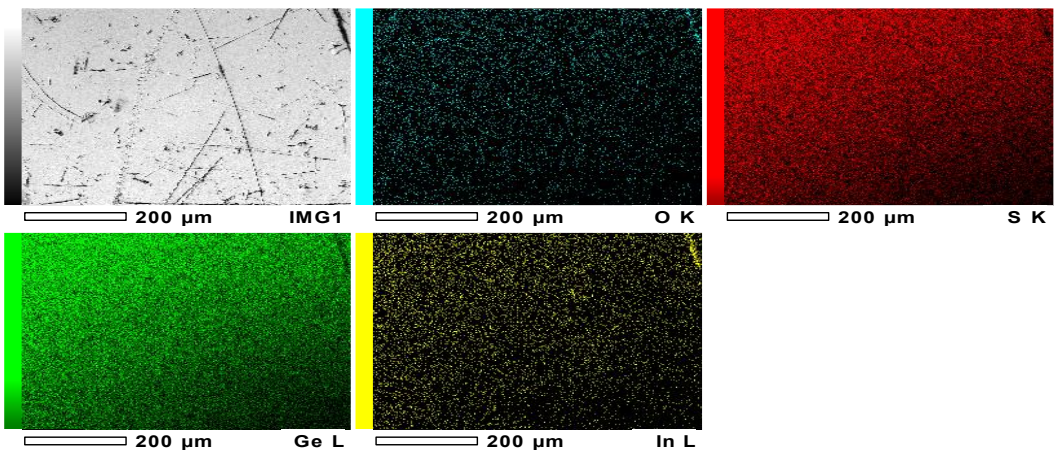

Fig 6.6 EDX images of the sample showing presence of the individual elements in the sample with 2% indium concentration

6.5.3 (0.96)$GeS_{1.5}$ - (0.04)In

The IV characteristics of the sample is given below in figure 6.7. The relative response showed a distinct difference between the inert argon-saturated and CO_2-saturated electrolytes.

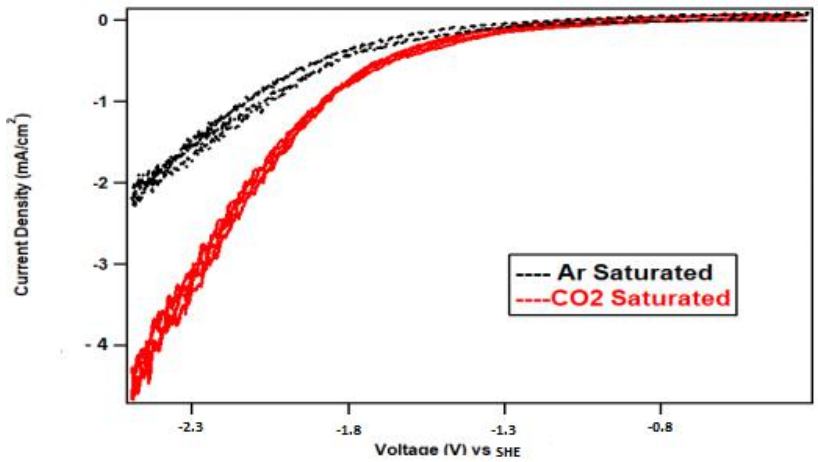

Fig. 6.7 The IV response in CO_2 and inert electrolyte

The product selectivity remained similar to the previous sample however the IV difference between CO_2-saturated and Ar-saturated electrolytes was stark. This meant that the reduction current in the CO_2-saturated electrolyte was higher than that in the inert saturated electrolyte. Thus, Hydrogen Evolution Reaction (HER) was taking place in the argon environment but the competing reaction of CO_2RR was taking place in the CO_2-saturated electrolyte which was significantly increasing the reduction current in comparison to the current in inert electrolyte. Experiments conducted both at the Nishigali lab, Osaka University and in our own lab, initially showed the detection of methane gas. This product obtained after an 8-electron reduction process is considered to be a useful product for commercial purposes. The methane FE was calculated between 29% to as high as 40%. However the continuous usage of the sample failed to reproduce methane repeatedly and therefore bringing the reliability of the data under question. It was for this reason that the sample was not further studied extensively. It is our contention that the sample's structural attributes were changed on repeated experiments at high current density (more than 7 mA/cm^2) which caused methane production to cease. The table showing the faradaic efficiency during the CO_2 reduction experiments is shown

in table 6.4 followed by the EDX measurement in table 6.5 and EDX image in figure 6.7. The products that could be obtained repeatedly were CO and hydrogen. All the electrochemical experiments were conducted for a duration of 50 and 60 minutes and were repeated multiple times and the average value for FE has been reported.

Table 6.4 FE for the sample at different potentials along with current density

		Faradaic efficiency (%)	
Potential (V) (vs Ag/AgCl)	**Current Density (mA/cm^2)**	**CO**	**H_2**
- 1.80	0.95	-	103
- 2.0	4.01	40.5	25.7
- 2.2	6.98	29.2	71.6
Cyclic (-1 to -2.5)			

Characterization:

Table 6.5 Elemental analysis of the bulk samples by EDX

Element	Weight %	Atomic %	Error %
Oxygen	3.13	9.42	0.35
Sulfur	34.59	51.88	0.16
Germanium	51.79	34.31	0.24
Indium	10.48	4.39	0.67
	100.00	100.00	

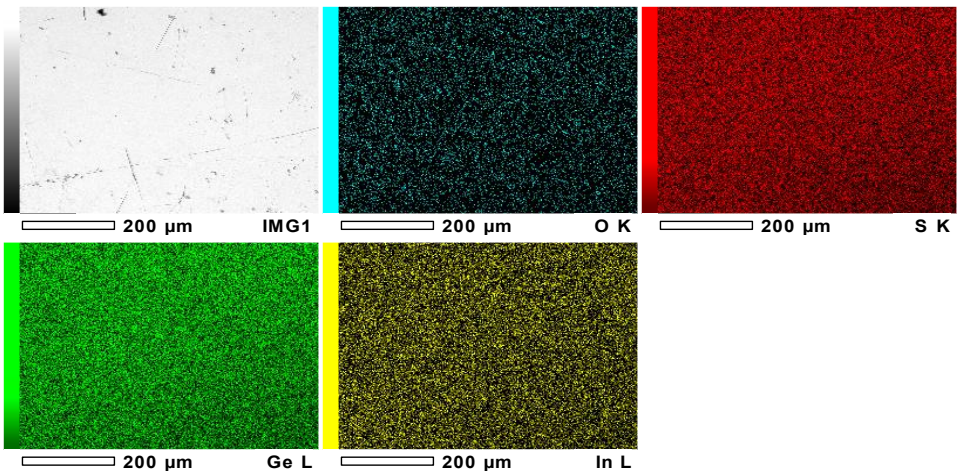

Fig. 6.7 EDX images for the sample with Indium concentration. of 4%

The XPS analysis was also conducted for the unused sample in order to sensitively measure the surface layer. Any difference between EDX and XPS results might be able to shed light on the reasoning for the initial detection of methane. It was our contention that slight changes in the concentration of indium cannot be the reason behind product selectivity. The local electrode structure could be different but the correct analysis could only be drawn from a sensitive surface layer analysis. XPS has a resolution of 5-10 nm but on the other hand, EDX has a depth resolution of up to 2 microns and hence it is reasonable to expect detection of elements with small signal during XPS, which may not had been detected during the EDX analysis.

The XPS measurement was done and the surface spectrum is shown in figure 6.8. Presence of phosphorus was detected which was missed during the EDX analysis. This phosphorus presence was not detected during the XPS measurement of samples with different indium concentrations. On the basis of phosphorus detection, we suggest that this was a surface impurity on the surface of samples with 4% indium concentration, and could be the reason behind methane production. The erosion of oxide layer from the surface in the used sample (at high current densities) may had resulted in the erosion of the phosphorus as well. This erosion could had subsequently caused the methane evolution to stop. Thus, we speculate that the methane production was a result of phosphorus doped germanium-sulfur-indium surface layer.

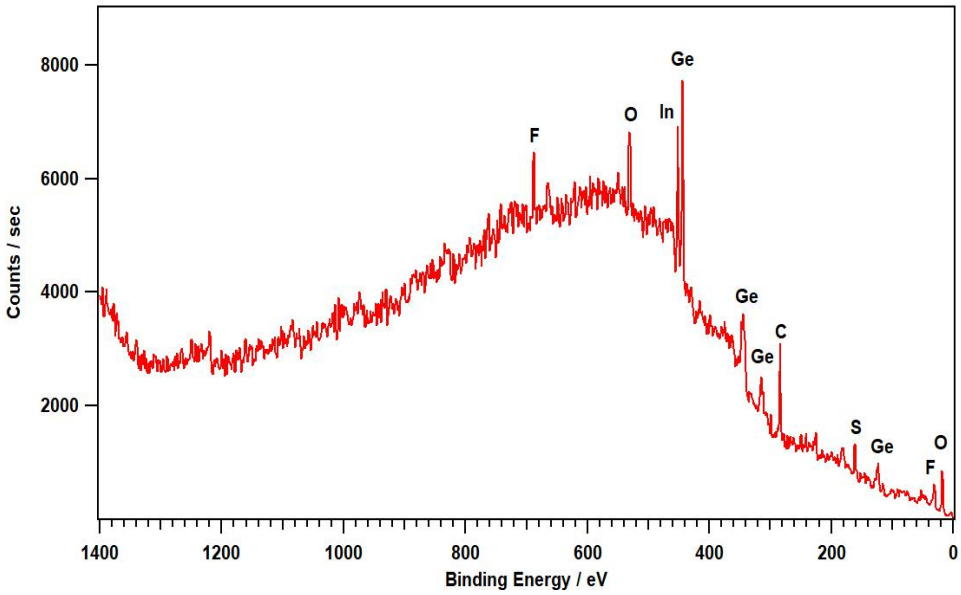

Fig. 6.8 XPS survey spectra of the sample

6.5.4 (0.94)$GeS_{1.5}$ - (0.06)In

The IV characteristics of the sample is shown in figure 6.9. The relative response showed an opposite trend where the current density between the inert Argon saturated environment was found to be higher than in the CO_2 saturated electrolyte. This meant that the HER was the dominant reaction and the electrode was more akin to generating hydrogen.

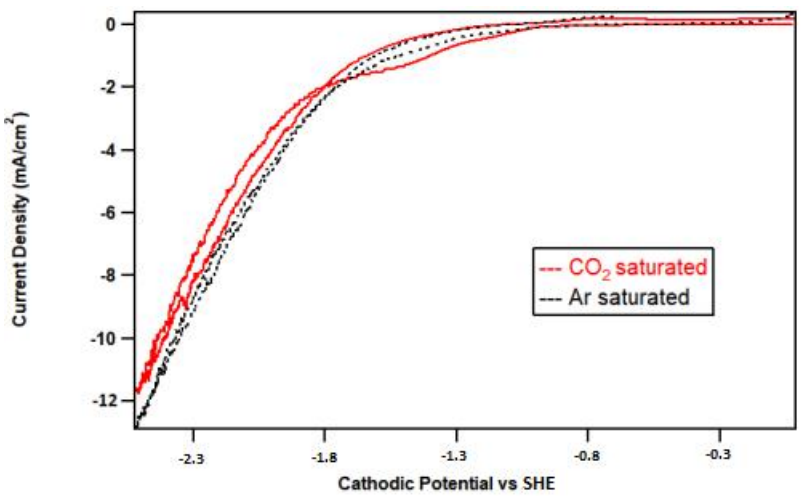

Fig. 6.9 The IV response in CO_2 and inert electrolyte

The sample produced mainly hydrogen as a product and CO was only observed only at one potential but as with previous samples, discharge of brown layer was witnessed at very negative potentials. Since chalcogendies are stable in acids while oxides are not, this layer was suggested to be Indium-oxide. However EDX image from the craters in samples with concentration of 5% provided a greater testimony to the existence of the oxide. Table 6.6 shows the the FE towards CO and H_2 during CO_2RR. The experiments were conducted for a minimum of 45 minutes. The gas sampling from the IV cycle was conducted for the duration of 5 cycles. The EDX elemental table can be seen in table 6.7 and the EDX images in figure 6.10.

Table 6.6 FE for the sample at different potentials along with current density

		Faradaic efficiency (%)	
Potential (V) (vs Ag/AgCl)	**Current Density (mA/cm^2)**	**CO**	**H_2**
- 1.80	1.80	-	93.94
- 2.0	2.60	-	98.30
- 2.2	5.60	22.4	87.30
Cyclic (-1 to -2.5)		18.4	79.30

EDX Measurement:

Table 6.7 Elemental analysis of the bulk samples by EDX

Element	**Weight %**	**Atomic %**	**Error %**
Oxygen	2.65	8.37	0.32
Sulfur	32.26	50.74	0.14
Germanium	48.16	33.46	0.21
Indium	16.92	7.43	0.56
	100.00	100.00	

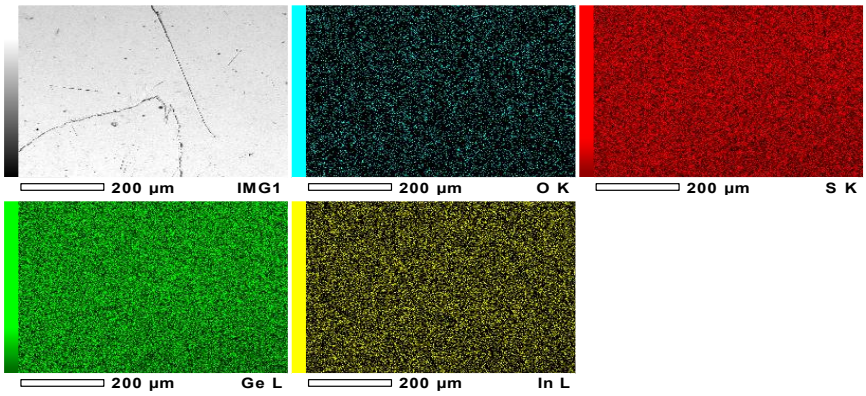

Fig. 6.10 EDX images for the sample with Indium concentration of 6%

Table 6.8 FE for the sample at different potentials along with current density

		Faradaic efficiency (%)	
Potential (V) (vs Ag/AgCl)	**Current Density (mA/cm^2)**	**CO**	**H_2**
- 1.80	1.80	13.9	82.17
- 2.0	1.30	3.89	93.90
- 2.2	3.30	3.44	92.69
Cyclic (-1 to -2.5)		12.9	85.70

6.5.5 $(0.88)GeS_{1.5}$ - (0.12)In

The IV characteristics of this sample shown in figure 6.11 and reflected a clear difference between the inert and CO_2 saturated electrolytes.

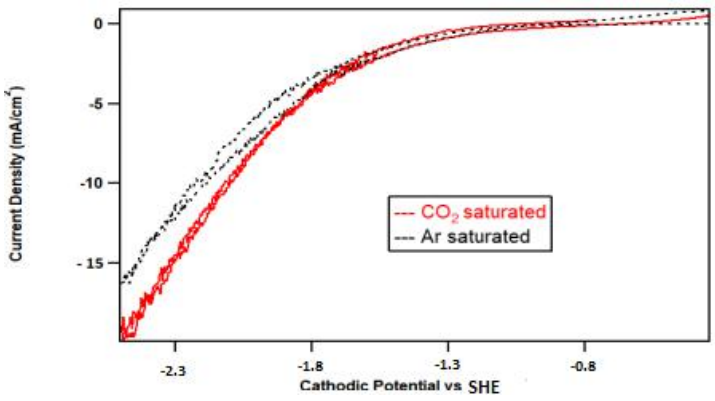

Fig. 6.11 The IV response in CO_2 and inert electrolyte

Despite the high mettalic content, the current density remained low which is suggested to be again to be from the indium oxide layer formation. The layer can be removed from a strong oxidizing agent. Concentrated sulfuric acid was used for the treatment however the current density continued to remained low. The CO production from CO_2RR remained minute as well and hence there was limited interest pursuing further investigation on the sample. The results are shown in table 6.8. The samples were experimented for 45 minutes and 60 minutes. EDX analysis was not conducted for this sample.

6.5.6 $(0.95)GeS_{1.5}$ - (0.05)In

This sample was found the most promising for the electrochemical reduction of CO_2. The samples were experimented at multiple time duration for up to 80 C. The IV response of the sample is shown in figure 6.12. We contend that a reason for a better and more stable electrochemical response has to do with the flatter structure of the sample.

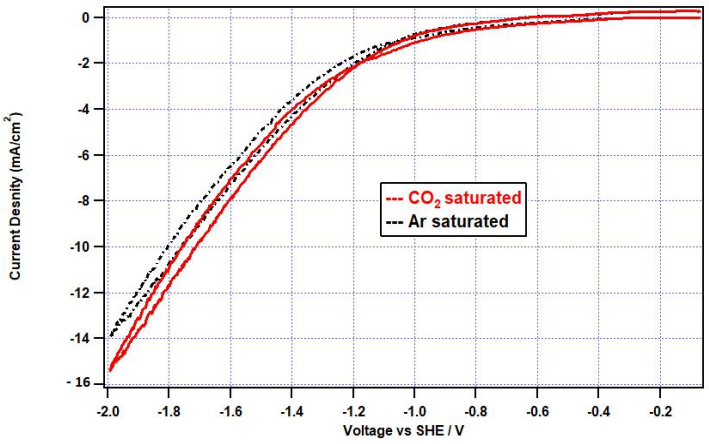

Fig 6.12 The IV response in CO_2 and inert electrolyte

As seen in all the previous samples, the EDX samples of samples with 5% indium concentration also showed oxygen content that was introduced during the furnace process. The photo-response of the samples was measured by excitation spectroscopy to observe the excitation response in room temperature however the samples did not exhibit any reaction to the blue laser light (corresponding to its band gap potential), possibly due to the amorphous nature. As mentioned before, higher recombination rate can cause the absent photo-respose [31-32]. The elemental composition of the samples is shown in table 6.9.

EDX measurement:

Table 6.9 Elemental analysis of the bulk samples by EDX

Element	Weight %	Atomic %	Error %
Oxygen	1.57	4.88	0.36
Sulfur	34.72	53.91	0.17
Germanium	53.86	36.94	0.24
Indium	9.86	4.27	0.68
	100.00	100.00	

The Ge-S-In samples of 5% indium concentration was selected for reporting the electrochemical reduction of CO_2 because of its flatter surface. The IV response of this sample as previously mentioned, had exhibited a slightly higher current density for CO_2 saturated electrolyte at the same negative cathodic potentials, which reflected activity towards the electrochemical reduction of CO_2. The range of cathodic potential was chosen in light of the region of increased activity from the comparative IV response between CO_2 and Ar (shown in figure 6.12). The FE for all the potentials were plotted in figure 6.13 showing increased electrochemical reduction of CO_2 from -1100 mV to -1700 mV vs SHE.

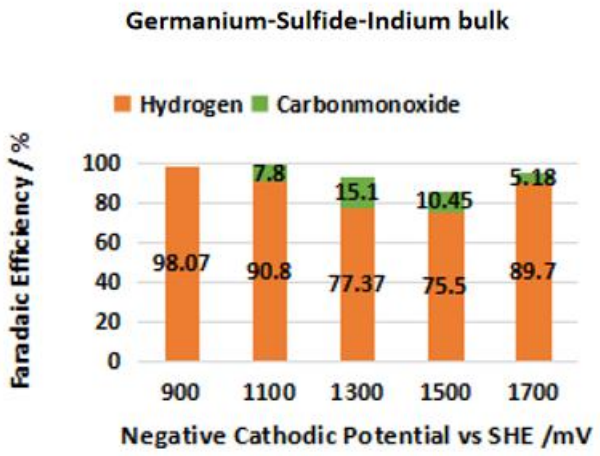

Fig. 6.13 Faradaic Efficiency against negative cathodic potentials for bulk samples with 5% Indium concentration in Germanium-Sulfide-Indium glass electrode: (1-x)GeS1.5- (x)In where x=5

Highest faradaic efficiency (FE) of CO observed was 15.1 % at -1300 mV vs SHE. The bulk amorphous glass exhibited no CO_2RR at 900 mV vs SHE and the reduction remained low from 1100 mV at about 7.8% but increased to its maximum at -1300 mV vs SHE, reducing again to single digits from -1700 mV vs SHE. Hydrogen was the parasitic product from these experiments.

It was observed that the maximum current density for stable operation of the samples was 5 mA/cm^2 after which a brown layer, similar to the previous samples, was observed. The surface degradation was seen in experiments at cathodic potentials more negative than -1500 V vs SHE. EDX analysis of the used samples in figure 6.14 showed an overlap of indium and oxide atoms in structural craters. The origin of such craters lies during the fabrication process. The overlap was not clearly visible in samples without clear craters.

We suggest that the EDX image indicates formation of indium oxide, observed as a brown layer after experiments at potentials more negative than 1500 mV vs SHE.

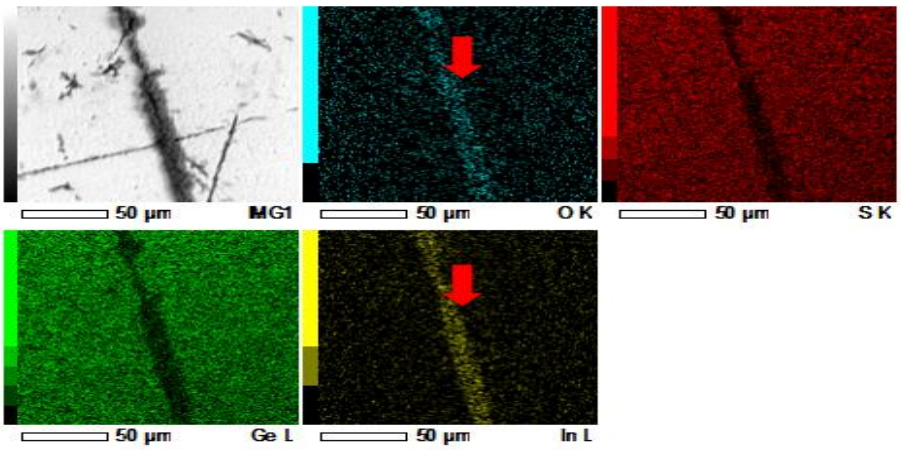

Fig. 6.14 EDX images of used samples indicating overlap of In and O atoms (red arrows) in structural craters.

EDX measurement of the crater was also conducted in order to confirm the theory. Indium and oxygen content should be higher if our hypothesis is true. The EDX image is shown in figure 6.15 while the elemental table can be seen in table 6.10. Indium content as well as the oxygen content was found to be higher in the crater which gave merit to the hypothesis that indium oxide was eroding off the surface. Carbon content was observed however this is a common source of surface poisoning. As mention before, the sulfur deficiencies observed in the samples is characteristic of amorphous chalcogenide glasses [38].

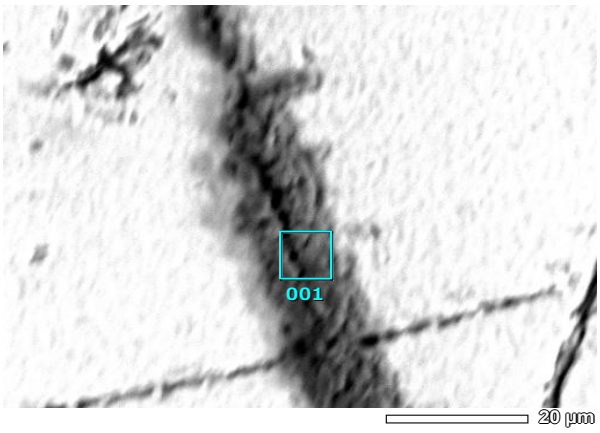

Fig. 6.15 EDX image of the crater. The experimental analysis showed an increase of Indium content

Table 6.10 Elemental analysis of the surface crater

Element	Weight %	Atomic %	Error %
Oxygen	25.6	35.8	0.21
Sulfur	8.9	5.88	0.14
Germanium	20.86	6.35	0.27
Indium	24.21	8.9	0.55
Carbon	20.42	43.07	0.81
	100.00	100.00	

As discussed in section 2.6, the reduction of CO_2 to carbon could also be the source of carbon content [39]. This carbon could had subsequently settled into the crater. Thus, it can be said with reasonable certainty that the nature of surface degradation, can be accounted as indium oxide, produced after electrochemical reduction at current densities higher than 5 mA/cm^2.

XPS analysis was conducted as well since it has a depth resolution of 5-10 nm, which helps in analyzing the surface layer and identification of oxidation states and is shown in figure 6.16. The XPS peaks were assigned [39] using the references available on the online NIMS database for XPS spectra. The curve-fitted XPS spectra identify the presence of GeS_2 [40] and In_2S_3 [41] along with In_2O_3 [42] on the surface. Thus, the

surface layer of the chalcogenide glass structure consisted of sulfides [43] along with minor presence of In_2O_3.

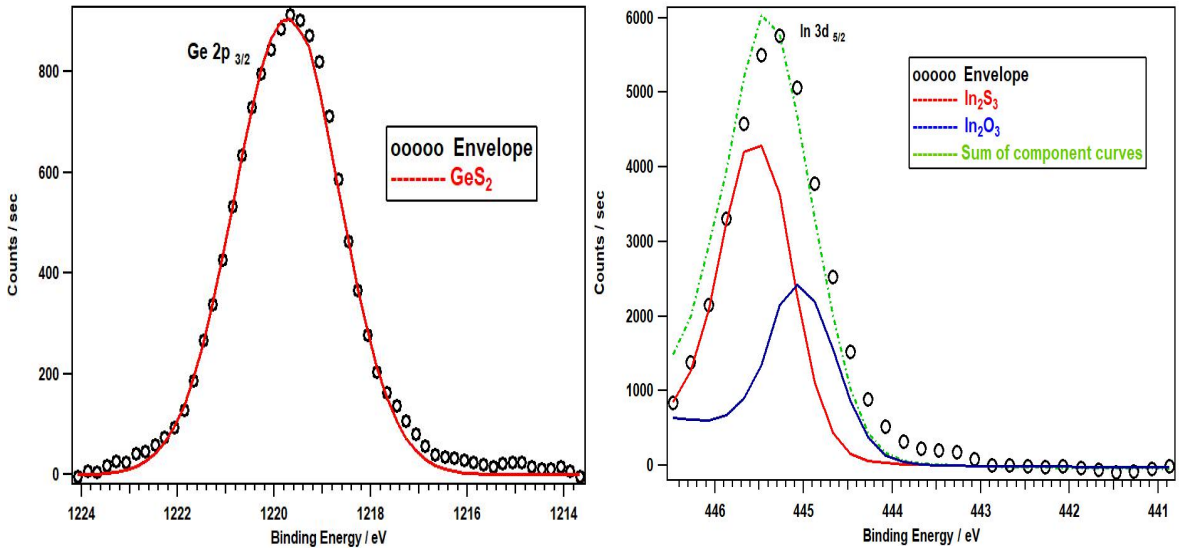

Fig 6.16 Fitted XPS spectra of Ge (left) and In (right), indicating that the surface is predominantly made up of metal sulfides; GeS_2 and In_2S_3 with smaller presence of In_2O_3.

The samples were tested for multiple time durations at the best performing potential of -1300 mV vs SHE. This allowed maximum columbs transfer of 80 C. The extended use of sample at -1300 mV showed almost constant FE of around 15% for CO production and can be seen in figure 6.17.

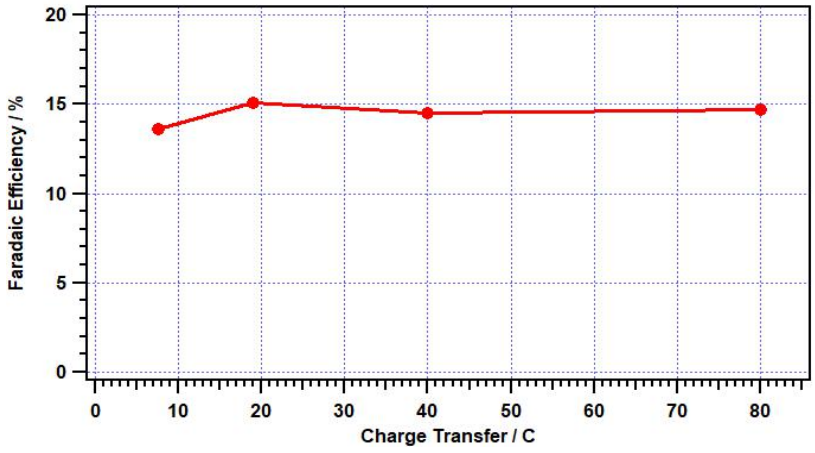

Fig. 6.17 Faradaic Efficiency of CO at extended use of electrode at -1300 mV vs SHE

The impedance of the samples was measured to be about 10^7 ohms (figure 6.18). The subsequent current seen at the electrode during the experiments were associated to the

electrochemical propensity for CO_2-reduction and surface activity however the bubble formation (attributed to active sites) were observed to be dependent on the distance from the ohmic contact. The lesser the distance, the higher was the onset of bubbles on the surface.

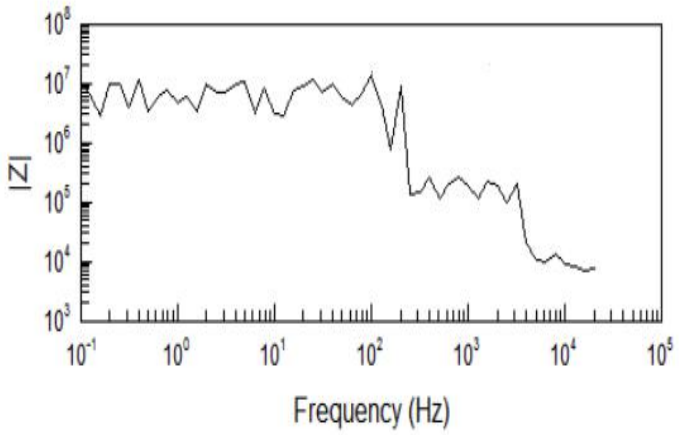

Fig. 6.18 The Z-diagram plot for the sample to gauge the flat-band potential of the samples

The attempt to plot the flat-band potential was unsuccessful due to the high resistance. The next phase of the study involved using the powdered form of the catalysts. The preparation of the CP-assisted chalcogenide particle electrode was carried out by crushing the bulk sample into micron size particles in order to study the impact of low coordination sites that exist in the particle form of the material and allow smaller series resistance in lateral direction. The change in the surface area has an impact on the exposure of the Ge-S-In material to the CO_2-saturated electrolyte. Carbon paper was used as the substrate because of its hydrophobic nature. The CP substrate is made up of a composite of carbon and carbon fibers, allowing not only high conductivity but high porosity. We speculated that the structural void in CP allows for the loaded catalysts to form unique and unconventional reaction sites as opposed to those on extremely flat electrode structures.

Electrodes were prepared by affixing a copper wire to the CP and the exposed portion of the copper wire was covered with epoxy to avoid any interaction between the electrolyte and the ohmic contact. For the particle-chalcogenide electrode, the bulk sample was crushed to micron size particles. A solution was prepared with ethanol as the solvent and

nafion solution as the adhesive material along with the crushed particles in the ratio 30:5:1, respectively. A 50 µl solution was then drop casted onto 1 cm^2 of carbon paper, which acted as a substrate. Figure 6.19 shows the different stages of the electrode preparation.

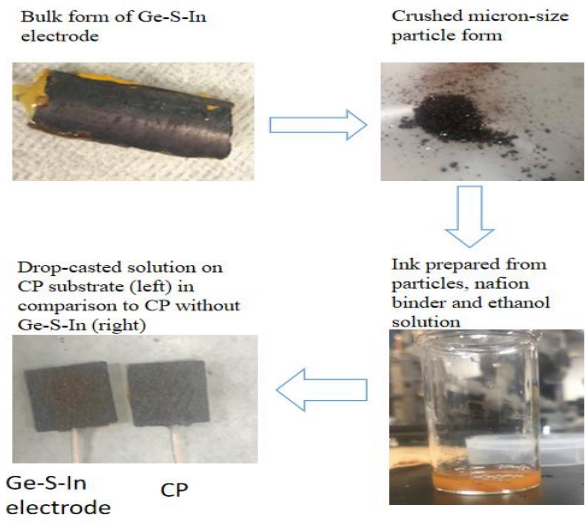

Fig. 6.19 Preparation of samples from bulk to particle form.
Electrodes with structure (1-x)GeS1.5- (x)In where x=5. Germanium-Sulfide-Indium

The IV response of the particle-based electrode in CO_2-saturated and Ar-saturated electrolytes is shown in figure 6.20. In comparison to the IV response of bulk-based electrode (figure 6.12), particle-based electrode reflected higher current density in CO_2-saturated electrolyte, which is an indication of higher CO_2RR activity [44] and confirmed that the change in structural form leads to different IV response.

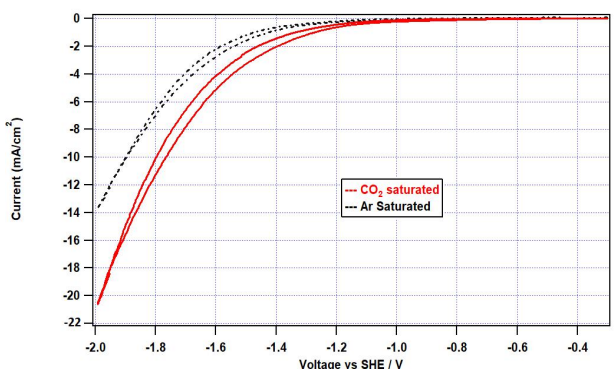

Fig. 6.20 IV response of the CP-supported particle electrode in CO_2-(red) and Ar-(black) saturated electrolyte

Figure 6.21 shows the faradaic efficiency difference between samples with and without Ge-S-In. CO which was observed in bulk samples was almost non-existent in particle chalchogens however formic acid with faradaic efficiency of upto 26.1% was observed. Formic acid was also observed in control samples without the chalcogenide particles however the maximum FE was 7.1%. The jump in formic acid production can thus be associated with the presence of the chalcogenide particles while the change between CO_2-reduced products is associated to the structural differences between the bulk and CP-assisted chalcogenide material.

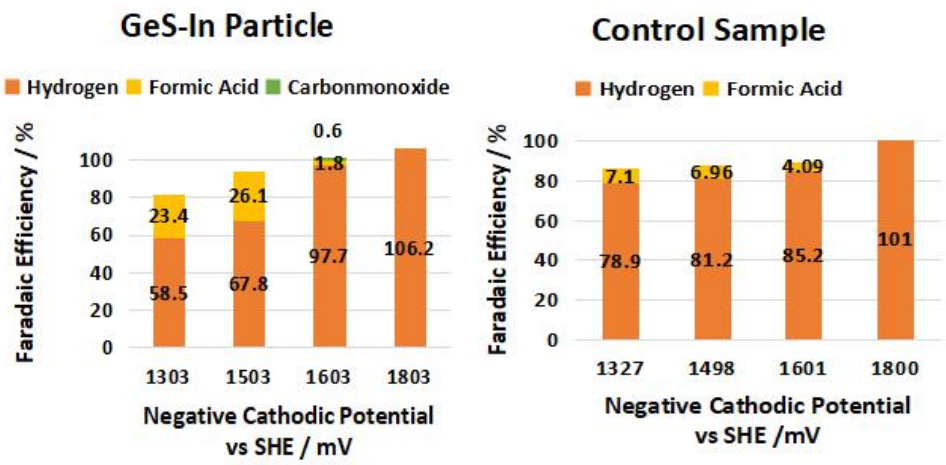

Fig. 6.21 Faradaic Efficiency against negative cathodic potential for particle-form samples (left) and Control samples (without GeS-In paticles)(right)

The extended use of the electrode at -1503 mV vs SHE can be seen in figure 6.22 where the FE towards formic remained above 25% after a passage of more than 80 C. Increased surface coverage by H ions and intermediate species during CO_2RR experiments have been reported to impact the evolution of products [45].

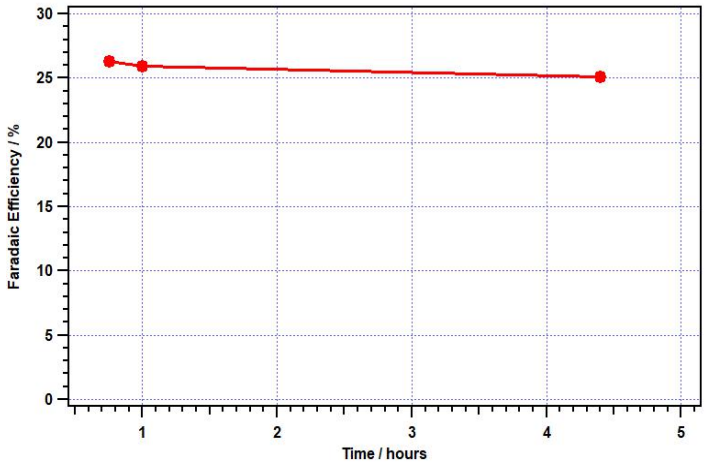

Fig. 6.22 Faradaic efficiency of formic acid at extended use of CP-supported particle electrode at -1503 mV vs SHE

The change in product selectivity between bulk-based and particle-based electrodes is due to the difference in reduction mechanism. This change in mechanism originates from the difference in local electrode structure and activity, which in turn affects the local chemical kinetics [46]. The generally agreed first step in the reduction mechanism for CO_2RR [47] is considered to be the formation of radical CO_2 at the active sites. Subsequently, the reduction direction on the bulk-based and particle-based electrodes take different routes since the binding energies for the intermediate species should differ on the bulk glass surface and CP-supported particle surface. CO production occurs primarily through a key carbon-bound intermediate, COOH, while formic production proceeds through a key oxygen-bound intermediate, OCHO [48]. In view of the products observed during CO_2RR experiments, we theorize that bulk-based electrodes show more propensity to the carbon-bound intermediate, while the the oxygen-bound intermediate binds more strongly with the CP-supported particle-based electrode. A proposed reduction pathway for the materials is presented in figure 6.22.

This difference in specie adsorption due to surface area changes has been previously studied by Riske *et. al* and Batista *et. al.*, [49-50] who had shown that the higher density of low-coordinated sites (corners, steps and kinks) account for higher activity which changes the proton flux thus causing local pH shifts. A more recent study [20] had attempted to go a step further to quantify these proton flux changes within the diffusion layer and show the impact of such changes in terms of CO_2RR activity. The increased activity due to low coordinate sites corresponded to our observation of higher current density and higher faradaic yield in particle-based electrode relative to bulk-based electrode, for the same cathodic potentials. We thus theorize that the increased current density causes the proton flux towards electrode to be higher, thereby reducing the local

pH around particle-based electrodes, hence impacting the product selection during the experiments.

The presence of formic acid in CP-assisted chalcogenide particles and our speculation of OCHO as an intermediate step is in agreement with the study by Norskov *et. al.* [51] which had concluded that the presence of promoters on electrode surface, facilitate the production of bidentate intermediates, an intermediate step [48] for formic acid production. Since CP based control electrode had produced formic with upto 7% FE, we can speculate that the deposition of chalcogenide particles allow an electrode-promoter configuration, similar to the one envisioned in [21], which results in the enhancement of bidentate adsorption and thus increase in formic acid yields. In conclusion, it is our hypothesis that the structural differences between bulk and particle assisted electrodes, allows difference in reaction activity and current density which subsequently impact the local pH and binding energies for key intermediates to the electrode, thus allowing the change in product selectivity.

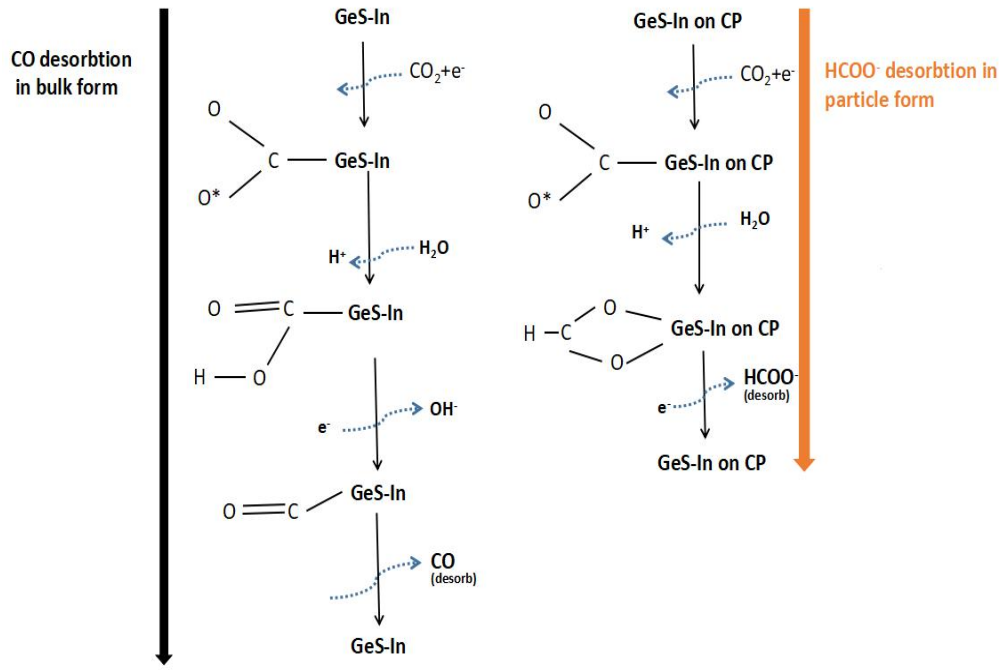

Fig. 6.23 Proposed reduction pathway. Bulk samples produce CO while the particle samples show more propensity for $HCOO^-$ production

6.6 Summary

1. Electrochemical reduction of CO_2RR was conducted using amorphous Ge-S-In chalcogenide glasses, which has never previously been reported.
2. Ge-S-In chalcogenide glasses were found to be new and active electrode material for CO_2RR.
3. The results showed that the photo-response, characteristic of chalcogenides, was missing, possibly due to the high recombination rate of amorphous, disordered structure.
4. The sulfide glasses were unstable at high current densities (higher than 5 mA/cm^2) and the position and size of ohmic contact had a significant impact on the current generation and hence the electrochemistry of this chalcogenide.
5. Methane was detected several times in some of the chalcogenide samples with 4% indium concentration however its reproducability remained elusive while CO in bulk form was reliable.
6. XPS measurements showed the presence of phosphorus on the surface layer of samples with 4 % indium concentration and this may had contributed to the evolution of methane.
7. Experiments were conducted in bulk and particle form of the material with the samples having 5 % indium concentration. The difference in structural form yielded different products. The samples with 5% concentration provided consistent results and this was mainly due to the flatter structure of the electrode rather than the choice of indium metal concentration.
8. About 15% faradaic efficiency for CO production was observed in bulk form while formic acid with up to 26% faradaic efficiency was measured in powder form.
9. The EDX measurement of these electrode materials reflected the erosion of indium oxide from the surface after CO_2RR experiments at high negative potentials. This could be subsequently removed after cleaning with a strong oxidising agent such as concentrated sulfuric acid.
10. The curve-fitted XPS measurement detected the presence of GeS_2, In_2S_3 and In_2O_3 on the surface, which corresponds to the phase diagram of the Ge-S-In glasses.
11. This study helped to shed light on the possibility of using a new class of cheap materials as possible electrodes for CO_2RR and elucidates the factors that can impact future direction in this field.

12. Chalcogenide studies have focused primarily on the photoelectrochemical reduction however these results provide a strong merit for introducing metal in chalcogenide glass structures for electrochemical reduction of CO_2.

13. The activity for CO_2 reduction and the change in product selectivity reflects that further efforts to improve the glass structures can be undertaken to increase the faradaic efficiency and selectivity of the products.

14. These amorphous glass structures are fabricated by 'Conc. Quenching' Technique, which is used in industrial scale manufacturing of glasses. Hence the fabrication cost of such amorphous chalchogenides on commercial scales could be low, which can pave the way for the production of financially feasible CO_2 reduction catalysts on a mass scale.

6.7 References

1. Comerford J., Ingram I., *Green Chem*., 2015, **17**, 1966-1987
2. Hautala J., Taylor P., *Journal of Non-Crystalline Solids*, 1992, **141**, 24-34
3. Singh P.V., Dwivedi D.K., *Ferroelectrics*, 2017, **520**, 256-273
4. Zakery, A., Elliott S., *Journal of Ovonic Research*, 2005, **1**, 7 – 19
5. Minami T., Hayashi A., Tatsumisago M., *Solid State Ionics*, 2006, **177**, 2715-2720
6. Chern G., Lauks I., *J. Appl. Phys*., 1982, **53**, 6541-6549
7. Dobson J.C., McLarnon F.R., Cairns E.J., *J Electrochem Soc.* 1986, **133**, 2069–2076
8. Warin D., Tomczuk Z., Vissers D.R., *J. Electrochem Soc,* 1986, **130**, 64–70
9. Weaver M.J., Inman D. *Electrochim Acta*, 1975, **20**, 929–936
10. Tu W., Zhou Y., Zou, Z., *Adv. Mater*., 2014, **26**, 4607−4626.
11. Halmann, M., *Nature*, 1978, **275**, 115−116.
12. Russell P. G., Kovac N., Srinivasan S., Steinberg M., *J. Electrochem. Soc.*, 1977, **124**, 1329−1338.
13. Bocarsly A. B., Tachikawa H., Faulkner L. R., Photonic Electrochemistry. In Laboratory Techniques in Electroanalytical Chemistry, **2nd ed**., revised and expanded; Kissinger, P. T., Heineman, W. R., Eds.; *CRC Press: Boca Raton, FL, USA*, 1996.
14. Rajeshwar K., Ibanez J. G., Environmental Electrochemistry: Fundamentals and Applications in Pollution Sensors and Abatement; *Academic Press: San Diego, CA, USA*, 1997.
15. Berger L. I., Semiconductor Materials; CRC Press: Boca Raton, FL, USA, 1996.
16. Wang J., Tafen D. N., Lewis J. P., Hong Z., Manivannan A., Zhi M., Li M., Wu N., *J. Am. Chem. Soc*., 2009, **131**, 12290−12297.
17. Li J., Wu N., *Catal. Sci. Technol*., 2015, **5**, 1360-.
18. Meng F., Hong Z., Arndt J., Li M., Zhi M., Yang F., Wu N., *Nano Res*. 2012, **5**, 213−221.
19. Aurian-Blajeni B., Habib A., Taniguchi I. Bockris J. O., *J. Electroanal. Chem. Interfacial Electrochem*., 1983, **157**, 399−404.
20. Jang J.-W., Cho S., Magesh G., Jang Y. J., Kim J. Y., Kim W. Y., Seo J. K., Kim S., Lee K.-H., Lee J. S., *Angew. Chem., Int. Ed.*, 2014, **53**, 5852−5857.
21. Nozik A. J., Philos. Trans. R. Soc., A, 1980, **295**, 453−470.
22. Wang W.-N., Soulis J., Yang Y. J., Biswas P., *Aerosol Air Qual. Res.*, 2014, **14**, 533.
23. Lewis N. S., *Acc. Chem. Res*. 1990, **23**, 176−183.
24. Asadi M., Kumar B., Behranginia A., Rosen B., Baskin A., Repnin N., Pisasale D., Philips P., Zhu W., Haasch R., Klie R.H., Karl P., Abiade J., Salehi-Khonjin A., *Nat. Commun.*, 2014, **5**, 5470
25. Cui X., Lee G. H., Kim Y. D., Arefe G., Huang P. Y., Lee C., Chenet D., Zhang X., Wang L., Ye F., Pizzocchero F., Jessen B., Watanabe K., Taniguchi T., Muller D., Low T., Kim P., *Nat. Nanotechnol*., 2015, **10**, 534 –540.
26. Hackerman K., *J. Electrochem. Soc.*, 1983, **130**, 607-613
27. Xia Z., Freeman M., Zhang D., Yang B., Lei L., Li Z., Hou Y., *ChemElectroChem,* 2018, **5**, 253 – 259
28. Li G., Zhang D., Qiao Q., Yu Y., Peterson D., Zafar A., Kumar R., Curtarolo S., Hunte F., Shannon S., Zhu Y., Yang W., Cao L., *J. Am Chem.Soc*,. 2016, **138**, 16632-1663
29. Li H., Tsai C., Koh A. L., Cai L. L., Contryman A., Fragapane W., Zhao A., Han J., Manoharan H., Abild-Pedersen F., Norskov J. K., Zheng X. L., *Nat. Mater*, 2016, **15**, 48– 53
30. Chekulaev D., Garber V., Kaplan A., *J. Appl. Phys*., 2013, **113**, 143101.
31. Sinton R., Swanson R., *IEEE Trans. Electron Devices ED-34*,1987, 1380.

32. Kassim A., Min H., Siang L., Nnglingam S., *Chalcogenide Letters*, 2011, **8**, 405 – 410
33. S.M. Ho, *Middle-East Journal of Scientific Research*, 2016, **24**, 445-449.
34. Yuan P., Wang A., Luo X., Xue Y., Zhang L., Feng *J., Biosensors and Bioelectronics*, 2019, **126**, 187-192
35. Zhang L., Fang X., Xue Z., Chen L., Wang A., Han D., Wang Z., Feng J., *Journal of Colloid and Interface Science*, 2019, **536**, 556-562.
36. Hewak D., Brady D., Curry R., Chalcogenide Glasses for Photonics Device Applications. In: Murggan GS (ed.) Photonic Glasses and Glass-Ceramics. Kerala: *Research Signpost* (2010) 29–102
37. Manos M. J., Malliakas C., Kanatzidis M., *Chemistry*, 2007, **13**, 51-58.
38. Kusunoki I., Sakai M., Igari Y., Ishidzuka S., Takami T., Takaoka T., Nishitani-Gamoc M., Ando T., *Surface Science*, 2001, **492**, 315-328
39. Y. Hori, Konishi H., Futamura T., Murata A., Koga O.,Sakurai H., Oguma K., *Electrochimica Acta*, 2005, **50**, 5354-5369
40. Morgan W., Van Wazer J.*„J. Phys. Chem*., 1973, **77**, 964-969.
41. Battistoni C., Gastald L., Lapiccirella A., Mattogno G., Viticoli C., *J. Phys. Chem. Solids*, 1986, **47**, 899-903.
42. Kazmerski L., Jamjoum O., Ireland P., Deb S., Mickelsen R., Chen W., *J. Vac. Sci. Technol.*, 1982, **19**, 467-486.
43. Boncheva-Mladenova Z., Ivanova Z., *Journal of Non-Crystalline Solids*, 1978, **30**, 147-153
44. Li F., Zhang H., Ji S., Liu W., Zhang D., Zhang C., Yang J., Yang F., Lei L., *Int. J. Electrochem. Sci*., 2019, **14**, 4161 – 4172
45. Kuhl K., Cave E., Abramc D., Jaramillo T., *Energy Environ. Sci*., 2012, **20**, 7050-7059.
46. Raciti D., Mao M., Park J., Wang C., *J. Electrochem. Soc*., 2018, **165**, F799-F804.
47. Schouten K. J. P., Kwon Y., van der Ham C. J. M., Qin Z., Koper M., *Chem. Sci.*, 2011, **2**, 1902.
48. Feaster J., Shi C., Cave E., Hatsukade T., Abram D., Kuhl K., Hahn C., Nørskov J., Jaramillo T., *ACS Catal*., 2017, **7**, 4822–4827.
49. Reske R., Mistry H., Behafarid F., Cuenya B., Strasser P., *J. Am. Chem. Soc*., 2014, **136**, 6978 – 6986
50. Baturina O., Lu Q., Padilla M., Le X., Li W., Serov A., Artyushkov K., Atanassov P., Xu F., Epshteyn A., Brintlinger T., Schuett M., Collins G., *ACS Catal.*, 2014, **4**, 3682-3695.
51. Peterson A., Nørskov J., J. Phys. *Chem. Lett*., 2012, **3**, 251– 258.

.

CHAPTER 7

Oxide-based chalcogenide material - Cu_2O

The previous chapter reported the practical usability of chalcogenide sulfide materials where the electrochemical activity had been observed to be higher in particle form. Therefore, in our next study we decided to use the same micron-sized powder catalyst but of a more stable chalcogenide. Figure 6.1 had shown the periodic table for the elemental sustainability of the materials in future. Oxide-based materials are viable materials in term of long-term availability and therefore metal-based oxides were chosen since they have recently been gaining attention for their high selectivity.We decided to employ Cu-based oxide as copper had been reported to be a good active material for CO_2 reduction. This choice allowed us to keep focus on chalcogenide while using copper as well since it is the most active element for muti-carbon product production. Furthermore, the electrochemical experiments with micron-size catalyst particles provided insight into the impact of using particles with low volume to surface area, which has not been reported previously.

7.1 Introduction to Cuprous Oxide (Cu_2O)

Over the past three decades, researchers have evaluated lots of metals as electrodes for CO_2 reduction in aqueous solutions. While these metal electrodes show decent CO_2 electroreduction performances, they usually suffer from very high prices, limited availability, as well as rapid loss of CO_2 reduction activity, which seriously hinder their large-scale practical applications. To address these issues, several naturally abundant and chemically stable transition-metal oxides have been recently explored as potential CO_2 electroreduction catalysts to replace the expensive and easily deactivated metals [1]. Among these materials, the spinel-type oxide of Cu_2O seems to be one of the most competitive candidates for electrocatalytic CO_2 reduction. Cuprous oxide (Cu_2O) is one of the three stable oxide forms of Cu having an oxidation state of +1. The unit cell of Cu_2O exists of 4 Cu atoms and 2 O atoms and has a lattice constant of 4.2696. Cu atoms are arranged in a face-centered manner while O atoms are arranged in a body-centered manner. Cu atoms are linearly coordinated to two O atoms while O atoms are tetrahedrally coordinated to four Cu atoms (see figure 7.1). Cu_2O usually crystallizes into cubes with size ranging from 10 nm to 10,000 nm. It physically exhibits a reddish orange color [2-3].

Cu_2O nanowires and polyhedrons can also be obtained by tailoring the synthesis condition. There are many review articles which discuss the various techniques applied to fabricate Cu_2O particles and are listed in figure 7.2. [4-5].

The catalyst used for this study was procured from Sigma Aldrich. They had employed liquid phase Cu_2O synthesis or wet chemical reduction and electrochemical deposition. In the wet chemical reduction method, Cu_2O particles are chemically formed by mixing Cu^{2+} precursor salts with reducing agents and other additives e.g. surfactants and precipitators. NaOH is typically used to precipitate Cu^{2+} into $Cu(OH)_2$ before adding the reducing agent to convert $Cu(OH)_2$ to Cu_2O [6-9]. The size and morphology of Cu_2O is sensitive to the composition of reagents used which influence the relative growth of (100) and (111) planes.

In electrochemical reduction, electric current is supplied to simultaneously convert Cu^{2+} precursor salts and grow Cu_2O on a conducting support substrate. The electroplating bath typically consists of the Cu^{2+} precursor salt and chelating agent such as lactic acid. The pH of the bath is adjusted to alkaline condition by addition of NaOH. Morphology is controlled by the applied potential, pH and the nature of the growth substrate.

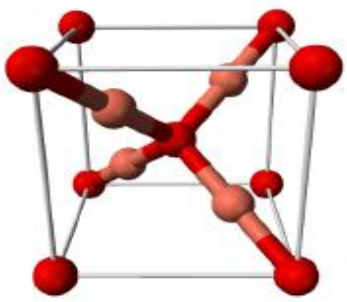

Fig. 7.1 Unit cell of Cu_2O [4]

7.2. Cu_2O for CO_2 reduction

There have been a handful of studies regarding Cu_2O as electrocatalyst for CO_2 conversion. Most of these reports reported the production methanol as a major CO_2 product. In 1991, Frese *et. al.* [10] was the first to study Cu_2O when he demonstrated direct CO_2 reduction to methanol. Different structures of electrode were compared; anodized Cu foil, thermally air-oxidized Cu, and air-oxidized Cu on oxidized Ti at various potentials. The highest rates for methanol were observed from anodized Cu. It

was suggested that binding strength of CO_2 and CO on Cu_2O active sites had facilitated hydrogenation of CO to CH_3OH.

Another group had followed a similar approach [11] and different methods to oxidize copper (Cu_2O) had been tested. This study had also reported methanol as the major CO_2 product with trace amounts of CO. They had compared anodized Cu, thermally air-oxidized Cu, and electrodeposited Cu_2O and showed highest methanol rates and faradaic efficiency with electrodeposited Cu_2O. Potential-dependent methanol formation from CO_2 was evaluated between -1.0V and -2.0V (SCE) and it was observed that the rates had started to decrease after electrolysis for more than 30 minutes and simultaneously, CH_4 formation had started to increase. Cu_2O was also concurrently being reduced and was suggested as the reason for reduction in activity. Although a high methanol rate was reported on electrodeposited Cu_2O but the reproducibility of sample preparation and the stability of the sample was the bottleneck. The Cu (I) was suggested to be key to high CH_3OH generation. In another study [12], the Cu_2O catalyst was prepared by a chemical reduction synthesis and carbon related substrate was used. Again, methanol was used and the catalysts were reported to be stable based on cyclic voltammetry data. However, it was reported in [12] that preparation of different thicknesses of oxidized Cu by annealing it in air, can produce a host of different products. The observation was that Cu_2O was able to reduce CO_2 to CO at less negative potentials at good production rates, about 20 times better than those reported by Hori for Cu samples. The products reported included ethane, ethanol but there was no observation of methane or methanol. It was suggested that the increase in CO faradaic efficiency and production rate was due to the presence of grain boundaries in increased concentrations. This had resulted due to the unstable atomic coordination because of the reduction of Cu_2O films.The high number of low coordinated sites is suggested to enhance the formation of hydrocarbons, particularly ethylene and methane [13].

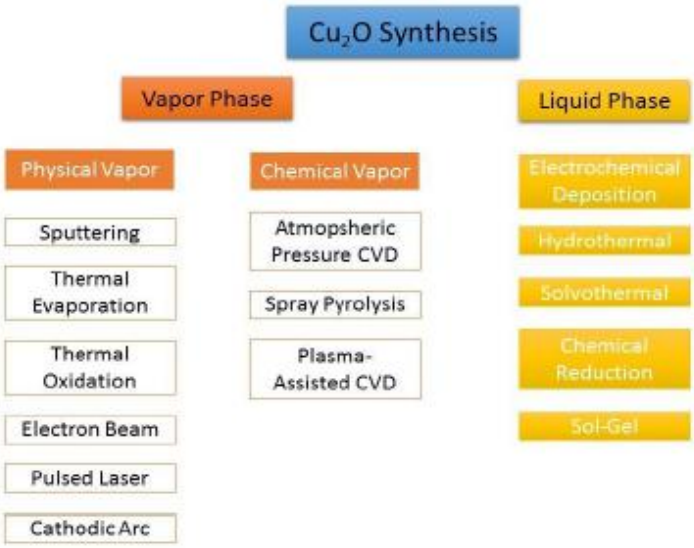

Fig. 7.2 Different methods of Cu_2O fabrication [4-5]

Terunuma *et. al.* [14] had found that surfaces containing copper oxide demonstrated higher activity for hydrocarbon production than metallic Cu. This was suggested to stem from the higher affinity for Cu metal to the adsorbed oxygen. However, surface of the Cu_2O catalyst has a better ability to adsorb CO compared to the Cu metal, and since CO is an intermediate for many of the hydrocarbon products, the surface of the product selectivity could be significantly improved if Cu_2O catalyst is used for CO_2RR. Another recent report [15] had suggested that using electrodeposited Cu_2O increased the faradaic efficiency towards C_2H_4 and production of C2, C3 and C4 products reached over 10%. The authors had suggested that Cu (I) can bind with the intermediate species of electrochemical reduction of CO_2 and this is a critical factor in forming carbon intensive products [15]. The potential range was between -0.6 V to -1.8 V vs. RHE (-1.2 V to -2.4 V vs. Ag/AgCl) and the carbon intensive products were found to be forming at negative potentials. The experiments conducted for longer duration showed that C3 and C4 products had decreased linearly to the decrease of oxidation state from from Cu(I) to Cu(0). The results suggested that product selectivity was directly dependent on the oxidation number of the Cu specie in the catalyst.

Another study [16] had worked with the electrodeposited Cu_2O film and reported production of C_1 and C_2 species. Increase in the roughness of Cu_2O had shown a larger current towards CO_2RR and hence increased activity. The authors had suggested a reduction mechanism which shows that the first step was the transfer of electron for

formation of COOH which then hydrogenates to adsorbed CO and H_2O. The intermediate CO* can than reduce to CH_4 or to a C2 product and the C2 product could further reduce to ethylene or ethanol. As discussed before, the thickness of Cu_2O film can increase current density and this has a direct impact on the selectivity of the C2 products. The thickness required for production of C_2 products was determined to be 1.7-3.6 μm and the increase of thickness, reduces the faradaic yield for all CO_2RR products and increases hydrogen propensity.

The stability of the Cu_2O is also extremely important for the commercial use of CO_2RR. It has been discussed [17] that there can possibly be two methods to ensure the stability. One method involves preventing the deterioration of the electrode by maintaining the dispersion of particles and the second method involves employing ways to stop the poisoning of Cu_2O active sites. The study [17] had claimed that the formation of Cu_2O/ZnO inter-mixture allows increased period for Cu_2O electrode stability. It was suggested that the presence of zinc oxide improves the bonding between copper and CO thus improve the selectivity of the products [18]. Nanowires made from Cu_2O nanowire along with Sn were shown to increase the activity and stability [19]. It was claimed that the CO_2RR activity caused binding between the cuprous oxide and tin and the stability of the electrode had been improved. This reflected an extremely good product selectivity which was because of the presence of Sn atom which disrupted the multifold sites on the Cu_2O catalyst. The addition of gold to the cuprous oxide on electrode was able to bring the overpotential down and increase faradaic yields towards CO to more than 90% [20].

A recent study [21] reported improvement of efficiency towards ethylene (C_2H_4) by using Cu_2O catalysts grown on graphite sheets functionalized with ionic liquid while CH_4 and C_2H_6 along with other products were also reported. Novel metal organic framework in Cu_2O-based electrodes have also been reported [22] to improve faradaic efficiency towards CH_4 while producing other higher order carbon products. The role between oxide layer and metal phase and their contribution towards product selectivity in CO_2RR has also been an issue of debate [23-24]. It was demonstrated by Kim *et. al.* [24] that electrodeposited Cu_2O can aid in the selective formation of C_2H_4 over CH_4 and had concluded that both the oxide component and metal, play a role in the selective electroreduction of CO_2 toward multi-carbon products. Previous works have shown that the product selectivity of Cu_2O is dependent upon the morphology and size of the oxide particles while the formation of Cu^0 with O vacancies within these Cu_2O particles during CO_2RR is also considered as an important factor in the efficacy of Cu_2O as catalysts [25-26]. It has been suggested [21] that the oxide matrix plays a key role in maintaining

high performance of oxide-derived Cu^0 and that the grain boundaries impacts the product selectivity during CO_2RR.

For this study, we decided to use carbon fiber paper (CP) as the substrate material because it has proven durability and is perfectly suited for catalyst backing layer and is an affordable alternative to woven carbon cloth gas diffusion layer materials in fuel cell applications [27]. The manufacturing process of the CP is by acquiring acrylonitrile by refining oil and then spinning the acrylonitrile into a yarn. This product is subsequently heated at extremely high temperature to remove any unwarranted components. The major properties of carbon paper are its low electrical resistivity, excellent handling, great strength and negligible electrochemical corrosion. Its specific strength, is usually calculated by dividing the tensile strength and is determined to be 10 times sturdier than iron and thus it features high tensile strength and are connected securely by carbon to make it durable for electrochemical experiments [27]. CP also never rusts and its stability in extreme conditions makes it a reliable substrate for electrode. The light weight allows it to be more flexible. The surface porosity in CP structures has been reported to change both reagent and product transport pathways [28] and these changes in transport phenomena have shown to increase current density and change product selectivity [29-30]. The thickness model of CP used in this study was H-0120.

Since most studies have used smaller sizes of Cu_2O particles in combination with either copper metal [31-34] or glassy carbon [22, 35], it was our hypothesis that the use of larger size of Cu_2O particles supported on a structurally porous CP substrate would offer new product distributions.

The electrodes were prepared by affixing a copper wire to the CP substrate. A solution was prepared with Ethanol as the solvent and nafion solution as the adhesive material along with the Cu_2O particles in the ratio 30:5:1, respectively. A 50 µl solution was then drop casted onto 1 cm^2 of carbon paper, which acted as a substrate. Figure 7.3 shows the different phases of the electrode preparation.

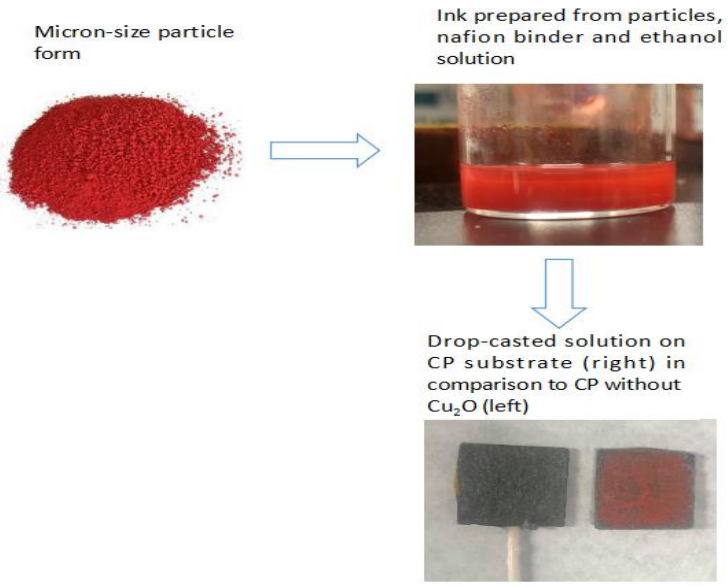

Fig. 7.3. Preparation of Cu_2O electrodes

7.3 Results and Discussion for Cu_2O catalysts

The SEM images of the Carbon Paper (CP) substrate are shown below for different resolutions. The images reflect the porous surface structure of carbon fibers on the carbon substrate which allow for the loaded catalysts to form unique and novel reaction sites that may otherwise not be possible on flatter substrates. Figures 7.4, 7.5 and 7.6 show the hydrophobic composite of carbon and carbon fibers reflecting the higher porosity and enhanced structural rigidity than carbon cloth.

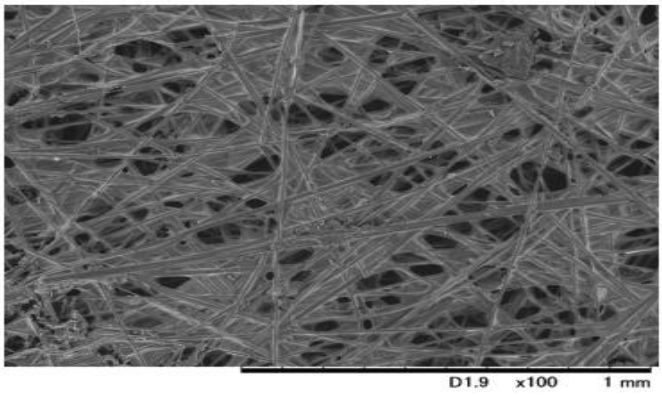

Fig 7.4. Carbon Paper at x100 resolution

.

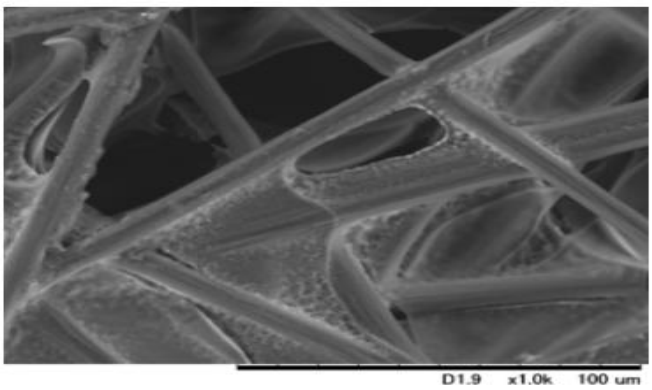

Fig. 7.5 Carbon Paper at x1000 resolution

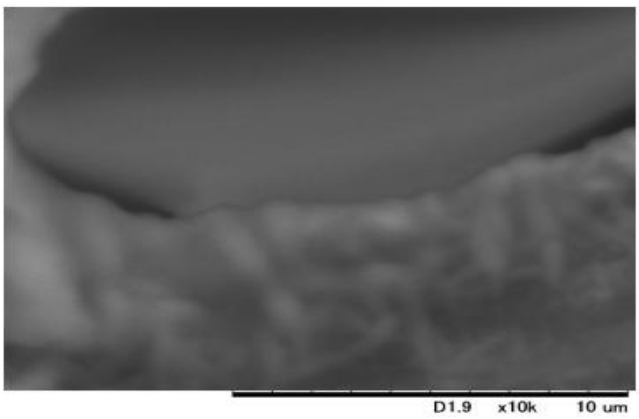

Fig. 7.6 Carbon Paper at x10000 resolution

The relative response between the CO_2 saturated and Ar saturated environment is given below. The current response was nominal which reflected that although Cu_2O was active towards the electrochemical reduction of CO_2, the proton concentration can also be reduced to hydrogen gas. This reflects that hydrogen would be the competing reaction.

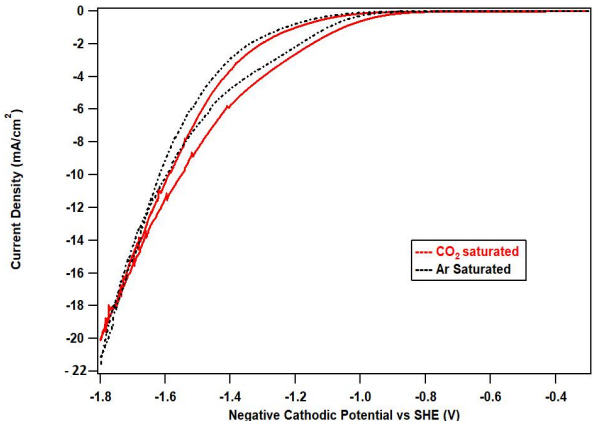

Fig. 7.7 IV response of Cu_2O particles in CO_2 saturated (solid red line) and Ar-saturated (dotted black line) electrolytes.

A loading of amount of 1 and 2 mg/cm^2 was tested for CO_2 electrochemical reduction. Studies using an of order of magnitude less loading have suggested that the impact of more loading should result in better faradaic yields for CO_2 reduction [6, 36]. The size of each Cu_2O particle in our study was between 1 to 6 μm, that allowed for a different surface area and orientation to the previously reported studies. Figure 7.8 shows the Cu_2O particle size distribution from EDX analysis.

The relative IV response in CO_2 saturated and inert environment showed a nominal difference in current densities. A stirrer at 300 rpm had been employed to ensure that the bubble formation did not impact the current densities. It is pertinent to mention that the exclusion of stirrer can drastically change the IV response. As an example, for loading amount of 1 mg/cm^2, it was reported by Chang *et. al*. [36] that the current density for Cu_2O on carbon cloth was 6 mA/cm^2 at -1.7 V vs SCE and the use of stirrer had not been mentioned. However, we observed current densities at almost 11 mA/cm^2 with a stirrer at around the same potential and loading. The size of the Cu_2O particles in this study however was almost twice larger.

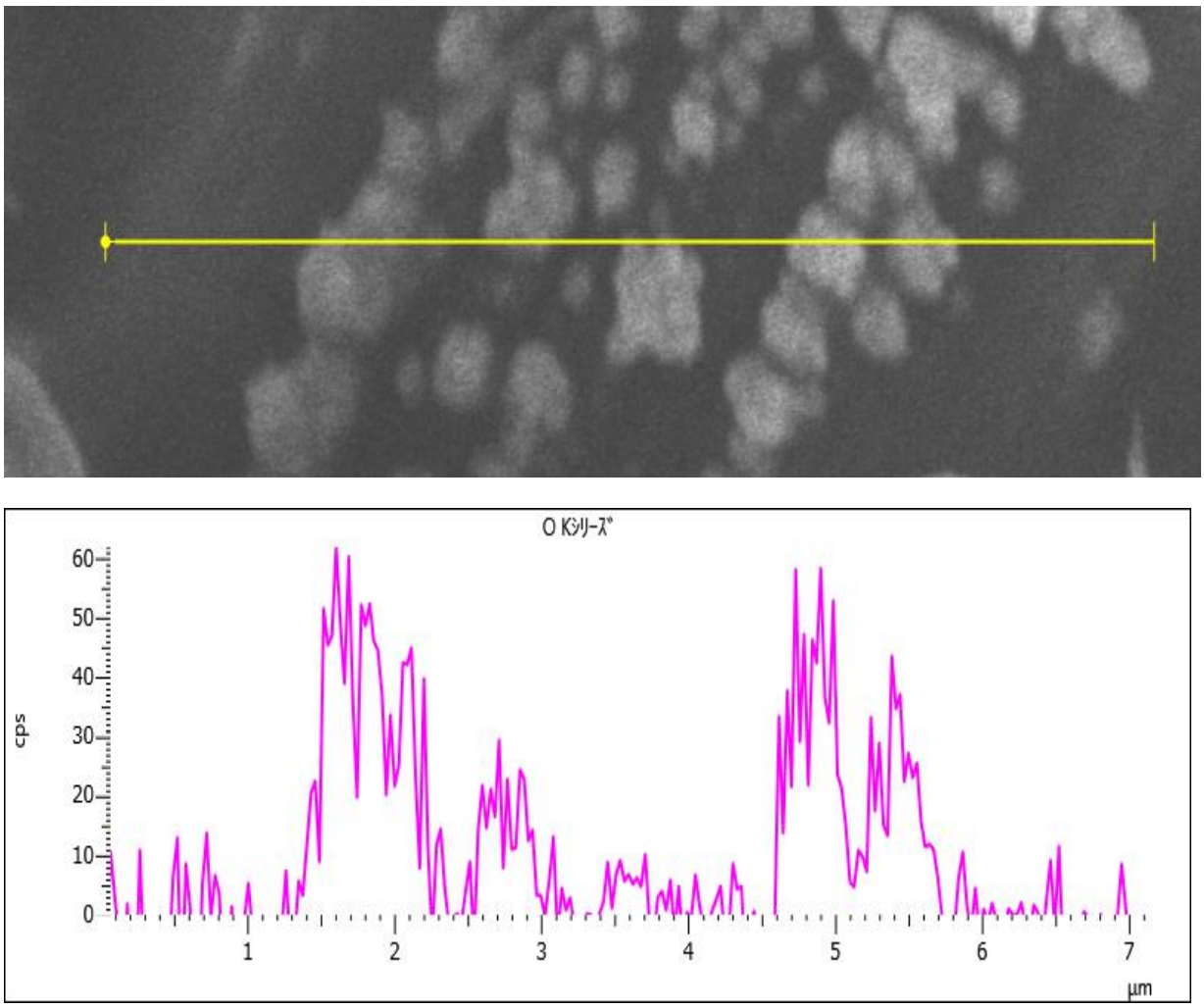

Fig. 7.8 The EDX analysis of the size distribution of Cu_2O particles

The difference in the particle concentration between electrodes employing loading of amount of 1 mg/cm^2 (left) and 2mg/cm^2 (right) can be seen below from figures 7.9 to 7.14 (obtained using Hitachi Miniscope TM-1000).

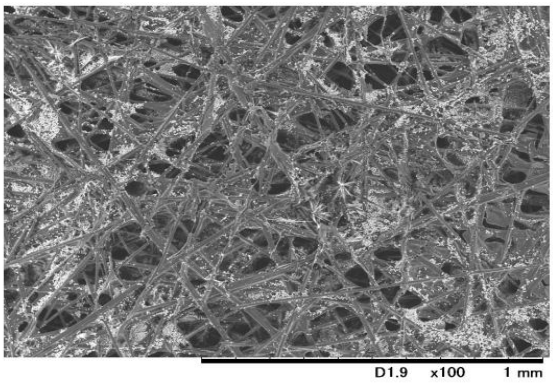

Fig. 7.9 Carbon Paper at x100 resolution

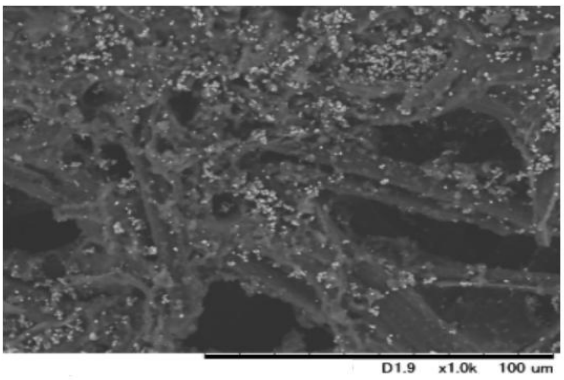

Fig. 7.10 Carbon Paper at x100 resolution

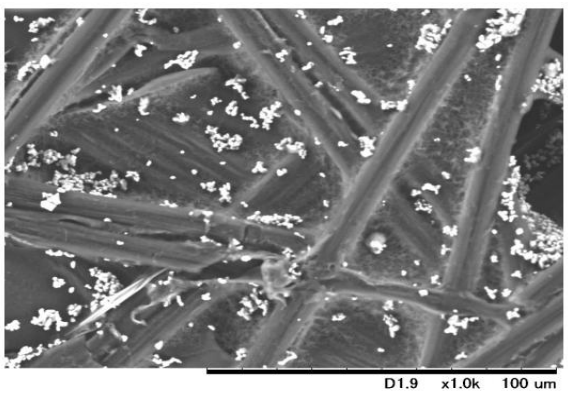

Fig/ 7.11 Carbon Paper at x100 resolution

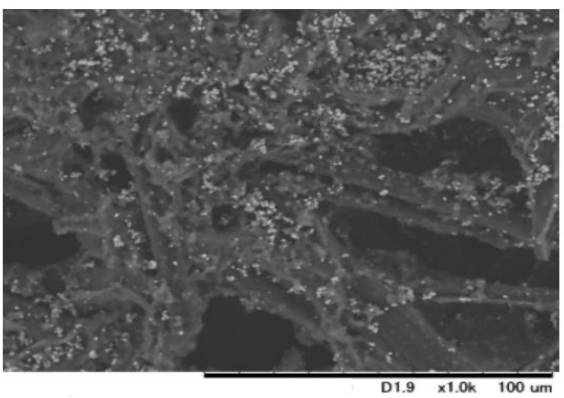

Fig. 7.12 Carbon Paper at x100 resolution

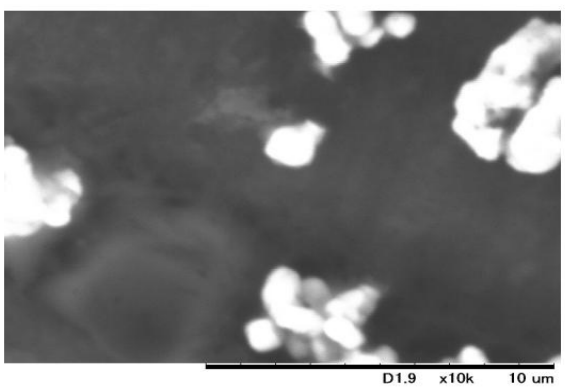

Fig. 7.13 Carbon Paper at x1000 resolution

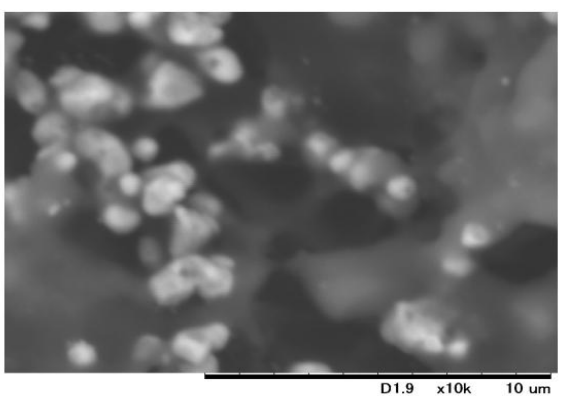

Fig. 7.14 Carbon Paper at x1000 resolution

In order to see more clearer SEM images and the individual distribution of the cuprous oxide particles with loading of 2 mg/cm^2 and also obtain the EDX elemental analysis, Hitachi SU8020 high resolution scanning electron microscope with EDX analysis was used for the characterization and is shown in figure 7.15.

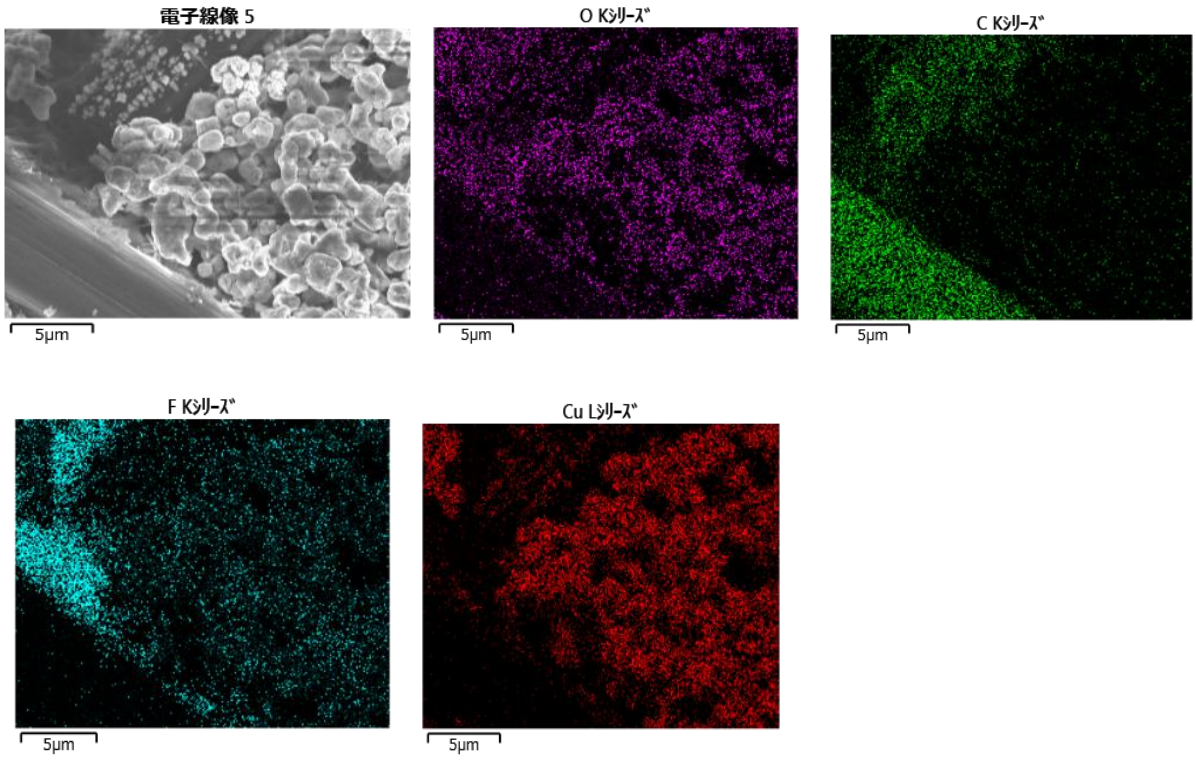

Fig. 7.15 SEM/EDX analysis of cuprous oxide loaded electrode showing the constituent elements.

7.3.1 CO_2RR experiments

The Carbon Paper (CP) was tested for the electrochemical reduction of CO_2 in order to gauge its response. Formic acid and hydrogen were evolved as a resultof CO_2RR on CP. The formic acid was produced at the onset of 1300 mV vs SHE but the faradaic efficiency was about 7%. The faradaic efficiency kept on going on a downhill reaching less than 4% from the 1600 mV and than dropping to zero. Hydrogen remained the dominant product from the CO_2RR showing that carbon paper can be a stable electrode with limited propensity for the electrochemical reduction of CO_2. The faradaic efficiency response of CP is shown below in figure 7.16. The experiments were conducted at least twice and the average FE has been recorded for each potential.

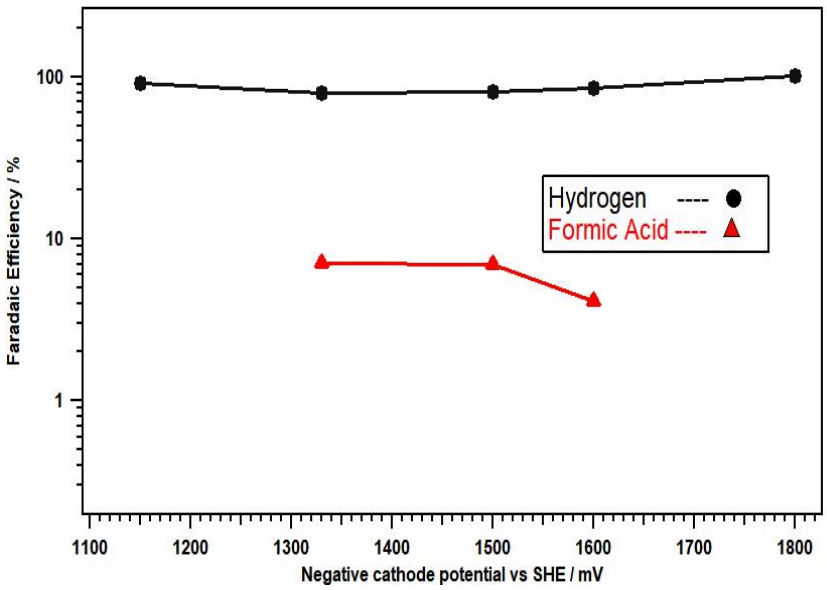

Fig. 7.16 Faradaic Efficiency against negative cathodic potential for control samples (CP without Cu_2O)

The electrochemical reduction of CO_2 using micron-sized Cu_2O particle catalysts produced formic acid as the major product as opposed to some previous studies [10, 36] where methanol was the dominant product. Ethylene and carbon monoxide were produced as the secondary products. The faradaic efficiency of these products varied with the cathodic potential and are shown in figure 7.17.

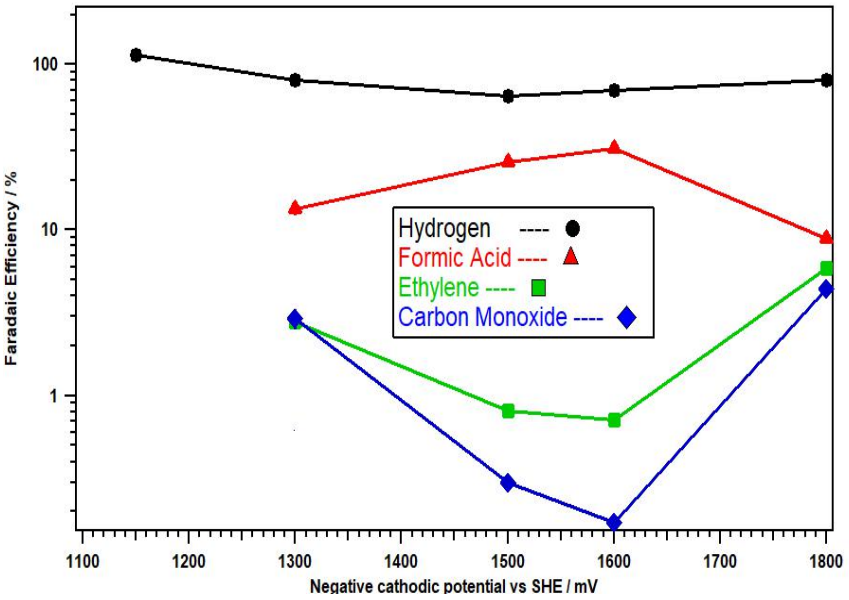

Fig. 7.17 Faradaic Efficiency (base-10 log) against negative cathodic potential for Cu_2O samples with 2 mg/cm^2 loading

A base-10 log scale was used for the y-axis in the FE vs Potential graphs so as to better represent the trend between FE and cathodic potential. The experiments were conducted for 35 minutes. The ethylene presence was detected from the onset of CO_2 reduction at -1300 mV *vs* SHE. The FE for ethylene was 2.8% at the onset potential, which decreased to almost 0.7% at -1600 mV *vs* SHE, and then went up again to 5.9 % at a potential of 1800 mV *vs* SHE. The faradaic efficiency for CO followed a similar trend to C_2H_4, whereby its FE decreased at potentials of -1500 mV and -1600 mV but increased to almost 5.1% at -1800 mV. The formic acid however showed an opposite trend with a FE of 13.3% at -1300 mV, which reached upto 31% at -1600 mV and then decreased to about 8.8% at -1800 mV.

This inverse trend between faradaic efficiency of formic acid and C_2H_4, CO can possibly reflect different origins of CO_2RR. Control electrodes (carbon paper) generated formic acid during CO_2RR (figure 7.16) but the maximum faradaic efficiency was only 7% at -1300 mV *vs* SHE. However, the faradaic efficiency of formic acid was significantly increased when cuprous oxide particles were employed. It can be observed that at potentials of -1500 and -1600 mV *vs* SHE, the Cu_2O catalysts aid in enhancing the faradaic yields of the primary product (formic acid) being produced on the CP substrate during CO_2RR. For potentials outside this range, Cu-based catalyst played a more active role in the formation of CO and C_2H_4. It has been reported that CO formation on Cu_2O aids in suppressing HER [37] and increases conversion of hydrocarbon products since CO acts an as intermediate specie [38] for higher order carbon products. This explains why CO and C_2H_4 had followed a similar trend where increase of CO lead to increase of C_2H_4 while decrease of CO meant lower FE for C_2H_4. Interestingly, methane was not detected in any of the experiments, which corresponds to no noticeable methanol presence since both are chemically similar.

For the experiments conducted at potentials more negative than -1800 mV *vs* SHE, the current density increased to more than 20 mA/cm^2, causing slight color degradation of the electrodes, which may be a reflection of Cu_2O erosion. The increase of nafion binder ratio during the electrode preparation can possibly help to maintain electrode stability [39]. Electrodes with Cu_2O loading of 2 mg/cm^2 were experimented for multiple time duration of 35 min, 60 min, 90 min and 120 min at -1300 mV and -1600 mV *vs* SHE and this time dependence of the products is shown in figure 7.18 and 7.19, respectively. A subtle trend could be observed for both potentials: a gradual decrease of FE for formic acid was observed while C_2H_4 especially at -1300mV *vs* SHE slightly increased with

time. This can originate from the thermodynamic reducibility of the Cu_2O phase under CO_2 reduction conditions, which has been a major concern for attempts to use the Cu oxidation state to control selectivity for CO_2 reaction products [40]. The pourbaix diagram for Cu in aqueous solutions [41] indicates that Cu^0 is more stable at negative potentials *vs* SHE at neutral pH. From the results presented here, it can be speculated that at least a partial reduction of the Cu_2O component has been taking place with time which impacts the product selectivity during CO_2RR.

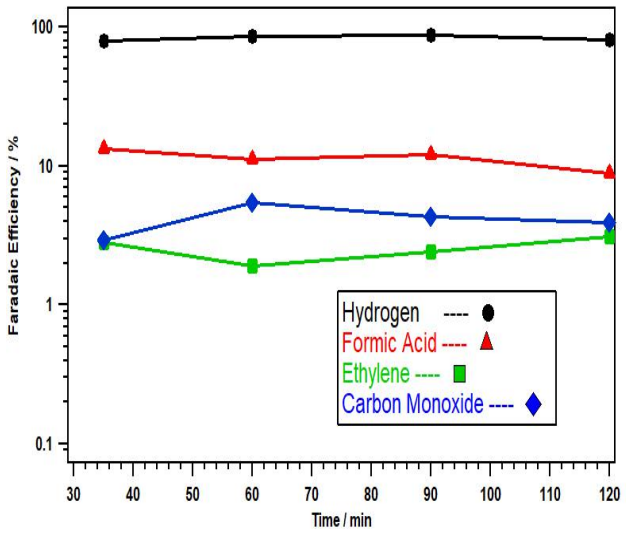

Fig. 7.18 Time dependent faradaic efficiency for Cu_2O samples at -1300mV

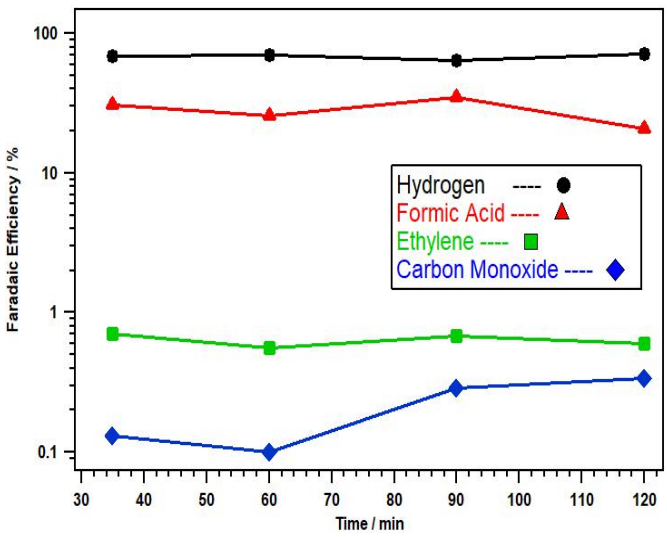

Fig. 7.19 Time dependent faradaic efficiency for Cu_2O samples at -1600mV

In order to analyze the impact of loading amount of catalyst on the trend originating from the Cu_2O/CP, 1mg/cm^2 of Cu_2O was tested for CO_2RR and the faradaic results are shown in figure 7.20. Formic acid continued to remain the dominant product from CO_2RR and the maximum faradaic yield of 13% was seen at -1600 mV. This observation corresponded to the result from samples with 2mg/cm^2 loading. However the faradaic efficiency was less than half. In comparison with the control electrode CP, FE of formic acid was still almost twice greater. Lower loaded catalysts show evidence that product selectivity is affected by the competing H_2 reaction on the carbon fiber support and the sizable diminishing of active sites is suggested to decrease the overall activity for CO_2RR.

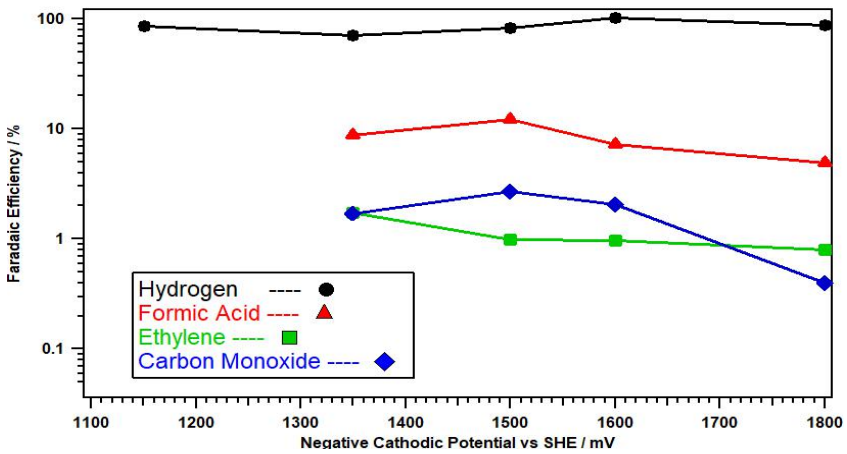

Fig. 7.20 Faradaic Efficiency (base-10 log) against negative cathodic potential for Cu_2O samples with 1 mg/cm^2 loading

To gauge the response for longer time duration, samples with loading of 1 mg/cm^2 were analyzed for experimental duration of of 35 min, 60 min, 90 min and 120 min at -1300 mV vs SHE. This time dependence of the products has been reproduced in figure 7.21. The hydrogen and formic acid production was steadily stable with time. Ethylene and CO was produced but the production of CO seemed to drop with time. This could be explained in terms of the Cu reduction mentioned beforehand. Since it is our contention that Cu reduction plays a role in the production of C2 product, we believe that the CO produced was acting as a feedstock for the C_2H_4 production. Therefore essentially it is our hypothesis that Cu^{2+} reduced with time. The reduced Cu used the CO as a feedstock for C_2H_4. Since the FE of the C_2H_4 and CO was only around 1-3%, the trend is very subtle and not clearly visible.

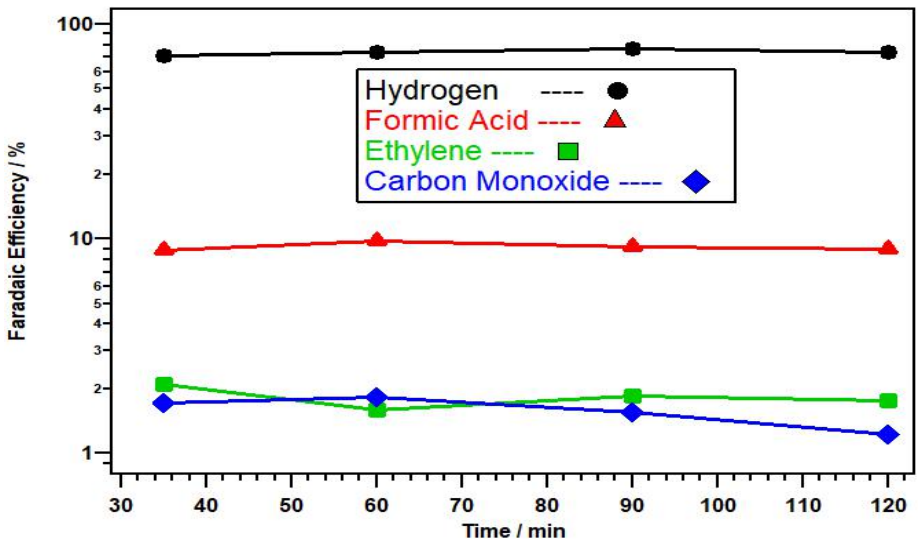

Fig. 7.21 Faradaic Efficiency (base-10 log) against negative cathodic potential for Cu_2O samples with 1 mg/cm^2 loading

7.3.2 Origins of CO_2 reduction

Recently in 2018, L. Mandal *et. al.* [42] did a comprehensive study on the origins of CO_2RR in Cu_2O in three structures: nanoneedles, nanocrystals and nanoparticles. They analyzed reaction free energy profiles of CO_2RR at the density functional theory (DFT) level, using the Vienna ab initio simulation package. The calculated binding free energies of intermediates on $Cu_2O(111)$, and $Cu_2O(200)$ surfaces [in eV] are given in figure 7.22. They suggested that proton reduction to form surface-bound hydrogen is energetically more favorable than CO_2R pathways on Cu_2O (111). But the reduction of the second proton to release H_2 requires an energy increase of 0.66 eV. Also the reduction of a subsurface O atom to form surface-bound OH on Cu_2O (111) is energetically very favorable, but the further reduction of surface-bound OH to H_2O is slightly energy uphill. If the potential bias becomes more negative than −0.07 V, it becomes feasible to have reduction of Cu_2O to reduce surface-bound hydroxyl groups to H_2O. At more negative bias potential (<−0.78 V), the reduction of surface-bound CO is also possible, leading to hydrocarbon products. Similarly for Cu_2O (200) peak,the reduction of subsurface O atoms to form surface-bound hydroxyl groups, and ultimately H_2O, is more favorable.

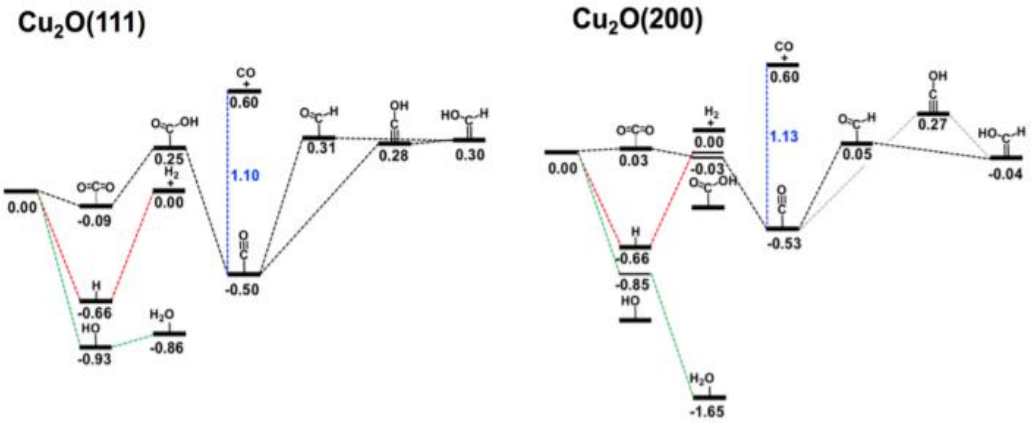

Fig. 7.22 DFT-optimized geometries and relative free energies of intermediates of HER (red dash line), CO2RR (black dash line), and Cu_2OR (green dash line) on Cu_2O (111), and Cu_2O (200) [42]

Mandal *et. al.* therefore concluded that the reduction of Cu_2O on Cu_2O (111) and (200) is more favorable than the HER or CO_2RR and so the reduction of Cu_2O to Cu is expected to proceed first. In our XRD analysis after CO_2RR (figure 7.23), Cu_2O (111) and (200) peaks were clearly present and Cu presence was not detected. The reason for this observation was also answered in [42] where they showed an in-situ raman spectroscopy of the reduction of CO_2 on Cu_2O (the results of which are reproduced in figure 7.21). The black curve in figure 7.21, shows the spectra taken before constant current is applied, red curve is after 400s of electrochemical CO_2RR and blue curve represents the spectra at open circuit potential immediately after the experiment stopped. It can be seen that Cu_2O peaks identified at 528 and 623 cm^{-1}, are not present during the CO_2RR experiment but reappear immediately after the stopping the experiment. This indicates that copper catalyst under open circuit condition can easily undergo surface re-oxidation within seconds.

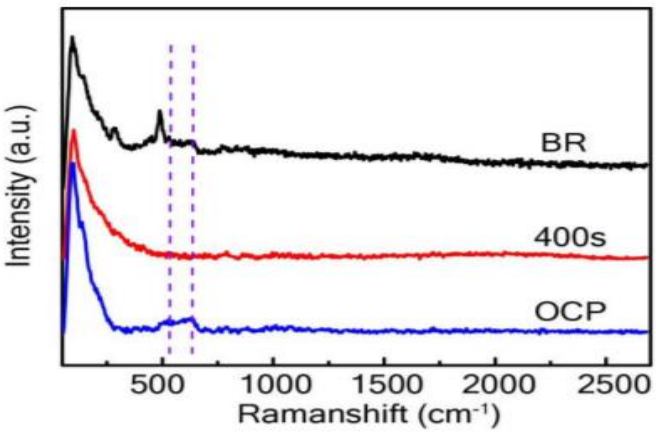

Fig. 7.23 In-situ Raman spectra of Cu2O nanocrystals at -1 mA/cm^2 for 800 s [42].

7.3.3 EDX and XRD characterization

Energy Dispersive X-ray (EDX) spectroscopy was used to analyze the elemental composition of cuprous oxide electrode for loading amount of 2 mg/cm^2 and is shown in table 7.1. The Cu/O ratio was approximately 1.5 due to the higher presence of Cu in the Cu_2O structure. The possibility of substrate oxidization and margin of error in EDX measurement may be the reason for the deviation from the expected Cu/O ratio of 2. Carbon was detected from the substrate while potassium presence was a result of the reduction of K+ ions [11] present in the electrolyte. Fluorine was detected due to the hydrophobic polymers on CP that assist in suppressing the CO_2RR activity on CP.

Table 7.1 Elemental analysis of Cu_2O/CP electrode after CO_2RR experiments

Element	Atomic %
Copper	11.44
Oxygen	7.50
Carbon	69.58
Fluorine	10.83
Potassium	0.64
	100.00

The XRD data of our electrode in figure 7.24 shows only Cu_2O and carbon peaks before and after CO_2RR. The peak positions are in good agreement with those for Cu_2O powder obtained from the International Center of Diffraction Data card (JCPDS file no. 05-0667) confirming the formation of a single cubic phase Cu_2O with a cuprite structure, [43] where the oxygen atoms form a body centred cubic lattice while copper atoms form a face-centred cubic lattice such that every copper atom is half-way between two oxygen atoms. The peaks with 2θ values of 29.6, 36.5, 42.4, 61.5, 73.6 and 77.6 correspond to the crystal planes of 110, 111, 200, 220, 311 and 222 of crystalline Cu_2O, respectively. Peaks originating from the substrate were observed at 2θ value of 26.5 and 54.6 [44]. No characteristic peaks of Cu metal or CuO were observed in the XRD patterns, indicating that phase-pure cuprous oxide existed on the sample.

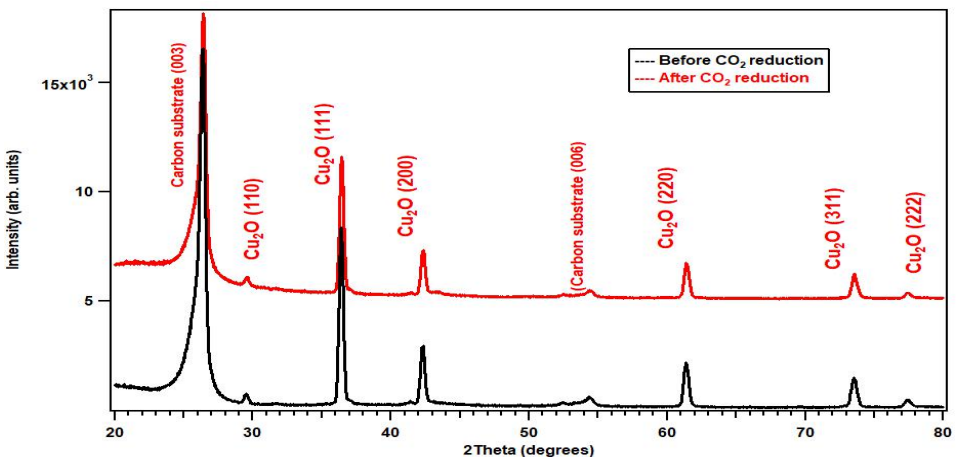

Fig. 7.24 Cu_2O XRD peaks before (black) and after (red) CO_2RR.

7.3.4 Reduction pathways

The proposed pathway for C_2H_4 reduction from CO_2 is shown in figure 7.25. The production of formic acid during the CO_2RR experiments is suggested to originate from the difference in binding energy for the intermediate species. CO production occurs primarily through a key carbon-bound intermediate, COOH, while formic production proceeds through a key oxygen-bound intermediate, OCHO [45]. Since formic acid was also observed from experiments involving control electrodes (CP), it reflects that the

surface of carbon paper has a propensity towards OCHO and the presence of Cu-based catalysts assist in enhancing the faradaic yields of formic acid. The modification of reaction energy for formic acid generation due to Cu has been previously reported in DFT studies of Peterson *et. al.* [46] and Shin *et. al.* [47]. The selectivity towards C_2H_4 instead of CH_4 is also an important observation. Hori *et. al*. [49] had previously compared a series of different orientations of single crystal Cu and had shown that C_2H_4 formation was strongest on Cu (711) surfaces while Baturina *et al.* [50] and Riske *et. al.* [51] had also suggested that C2 products are produced during CO_2RR on low-coordination sites and low-index facets (edges, defects, and corners) due to their similarity to Cu (311), Cu (511), and Cu (711). We believe that the partial reduction of Cu_2O particles and the oxygen vacancies has an impact on the grain boundaries [31-32] and allow formation of low coordination surface sites which cause preferential production of C_2H_4 via formation of C_2O_2 intermediate adsorbed specie. A factor in the performance of Cu_2O during CO_2 electrolysis is believed to originate from the hydroxide ions (OH^-) that are generated during CO_2RR at the electrode surface. The rise of local pH close to the surface layer has been reported to limit the reduction of Cu_2O to metallic Cu at the electrolyte interface, which assists in the continuous generation of C_2H_4 [52].

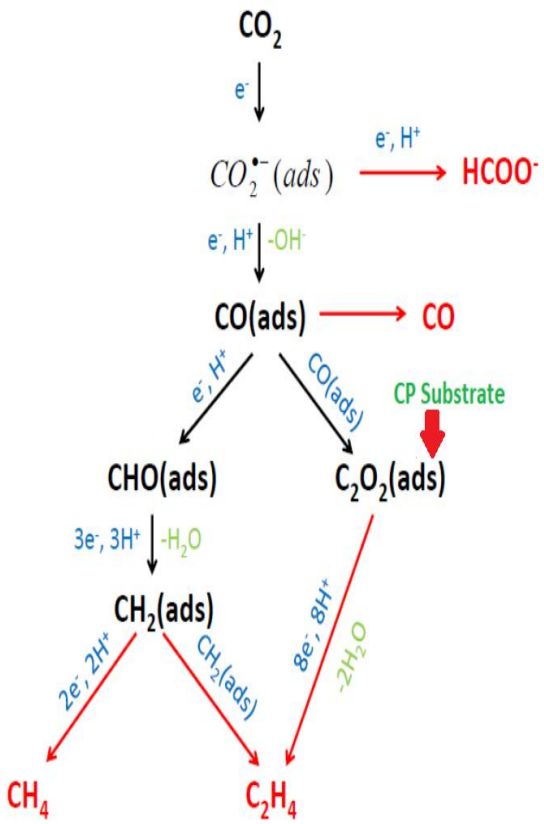

Fig. 7.25 Proposed reduction pathway

7.4 Cobolt Oxide (Co_3O_4)

As discussed in the second chapter, metal electrodes have shown to be very active for CO_2 electroreduction but are usually prone to limited availability and suffer from very high prices as well as rapid loss of CO_2 reduction activity [53]. These issues cause hindrances to commercial viability and thus to address such issues, several naturally abundant and chemically stable transition-metal oxides have been investigated. [54] Among these materials, the spinel-type oxide of Co_3O_4 has been one of the most competitive candidates for electrocatalytic CO_2 reduction. Cobolt oxide is not just environmental friendly but have a low cost and has abundance in reserves. The structure of Co_3O_4 is a normal spinel structure with Co^{2+} ions in tetrahedral interstices and Co^{3+} ions in octahedral interstices. This interesting and strange crystal structure allows it to have high environmental stability [55]. Despite the advantages, Co_3O_4 has not generally shown high catalytic CO_2 reduction performance [56]. This has been primarily ascribed to the very low amount of active sites and poor electrical conductivity. Therefore, it is important to have a material with abundant active sites and high electrical conductivity which can greatly promote the electrocatalytic CO_2 reduction performances. Previously, a DFT model of transition-metal-oxide-based atomic layers had showed abundance of active sites and high electrical conductivity [57].
One study [58] had reported fabricating ultra-thin Co_3O_4 layers and had suggested that having such atomic-level thicknesses meant that the significant portion of Co atoms could be exposed on the surface which would allow those surface atoms to have lower coordination number compared with interior atoms. This was confirmed in the X-ray absorption fine structure spectroscopy. It was also shown in another report [59] that low-coordinated surface metal cations of transition-metal oxides act as the main adsorption sites for CO_2 in the reduction processes. Formic acid with upto 80% FE was obtained as a result of the CO_2RR experiments in the subsequent study based on the DFT calculations [60].

It has also been shown by Density Functional Theory (DFT) calculations that ultra-thin Co_3O_4 have large density of states at the conduction band edges as compared to their bulk counterparts [57] and the results have been reproduced in figure 7.26. Also, the charge density around the conduction band edge in thin layers of cobalt oxide increase noticeably and are more dispersive than in the bulk form. This is beneficial for fast carrier transport which is required for the electrocatalysis of CO_2. Additionally, thin layers have distortion in structures which can lower the surface energy thereby increasing

stability of the oxide structures. Cobalt oxide ultra-thin layers can also have lower corrosion rates and longer durability [58].

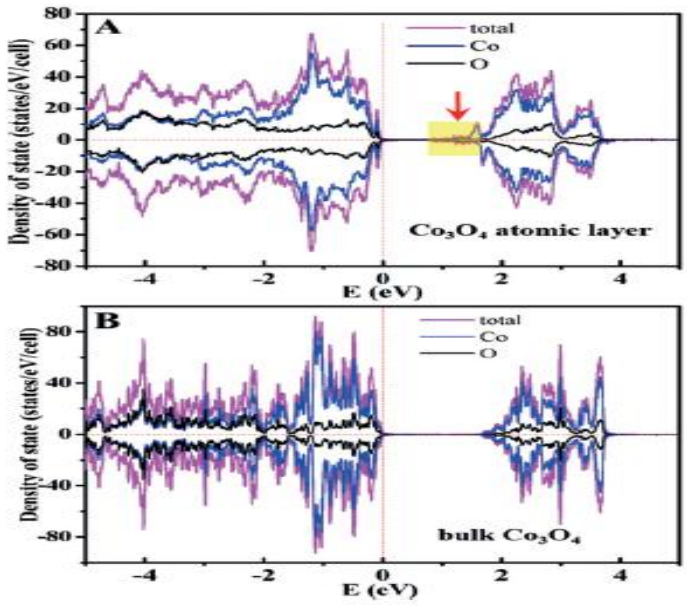

Fig. 7.26 DOS in thin film (A) and bulk (B) of Co_3O_4 [57]

Since the ultra-thin layers have a large number of unsaturated surface atoms, they serve as the active sites for CO_2 reduction into valuable end-products. In a previous research [58], two thicknesses of 1.72 nm and 3.51 nm, were used along with bulk Co_3O_4. The bulk oxide layer had shown poor electrocatalytic properties for the entire potential range while the thin layers had shown increased CO_2 reduction.

The 1.72 nm thick Co_3O_4 layers had shown 0.68 mA/cm^2 of current density at 0.88V versus the saturated calomel electrode (SCE) while the 3.51 nm thick layer had registered a current density 15 times smaller. The 1.72 nm thick Co_3O_4 layers exhibited a maximum faradaic efficiency of 64.3% at 0.88 V vs. SCE, which was higher than the 51.2 % for 3.51 nm thick Co_3O_4 layers and 18.5% for the bulk counterpart.

It is for this reason that we decided to attempt a particle-based electrode. It was our contention that using the particles, instead of Co_3O_4 thin films, could further increase the conductivity because of increase in DOS near the conduction (surface) edges. Since thinner layers show lower coordination sites and more density of states compared to bulk, we speculated that it would be interesting to test particle-based electrodes and see the comparative differences. Such an electrode would also offer a different surface area to

volume ratio to the previous studies [58, 60] and may result in more enhanced performance during electrochemical reduction.

In order to check this hypothesis, we employed the same method as used for the fabrication of Cu_2O electrodes.The electrodes were prepared by affixing a copper wire to the CP substrate. A solution was prepared with Ethanol as the solvent and nafion solution as the adhesive material along with the Co_3O_4 particles in the ratio 30:5:1, respectively. A 50 µl solution was then drop casted onto 1 cm^2 of carbon paper, which acted as a substrate. Figure 7.27 shows the ink and the difference between control and Co_3O_4 electrodes.

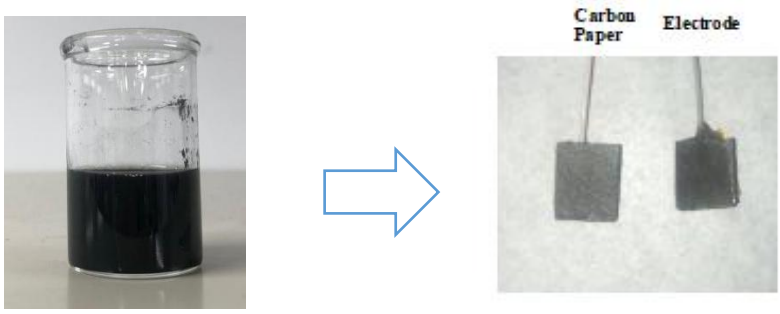

Fig. 7.27 Preparation of the Co_3O_4 electrode; Ink (left) and electrode vs CP comparison (right)

The response from the electrochemical experiments is shown in figure 7.28. The electrochemical reduction started from the onset potentials and reflected that the particle electrode was showing activity and reasonable current density. As the cathodic potential became more negative and reached -1000 mV vs SHE, acetic acid and formic acid was produced with FE as high as 21 % and 8 %, respectively. The trend continued up till 1300 mV when acetic acid dropped down to zero and the formic acid became negligible as well while hydrogen FE started to exceed 80%.

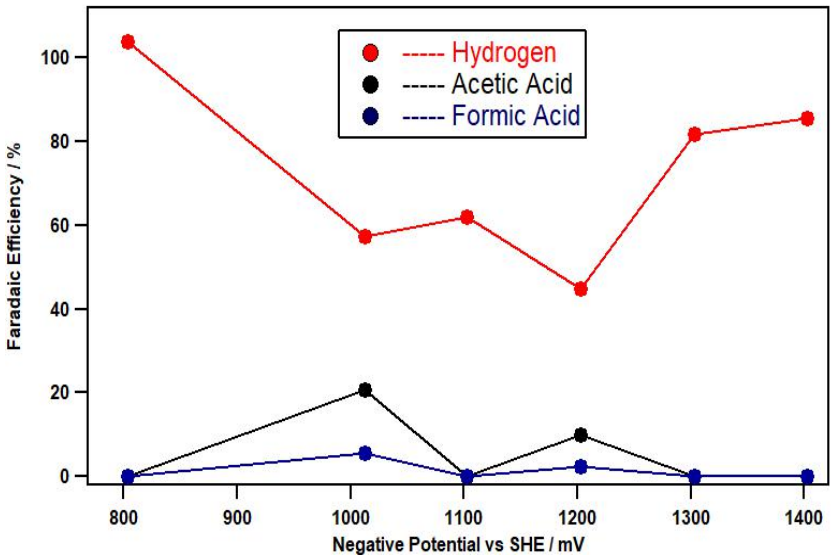

Fig. 7.28 FE trend vs applied potential for Co_3O_4

In order to see the practical viability of the samples on a larger time frame, experiments were conducted with 4 cm^2 electrode area. Initial electrode size was 1 cm^2 while the bigger electrode area had 4 times the area. The duration of the experiment was also increased from 45 minutes to 3 to 4 hours. The passage of more coulombs in each experiment would allow us to gauge the production of acetic acid with time and hence a trend line would be obtained for those extended periods. The experiments were also tested at different pH in order to observe the impact of changing H^+ concentration.
The first experiment to obtain a trend line for acetic acid production was conducted in an electrolyte molarity of 0.1M for $KHCO_3$ electrolyte for a total duration of 2 hours. The value of formic acid and acetic acid in ppm is shown in table 7.2. As can be seen below, there was no acetic acid observed.

Table 7.2 FE for the sample at different potentials along with current density

	ppm	
Coulombs Transferred	**Acetic Acid**	**Formic Acid**
36.8	0.9	0
71.6	1.6	0
122.9	2.1	0

It was then decided to change the molarity of the electrolyte in order to observe its impact on acetic acid production. CO_2 reduction can be achieved in the electrochemical reduction of $KHCO_3$ even without CO_2 bubbling, however, the production and faradaic efficiencies are very low. If assuming that HCO^{3-} is the active species, high $KHCO_3$ concentration should lead to high CO_2 reduction. The absolutely certain part was that the increase in HCO^{3-} species should increase the current. Experiments showed that the current density did increase from the 5 mA/cm^2 registered in the 0.1 M electrolyte to 11 mA/ cm^2 in 0.5 M. However the electrochemical reduction of CO_2 was still not taking place which meant that either there was a problem with the analysis system or that the mechanism of reduction was different than previously perceived.

Table 7.3 FE for the sample at different potentials along with coulombs transferred

	ppm	
Coulombs Transferred	**Formic Acid**	**Acetic Acid**
63.8	0.9	0
172.9	4.0	1.8
301.3	3.0	0
341.7	3.1	0
370	3.4	0

If the mechanism of the CO_2 reduction was due to the reduction of Co^{2+} and Co^{3+} ions to Co^0 which is the pure metal phase, then the dense packing of catalysts due to the increase

in the loading amount should increase the concentration of the products produced from CO_2RR. The standard redox potential between Co^0/Co^{2+} is -0.28 V which is more negative than the redox potentials for reduction of CO_2 into different products (generally between +0.2 V to -0.2 V vs SHE). Therefore if the reduction mechanism is driven by redox reactions at the surface, than the loading amount change should make an impact. So therefore in the next attempt, the loading amount of Co_3O_4 catalyst was increased from 2 mg/cm^2 to 4 mg/cm^2. However as can be seen in table 7.4, the result remained similar and thus we concluded that the mechanism was not driven only by the surface redox reactions.

Table 7.4 FE for the sample at different potentials along with coulombs transferred

	ppm	
Coulombs Transferred	**Formic Acid**	**Acetic Acid**
96.5	1.1	0
287.3	3.3	0
413.4	3.5	0
493.1	3.7	0

In addition to the catalyst material, the pH and local pH are known to affect the selectivity of the reaction as was discussed in detail in section 2.4. Most of the work shown in this thesis has been investigating the effect of experimental conditions on the performance of the catalysts by changing only the the applied electrode potential. In order to fill that gap and study the effect of the pH on CO_2RR selectivity and understand the role of proton concentration on the catalytic process, we changed the pH of the electrolyte and gauged the impact. Table 7.5 shows the results for the 8-electron acetic acid production.

Table 7.5 FE for the sample at different potentials along with current density

		Acetic Acid	
Time (min)	**pH**	**ppm**	**FE (%)**
40	7	21	8.2
80	7	29	7.39
40	7	2	1.4
80	7	5	1.51
180	8.86	1.89	1
40	10	11	4.8
40	10	9	4.5
120	12.9	1.7	<1

The results continued to be elusive and reaffirmed the speculation that the reduction mechanism of CO_2 may be a result of a combination of factors. The change in oxidation state of surface Co^{2+} to Co^{3+} ions as well as general electrode stability may be the causes for inconsistent results. An in-situ analysis is required to understand the exact dynamics of such redox reactions. However, we contend that the combination of redox potential reactions between the Co^0/Co^{2+} (which occurs at -0.28 V vs SHE) and Co^{2+}/Co^{3+} redox couple reaction (which occurs at more positive potential) results in inconsistency for CO_2 reduction. Furthermore, the molar amount of available electrons through Co^0/Co^{2+} and Co^{2+}/Co^{3+} redox couples would be limited and dependent on the prior experimental conditions of the electrode. Therefore it is our conclusion that conventional electron transfer models may not had played the main role in CO_2RR and it was actually the redox couple reactions which was the source for CO_2 reduction into acetic and formic acid.

7.5 Summary

The first part of study was related to the electrochemical reduction of CO_2 on micron-sized particles of Cu_2O supported on carbon paper substrate. The loading amount of catalysts was 1 mg/cm^2 and 2 mg/cm^2 and the size of the catalyst particles was measured to be 2.5 to 5.5 micron.

1. The CO_2RR experiments showed that formic acid was the major product along with C_2H_4 and CO.
2. The use of these catalysts with relatively bigger size on a hydrophobic carbon paper substrate helped to narrow the selectivity of the products in comparison to copper metal, where more number of products are observed.
3. The carbon paper substrate also produced formic acid during CO_2RR experiments which reflected that the substrate has a higher propensity for bidentate (OCHO) adsorption.
4. The use of micron-sized cuprous oxide catalysts demonstrates extremely effective selectivity towards C2 ethylene as compared to other higher-order carbon products.
5. The use of particles with smaller area to volume ratio was able to allow a Cu_2O structure, wherein the reduced Cu^0 with oxygen vacant sites had an impact on the grain boundaries and allowed selective production of C_2H_4 from among the possible multi-carbon products.
6. Formic acid production is believed to have originated from the CP substrate, while the presence of Cu-based catalysts caused a potential dependent enhancement of its faradaic efficiency.
7. The production of formic acid as liquid product is also more important due to its higher relative profitability index; a term defined by the ratio of economic value to the required amount of electrical energy per mole of products.
8. Cuprous oxide catalysts suffered from aggregation and further increasing the loading amount from 2 mg/cm^2 does not significantly change the product distributions.
9. Since energy level calculations have shown that the reduction of the bulk phase is more likely than surface reduction of Cu_2O grains, it was our speculation that the surface layer may exist as a hybrid structure made up of oxidised Cu at the interface with H_2O molecules, along with a neighboring Cu^0 component beneath.

A similar method was followed for testing the electrochemical reduction of CO_2 using Cobalt oxide with loading amounts of 2 mg/cm^2 to 4 mg/cm^2. The theoretical calculations had shown thinner films of the oxide can have enhanced conductivity and density of states near the conduction (surface) edge.

10. Acetic acid and formic acid were inconsistently produced from the electrochemical reduction. Acetic acid has never previously been reported for Co_3O_4 catalyst.
11. The faradaic efficiency remained inconsistent when the electrode size was increased from 1 cm^2 to 4 cm^2.
12. The inconsistency in the results for Co_3O_4 catalysts reflect that the mechanism of reduction process is not determined by the surface area alone.
13. Co_3O_4 particles significantly enhanced the current density as compared to carbon paper or Cu-based catalysts and this was some indication of CO_2RR activity. However it is our contention that the role of Co_3O_4 is determined by a combination of factors and that the surface redox reactions of the surface Co ions act as reducing agents for CO_2.

Author's note: Work in this chapter has been accepted and is going through publication process in the Asian Journal of Nanoscience & Materials.

7.6 References:

1. Zhang W, Hu Y. , Ma LB, Zhu GY, Wang Y, Xue X, Chen P.R., Yang S.Y., Jin Z, P, *Adv. Sci.* 2018, **5**, 1700275
2. Chen, K., D. Xue D., *International Journal of nanotechnology* **10**, 4-12.
3. Meyer, B.K., A. Polity, D. Reppin, M. Becker, P. Hering, B. Kramm, P.J. Klar, T. Sander, Reindl C., Heiliger C., Heinemann M., Muller C., Ronning C., *Semiconductors and Semimetals* 2013*,* **88**, 201-226.
4. Zoolfakar A.S., R.A. Rani, A.J. Morfa, O'Mullane A., Kalantar-zadeh K., *Journal of Materials Chemistry C* 2014, **2**, 5247–5270.
5. Filipic, G. and U. Cvelbar. 2012. "Copper Oxide Nanowires: A Review of Growth." *Nanotechnology* **23,** 1-16.
6. Dang T., Le, T, Blanc E.F, Dang M., *Adv. Nat. Sci. Nanosci. Nanotechnol.,* 2011, **2**, 15009-15015.
7. John W., Ayi A., Chinyere A., Providence A., Bassey I., *Advanced Journal of Chemistry-Section A,* 2019, **2**,175-180.
8. Gomaa E., Abdel H., Mahmoud M., El Kot D., *Adv. J. Chem.A*, 2019, **2**, 1-
9. Ayesha K., Audi R., Rafia Y., Ren C., *Int Nano Lett*., 2016, **6**, 21-
10. Frese K.W., J*ournal of Electrochemical Society,* 1991, **138**, 3338.
11. Le M., Ren M., Zhang Z., Sprunger P. T., Kurtz R. L., Flake J. C., *Journal of the Electrochemical Society*, 2011, **158**, 45.
12. Li C. W., Kanan M. W., *Journal of the American Chemical Society,* 2012, **134**, 7231.
13. Tang, W., A. A. Peterson, A. S. Varela, Z. P. Jovanov, L. Bech, W. J. Durand, S. Dahl, Norskov J., Chorkendorff I, *Physical Chemistry Chemical Physics* 2012, **14**, 76-81.
14. Terunuma Y, Saitoh A, Momose Y., *Journal of Electroanalytical Chemistry.* 1997, 15, **434**, 69-75.
15. Kim D., Lee S., Ocon J.D., Jeong B., Lee J.K., Lee J., *Physical Chemistry Chemical Physics.* 2015, **17**, 824-30.
16. Ren D, Deng Y., Handoko A.D., Chen C.S., Malkhandi S., Yeo B.S.. *ACS Catalysis*. 2015 Mar 31;**5**(5):2814-21.
17. Albo J, Sáez A, Solla-Gullón J, Montiel V, Irabien A. *Applied Catalysis B: Environmental*. 2015, **176**, 709-17.
18. Andrews E, Ren M, Wang F, Zhang Z, Sprunger P, Kurtz R, Flake J., *Journal of the Electrochemical Society*. 2013, **160**, H841-6.
19. Zhao Y., Wang C., Wallace G.G., *Journal of Materials Chemistry A*. 2016.
20. Sarfraz S, Garcia-Esparza AT, Jedidi A, Cavallo L, Takanabe K., *ACS Catalysis*. 2016, **6**, 2842-51.
21. Wang W., Ning H., Yang Z., Feng Z., Wang J., Wang X., Mao Q., Wu W., Zhao Q., Hu H., Song Y., Wu M., *Electrochimica Acta*, 2019, **306**, 360.
22. Tan X., Yu C., Zhao C., Huang H., Yao X., Han X., Guo W., Cui S., Huang H., Qiu J., *ACS Appl. Mater. Interfaces*, 2019, **11**, 9904.
23. Lee S., Ocon J. D., Son Y., Lee J., J. Phys. Chem. C, 2015, **119**, 4884.
24. Kim D., Lee S., Ocon J. D., Jeong B., Lee J. K., Lee J., Phys. Chem. Chem. Phys., 2015, **17**, 824.
25. Lum Y., Ager J.W., Angew. Chem. Int. Ed., 2018, **57**, 551.
26. Eilert A., Cavalca F., Roberts F.S., Osterwalder J., Liu C., Favaro M., Crumlin E.J., Ogasawara H., Friebel D., Pettersson L.G., Nilsson A., *J. Phys. Chem. Lett.* 2018, **8**, 285.
27. Meng C., Liu C., Fan S., *Electrochemistry Communications*, 2009, **11**, 186-189
28. Burdyny T., Smith W.A., Energy Environ. Sci., 2019, **12**, 1442.
29. Kas R., Kortlever R., de Wit P., Milbrat A., Luiten-Olieman M., Benes N., Koper M., Mul G., *Nature Communications*, 2016, **7**, 10748.

30. Hana X., Wang M., Linh M., Bedford N., Woehl T., Thoi S., *Electrochimica Acta*, 2019, **297**, 545.
31. Lee S., Kim D., Lee J., *Angew Chem Int Ed Engl*, 2015, **54**, 14701.
32. Ren D., Ang BS-H., Yeo B.S., *ACS Catalysis*, 2016, **6**, 8239.
33. Li C.W., Ciston J., Kanan M.W., *Nature*, 2014, **508**,504.
34. Kim D., Kley C.S., Li Y., Yang P., *PNAS*, 2017, **114**, 10560.
35. Ning H., Mao Q., Wang W, Yang Z., Wang X., Zhao Q., Song Y., Wu M., *Journal of Alloys and Compounds*, 2019, **785**, 7.
36. Chang, T, Liang R, Wu, P, Chen, J.Y and Hsieh, Y.C., *Material Letters*, 2009, **63**, 1001
37. Hori Y., Murata A., Takahashi R., Suzuki S., *Chem. Lett*., 1987, **16**, 1665.
38. Hori Y., Murata A., Takahashi R., *J. Chem. Soc., Faraday Trans*., 1989, **85**, 2309.
39. Bugayonga J., Griffin G.L. *ECS Trans.,* 2013, **588**, 81.
40. Li C.W., Ciston J., Kanan M.W., *Nature*, 2014, **508**, 504.
41. Wanatabe M., Shibata M., Kato A., Azuma M., Sakata T., *J. Electrochem. Soc.*, 1991, **138**, 3382.
42. Mandal L., Yang K.R., Motapothulav M.R,. Ren D., Lobaccaro P., Patra A., Sherburne M., Batista V.S., Yeo B.S., Ager J.W., Martin J., Venkatesan T. *ACS Appl. Mater. Interfaces*, 2018, **10**, 8574.
43. Kooti M., Matouri L., *Transaction F: Nanotechnology*, 2010, **17**, 73.
44. Zhang X., Lu X., Shen Y., Han J., Yuan L., Gong L., Xu Z., Bai X., Wei M., Tong Y., Gao Y., Chen J., Zhou J., Wang L.Z., *Chem. Commun*., 2011, **47**, 5804.
45. Jeremy T., Chuan S., Etosha R., Toru H., David N., Kendra P., Christopher H., Nørskov J., Jaramillo T., ACS Catal., 2017, **7**, 4822.
46. Peterson A. A., Abild-Pedersen F., StudtF., Rossmeisl J., Nørskov J,, *Energy Environ. Sci*., 2010, **3**, 1311.
47. Shin H. S., Song J. Y., Jiang Y., *Mater. Lett.*, 2009, **63**, 397.
48. Meenesh R., Singha L., Clarka, B., Bella A., *PNAS*, 2015, **112**, 6111.
49. Hori Y., Takahashi I., Koga O, Hoshi N., *Journal of Physical Chemistry*, 2002, **106**, 15.
50. Baturina O., Lu Q., Padilla M., Le X., Li W., Serov A., Artyushkova K., Atanassov P., Xu F., Epshteyn A., Brintlinger T., Schuette M., Collins G., *ACS Catal.*, 2014, **4**, 3682.
51. Reske R., Mistry H., Behafarid F., Cuenya B.R., Strasser P., *J. Am. Chem. Soc.*, 2014, **136**, 6978.
52. Ko C., Lee W., *Surf. Interface Anal.*, 2010, **42**, 1128.
53. B. Jermann, J. Augustynski, Long-term activation of the copper cathode in the course of CO2 reduction, *Electrochimica Acta*, 1994, **39**, 1891-1896.
54. Da-Ming Feng, Yun-Pei Zhu, Ping Chen and Tian-Yi Ma, *Catalysts* 2017, **7**, 373
55. Y. F. Sun, S. Gao, F. C. Lei, J. W. Liu, L. Liang, Y. Xie, *Chem. Sci.* 2014, **5**, 3976–3982;
56. X. F. Huang, T. C. Cao, M. C. Liu, G. H. Zhao, *J. Phys. Chem. C* 2013, **117**, 26432–26440
57. Y. F. Sun, Q. H. Liu, S. Gao, H. Cheng, F. C. Lei, Z. H. Sun, Y. Jiang, H. B. Su, S. Q. Wei, Y. Xie, *Nat. Commun*. 2013, **4**, 2899
58. S. Gao, X. Jiao, Z. Sun, W. Zhang, Y. Sun, C. Wang, Q. Hu, X. Zu, F. Yang, S. Yang, L. Liang, J. Wu, and Yi Xie, *Angew. Chem. Int. Ed*. 2016, **55**, 698 –702
59. M. Chiesa, E. Giamello, *Chem. Eur. J.* 2007, **13**, 1261–1267
60. S. Gao, Y. Lin, X. Jiao, Y. Sun, Q. Lao, W. Zhang, D. Li, and Yi Xie, *Nature*. 2016, **529**, 65-69

Chapter 8

Conclusion

This dissertation has focused on the comparative study of materials for the electrochemical reduction of CO_2. The first step in this research was to realize a practical electrocatalysis system, which employed conventional metal electrodes of gold and tin in combination with concentrated photo-voltaics (CPV) and irradiation under natural sunlight. A novel MPPT circuit was used to ensure maximum power matching between the CPVs and electrochemical cells. A 4.3% solar-to-fuel efficiency with formic acid as the end-product, was achieved which is higher than the efficiency observed in plants and trees. The study confirmed the practical viability of a CO_2-reduction system and the important results are:

- Multijunction concentrated photovoltaics can be used in combination with electrochemical cells for the practical application of CO_2-reduction systems under natural conditions.
- The solar-to-fuel efficiency of about 4.3% was achieved with formic acid as the end-product and this figure is twice more than the efficiency observed in nature.

Since the faradaic efficiency in our previous study had remained low, our next focus was on the use of nanoparticle-sized metals. The exclusive deposition of metal-based nanoparticles has been gaining popularity but studies on the co-deposition of such nanoparticles have been limited. Therefore, the fifth chapter of this dissertation discusses the role of co-deposited nanoparticles of copper and gold. Gold produces CO while copper can generate multi-carbon products with CO as an intermediate. It was our contention that such a co-deposition would produce a composite reaction however the size of Au nanoparticles employed in this study did not allow the production of CO, instead favoring hydrogen evolution. Conductive glass material of FTO was used as a substrate for the first half of this study resulting in formic acid production as the dominant product while indicating that the co-deposition had lead to an increase in faradaic efficiency. Consequently, we decided to use alloy structure of In-Sn as a substrate material with co-deposition and exclusive deposition of copper and gold nanoparticles. This answered multiple questions; the impact of using an alloy electrode for formic acid generation, the changes in results as a result of co-deposition of particles and the individual role of NPs in the CO_2RR experiments. The results showed that In-Sn alloy produced formic acid with a decent faradaic efficiency but the exclusive deposition of copper nanoparticles was able to significantly improve the faradaic efficiency and production rates towards formic acid. Gold nanoparticles only favored hydrogen

generation and so the co-deposited electrode gave a mixed performance during CO_2RR experiments and thus a composite reaction did not take place. The main finding could be summed up as:

- The use of arc plasma deposited copper-based nano-sized particles can increase the faradaic efficiency as well as the production rates for the products generated from the substrate material.

The sixth chapter of this dissertation attempted to focus on the elemental sustainability for long-term commercial applications in this field and diverted attention towards new and novel electrode material. Transition-metal chalcogenides have attracted considerable interest because of their electrochemical and mechanical properties however the use of amorphous chalcogenide glasses had never been attempted. Therefore, we employed bulk germanium-indium-sulfide-based amorphous glasses for CO_2 reduction and were able to show its activity for CO_2 reduction. CO was generated as a result of CO_2RR with a faradaic efficiency of about 15% however the particle-form of the same glass material, supported on carbon paper substrate, generated formic acid as a result of electrochemical reduction of CO_2 with a faradaic efficiency of up to 26%. The use of chalcogenide glasses showed that this class of material is active towards CO_2 reduction and that a change in product selectivity is also witnessed as a result of difference in geometric phases. The result from the study can be summed up as:

- Amorphous chalcogenide sulfide glasses are active for CO_2 reduction and change in the geometric form of the material can affect the product selectivity as well as the faradaic efficiency.

Our subsequent direction was towards finding a chalcogenide-based and particle-form catalyst but from a different, more active material. Our research had found copper to be the most active towards producing carbon-intensive products while more recently, oxide-based chalcogenide catalysts have begun to gain attention due to their decent faradaic efficiency and selectivity for electrochemical reduction of CO_2. Therefore, the seventh chapter discussed the use of copper-based oxide, with a size distribution in single-digit microns, for its usability in CO_2-reduction studies. The study demonstrated selectivity towards C2 ethylene with no CH_4 presence. It was our assessment that the use

of particles with smaller area to volume ratio was able to allow a unique Cu_2O structure, wherein the reduced Cu^0 with oxygen vacant sites formed beneath the surface oxide layer. This allowed selective production of C_2H_4 from among the possible multi-carbon products. Formic acid production was also observed which is believed to have originated from the carbon paper substrate while presence of Cu-based catalysts had caused a potential dependent enhancement of its faradaic efficiency. Thus:

- Use of copper-based oxide particles in micron size can narrow the product range from CO_2RR and increase selectivity towards C2-based C_2H_4 from among the higher-order carbon products.

Figure 8.1 below sums up the study titles, results obtained and novelty along with a comparison with the past reported results for the this doctoral study.

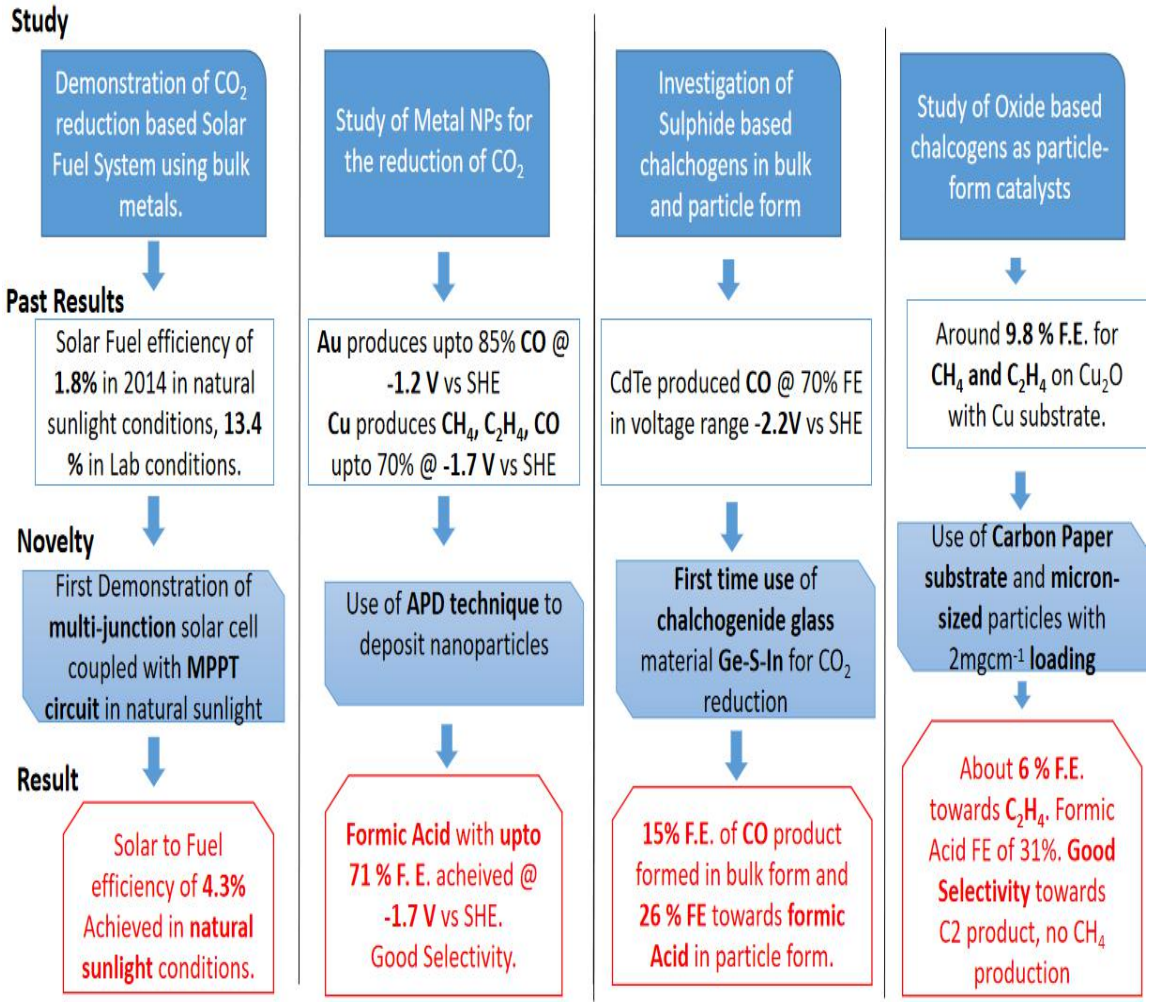

Fig 8.1 Summary of the doctoral research

The salient points from the electrochemical response with changing size of the catalyst materials have been summed up in figure 8.2. and lists the relative advantages and disadvantages in terms of CO_2 activity.

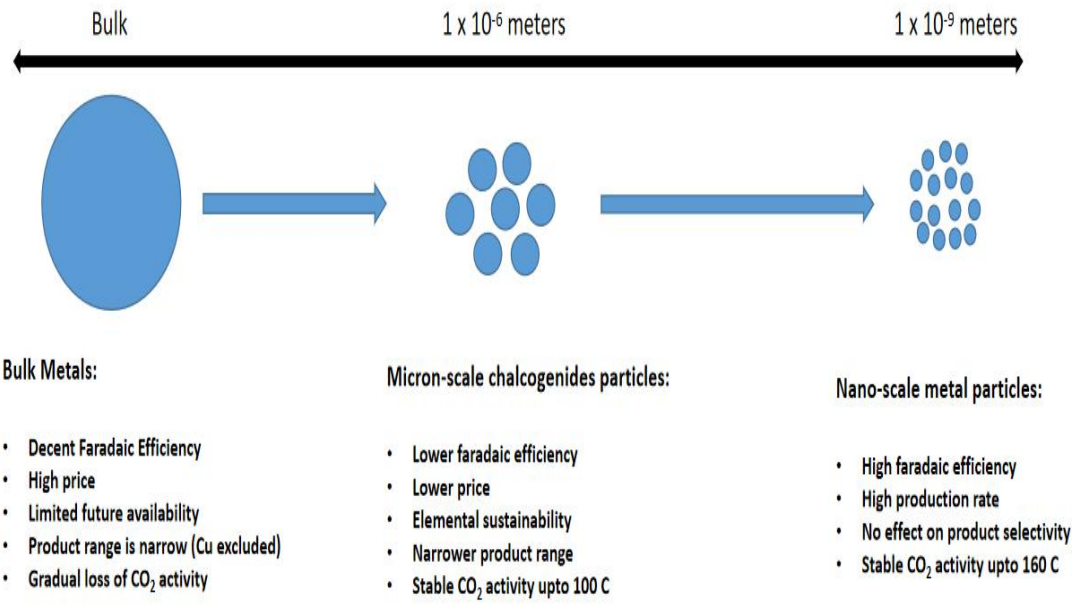

Fig. 8.2 Comparative difference in activity with change in sizes of electrode material

Based on the results presented in this thesis, it can be concluded that the choice of electrodes can be based on the following factors:

Production of carbon-intensive products:

Copper has been a staple for generating electron-intensive end-products from CO_2 reduction however, oxide form of copper can help to narrow the selectivity to C2 product at the cost of lower faradaic efficiency.

Increasing faradaic efficiency and production rate:

Cu-based arc plasma deposited metal nano-particles can increase the faradaic efficiency as well as the production rates from the substrate material at the expense of increased fabrication cost of electrodes.

Choosing a substrate with limited CO_2 activity:

Carbon Paper substrate that is coated with flourine-based hydrophobic polymers can suppress the CO_2 reduction activity which allows catalysts deposited on the substrate to be the only source towards electrochemical reduction. This results in a lower faradaic efficiency but allows to test the efficacy of various catalyst materials for CO_2 reduction.

Lowering the electrode material cost:

Chalcogenide-based glass electrodes can lower the cost of production for commercial-scale fabrication of electrode materials active for CO_2 reduction. Comparatively lower faradaic efficiency is the trade-off for fabrication of cheap electrode materials.

In conclusion, this doctoral research indicates that high efficiency and renewable energy-source of concentrated photovoltaics (CPV) can be effectively used to power the electrochemical reduction of CO_2. The faradaic efficiency however remains below par if bulk metals are employed. The use of novel electrode structures can offset this bottleneck and the comparative analysis of the various reports discussed in this thesis indicate that the Cu-based powdered catalysts used in tandem with metal alloy based substrate can allow stable electrochemical reduction within confined experimental parameters. Thus, an efficient solar-to-fuel system employing concentrated photovoltaics along with Cu-based nanoparticles deposited on In-Sn substrate can be considered as a viable solution for creating a carbon-neutral and environmentally sustainable society.

Future Prospects:

The highest faradaic efficiency achieved in this dissertation was with the use of an alloy-based electrode. Since metals have been extensively studied during the last few decades, the use of metal alloys can be an interesting avenue for future research direction since mixed-metal systems have been reported to deviate from a scaling relation of activities observed in the constituent metals. The coupling effect in alloy systems alter the binding of intermediates and change the local atomic arrangement at the active sites. Thus, such systems have the potential to achieve higher efficiency and selectivity in the

field of CO_2 electroreduction catalysis. This doctoral research also indicates that the deposition of Cu nanoparticles on mixed-metal systems can further improve the faradaic efficiency as well as production rates. Furthermore, the deposition of powdered catalysts on the electrochemically-neutral carbon paper substrate, also shows promise for further research on the exclusive role of the catalysts with limited interaction from substrate.

List of publications and conference presentations

Journal Publication:

1. F. S. Khan, M. Sugiyama, K. Fujii. Y. Nakano, Arc plasma deposited copper and gold nanoparticles on FTO substrate for electrochemical reduction of CO_2, Adv. Nanoscie. Nanotech. 2019, 3, 1-4.

2. F. S. Khan, M. Sugiyama, K. Fujii, Y. Nakano, Electrochemical Reduction of CO_2 using Cuprous Oxide Particles Supported on Carbon Paper Substrate, Asian J. Nanosci. & Mat., (Accepted and under publication)

3. F. S. Khan, M. Sugiyama, K. Fujii. Y. Tveryanovich, Y. Nakano, Electrochemical reduction of CO_2 using Germanium-Sulphide-Indium amorphous glass structure, Heliyon (Accepted, with minor revision suggested by editor)

4. F. S. Khan, M. Sugiyama, K. Fujii, Y. Nakano, Electrochemical reduction of CO_2 to formic acid using arc plasma deposited copper nanoparticles on In-Sn alloy, Mater. Res. Express (Revision not yet submitted)

5. F. S. Khan, D. Yamashita, K. Watanabe, M. Sugiyama, A. Bocarsly, Y. Nakano, Solar Fuel generation via reduction of CO_2 using Concentrator Photovoltaics under intermittent sunlight (Not yet submitted)

Conferences:

1. F.S. Khan, D. Yamashita, M. Sugiyama, K. Fujii. A. Bocarsly, Y. Nakano, Solar Energy Conversion via reduction of CO_2 using Concentrator Photovoltaics, IPS-22, China (conference proceeding)
2. F.S. Khan, M. Sugiyama, K. Fujii. Y. Nakano, Electrochemical reduction of CO_2 by Arc Plasma Deposition of copper and gold composite nano particles, Nanoscience Meet 2018, Indonesia.